Respect to the CEI 211-4 specifications, in the two dimensional model the effect of the terrain has been considered through image wires (with current $-I_i$), placed at an height

$$h_i' = h_i + 503\sqrt{\frac{2\rho_g}{f_0}}\exp(j\frac{\pi}{4})$$

below the terrain, where h_i is the height of the wire *i* respect to the terrain, f_0 is the frequency and ρ_g is the mean resistivity of the terrain [6]. However, in our case ($\rho_g = 8\,\Omega\,\mathrm{m}$), we have found that the contribution of the images of the real wires is not so significant.

Three dimensional model

In the three dimensional model, with respect to the two dimensional model, the real wires of the power lines are represented as a sequence of linear segments. Moreover, the images of the real wires are not considered. With reference to Fig. 2, the contribution to the magnetic field given by the segment P_1P_2 is

$$\vec{B}_{P_1P_2}(\vec{r}) = \frac{\mu}{4\pi} I\int_{P_1}^{P_2}\frac{\hat{s}\times\hat{r}}{r^2}\,dl = \frac{\mu}{4\pi} I\hat{u}\int_{P_1}^{P_2}\frac{\sin(\theta)}{r^2}\,dl = \frac{\mu}{4\pi d} I\hat{u}(\cos(\theta_1)-\cos(\theta_2))\,,$$

with $\hat{u} = \hat{s}\times\hat{t}$. The overall magnetic field generated by a power line, with *M* wires subdivided in *N* segments, is

$$\vec{B}(\vec{r}) = \frac{\mu}{4\pi}\sum_{i=1}^{M} I_i\left[\sum_{j=0}^{N+1}\frac{\hat{u}_{i,j}}{d_{i,j}}(\cos(\theta_{i,j})-\cos(\theta_{i,j+1}))\right].$$

Outside the region of interest, the wires are approximated with two semi-infinite segments, so

$$\theta_{i,0} = 0 \quad \theta_{i,N+2} = \pi\,.$$

Results

In Fig. 3 we show a comparison result for the two and the three dimensional model. In every point we have measured the magnetic field 2 m over the floor. Besides the estimated value, an error bar representing the maximum and minimum values relative to an uncertainty of 2 m in the position is showed. The area is near a power line tower, that is the worse situation respect to the straight wire approximation assumed in the two dimensional model. In spite of this, we see that the two dimensional model can be used to verify the Italian regulations compliance of power lines, even if the three dimensional model has higher accuracy and almost the same implementation complexity.

Using a numerical model and the power line current recording we can characterize the magnetic field generated by the power line. Besides contour maps, a product obtainable with a numerical model is shown in Fig. 4.

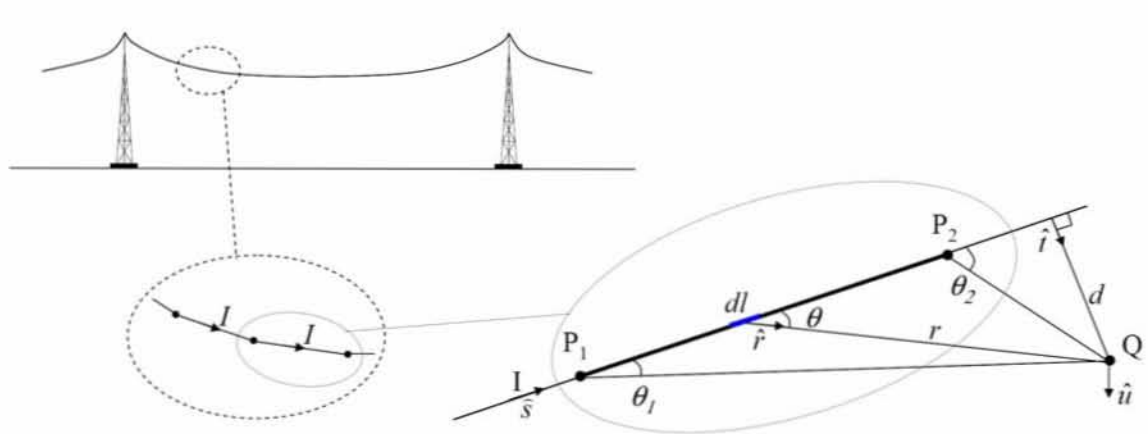


Fig. 2: Three dimensional model geometry for the evaluation of the magnetic field.

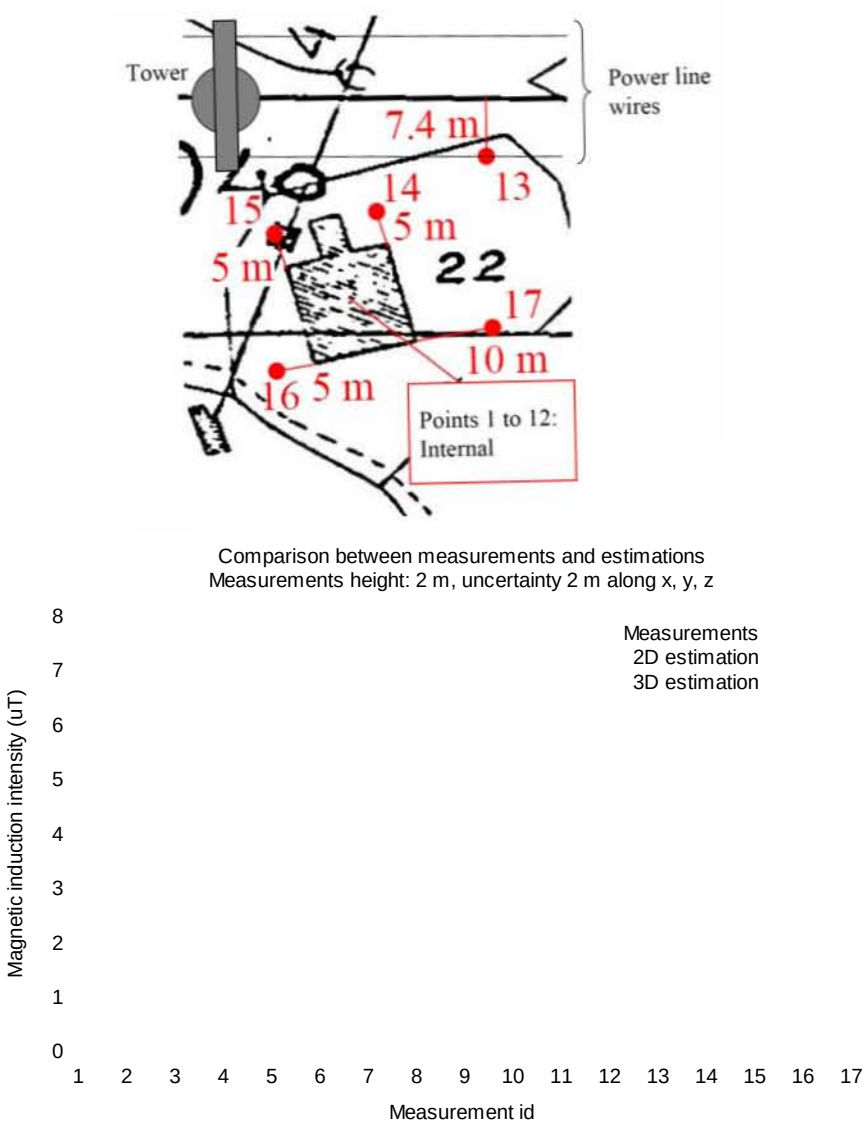


Fig. 3: Comparison between the two and three dimensional model results. Up: position of the measurement points. Down: comparison results. The estimated values are indicated by diamonds. The error bars are relative to assuming a topography and position accuracy of 2 meters.

Electric field model

We have used two 2D models to estimate the electric field generated by power lines. The first one is the model indicated by the Italian regulations CEI 211-4. The second one includes the topography and buildings effects, and is based on the Methods of Moments with pulse basis functions and point matching. We also discuss the 3D extension of the last model, using the AIM formulation in order to reduce the computational complexity of the algorithm. In the following, we describe these models and the results obtained with the 2D models. Results obtained with the 3D AIM model will be shown at the conference.

CEI 211-4 model

As sketched in Fig. 5, the CEI 211-4 numerical model for the electric field generated by power line is the simplest one. The wires of the power line are assumed infinitely straight and parallel, the terrain is assumed perfectly flat and at 0 V potential.

In this case, the electric charge q_i on wire i is obtainable solving the linear system $V = SQ$, where Q and $V = [\psi_i - \psi_0 = \psi_i]$ are the vector containing the electric charge and the voltage of the wires, respectively, and the elements of the elastance matrix S are given by

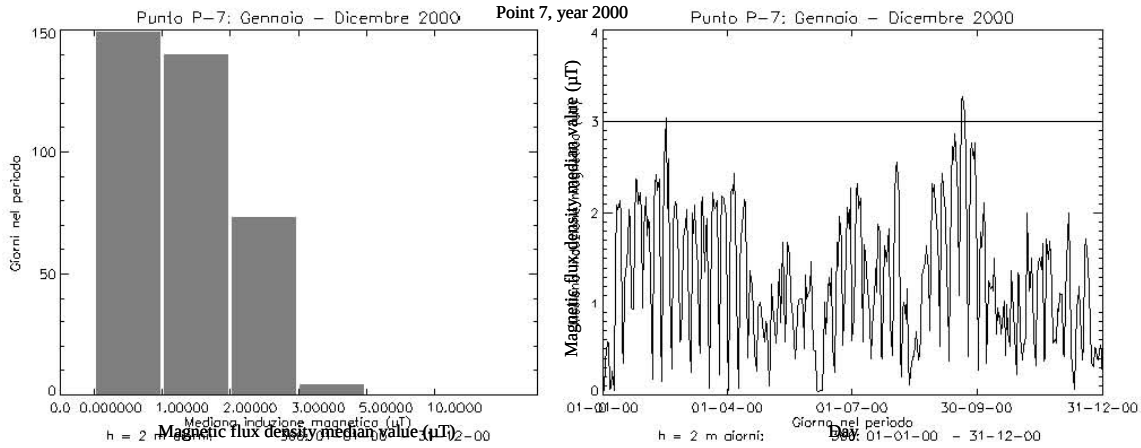


Fig. 4: Median value histogram (left) and graph (right) of the magnetic field as evaluated by the numerical model. The value of 3 μT is the limit indicated by the Italian regulations for a new plant or building.

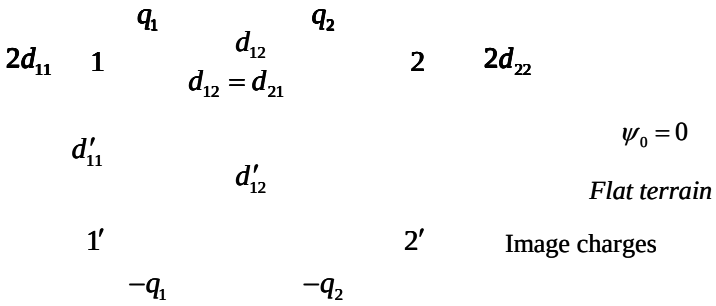


Fig. 5: CEI 211-4 electric field model geometry.

$$s_{ij} = \frac{1}{2\pi\varepsilon} \ln\left(\frac{d'_{ij}}{d_{ij}}\right).$$

When the electric charges are determined, the electric field follows

$$\vec{E}(\vec{\rho}) = \frac{1}{2\pi\varepsilon} \sum_{i=1}^{M} q_i \frac{\vec{\rho} - \vec{\rho}_i}{\vec{\rho} - \vec{\rho}_i}^2 - \frac{1}{2\pi\varepsilon} \sum_{i=1}^{M} q_i \frac{\vec{\rho} - \vec{\rho}'_i}{\vec{\rho} - \vec{\rho}'_i}^2 ,$$

where a primed quantity denotes the position of an image and *M* is the number of wires.

Full 2D model

The full 2D model includes the presence of building and a not flat terrain, as sketched in Fig. 6. It employs a Method of Moments using pulse basis functions to describe the buildings and the terrain, and the point matching technique.

The electric charge on the wires and the amplitude of the linear charge distribution on the segments are again evaluated solving the linear system $V = SQ$, where the first M elements of the vectors Q and V are the charge and the voltage of the wires, respectively, and the remaining ones are the amplitude of the linear charge distribution and the voltage (0 V) of the N_S segments representing the buildings and the terrain. The elements of the elastance matrix S are now given by

$$s_{ij} = \begin{cases} \frac{1}{2\pi\varepsilon} \ln\left(\frac{d'_{ij}}{d_{ij}}\right) & \text{for } 1 \le j \le M \\ \frac{T'_{ij} - T_{ij}}{2\pi\varepsilon} & \text{for } M+1 \le j \le M + N_S \end{cases}$$

where

$$T_{ij} = \frac{1}{L_j} \int_{-L_j/2}^{L_j/2} \ln\left(\left|\vec{\rho}_i - \vec{\rho}_j - \ell\vec{\ell}_j\right|\right) d\ell$$

$$T'_{ij} = \frac{1}{L_j} \int_{-L_j/2}^{L_j/2} \ln\left(\left|\vec{\rho}_i - \vec{\rho}'_j - \ell\vec{\ell}'_j\right|\right) d\ell$$

and L_j is the length of segment *j*, $\hat{\ell}_j$ is its direction, $\vec{\rho}_i$ and $\vec{\rho}_j$ are the position of the wire *i* and of the center of segment *j*, respectively. The electric field is then evaluated as

$$\vec{E}(\vec{\rho}) = \frac{1}{2\pi\varepsilon}\sum_{i=1}^{M} q_i \frac{\vec{\rho}-\vec{\rho}_i}{\left|\vec{\rho}-\vec{\rho}_i\right|^2} - \frac{1}{2\pi\varepsilon}\sum_{i=1}^{M} q_i \frac{\vec{\rho}-\vec{\rho}'_i}{\left|\vec{\rho}-\vec{\rho}'_i\right|^2} +$$

$$+\frac{1}{2\pi\varepsilon}\sum_{i=M+1}^{M+N_s}\frac{q_i}{L_i}\int_{-L_i/2}^{L_i/2}\frac{\vec{\rho}-\vec{\rho}_i-\ell\hat{\ell}_i}{\left|\vec{\rho}-\vec{\rho}_i-\ell\hat{\ell}_i\right|^2}d\ell - \frac{1}{2\pi\varepsilon}\sum_{i=M+1}^{M+N_s}\frac{q_i}{L_i}\int_{-L_i/2}^{L_i/2}\frac{\vec{\rho}-\vec{\rho}'_i-\ell\hat{\ell}'_i}{\left|\vec{\rho}-\vec{\rho}'_i-\ell\hat{\ell}'_i\right|^2}d\ell\,,$$

where the primed entities are relative to the images.

Results

In Fig. 7 we show the comparison between measurements and estimations for two transverse sections respect to the power line in the area under analysis. We consider the presence of the buildings, but do not consider the other obstacles (trees, etc.). This is not enough to obtain a good accuracy. However, the model can give some information about the position of the points were measure the electric field. The power line voltage is almost constant, so we can characterize the electric field generated by the power line by such measurements.

In order to obtain a better accuracy, we can model the power line and the buildings in three dimensions. This brings to increase the number of basis functions, leading the application of the Method of Moments to an unfeasible requests on computational time and/or dynamic memory. An efficient method can be adopted, and in the following we discuss about the use of the AIM formulation in the 3D problem corresponding to the geometry sketched in Fig. 6.

On the use of Adaptive Integral Method

A three dimensional analysis of the area of interest through the Method of Moments to estimate the electric field generated by a power line could be more accurate than a the 2D model, but it leads to unfeasible requests on computational time and/or dynamic memory. In such case the use of a computationally efficient scheme of the Method of Moments gives the opportunity to carry out a 3D analysis. In the following we discuss some implementation notes of the Adaptive Integral Method (AIM). Some results will be presented at the conference.

The Adaptive Integral Method (AIM) [4], [5] has been widely used to solve electromagnetic scattering and radiation problems involving large objects. Its implementation in a Method of Moments (MoM) approach allows, when used with an iterative solver, to accelerate the matrix-vector multiplication and to reduce the number of matrix elements to be stored. In particular, the computational complexity of a matrix-vector multiplication is in the order of $O(N^2)$ using the conventional MoM, where *N* is the number of unknowns, but using the AIM reduces it to $O(N^{1.5}\log N)$ and $O(N\log N)$ for surface and volume scattering, respectively.

The AIM exploits the convolutional property of the free space Green's function. In particular, the interaction between the basis and the testing functions are divided into near and far interactions. The near-interactions matrix elements are evaluated as in the conventional MoM. The other elements (far-interactions matrix elements) are approximated using an auxiliary set of basis function, placed on a uniform cartesian grid. Such auxiliary set of basis function are almost equivalent to the MoM basis function with reference to the elastance matrix elements [5]. By virtue of the auxiliary function are placed on an uniform cartesian grid, and due to the convolutional form of the free space Green's function, the matrix-vector product relative to the far-interactions matrix elements can efficiently evaluated through Fast Fourier Transforms (FFT's).

In case of a half-space limited by a perfectly conductor plane (Fig. 6, extended to three dimensions), the pertinent Green's function doesn't exhibit a convolutional form, so the AIM formulation cannot be applied directly. However, we can exploit the image principle and apply the AIM formulation on the actual object and on its image, increasing the number of points of the uniform cartesian grid to be considered. On the contrary, we can individually consider the real and the image term in the Green's function. In such case, the reflected term exhibits a correlation form on a space variable and its matrix-vector product contribution can be again evaluated by FFT's without increase the number of points of the uniform cartesian grid.

In particular, the needed direct FFT's samples can be obtained from the direct FFT's samples of the auxiliary basis functions of the real objects, obtaining an algorithm with almost the same computational complexity and

dynamic memory requested by the algorithm for the analysis of the object in free space.
In our implementation, the AIM formulation is applied only to the terrain and buildings. The wires of the power line (few unknowns) are considered as in the classical MoM, in order to reduce the number of FFT points along the *z* direction.
Assumed the ground plane at $z = 0$ position, the Green's function has the form

$$g_d\left(\vec{\rho}-\vec{\rho}',z-z'\right)+g_i\left(\vec{\rho}-\vec{\rho}',z+z'\right)=\frac{1}{4\pi\varepsilon\sqrt{\left|\vec{\rho}-\vec{\rho}'\right|^2+(z-z')^2}}-\frac{1}{4\pi\varepsilon\sqrt{\left|\vec{\rho}-\vec{\rho}'\right|^2+(z+z')^2}},$$

where $\vec{\rho}-\vec{\rho}'$ is the distance between source and test position in the *xy* plane. Considering the unknowns images, we have to evaluate

$$\sum_{p'=0}^{N_x-1}\sum_{q'=0}^{N_y-1}\sum_{r'=0}^{N_z-1} g_i\left((p-p')\delta_x,(q-q')\delta_y,2h_z+(r-r')\delta_z\right)\psi(p',q',r')=g_i\left(p\delta_x,q\delta_y,2h_z+r\delta_z\right)\otimes\psi(p,q,-r),$$

where $\otimes$ denotes the three--dimensional convolution, $\delta_{x,y,z}$ denote the cartesian grid spacing along the *x, y* and *z*, respectively, h_z is the minimum *z* coordinate of the cartesian grid enclosing the object (0 in our case), and ψ denotes the auxiliary source values.
If $\Psi(i,j,k)$ denotes the FFT samples of $\psi(p,q,r)$, the FFT samples of $\psi(p,q,-r)$ are given by $\Psi(i,j,-k)=\Psi(i,j,N_z-k)$, being N_z the number of FFT points along the *z* direction.
So, the presence of image sources involves only the multiplication in the transformed domain. The overall computational complexity is dominated by the number of operations required by the direct and inverse FFT and it is almost the same of the free-space case. With similar consideration we can apply the AIM technique also in structure with one or more ground planes, parallel to the coordinate's planes. Such consideration can be useful in evaluation of capacitance for an arbitrary shaped three dimensional structure in the presence of such ground planes.

Conclusions
We have discussed about the use of numerical models of electric and magnetic fields generated by power lines to evaluate the human exposure level. The results obtained from numerical models are been compared to measurements. In case of the magnetic field, a 3D model can be efficiently used, with almost the same complexity of a 2D model. In case of electric field, a 2D numerical model hasn't a good accuracy, even consider the effects of buildings and topography, and measurements are necessary. In such case, a numerical model can be used to choose the measurement's points.
A 3D model can increase the accuracy. We have given some implementation notes about such model (AIM). Results will be shown at the conference.

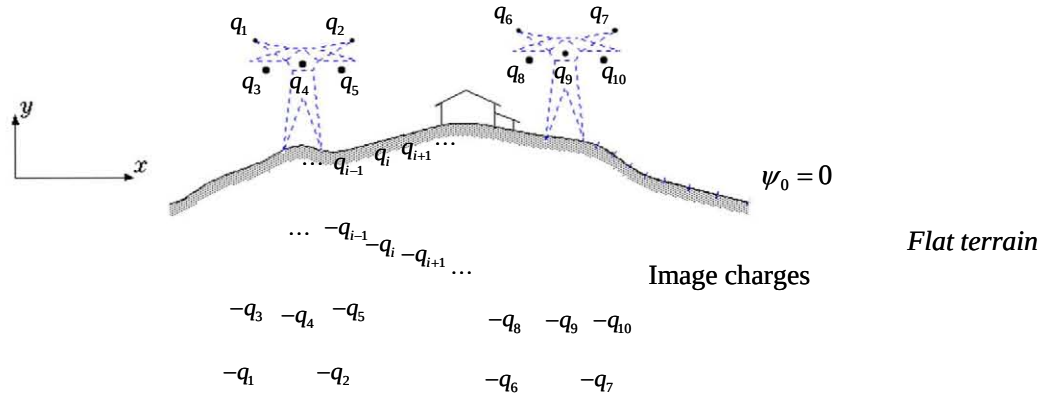


Fig. 6: Full 2D electric field model geometry.

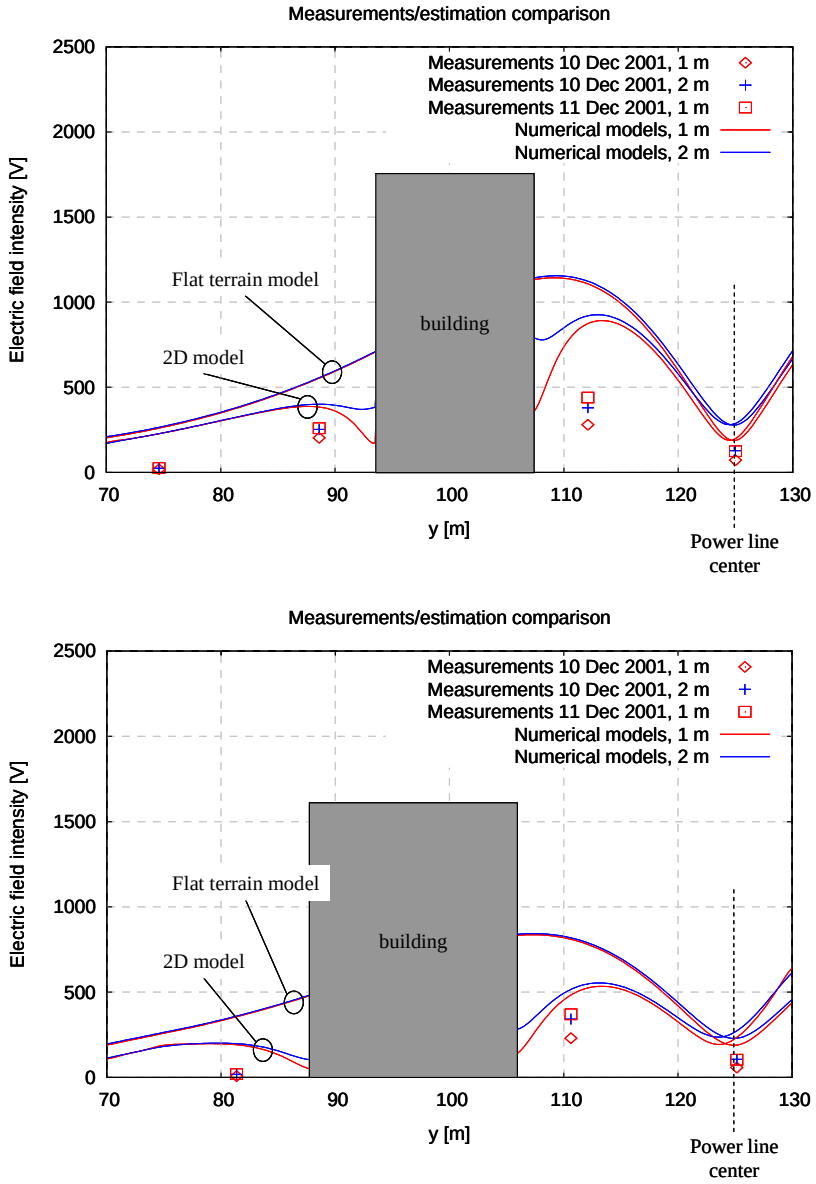


Fig. 7: Comparison between flat terrain and full 2D model results. Two different transverse sections respect to the power line are considered. The number in the legends refers to the quote of the test point.

Bibliography

[1] M. Calamia, "Comune di Montespertoli + 38 contro TERNA S.p.A. – GRTN S.p.A.", *Relazione Tecnica del CTU, 10th April 2002*, filed at Florence Civil Court (Firenze, Italy, in italian).

[2] M. Calamia, "Comune di Montespertoli + 38 contro TERNA S.p.A. – GRTN S.p.A.", *Nota Integrativa alla Relazione Tecnica del 10th April 2002*, 28th August 2004, filed at Florence Civil Court (Firenze, Italy, in italian).

[3] R. F. Harrington, "*Field Computation by Moment Methods*", McMillian Company, New York, 1968.

[4] E. Bleszynski, M. Bleszynski, and T. Jaroszewicz, "AIM: Adaptive integral method for solving large-scale electromagnetic scattering and radiation problems", *Radio Science*, vol. 31, n. 5, Sept.-Oct. 1996, pp. 1225-1251.

[5] C. F. Wang, L. W. Li, P. S. Kooi, and M. S. Leong, "Efficient Capacitance Computation for three-dimensional Structures Based on Adaptive Integral Method", *Progress in Electromagnetics Research PIER*

30, 2001, pp. 33-46.

[6] A Report of the IEEE Magnetic Fields Task Force of the AC Fields Working Group of the Corona and Field Effects Subcommittee of the Transmission and Distribution Committee, "Magnetic Fields From Electric Power Lines Theory And Comparison To Measurements," *IEEE Transactions on Power Delivery*, vol. 3, n. 4, October 1988, pp. 2127–2136.

Overview of IEEE / ISO 11073 RF Wireless: Point-of-care medical device communication – Transport Profiles – Guidelines for the use of RF wireless technology

Joseph J Morrissey

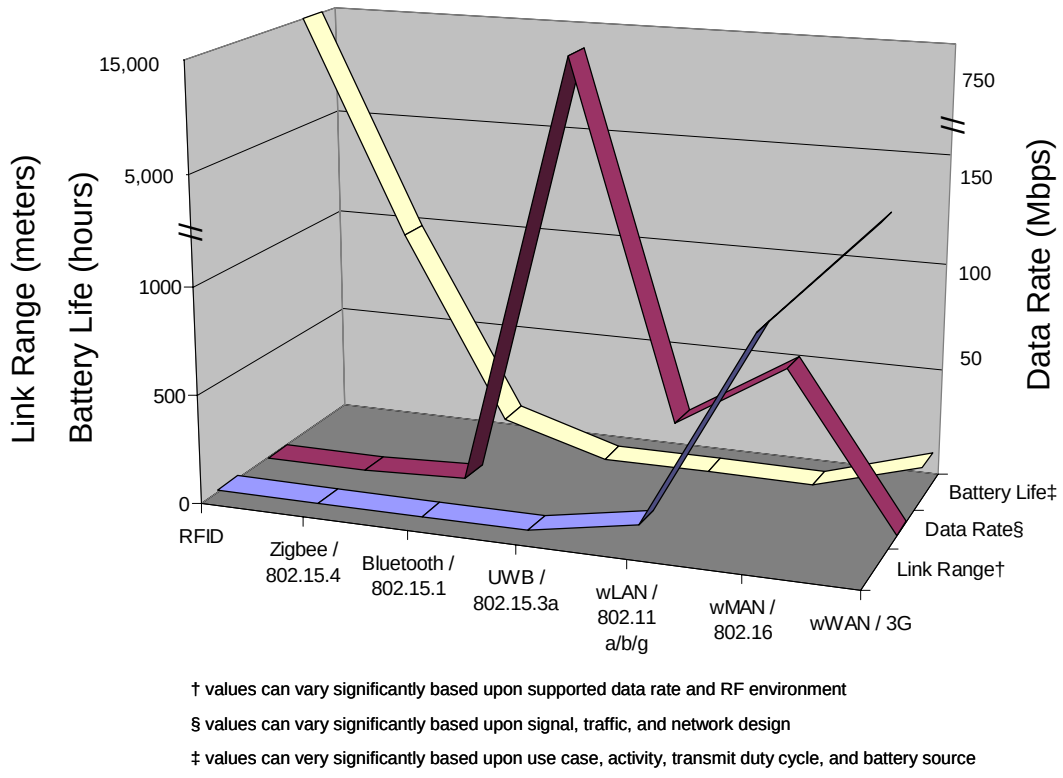
Motorola Labs, 8000 West Sunrise Blvd, Ft. Lauderdale, FL 33322

Abstract: The IEEE / ISO 11073 RF wireless series of standards provides an overview and analysis of the issues related to the use of radio frequency (RF) wireless technology for the transport of data both to and from point-of-care (PoC) medical devices. Currently, several different RF wireless technologies exist that might be applicable, each with different capabilities, stages of maturity in terms of standardization, and active implementation in medical devices and healthcare facilities. It is recognized that RF technologies are rapidly evolving, and new options may become available (or sufficiently established) in the near future offering additional (perhaps superior) solutions for PoC medical device data transport needs. Therefore, the IEEE / ISO 11073 RF wireless series of standards avoids being overly prescriptive but instead aims to assist end users in identifying the necessary requirements and considerations to select an appropriate RF wireless technology solution. Guidance is offered with the objective of allowing medical device manufacturers, wireless equipment manufacturers, healthcare providers, government agencies and any other stakeholders to make reasonable judgments regarding the performance and practical implementation of wireless solutions.

Introduction: Incorporation of wireless technology into point of care (PoC) medical devices has the potential to offer significant benefits to healthcare, specifically home- and mobile- based disease management. An initial IEEE / ISO 11073-30500 Framework and Overview standard outlines use case scenarios to estimate, compare, and contrast the performance of known technologies operating on personal area (wPAN), local area (wLAN), metropolitan area (wMAN), regional area (wRAN), and wide area (wWAN) networks. Major considerations in evaluating performance are 1) the physical requirements of data transport, 2) the quality of service (QoS) requirements associated with the data being transported, and 3) the capabilities of the wireless system. Also considered are related issues such as network architecture, EMI/EMC, co-existence with other data streams, security, cost, power consumption, and technology configurability. Such comparisons are not necessarily intended to endorse an optimal solution, because widely different needs, resources, sizes, and environments associated with healthcare facilities may have a large influence on determining appropriate solutions.

Understanding how these wireless technologies support different quality of service (QoS) requirements (reliability, latency, priority, bandwidth) and how transmit power, link range, battery life and other characteristic features are related to performance is essential [Figure 1]. Optimal performance will largely depend upon the criticality of the medical data and the specific needs and resources of the end user. Related issues include network architecture, EMI/EMC, co-existence with other data streams, security, cost, and technology configurability.

Figure 1. General Overview of Wireless Technology Categories



† values can vary significantly based upon supported data rate and RF environment

§ values can vary significantly based upon signal, traffic, and network design

‡ values can very significantly based upon use case, activity, transmit duty cycle, and battery source

Quality of Service (QoS) requirements for medical data [Table 1] are defined in terms of reliability, latency, priority, and bandwidth. The ability of a wireless technology to provide necessary service to medical data in this context would define its QoS support. A variety of different medical devices exist within any given healthcare facility, with medical data streams having different levels of criticality. While some may be good candidates for wireless chip sets, others may perform better on conventional wired systems. This distinction may not be intuitively obvious to medical device and wireless manufacturers or end users without careful consideration of a complex set of variables. Several other considerations, namely increased benefits of mobility of both patients and healthcare staff, must also be considered. It is entirely possible that the added benefits outweigh certain reductions in QoS support.

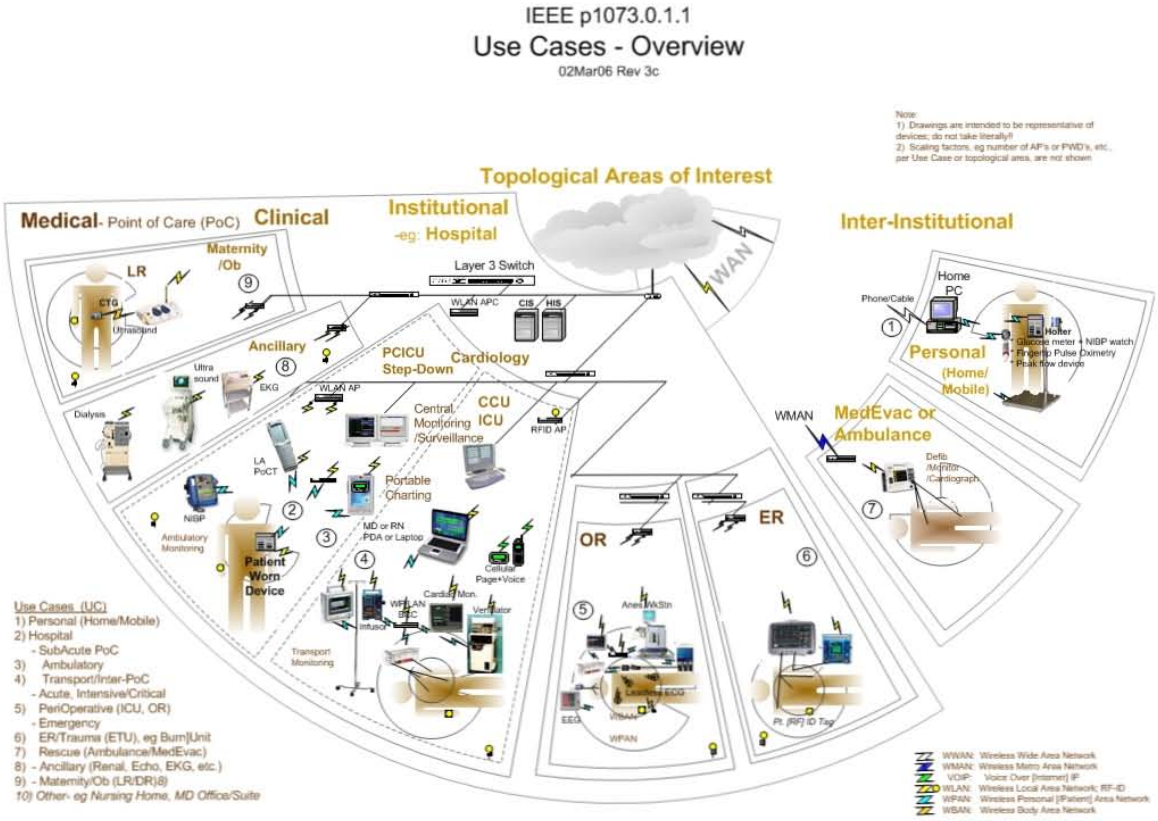
Table 1. QoS requirements for different categories of medical device data

Data Type	Reliability	Latency	Priority	Bandwidth
Alarms / Alerts (Real-Time)	++++ [AAMI EC-13 - onset of asystole to alarm report]	< 250-500 ms [< 10 sec to central station; AAMI EC-13 - onset of asystole, bradycardia or tachycardia to alarm] < 3 s communication latency	++++	+ (64 bytes/alarm) [intermittent]
Positional alert (Real-Time)	++++	< 3 s communication latency	++++	64 bytes /alert [intermittent] (data is per sensor)
Patient state change (Real-Time)	++++	< 3 s communication latency	++	64 bytes/ state change [intermittent] (data is per sensor)
Sensor watch dog / heartbeat	++++	< 1 min communication latency; ~ 1 time per hour	++	64 bytes/ state change [intermittent]
Reminder (Real-Time)	++++	< 3 s to receive from health care system	++	1632bytes/reminder [intermittent]
Waveforms (Real-Time)	+++	< 300 ms (e.g., during balloon pump in OR / ICU) < 3 s to central station < 7 s for telemetry to in-room monitor	+++	+++ [continuous] EEG: 120-4000+ bit/s (3-12 channels / minimal, monitoring, diagnostic) EEG: 120-250 bit/s (minimal, upper-end, BIS™) Ventilator: 50 - 60 bit/s Sp02: 50 – 120 bit/s
Video/Audio (Real-Time)	+++	< 300 ms	++	4Mbit/s (Bi-directional MPEG2 encoded 320X240 @30fps or 640X480 @30fps audio/video streams) 20Mbit/s (Bi-directional HDTV MPEG-4 video stream; 80kbit/s for VoIP)
Physiologic Parameters (Real-Time) [e.g., episodic bp, hr, SpO_2, $ETCO_2$, temp]	+++	< 10 s to central station < 3 s communication latency from nurse to clinician	+++	+ (20 bytes/param at 1/2 to 1 to 5 Hz) [episodic]
Non-Real-Time Parameters	+++	< 15 s time critical PoCT < 60 s otherwise (CLSI PoCT1-A) < 60 minutes for time-stamped, non time-critical items	++	600 bytes/measurement (CLSI PoCT1-A DML)
Non-Real-Time Events	+++	< 3 s in room < 5 s to central station	++	+ [intermittent]

Control/Settings	+++	< 3 s in room < 5 s to central station	+++	+ [manual]
History / archive retrieval	++	< 5 s pushing < 5 s pulling	+	+++ [manual, bursty]
Web Browsing	++	< 5 s pushing < 5 s pulling	+	+++ [manual, bursty]

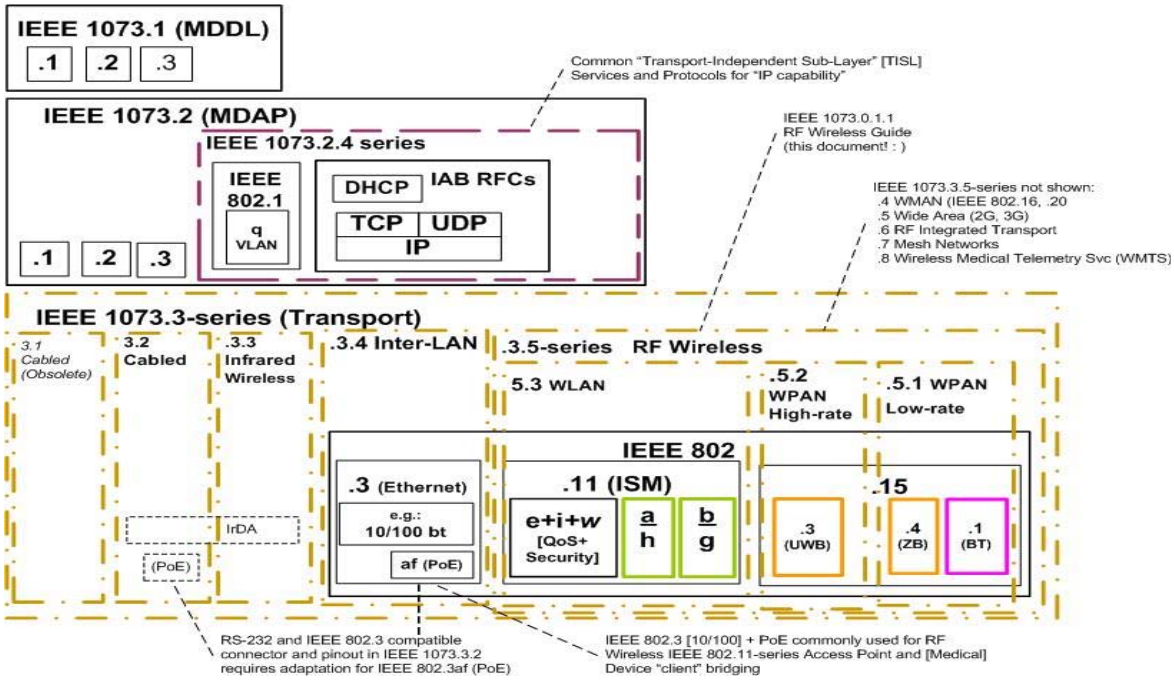
In order to address the use of wireless technology in healthcare, realistic use case scenarios have been developed to allow visual navigation of relevant issues involving QoS requirements and support [Figure 2]. These use cases represent a broad range of typical hospital-, home-, and mobile- healthcare scenarios ranging in degree of criticality and complexity.

Figure 2. Use case topological overview



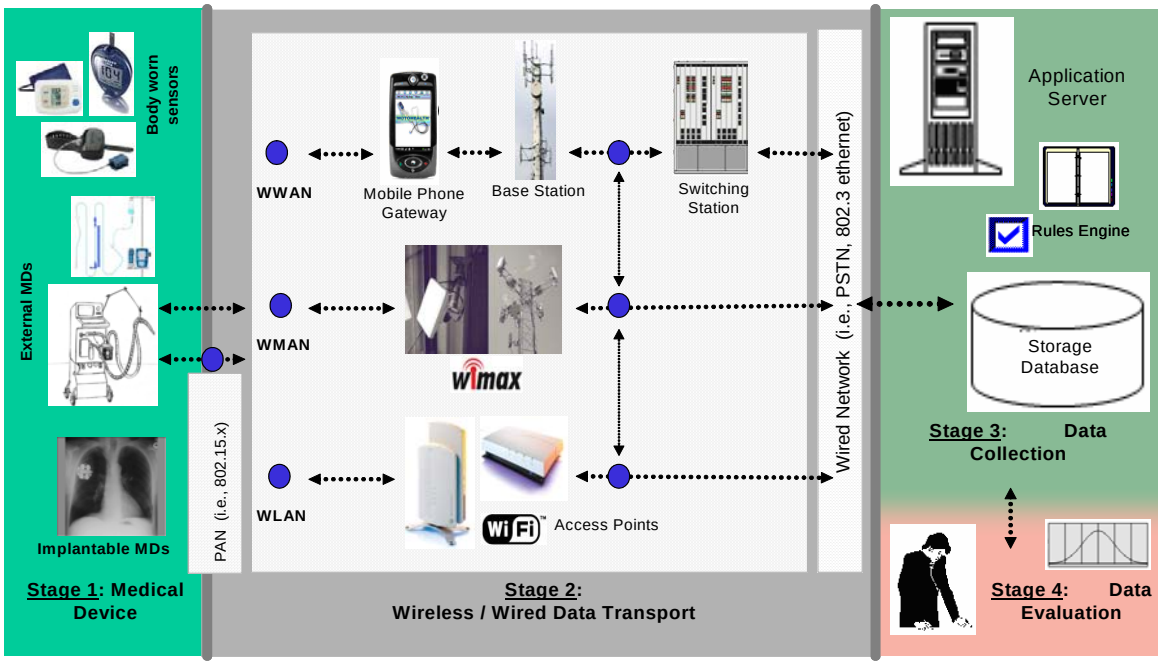
Medical data will often traverse several wireless links en route to the end server / healthcare professional, topological considerations that take different systems into account are necessary [Figure 3]. This example focuses on in-hospital IEEE 802.11 and IEEE 802.15 standards. Other hospital-, home-, or mobile-scenarios were not included to avoid complexity.

Figure 3. Topology Architecture



As medical devices become wirelessly enabled, the definition of a "medical device" becomes ambiguous. IEEE / ISO 11073 standards subdivide different stages of medical data transport [Figure 4] to offer some clarification for future assessment and regulation. Traditional definitions of the US-FDA [http://www.fda.gov/cdrh/devadvice/312.html] and UK-MHRA [http://www.mhra.gov.uk/] generally define MDs as products placed on market for patient health / safety that undergo regulatory approval (i.e., CE mark in the EU, FDA approval in the US) and do not address transport of information across wireless links or networks. In the broadest sense, a wireless MD might also include the host (e.g., data collection unit, server, nurse station) and the wireless links (e.g., IEEE 802.11x, IEEE 802.15.x, IEEE 802.16™, telecomm network, IEEE 802.3).

Figure 4. Stages of wireless medical devices



Summary: Proposed, ongoing, and completed IEEE / ISO 11073 RF Wireless Standards [Table 2] will offer guidance to healthcare providers, medical device manufacturers / vendors, wireless equipment manufacturers / vendors, and relevant agency groups for the use wireless technologies for medical data transport. It is a goal of this standards activity to define optimal wireless profiles and promote plug-and-play operability between commercially available medical devices and wireless systems. The effort primarily considers wireless technologies having physical layer protocols defined by industry standards (i.e., IEEE, ISO, ANSI, ITU-R, ITU-T). Compatibility between data exchange formats and upper layer protocols is also an objective to facilitate efficient plug-and-play interfacing and information exchange.

Table 2. IEEE / ISO 11073 RF Wireless family of standards (those in bold are actively in development)

IEEE Project	Scope	Purpose
IEEE P11073-10101	Nomencature	numeric codes that identify items communicated between systems; partitioned code set that can be use din HL7 messages
IEEE P11073-10201	Domain Information Model (DIM)	Object oriented model: objects, attributes, and methods; all objects specified in ASN.1 notation
IEEE P11073-20000	Application profile – Framework and overview	Scope and purpose for application profile standards - sets and establishes structure for each of the component documents.
IEEE P11073-20400	Application profile – Network service - Framework and overview	Describes the role and types of network services contained within this subset, including their support of transport-specific technologies. This includes key capabilities such as: -Compatibility with IEEE 1073 transport profiles for wPAN, wLAN, wMAN, wWAN -Consistent with QoS outlined in IEEE 802.11e
IEEE P11073-20400	Application profile – Network service - Framework and overview	Describes the role and types of network services contained within this subset, including their support of transport-specific technologies. This includes key capabilities such as: -Consistent with QoS outlined in IEEE 802.11e -Compatibility with IEEE 1073 transport profiles for wPAN, wLAN, wMAN, wWAN
IEEE P11073-20401	Application profile – Network service - Directory	Find and bind services and systems on the network (e.g., a manager for a specific class of devices such as PoCT manager for manufacturer X's devices)
IEEE P11073-20402	Application profile – Network service – Quality of service (QoS) management	Provides a transport-neutral model for application level management of QoS capabilities. This includes detecting the QoS provided by an associated transport profile, as well as setting desired QoS parameters to be negotiated when a connection is established.
IEEE P11073-20403	Application profile – Network services - Location	Patient location, asset tracking, staff location and tracking [throughout supply chain (management) so not counterfeit, correct amount, etc.]
IEEE P11073-20404	Application profile – Network services - Identification	Patient ID, pharmacy ID, supply chain, RFID
IEEE P11073-20500	Application profile – Security – Framework and overview	Overview of issues and strategy for addressing security issues to support plug-and-play medical device communication; incl. security capabilities esp. to support patient demographics data communication[a] consistent / compatible with IEEE 802.11i and HL7 (1073.6.1.1)

IEEE P11073-00101	Technical Report	Guidelines and foundation for RF wireless transport profiles
IEEE P11073-30400	**Transport profile – Internet protocol (IP) [based]**	**Profile the application of IP technologies for use in medical device communication, compatible with IEEE 1073-based Ethernet or wPAN, wLAN, wMAN, wWAN profiles, including vLAN, IP, medical session, QoS, security, UDP, TCP, multicast discovery, addressing characters, wired to wireless infrastructure, etc.**
IEEE P11073-30500	**Transport profile – RF wireless – Framework and Overview**	**Presents the unique concerns and requirements relating to the use of RF wireless technologies for PoC medical device communication. Unique use cases addressed by RF wireless networks; links to guidelines doc 1073.0.0.1**
IEEE P11073-30501	Transport profile – RF wireless – Personal area networks (wPAN), Low-rate	Profile IEEE 802-series standards appropriate for low-rate PoC medical device data transport over short link distances (i.e., personal area networks). [802.15.1[4] Bluetooth, 802.15.4[4] ZigBee]
IEEE P11073-30502	Transport profile – RF wireless – Personal area networks (wPAN), High-rate	Profile IEEE 802-series standards appropriate for high-rate PoC medical device data transport over short link distances (i.e., personal area networks); Ultra wide band (UWB) [802.15.3a[4]]
IEEE P11073-30503	**Transport profile – RF wireless – Local area networks (wLAN)**	**Profile IEEE 802-series standards appropriate for high-rate PoC medical device data transport over in-building networks involving several patient areas (i.e.,802.11a[4], 802.11b[4], 802.11g[4], 802.11n[4] [data prioritization], 802.11i[4] [encrypted transmission to improve security]**
IEEE P11073-30504	Transport profile – RF wireless – Metropolitan area networks (wMAN)	Profile IEEE 802-series standards appropriate for high-rate PoC medical device data transport over large regional areas (i.e., metropolitan area networks) / Broadband / certain UWB technologies
IEEE P11073-30505	**Transport profile – RF wireless – Wide area networks (wWAN)**	**Profile existing licensed telecommunication standards appropriate for PoC medical device data transport over large / regional distances (i.e., wide area networks) / mobile phones (2G [GSM, CDMA, iDEN] and 3G [UMTS, CDMA2000])**
IEEE P11073-30506	RF Integrated Transport[s]	Profile above standards for integrated (e.g., WLAN / WPAN, WPAN / WWAN) data communication
IEEE P11073-30507	Transport profile – RF wireless – Mesh networks	Profile IEEE (802.11s[4], 802.15.5[4]) standards appropriate for low to medium-rate PoC medical device data transport over large / regional distances operating via multiple node relays (i.e., mesh networks)
IEEE P11073-30508	Transport profile – RF wireless – Wireless medical telemetry service (WMTS)	Profile future (IEEE 802-series, other) standards appropriate for PoC medical device data transport developed or modified for operation on WMTS bands

COUPLING TO SPECTACLE FRAMES FROM A 450 MHZ PERSONAL RADIO SOURCE OPERATING ANTERIORLY TO THE HEAD

A. D. BALL, N. E. EVANS, W. G. SCANLON[#], S. J. BURGESS and J. McLAUGHLIN

Centre for Communications Engineering, School of Electrical & Mechanical Engineering, University of Ulster, Shore Road, Newtownabbey, Co. Antrim, N. Ireland, UK, BT37 0QB
 # School of Electrical & Electronic Engineering, Queen's University of Belfast N. Ireland, UK, BT9 5AH.

The RF coupling potential of medium-power UHF personal radios operating in close proximity to wire framed spectacles was quantified in a scenario where the recommended minimum body–radio separation is not respected.

A custom and flexible FDTD simulator written in 'C' (COCA: Code for Coupled Antennas) was used for analysis, with a 2 mm atomically realistic adult head model truncated at the shoulders. The effects of radio orientation and spectacle shape (circular/square) on the polar pattern, induced current profile and SAR distribution was investigated. The undesirable effects of analysing tilted wire elements using the Yee algorithm were overcome by applying Dey-Mittra special update equations. The peak 1 g SAR was situated in the nasal bone region, due to localised parasitic-conductor contact at the bridge of the nose. This parameter was spectacle-shape dependent, as demonstrated by SAR values that were 70 % (rectangular frame) and 174 % (semi-rimless) greater than in the isolated (clean head) case of 3.98 W/kg, for a personal radio input power of 1 W. Partial eye screening occurred when both sets of conducting frames were in place. A maximum coupled current of 16 mA was computed in the semi-rimless frames.

Introduction

Personal radios, transmitting in the lower UHF range (435 MHz), have been identified as primary sources of interference when functioning in close proximity to body worn conductors (e.g. electronic sensing devices [1][2]). Similar effects can also be expected when a PR is operated close to the head, with the user wearing wire framed spectacles [3][4], whereby the minimum body-radio separation of 2.5 cm recommended by a range of manufacturers is not respected, thus placing the transmitting antenna very close to the face and eyes. This is of concern as the eyes are particularly sensitive organs due to their proximity to the surface of the head, their tendency to accumulate damage and cellular debris [5], as well as a limited ability to dissipate heat [6] due to relatively low levels of blood flow compared to other regions of the body.

To date, research into radiation effects in the presence of spectacles has been performed numerically for a cell-phone [7], Personal Digital Assistant applications [8][9], and by measurement [6][10]. The literature shows re-radiation effects [3] along with a rise in peak head SAR [3][8][9], in addition to frequency and spectacle-shape dependence of the average SAR in the eyes [8][9].

The objective of this work was to investigate the effects of a hand held 450 MHz radio fitted with a $\lambda/4$ monopole operated in front of the face (Figure 1a), with a self-developed FDTD program (COCA), by computing the antenna's input impedance, radiation pattern and SAR. These parameters were contrasted to the case when the PR user wore full wire-framed spectacles with rectangular lenses. Dey-Mittra's contour path model was implemented in COCA, enabling the typical practical scenario of a PR tilted by 45° (Figure 1b) to be scrutinised. Finally, COCA was employed to compute the currents induced in a semi-rimless spectacle frame fitted with circular lenses (Figure 1 c & d).

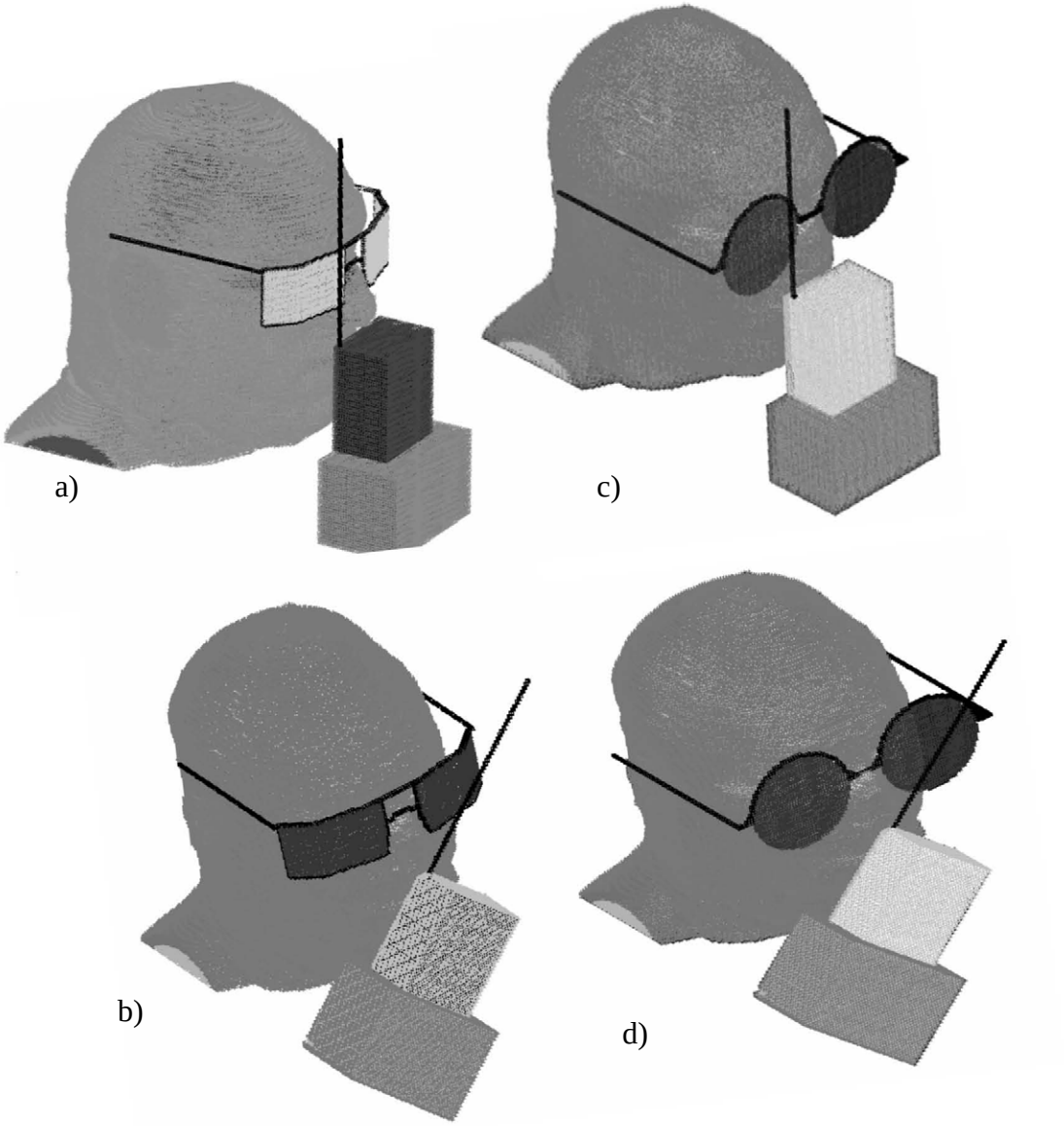


Figure 1: Anterior-head radio / monopole system (vertical & tilted), with wrapped hand. In a) and b) the spectacle frame is 166 mm (0.241 λ) wide, with 122 mm (0.177 λ) legs and lens apertures 68 mm x 40 mm (0.1 λ x 0.06 λ). Cases c) and d) have semi-rimless spectacles, with 152 mm (0.22 λ) legs and a lens diameter of 68 mm.

Methodology

The FDTD computations were performed in a 2 mm grid, using the Brooks anatomically realistic phantom [11] truncated to the head and shoulders. The dielectric properties of the 21 distinct tissue types used (Table 2) were computed at 450 MHz, using a public domain computer program[1] based on published 4-Cole-Cole parameters [12]. The phantom was adapted by removing the normally closed eyelids, so as to leave the eyes exposed as in normal radio use and to investigate the worst-case scenario at the frequency of interest [8][9].

[1] http://niremf.ifac.cnr.it/cgi-bin/tissprop/htmlclie/uniquery

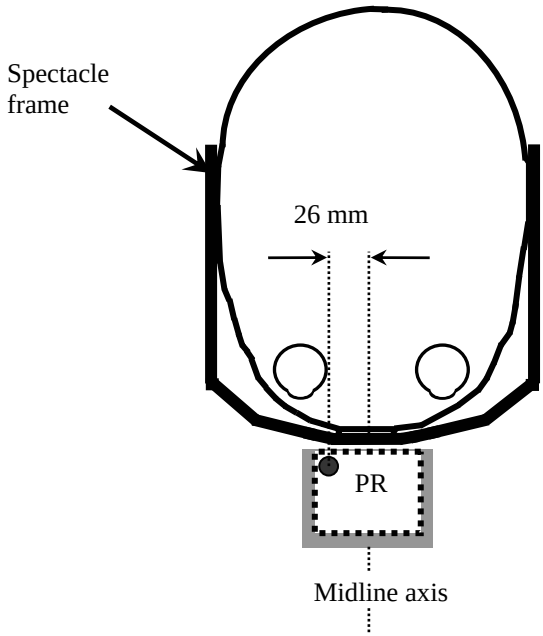


Figure 2: Horizontal section showing relative (rectangular lens) frame, antenna, radio and hand positioning.

The PEC box representing the handset was coated in a loss-less 2 mm insulating layer with $\varepsilon_r = 2$. The $\lambda/4$ monopole, made from 2 mm diameter wire, was corner-located on the top surface of the radio, on the edge nearest the head (4 mm) to mimic worst-case operational conditions (Figure 2). The hand was modelled as a 4 mm core of bone surrounded by a 6 mm layer of muscle and a 2 mm coating of skin, covering all three sides of the handset. The antenna was initially length-adjusted for resonance in isolation, Table 1.

Table 1: Input impedance of a vertical and tilted PR monopole in free space.

	Vertical PR	**Tilted PR**
COCA	74.31+j1.58 Ω	71.69-j1.17 Ω

Table 2: Tissue dielectric properties at 450 MHz.

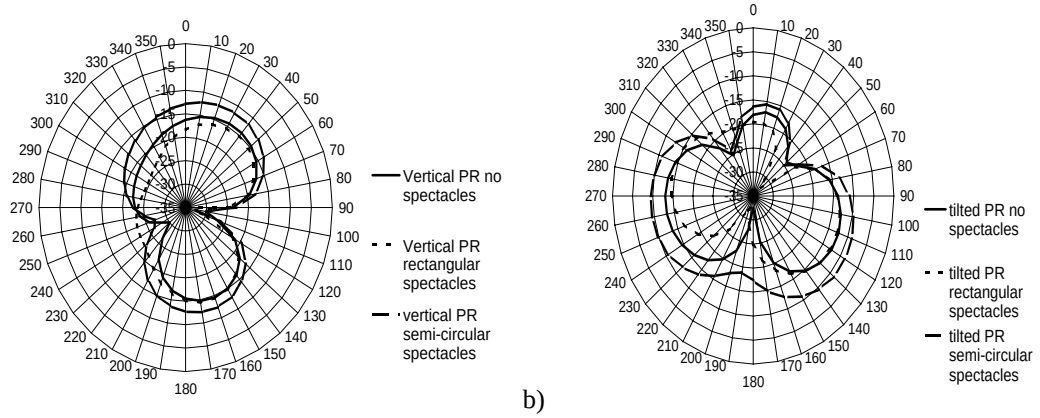
Material	**Conductivity σ (Sm^{-1})**	**Relative permittivity ε_r**
Blood	1.37	63.7
Blood vessel	0.57	46.6
Bone cancellous	0.24	22.2
Bone cortical	0.09	13
Bone marrow	0.03	5.6
Brain grey matter	0.76	56.5
Brain white matter	0.46	41.5
Cartilage	0.6	45
Cerebellum	1.05	54.7
Cerebro spinal fluid	2.26	70.5
Cornea	1.21	58.5
Eye sclera	1.02	57.2
Fat	0.04	5.5
Lens	0.68	47.8
Ligament	0.57	47
Lymph	0.89	61.23
Mucous membrane	0.69	49.2
Muscle	0.8	56.7
Nerve	0.46	34.9
Skin (dermis)	0.71	45.7
Vitreous humor	1.54	69

The conducting spectacle frame consisted of 2 mm square-section PEC: this was positioned for normal wear, terminating behind the ears. Loss-less optical-glass lenses with ε_r = 7.75 were fitted. The only body surface contact made by the frame was at the top of the nose and near the ears, with a separation of 2 mm (1 Yee cell) representing worst-case conditions.

Polar pattern alteration

At 450 MHz the human body acts primarily as a reflector; the low impedance presented to the wave by the body reduces the electric field nearby, whilst increasing the magnetic field. For antenna-body distances greater than $\lambda/4$ from the transmitter**,** a high impedance is presented to the approaching wavefront, which enhances the electric field at the same time as the magnetic field is reduced. At the far side of the body, away from the antenna, there is a deep null caused by power absorbed in tissue [13]. Because of the dominance of the magnetic field between the monopole and the frames, magnetic coupling occurs. This in turn causes an electric current to flow on the frames, which results in an increased electric field in their vicinity: the wire reradiates and the polar pattern changes.

In all cases studied, the radio is offset from the centre of the face. This results in asymmetric polar patterns as energy is absorbed in the head; see the deep null in Figure 3a). Both backward gains are enhanced by re-radiation from the spectacles: this effectively reduces null depths. The addition of either spectacle frame improves the forward gain and highlights the re-radiation due to induced currents. Tilting the handset has the effect of rotating the radiation pattern: Figure 3 b). Nulls appear both at the front and back of the head, but in the latter case are less pronounced than previously. The frontal null is created due to power absorbed in the nose. The increased forward gain was more noticeable with the square spectacles.



a) b)

Figure 3: E_Φ vertical far field patterns, with and without spectacles, for a) vertical and b) tilted personal radios.

Vertical PR SAR results

Computed SAR values were all scaled for an antenna input power of 1 W, and are summarised in Table 3. When the radio is beside the 'clean' phantom head there is detuning: the input resistance falls to 66.1 Ω and the reactance becomes capacitive, at -j0.72 Ω. With spectacles, the input resistance decreases further to 65.4 Ω, and the reactance becomes inductive.

Table 3: Computed input impedance and peak SAR in the head and eyes in the cases of a vertical and tilted PR proximal to the head. SAR levels were normalised against 1 W transmitter output power.

	Vertical PR			**Tilted PR**		
	Without spectacles	**With rectangular lenses**	**With semi-rimless lenses**	**Without spectacles**	**With rectangular lenses**	**With semi-rimless circular lenses**
Input impedance (Ω)	66.1-j0.72	65.4+j1.4	64.36-j0.7	68.73-j9.41	68.94-j6.4	72.82+j8.83
Peak head SAR (W/kg)						
1-g	3.98	6.77	10.89	3.31	8.53	5.38
10-g	2.65	2.75	2.89	2.14	2.41	2.22
1-g peak eye SAR (W/kg)						
Right	1.16	0.7	0.79	0.23	0.14	0.22
Left	0.35	0.31	0.35	1.01	0.51	1.08

Figure 4 shows the SAR profiles in the relevant vertical head sections, with 0 dB corresponding to maximum power dissipation in each case. For 1 g mass averaged SAR, the displacement of the hotspot in each instance is evident. Without spectacles the maximum SAR in the head was 3.98 W/kg; this occurred in the muscle *(oribicularis oris)* between the oral and nasal cavities, at a tissue depth of 12 mm and in a vertical plane displaced 4 mm towards the antenna from the head's midline axis. With the rectangular-framed spectacles, energy absorption is more spread out over the nose, with a peak 1 g SAR of 6.77 W/kg (a rise of 70 %), in the nasal bone region *(nasalis)* at 4 mm deep in the midline plane, due to localised parasitic-conductor contact at the bridge of the nose. In [8] and [9], it is reported that SAR is dependent on the shape and size of the wearer's spectacles. Similarly here, the SAR with semi-rimless spectacles is concentrated at the upper and lower extremities of the nose, rising to 10.89 W/kg, an increase of 174 % and 61 % compared to the isolated and rectangular-framed cases, respectively. Unsurprisingly, for a higher averaging tissue mass of 10 g, the peak SAR without spectacles was lower at 2.65 W/kg. Increases still occurred in the nasal region (though not as significant), up 3.77 % to 2.75 W/kg with the rectangular frames, and 9.1% to 2.89 W/kg with the semi-circular. The human head is a complex, highly detailed organ; indeed the human eye or pinna/external ear have masses of as little as 10 g [14]. Furthermore, certain cells or neurons in the brain can be misrepresented by 1 g of tissue [14]. An 8 mm^3 Yee grid is employed here, which could explain the relatively high 1 g semi-circular spectacle SAR result. This suggests that the peak 1 g SAR is associated with a single hot-spot rather than a general increase in SAR values within the user's head.

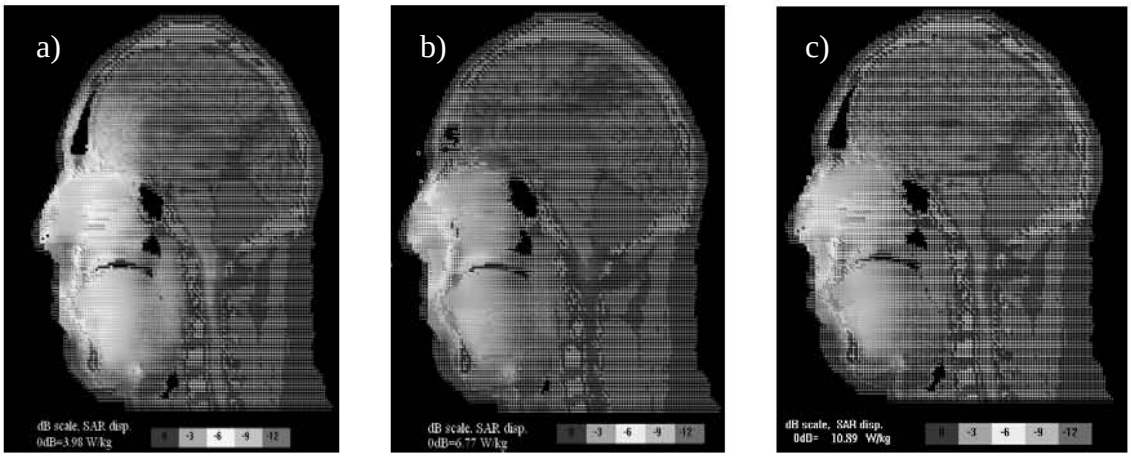


Figure 4: 1 g mass averaged SAR for a vertically-oriented PR beside head a) clean b) with rectangular-framed spectacles and c) with semi-circular frames.

Eye SARs were computed to establish conditions in this particularly sensitive body tissue. With the antenna passing 30 mm from the right eye, and without spectacles, the 1-g peak SAR was 1.16 W/kg. For the left eye, 80 mm from the antenna, the corresponding value was more than 70 % lower (0.35 W/kg). Partial eye screening occurred when both sets of conducting frames were in place; the 1-g SAR fell by 40 % in the right eye and 11.4 % in the left with the rectangular frames in use, as noted in Table 3. A similar phenomenon occurred with the semi-circular frames, with a 32 % SAR reduction in the right eye and an unchanged SAR in the left. All reported SARs were computed for a CW excitation, which implies that they would be further reduced if realistic TDMA duty cycles were taken into account: consequently, they are well within the IEEE guidelines for occupational users. SAR is, however, proportional to the antenna input power, which implies that if transmitter output level rises (a current trend in PR design as hardware improves) then safety limits are likely to be exceeded.

Tilted PR SAR results

Here, the PR was tilted by 45°, as illustrated in Figure 1b. Rotating the radio caused the free space input resistance to decrease by 4.12 %. However, turning the handset had a more noticeable effect on the input reactance, as it became more capacitive - see Table 3.

Placing the spectacles on the phantom caused both the input resistance and reactance to increase positively. Inclination of the radio caused the frame-free 1 and 10 g SARs to be 17 % and 19 % lower than in the vertical PR case, respectively, at 3.31 and 2.14 W/kg. The peak 1g SAR in the eye was situated close to the monopole's feedpoint, in the left eye (1.01 W/kg). Both peak eye SARs without spectacles were less than, or equal to, those with frames and the vertical radio. The 1 g mass averaged SAR profiles with and without spectacles are presented in Figure 5.

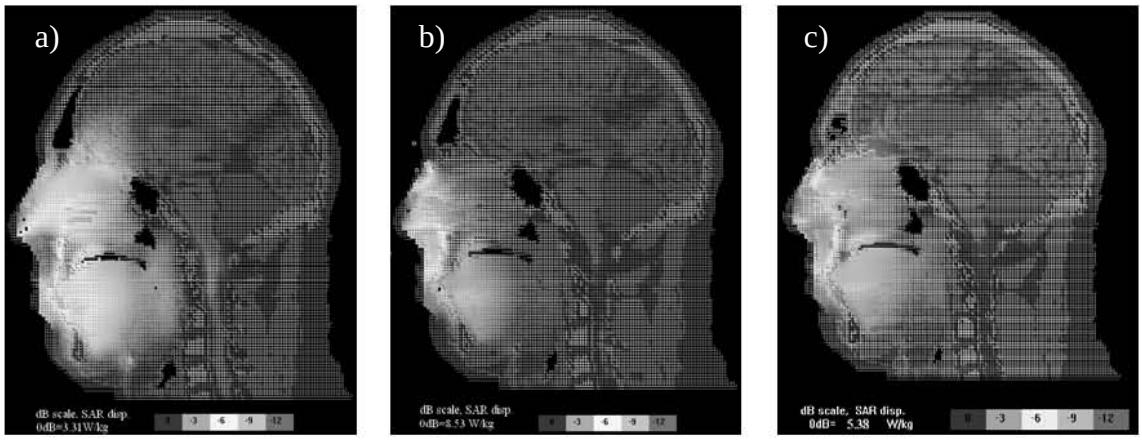


Figure 5: 1 g mass averaged SAR for a tilted PR close to head a) 'clean' b) with a rectangular frame and c) with semi-rimless circular lenses.

As with the vertical PR, the SAR hotspot without spectacles is situated between the oral and nasal cavities. With rectangular-framed spectacles, a second very distinctive concentration is generated at the top of the nasal bone region. There is less SAR 'spread' than in the corresponding vertical PR case (Figure 5b). For semi-circular frames, substantial SAR spreading is again evident.

With the rectangular frames the eyes were partially screened, as substantiated by the 50% reduction of the SAR in the eye nearest the antenna, and 39 % decrease in the other. However, only marginal changes occurred in the case of the semi-circular frames: SAR in the left eye increased by 7 % and decreased in the right by 4 %.

Induced currents

The induced current distribution on spectacle frames has previously been investigated at 1.5 GHz in [7], with a mobile telephone radiating 1 W close to the ear of an anatomically based head model. Two different types of spectacle frames were studied - one with rims and legs both metallic, and the other rimless, with metallic legs only. Current profile discontinuities were present in this model, where the nosepiece intersected each lens' outer contour and at the intersection of the metallic leg and outer rim. The discussion on circular frames has a number of similarities with electrically small loop antennas, which are equivalent to infinitesimal magnetic dipoles; the current distribution in loops of perimeter less than 0.3 λ is taken to be constant around the loop [16].

Computing induced current in a pair of spectacles is challenging in terms of EM simulation, as this creates a number of discontinuities. Because of this, the simulations here were done in two stages. Firstly, a 'flat' spectacle model was assembled (Figure 6a), after which the legs were bent, as depicted in Figure 6b.

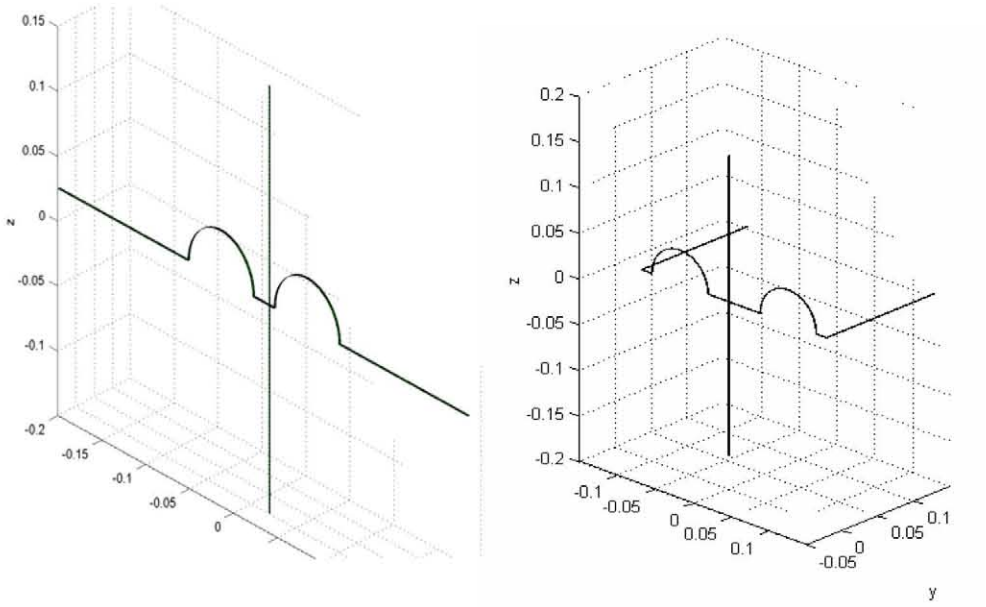


Figure 6: Dipole coupled to a) flat spectacle frame b) a spectacle frame with bent legs; in b) Zin= 64.4–j9.2 Ω.

This done, the induced currents were computed with COCA, as illustrated in Figure 7.

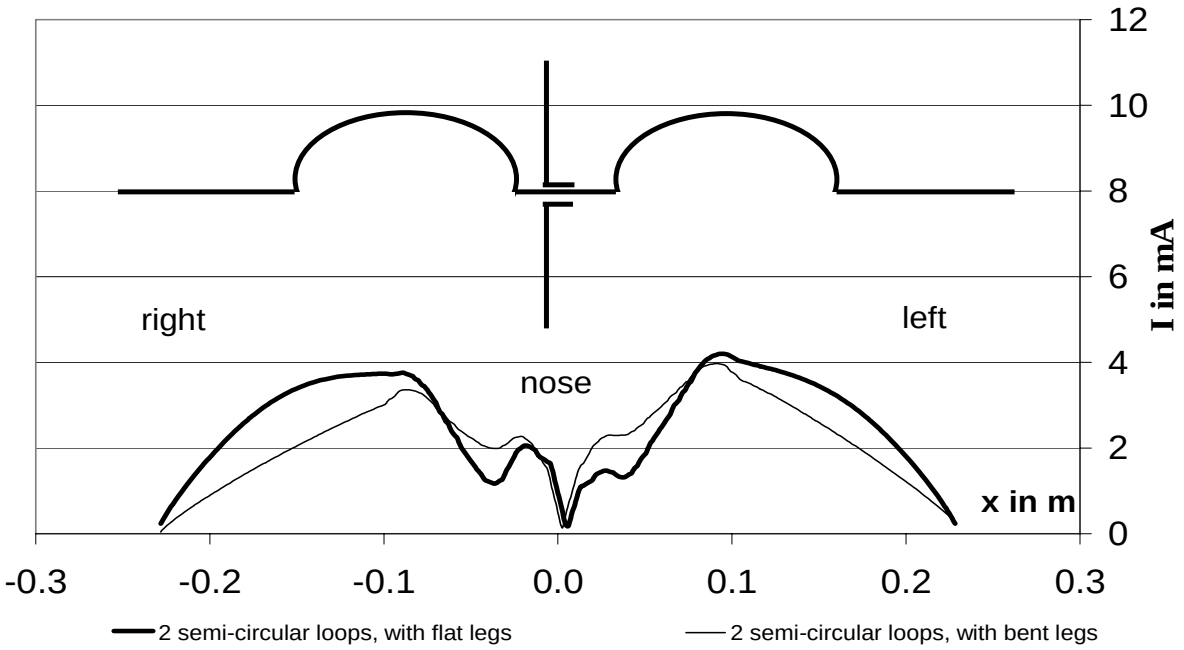


Figure 7: Induced current in the top section of half-rim wire frames adjacent to a 450 MHz dipole (P_{in} = 0.32 W).

The spectacles coupled to the dipole have an overall length of 0.6 λ: two pseudo standing waves are generated that reach minima at the outer extremities of the spectacle legs and at the middle of the nosepiece. Two small reflections at both nosepiece extremities (T junction) emerge, with current maxima of 4 mA at the top of each loop. Bending the legs by 90° causes the induced current to decrease overall. The currents computed are significant, reinforcing the source of the increased forward gains obtained.

Finally, the result of introducing the phantom head was investigated. The PR monopole was corner-located on the handset chassis and held to the right of the user's nose, as illustrated in Figure 2, causing the radiating antenna and case to be strongly coupled to the adjacent semi-circular lens. On this basis, the left lens was shadowed by the nose. This gave a smoother, full standing wave (Figure 8), with current maxima of 16 and 11 mA. The increased current magnitude is because of less detuning in this case, plus the majority of the energy radiated by the monopole is above the PR's 'groundplane'.

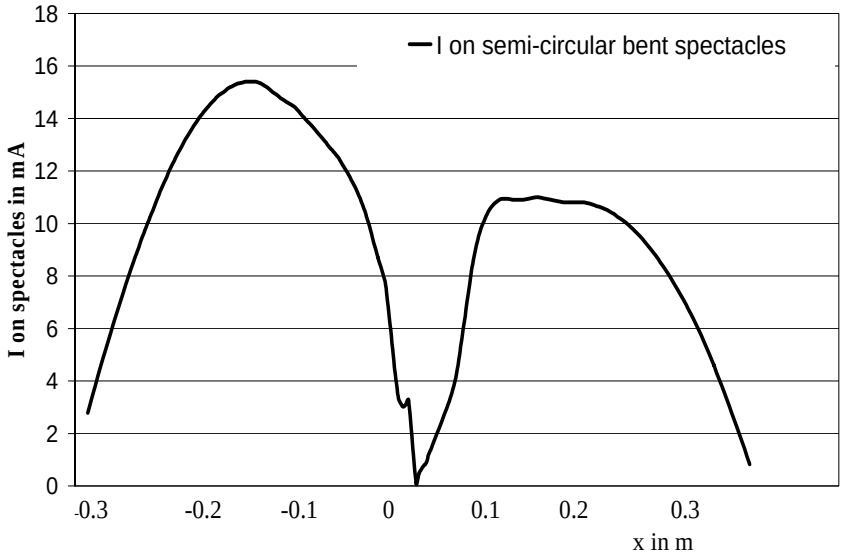


Figure 8: Induced current on semi-circular spectacles with 90° legs, coupled to a vertical 450 MHz monopole / case close to an anatomically realistic head (P_{in}= 0.32 W).

Conclusions

The coupling between a personal radio handset and the human head was investigated at 450 MHz, for two realistic radio orientations, vertical and tilted by 45°. For each orientation, a spectacle-free phantom was contrasted to a model wearing rectangular and semi-circular frames. In each simulation the polar pattern, SAR distribution and induced current profiles were computed.

Absorbed power levels were dependent on the PR's orientation and on the shape of the wire spectacle frames, as evidenced by a 1g SAR ranging between 3.31 and 10.89 W/kg. In the instance of the vertical PR, partial eye screening occurred when both sets of conducting frames were in place. This was only the case with the rectangular frames when the PR was tilted. In general, frame-conductor re-radiation enhances polar pattern forward gain and reduces backward-facing nulls.

Magnetic coupling between the PR and the semi-circular frames caused a cosine-like standing-wave to be developed on the frames, with unequal maxima on the right and left semi-circular loops because of obstructive tissue absorption.

References

[1] Ball A. D., Evans N. E., Troulis S. E., Scanlon W. G. and Burgess S. J., "RF interference (RFI) between uhf personal radios and biomedical monitoring sensors," *Proc. IEE Seminar on Telemetry and Telematics,* London, April 2005, pp. 4/1 - 4/5.

[2] Ball A.D., Evans N. E., Troulis S. E. & Scanlon W. G., "An FDTD study of the interaction between body-worn biomedical-monitor wires and a coupled 435 MHz dipole radiator," *Bioelectromagnetics 2005,* Dublin, June 2005, pp. 92-96.

[3] Troulis S.E., Ball A.D., Evans N.E. and Scanlon W.G., "SAR for adult and child users of 450 MHz Personal-radio handsets operating anteriorly to the head," *3rd International Workshop on Biological Effects of EMF,* Kos, Greece, Oct 2004, pp. 457-464.

[4] Ball A.D., "A Numerical Investigation of the Electromagnetic Coupling Between Body-Worn Conductors and UHF Antennas in Close Proximity," PhD Thesis, University of Ulster, Jordanstown, N. Ireland, 2006.

[5] Dimbylow, P.J. and Mann, S.M., "SAR calculations in an anatomically realistic model of the head for mobile communication transceivers at 900 MHz and 1.8 GHz," *Physics in Medicine and Biology,* Vol. 39, No. 10, Oct. 1994, pp. 1537-53

[6] Anderson, V. and Joyner, K.H., "Specific absorption rate levels measured in a phantom head exposed to radio frequency transmissions from analog hand-held mobile phones," *Bioelectromagnetics,* Vol. 16, No. 1, 1995, pp. 60-69.

[7] Wang J., Joukou T. and Fujiwara O., "Localized specific absorption rate in the human head in metal-framed spectacles for 1.5 GHz hand-held mobile telephones," *Trans. Inst. Electrical Engineers of Japan,* Vol. 118-A (11), 1998, pp. 1234–1240.

[8] Whittow, W.G. and Edwards, R.M.,"A study of changes to specific absorption rates in the human eye close to perfectly conducting spectacles within the radio frequency range 1.5 to 3.0 GHz," *IEEE Transactions on Antennas and Propagation,* Vol. 52, No. 12, Dec. 2004, pp. 3207-12.

[9] Edwards, R.M. and Whittow, W.G., "Applications of a genetic algorithm for identification of maxima in specific absorption rates in the human eye close to perfectly conducting spectacles," *IEE Proceedings-Science, Measurement and Technology,* Vol. 152, No. 3, May 2005, pp. 89-96.

[10] Griffin D.W., "A microwave antenna method of measuring the effect of metal-framed spectacles on microwaves near the eye," *Proc. Antennas and Propagation Society International Symp.,* 1983, Vol 21, pp. 253-256.

[11] Mason, P. A., Ziriax, J. M., Hurt W. D., Walters T. J., Ryan K. L., Nelson D. A., Smith K. I. and D'Andrea J. A., "Recent advancements in dosimetry measurements and modelling," in Radio Frequency Radiation Dosimetry (B. J. Klauenberg and D. Miklavcic, Eds., Kluwer, Norwell, MA, 2000), pp. 141–155.

[12] Gabriel S., Lau R. W. and Gabriel C., "The dielectric properties of biological tissues: III. Parametric models for the dielectric spectrum of tissues," *Phys. Med. Biol.*, Vol. 41, 1996, pp. 2271-2293.

[13] James J.R., Mobile Antenna Systems Handbook, Artech House, 2nd Ed., 2001, ISBN 1580530079.

[14] Lin, J.C., "Specific absorption rates (SARs) induced in head tissues by microwave radiation from cell phones", *IEEE Antennas and Propagation Magazine*, Vol. 42, No. 5, Oct. 2000, pp. 138-1399.

[15] Lin, J.C., "Safety standards for human exposure to radio frequency radiation and their biological rationale," *IEEE Microwave Magazine*, Vol. 4, No. 4, Dec. 2003, pp. 22-26.

[16] Balanis C. A., "Antenna Theory, Analysis and Design," 2nd edition, John Wiley & Sons Inc., 1997.

[17] ANSI, ANSI / IEEE, (1992); *C95.1-1992: IEEE Standard for safety levels with respect to human exposure to radio frequency electromagnetic fields, 3 kHz to 300 GHz,* IEEE, New York.

[18] International Commission on Non-Ionising Radiation Protection, (1999): "ICNIRP statement - health issues related to the use of hand-held radiotelephones and base transmitters," *Health Phys.*, Vol. 70, No. 4, pp. 587- 593.

[19] Troulis S. E., Scanlon W. G., and Evans N. E., "Effect of a hands-free wire on specific absorption rate for a waist-mounted 1.8 GHz cellular telephone handset," *Phys. Med. Biol.*, Vol. 48, 2003, pp. 1675-1684.

EMF DOSIMETRY INSIDE THE EMBRYO EXPOSED BY THE PLANE WAVE IN THE FREQUENCY RANGE OF 10 MHZ TO 3 GHZ

HIROKI KAWAI[1], TOMOAKI NAGAOKA[1], SOICHI WATANABE[1], WOLFGANG KAINZ[2], KAZUYUKI SAITO[3], MASAHARU TAKAHASHI[3], AND KOICHI ITO[4]

[1]NATIONAL INSTITUTE OF INFORMATION AND COMMUNICATIONS TECHNOLOGY, 4-2-1 NUKUI-KITAMACHI, KOGANEI, TOKYO, 184-8795 JAPAN
[2]U.S. FOOD & DRUG ADMINISTRATION, 12725 TWINBROOK PARKWAY, ROCKVILLE, MD, 20852 USA
[3]RESEARCH CENTER FOR FRONTIER MEDICAL ENGINEERING, CHIBA UNIVERSITY, 1-33 YAYOI-CHO, INAGE-KU, CHIBA-SHI, CHIBA, 263-8522, JAPAN
[4] FACULTY OF ENGINEERING, CHIBA UNIVERSITY, 1-33 YAYOI-CHO, INAGE-KU, CHIBA-SHI, CHIBA, 263-8522, JAPAN

Abstract
This paper presents the computational electromagnetic field (EMF) dosimetry inside a woman-torso model, which is exposed to E- and H-polarised waves, in the first gestational month using the finite-difference time-domain (FDTD) method over the frequency range from 10 MHz to 3 GHz. First, parametric models for the dielectric spectrum of fetus and those of amniotic fluid are demonstrated. Second, the whole-body average SAR in the embryo is calculated, when the incident power density of plane waves is ICNIRP or IEEE occupational reference level. As a result, the maximum value is less than 0.4 W/kg (occupational limit) over the frequency range from 10 MHz to 3 GHz. Finally, the internal SAR distributions inside the torso model are also shown at 10 MHz, 100 MHz, and 1 GHz. As a result, the SAR distribution around the embryo is dependent on the frequency and polarized wave in the first gestational month.

1. Introduction

Today many devices emitting EMFs are widely used in the close vicinity of the human body. Consequently, the evaluation of the specific absorption rate (SAR) in various models, such as adults, children, and pregnant women and their fetuses is necessary. Especially the priority on EMF dosimetry in embryos and fetuses is growing [1]. In the early term of pregnancy, it could be possible that the embryos are exposed to EMFs when mothers do not know their pregnancy yet. Therefore, EMF dosimetry in the embryos is important.

Until now, Fleming and Joyner [2] have proposed the EMF dosimetry inside the embryo in 80-100 MHz and fetus across the range 300-1500 MHz, when the pregnant women are exposed to plane wave. In addition, Dimbylow [3] have presented the EMF dosimetry inside a whole-body pregnant woman and her developing fetus in 8-, 13-, 26- and 38-weeks of gestation at 50 MHz. However, the dosimetry inside the embryo over the wide frequency range have not minutely evaluated yet.

Hence, this paper presents the computational EMF dosimetry inside a woman-torso model, which is composed by five types of tissues, in the first gestational month, when the model is exposed to E- and H-polarised waves. Here, the EMF is calculated using the FDTD method [4] over the frequency range from 10 MHz to 3 GHz. Furthermore, the incident power density of plane waves is the international EMF reference revels (ICNIRP [5], IEEE [6], and occupational limit) in each frequency. Moreover, the internal SAR distributions inside the torso model are also calculated at 10 MHz, 100 MHz, and 1 GHz.

2. Models and method

2.1 Dielectric properties of embryo

The dielectric properties of biological tissues are very important parameters for the EMF dosimetry. Gabriel [7] has proposed parametric models for the dielectric spectrum of various types of tissues using the summation of 4-Cole-Cole equation. The dielectric properties at the target frequency are given by the following equation [7].

$$\hat{\varepsilon}(\omega) = \varepsilon_{\infty} + \sum_{n=1}^{4} \frac{\Delta\varepsilon_n}{1 + (j\omega\tau_n)^{(1-\alpha_n)}} + \frac{\sigma_i}{j\omega\varepsilon_0} \tag{1}$$

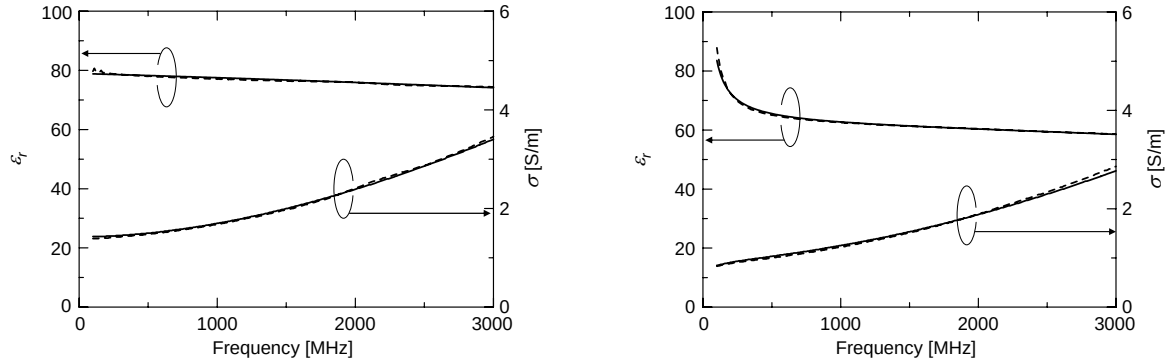
where ε_∞ is the material permittivity at terahertz frequency, ε_0 is the free-space permittivity, σ_i is the ionic conductivity, and $\Delta\varepsilon_n$, τ_n, α_n are material parameters for each dispersion region.However, parametric models of expectant tissues, which are the amniotic fluid, placenta, and fetus (embryo), have not proposed yet in [7].

In fetal tissues, substituted dielectric properties from adult tissues using the variation in the water content [8] are usually used [3]. In addition, the properties of placenta are about the same values of blood, because the composition of the two is about the same. Moreover, Luca *et al* [9] have proposed the parametric model of the conductivity of amniotic fluid over the frequency from 1 MHz to 1 GHz.

Ito *et al* [10] have demonstrated the measured dielectric properties of fetus of rabbit and those of amniotic fluid of human over the frequency range from 100 MHz to 3 GHz. However, their results cannot apply to the other frequency. Therefore, we present the parametric models using the Eq. (1), to expand the wide frequency range. Table 1 describes the parameters of amniotic fluid and those of fetus for the Eq. (1). These parameters are defined using the simplex method based on the differences between the estimated properties by Eq. (1) and measured values as shown in Fig. 1. The parameters can realize the minimization of the difference between the estimated and measured values. In this paper, the dielectric properties based on the parameters in Table 1 are used from 10 MHz to 3 GHz.

Table 1 Parameters of amniotic fluid and those of fetus for the Cole-Cole equation

Tissue	ε_∞	$\Delta\varepsilon_1$	τ_1 [ps]	α_1	$\Delta\varepsilon_2$	τ_2 [ns]	α_2	$\Delta\varepsilon_3$	τ_3 [μs]	α_3	σ_i
A_fluid	4	75	7.23	0.14							1.42
Fetus	4	57	8.38	0.10	6000	133	0.1	1.20E+06	318	0.10	0.12

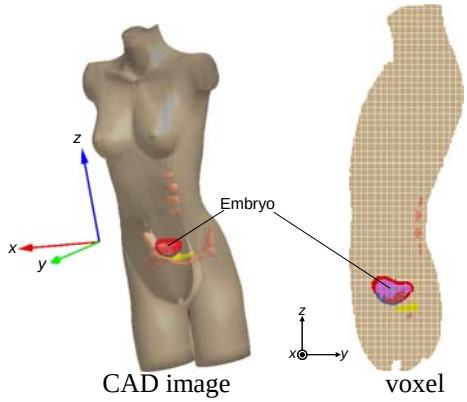


(a) Amniotic fluid (b) Fetus

Fig. 1 Graphic representation of dielectric properties of amniotic fluid and fetus using Eq. (1) and Table 1 (line) together with the measured data (dotted line) [10].

2.2 Numerical model

Figure 2 shows a woman-torso model in the first gestational month. This model was scaled down from a woman-torso model in the 35th gestational week based on the external shape and magnetic resonance (MR) images [11]. The model was segmented seven different types of tissues, which were body, bone, bladder, uterus, embryo, placenta, and amniotic fluid. However, in the first gestational month, the amniotic fluid and placenta have note generated yet. Hence, we substituted the dielectric properties of uterus for the values of the two.



CAD image voxel

Fig. 2 Torso model of woman in the first gestational month.

2.3 Numerical condition

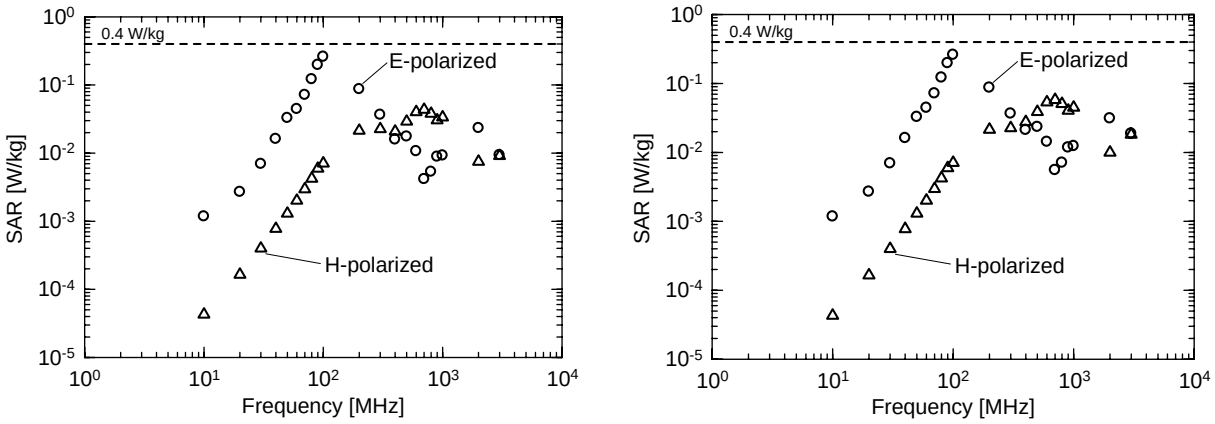
The FDTD software (X-FDTD ver. 6.3.8.3, by Remcom Engineering AG, PA, USA) was used for the EMF calculating inside the torso model. The parameters of FDTD calculation employed in this paper were as follows. The cell size was 2.5 mm. The numerical region was 190 × 150 × 413 cells (475 × 375 × 1032.5 mm^3). In addition, the absorbing boundary condition was the perfectly matched layer (PML) (eight layers).

Dielectric properties of the tissues, which were excluding the fetus, were based on the parametric models in [7]. Here, the properties of body was the 2/3 those of muscle. The incident waves were E- (E_z applied) and H-polarized (E_y applied) waves propagating from the front to the back of the model. The incident power density was from 1 to 5 mW/cm^2 (ICNIRP) or 1 to 10 mW/cm^2 (IEEE), which were the reference levels for occupational exposure to EMFs over the frequency range from 10 MHz to 3 GHz [5], [6].

3. Results

3.1 Whole-body average SAR

Figure 3 (a) and 3 (b) show the calculated results of the whole-body average SAR in the embryo over the frequency range from 10 MHz to 3 GHz, when the incident power density is ICNIRP or IEEE occupational level, which is dependent on the frequency. From Figs. 3 (a) and 3 (b), the SARs by E- and H-polarized waves are less than 0.4 W/kg (occupational limit) from 10 MHz to 3 GHz in both incident levels. In addition, the maximum value by the H-polarized wave is lower than that by the E-polarized wave in the estimated frequency range.



(a) ICNIRP (b) IEEE

Fig. 3 Whole-body average SAR inside the embryo by the plane waves' exposure (circle: E-polarized wave and triangle: H-polarized wave).

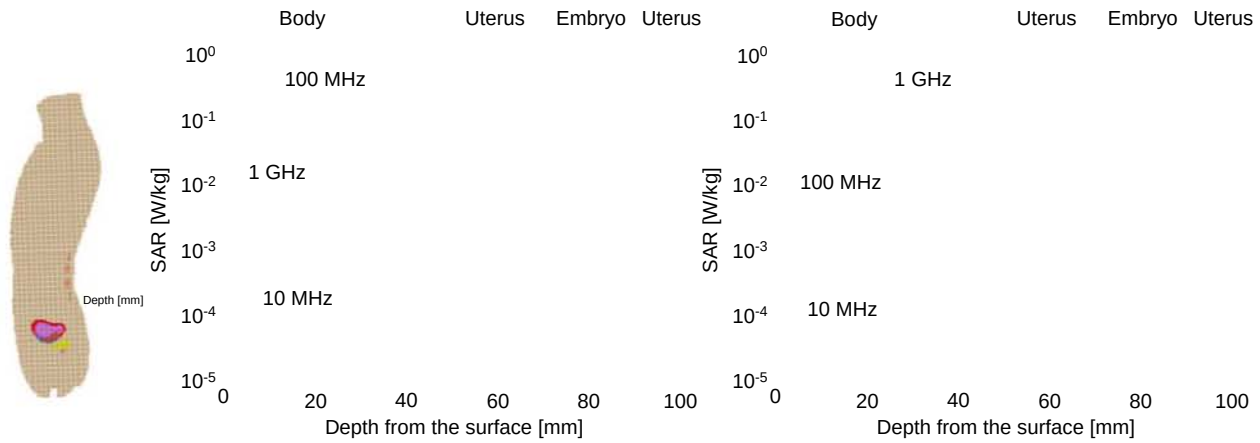
3.2 SAR distribution

Figure 4 (a) and 4 (b) illustrate internal SAR distributions on the observational line [see Fig. 4 (lef)] in the median plane of the torso model by the E- or H-polarized wave's exposure at 10 MHz, 100 MHz, and 1 GHz. Here, the incident power density was IEEE occupational reference level in each frequency.

From Fig. 4 (a), the attenuation curve of SAR by the E-polarized wave at 10 MHz is almost equal to that at 100 MHz while the absolute value is significantly different. At these frequencies, in addition, the SAR distribution is almost constant between the uterus and the embryo and higher than the SAR in the frontal body. On the contrary, the attenuation is abruptly varied by the standing wave at 1 GHz.

As shown in Fig. 4 (b), the attenuation curve of SAR by the H-polarized wave in each frequency is about the same. In addition, the peak SAR is arisen on the surface in each frequency. Moreover, the SAR in the embryo and that in the uterus are about the same.

From Fig. 4 (a) and (b), the SAR in the embryo is almost continually varied between the uterus and the embryo in each frequency and incident wave, because the embryo is very small in the first gestational month. These results suggest that the layered structure between the uterus and embryo is not necessary to evaluate the SAR inside the embryo in the first gestational month.



(a) E-polarized wave (b) H-polarized wave

Fig. 4 Internal SAR distributions on the observational line in the median plane of the torso model by the plane wave's exposure at 10 MHz (line), 100 MHz (dotted line), and 1 GHz (dashed-dotted line).

4. Conclusion

This paper presented the computational EMF dosimetry inside the woman-torso model, which was composed by five types of tissues, in the first gestational month using the FDTD method, when the model was exposed to the E- and H-polarized plane waves over the frequency range from 10 MHz to 3 GHz. First, the parametric models for the dielectric spectrum of fetus and those of amniotic fluid were demonstrated. Second, the whole-body average SAR inside the embryo was calculated, when the incident power density of plane waves was ICNIRP or IEEE occupational reference level. As a result, the maximum value in the embryo was less than 0.4 W/kg (occupational limit) by plane waves' exposure over the evaluated frequency range. Finally, the internal SAR distributions inside the torso model were also shown at 10 MHz, 100 MHz, and 1 GHz. As a result, the SAR distribution around the embryo was dependent on the frequency and polarized wave in the first gestational month.

As a further study, the same investigation as above will be done using pregnant and non-pregnant women models, which is segmented much different tissues.

References

[1] WHO, "Children's EMF Research Agenda," The International EMF Project, June 2004.
[2] A.H.J. Fleming and K.H. Joyner, "Estimates of absorption of radiofrequency radiation by the embryo and fetus during pregnancy," *Health phys.*, vol. 74, no. 2, pp. 149-159, Aug. 1998.
[3] P. Dimbylow, "Development of pregnant female, hybrid voxel-mathematical models and their application to the dosimetry of applied magnetic and electric fields at 50 Hz," *Phys. Med. Biol.*, vol. 51, pp. 2383-2394, Apr. 2006.
[4] K.S. Yee, "Numerical solution of initial boundary value problems involving Maxwell's equation in isotropic media," *IEEE Trans. Antennas Propagat.*, vol. 14, no. 3, pp. 302-307, Mar. 1966.
[5] ICNIRP, "Guidelines for limiting exposure to time-varying electric, magnetic, and electromagnetic fields (up to 300 GHz)," *Health Phys.*, vol. 74, no. 4, pp. 494-522, Apr. 1998.
[6] IEEE standard for safety levels with respect to human exposure to radio frequency electromagnetic fields, 3 kHz to 300 GHz, ANSI/IEEE Standard C95.1-2005, Apr. 2006.
[7] C. Gabriel, "Compilation of the dielectric properties of body tissues at RF and microwave frequencies," Brooks Air Force Technical Report, AL/OE-TR-1996-0037, 1996.
[8] J.L. Scheppes and K.R. Foster, "The UHF and microwave dielectric properties of normal and tumour tissues: variation in dielectric properties with tissue water content," *Phys. Med. Biol.*, vol. 25, no. 6, pp. 1149-1159, Nov. 1980.
[9] F.De Luca, C. Cametti, G. Zimatore, B. Maraviglia, and A Pachi, "Use of low-frequency electrical impedance measurements to determine phospholipid content in amniotic fluid," *Phys. Med. Biol.*, vol. 41, no. 9, pp. 1863-1869, Sept. 1996.
[10] K. Ito, H. Kawai, M. Takahashi, K. Saito, T. Ueda, M. Saito, H. Ito, H. Osada, Y. Koyanagi, and K. Ogawa, "Evaluation of the local SAR in a simple abdomen model of pregnant women at 150 MHz," in *Proc. 27th BEMS and EBA meeting*, (CD-ROM), no. 12-2, pp.133-136, Dublin, Ireland, June 2005.
[11] W. Kainz, S. Seidman, R. Qiang, and J. Chen, "The future of anatomical models - anatomical CAD models for numerical dosimetry and implant evaluations," in *Proc. 27th BEMS and EBA meeting*, (CD-ROM), no. P-A-55, pp. 270-272, Dublin, Ireland, June 2005.

ELECTROMAGNETIC POWER ABSORPTION IN CURVED BIOLOGICAL TISSUES

A. SHTROM, D. F. SOLDEA, and P. D. EINZIGER

DEPARTMENT OF ELECTRICAL ENGINEERING,
TECHNION - ISRAEL INSTITUTE OF TECHNOLOGY, HAIFA 32000, ISRAEL

Abstract
Coupled closely to highly absorbing tissues, a source of electromagnetic radiation, such as cellular or hyperthermia antenna, can be greatly affected by the curvature of the absorbing surface. Herein, our previous TE excitation models are extended as to incorporate the TM case, combining an effective and relatively simple procedure for obtaining closed-form corrections for the main power relations involved in the presence of curved-surface absorbing tissues. The derivation is introduced by considering two-dimensional prototype models of surface and line magnetic-type sources radiating in the presence of a half-space and an infinite circular cylinder. The power absorption efficiencies of the cylindrical model are shown to be tightly bounded, both from below and above, by those of the half-space (planar) models.

Introduction
Recently, the study of near-field interactions of electromagnetic sources with highly lossy media, utilizing the Leontovich surface impedance approach [1], [2], has led to analytic readily-interpretable expressions for the main power relations involved in such configurations, namely, source power efficiencies and specific absorption rate [3],[4],[5]. These models, corresponding to a semi-infinite absorbing medium in the vicinity of either finite (current line-source) or infinite (planar current-sheet) sources, lead to an explicit dependence of the power relations on both the geometrical and physical parameters and provided an effective mean for obtaining physical insight into the basic power absorption mechanisms as well as tight bounds and estimates on the power relations. In some realistic configurations, however, such as cellular phone interaction with living tissues [6], [7], electromagnetic hyperthermia-based treatments [8], [9], and highly-sensitive biosensing [10], [11], the absorbing structure's curvature effect should be incorporated into the model in order to render its implementation effective.

Herein, our previous TE excitation models [12] are extended as to incorporate the TM case, utilizing the Leontovich surface impedance approach [1], [2], applied for finite-size two-dimensional (2D) cylindrical absorbing medium. The resultant extension leads to a discrete Parseval's representation for the power relations in terms of the individual cylindrical harmonics' (spectral) power content. These expressions can be interpreted similarly as for the previous (planar) case but with a curvature correction term, continuously depending on the effective surface curvature and the source location. Inclusion of the curvature correction, whenever applicable, enables thereby better understanding and design of prototype systems involving electromagnetic sources closely coupled to highly lossy structures.

Methods
The 2D physical configurations, corresponding to the planar and the cylindrical models, are depicted in Figs. 1(a), 1(b) and Figs. 1(c), 1(d), respectively. Both configurations are characterized by the parameters μ, ε, and σ via: $k_0 = \omega\sqrt{\mu_0\varepsilon_0}$, $Z_0 = \omega\mu_0/k_0 = \sqrt{\mu_0/\varepsilon_0}$, $\sigma_0 = 0$, and $k_1 = \omega\sqrt{\mu_1\tilde{\varepsilon}_1}$, $Z_1 = \omega\mu_1/k_1 = \sqrt{\mu_1/\tilde{\varepsilon}_1}$, $\tilde{\varepsilon}_1 = \varepsilon_1\left(1 - j\sigma_1/\omega\varepsilon_1\right)$ where, assuming a harmonic time-dependence $e^{j\omega t}$, $\Im\{k_1\} \le 0$, and $\Im\{Z_1\} \ge 0$. The analysis and the results for the planar model are well known [2],[3],[4], and thus, summarized herein merely for the sake of comparison, completeness, and clarity. The excitation source locations for both models are given via $y' = d$ (the planar model) and $\rho' = a + d$ (the cylindrical model), where a and d denote the cylinder radius and the sources distance from the lossy tissues, respectively. Additionally, for line sources, $x' = 0$ (the planar model) and $\varphi' = 0$ (the cylindrical model).

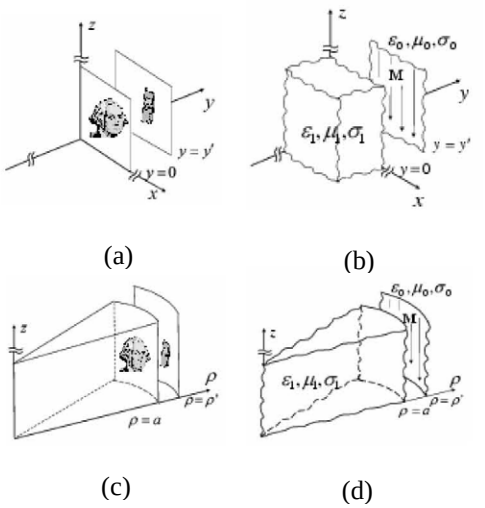


Figure 1: Physical configurations and models for the planar and the cylindrical approaches: (a) Physical configuration, (b) Planar model, (c) Physical configuration incorporating curvature correction, (d) Cylindrical model.

Source representations in terms of surface and line magnetic currents are denoted by $\mathbf{M}^S = -M^S \hat{\mathbf{z}}$ and $\mathbf{M}^L = -M^L \hat{\mathbf{z}}$ respectively, and given in Table 1.

Table 1: Magnetic current sources.

Current source	Planar model	Cylindrical model
M^S	$Ke^{jk_x x}\delta(y-y')$	$I\dfrac{e^{jq\varphi}\delta(\rho-\rho')}{2\pi\rho'}$
M^L	$I\delta(x)\delta(y-y')$	$I\dfrac{\delta(\varphi)\delta(\rho-\rho')}{\rho'}$

The power relations for both models, including radiation power, absorption power, source power, free space source power, power absorption efficiency, and power radiation efficiency, are given via

$$P_{r_{\substack{P\\C}}} = \mp\frac{1}{2}\Re\left\{\int_{\varphi} E_x H_z^* ds_{\substack{y\\ \rho}}^{+}\right\}, \tag{1}$$

$$P_{a_{\substack{P\\C}}} = \pm\frac{1}{2}\Re\left\{\int_{\varphi} E_x H_z^* ds_{\substack{y\\ \rho}}^{-}\right\}, \tag{2}$$

$$P_s = P_r + P_a, \tag{3}$$

$$P = P_s\big|_{\varepsilon_1=\varepsilon_0,\sigma_1=0}, \tag{4}$$

$$\eta_a = \frac{P_a}{P_s}, \tag{5}$$

and

$$\eta_r = \frac{P_r}{P_s} = 1-\eta_a, \tag{6}$$

respectively. Note that the distinguishing superscripts S and L (Table 1) and subscripts P and C (Eqs. (1)-(2)), corresponding to the surface and the line currents and to the planar and the cylindrical models, respectively, have been omitted in Eqs. (3)-(6) since these equations apply to both current sources and models. This rule is adapted throughout the entire paper for all the equations that apply to both current sources and models. The fundamental power relations in Eqs. (1)-(4) can be readily expressed in the spectral domain upon expending the transverse components of the electromagnetic field in terms of appropriate modes in conjunction with the Parseval's identity, as summarized in Table 2. The modal fields are represented via plane-waves (continuous spectrum) and cylindrical waves (discrete spectrum) for the planar and the cylindrical models, respectively. The spectral power densities, denoted by P_r, P_a, and P_s in Table 2, are expressed explicitly in Table 3.

Table 2: Spectral representation for the power relations.

Power	Planar-model,		Cylindrical-model,	
relations	current-sheet	line-source	current-sheet	line-source
P_r	$P\frac{\mathcal{P}_r(k_x)}{2}$	$P\int_0^{k_0}\mathcal{P}_r(k_x)\frac{dk_x}{\pi\beta_0}$	$P\mathcal{P}_{r,q}\frac{\left\|H_q^{(2)}(k_0\rho')\right\|^2}{4J_q^2(k_0\rho')}$	$P\sum_{q=-\infty}^{\infty}\mathcal{P}_{r,q}\frac{\left\|H_q^{(2)}(k_0\rho')\right\|^2}{4}$
P_a	$P\frac{\mathcal{P}_a(k_x)}{2}$	$P\int_0^{\infty}\mathcal{P}_a(k_x)\frac{dk_x}{\pi\left\|\beta_0\right\|}$	$P\mathcal{P}_{a,q}\frac{\left\|H_q^{(2)}(k_0\rho')\right\|^2}{4J_q^2(k_0\rho')}$	$P\sum_{q=-\infty}^{\infty}\mathcal{P}_{a,q}\frac{\left\|H_q^{(2)}(k_0\rho')\right\|^2}{4}$
P_s	$P\frac{\mathcal{P}_s(k_x)}{2}$	$P\int_0^{\infty}\mathcal{P}_s(k_x)\frac{dk_x}{\pi\left\|\beta_0\right\|}$	$P\mathcal{P}_{s,q}\frac{\left\|H_q^{(2)}(k_0\rho')\right\|^2}{4J_q^2(k_0\rho')}$	$P\sum_{q=-\infty}^{\infty}\mathcal{P}_{s,q}\frac{\left\|H_q^{(2)}(k_0\rho')\right\|^2}{4}$
P	$\frac{\left\|K\right\|^2}{4\mathcal{Z}_0}$	$\frac{k_0\left\|I\right\|^2}{8Z_0}$	$\frac{k_0\left\|I\right\|^2 J_q^2(k_0\rho')}{8Z_0}$	$\frac{k_0\left\|I\right\|^2}{8Z_0}$

Table 3: Spectral power densities and related functions for the spectral representation.

Planar model		Cylindrical model	
Power Densities And Related functions	Plane-wave Continuous -spectrum	Power Densities And Related functions	Cylindrical-wave Discreet-spectrum
$\mathcal{P}_r(k_x)$	$1+\lvert\Gamma(k_x)\rvert^2+2\Re\left\{\Gamma(k_x)e^{-j2\beta_0 d}\right\}$, $0\le k_x\le k_0$ 0 , $k_0<k_x$	$\mathcal{P}_{r,q}$	$1+\lvert\Gamma_q\rvert^2+2\Re\left\{\Gamma_q\dfrac{H_q^{(1)}(k_0a)H_q^{(2)}(k_0\rho')}{H_q^{(2)}(k_0a)H_q^{(1)}(k_0\rho')}\right\}$
$\mathcal{P}_a(k_x)$	$1-\lvert\Gamma(k_x)\rvert^2$, $0\le k_x\le k_0$ $-2\Im\{\Gamma(k_x)\}e^{-2\lvert\beta_0\rvert d}$, $k_0<k_x$	$\mathcal{P}_{a,q}$	$1-\lvert\Gamma_q\rvert^2$
$\mathcal{P}_s(k_x)$	$2+2\Re\left\{\Gamma(k_x)e^{-j2\beta_0 d}\right\}$, $0\le k_x\le k_0$ $-2\Im\{\Gamma(k_x)\}e^{-2\lvert\beta_0\rvert d}$, $k_0<k_x$	$\mathcal{P}_{s,q}$	$2+2\Re\left\{\Gamma_q\dfrac{H_q^{(1)}(k_0a)H_q^{(2)}(k_0\rho')}{H_q^{(2)}(k_0a)H_q^{(1)}(k_0\rho')}\right\}$
$\Gamma(k_x)$	$\dfrac{1-\mathcal{Z}(k_x)}{1+\mathcal{Z}(k_x)}$	Γ_q	$\dfrac{1-\mathcal{Z}_q w_q}{1+\mathcal{Z}_q w_q^*}\left(\dfrac{w_q^*}{w_q}\right)$
$\mathcal{Z}(k_x)$	$\dfrac{Z_1}{Z_0}\dfrac{\beta_1(k_x)}{k_1}\dfrac{k_0}{\beta_0(k_x)}$	$\mathcal{Z}_q$	$-j\dfrac{Z_1}{Z_0}\dfrac{J_q'(k_1a)}{J_q(k_1a)}$
$\beta_{0\atop 1}(k_x)$	$\sqrt{k_{0\atop 1}^2-k_x^2}$, $\Im\left\{\sqrt{k_{0\atop 1}^2-k_x^2}\right\}\le 0$	w_q	$j\dfrac{H_q^{(1)}(k_1a)}{H_q^{(1)\prime}(k_1a)}$

Results

The limit of high losses, associated with highly lossy tissues, renders $\lvert Z_1/Z_0\rvert\to 0$ (or equivalently $\lvert k_1/k_0\rvert\to 0$) and thus enables the implementation of the well known Leontovich surface impedance approach [1], [2]. This results in a closed-form and relatively simple asymptotic relations for both the planar and the cylindrical models, as summarized in Table 4. These asymptotic relations demonstrate that utilizing the Leontovitch approximation [1], [2] in conjunction with the Debye approximation [13] results in an asymptotic equivalence of the planar and the cylindrical models, when excited by surface currents.

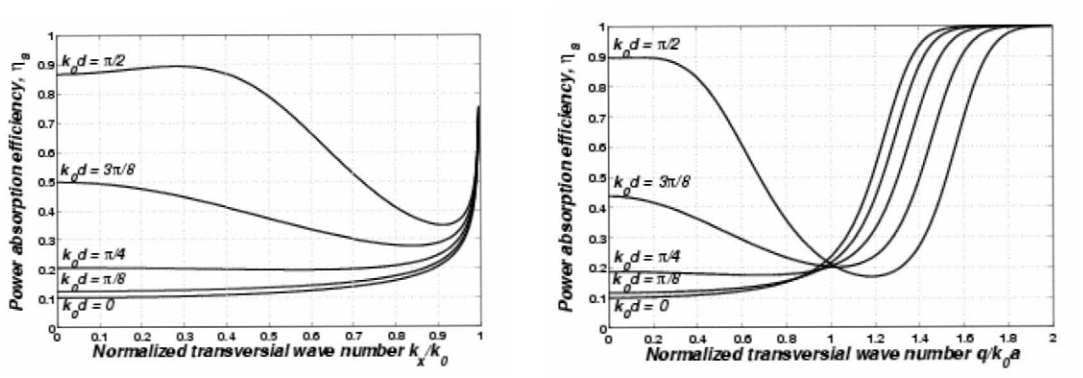
Table 4: The limit of high losses.

Asymptotic limits	Planar model	Cylindrical model
Leontovitch approx. [1],[2] $\left\lvert\dfrac{k_1}{k_0}\right\rvert\to\infty$ or $\left\lvert\dfrac{k_1a}{k_0a}\right\rvert\to\infty$	$\mathcal{Z}(k_x)\sim\dfrac{Z_1}{Z_0}\dfrac{k_0}{\beta_0(k_x)}$ $\Gamma(k_x)\sim 1-2\dfrac{Z_1}{Z_0}\dfrac{k_0}{\beta_0(k_x)}$ $\left.\dfrac{E_x(k_x)}{H_z(k_x)}\right\rvert_{y=0}\sim Z_1$	$\mathcal{Z}_q\sim\dfrac{Z_1}{Z_0}$ $\Gamma_q\sim\left[1-2\dfrac{Z_1}{Z_0}\Re\{w_q\}\right]\dfrac{w_q^*}{w_q}$ $\left.\dfrac{E_{\varphi,q}}{H_{z,q}}\right\rvert_{\rho=a}\sim -Z_1$
Leontovitch approx. [1],[2] & Debye approx. [13] $q=k_0a\sin\theta_q\to\infty$, $\sin\theta_q\ne 1$	$\mathcal{Z}(k_0\sin\theta_q)\sim\mathcal{Z}_q w_q$ $\Gamma(k_0\sin\theta_q)\sim\Gamma_q$	$\dfrac{H_q^{(2)\prime}(k_0a)}{H_q^{(2)}(k_0a)}\sim\pm j\dfrac{\sqrt{(k_0a)^2-q^2}}{k_0a}=\pm j\cos\theta_q$ $w_q\sim 1/\cos\theta_q$

Furthermore, this equivalence establishes an identical asymptotic lower bound on the power absorption efficiency ´s η_a^S in (5) for the planar and cylindrical waves in both models, as demonstrated in Fig. 2, i.e.

$$\eta_a^S \geq \eta_a^S \Big|_{\frac{k_x}{k_0}=0 \text{ or } \frac{q}{k_0 a}=0}, \tag{7}$$

in the range, $0 \leq k_0 d < \frac{\pi}{4}$.



(a) (b)

Figure 2: Power absorption efficiency vs. normalized transversial wave number, $Z_1 \ Z_0 = 0.1140 + j0.0658$: (a) Plane wave model ($k_0 a \to \infty$) [3], [4], [5], (b) Cylindrical wave model ($k_0 a = 10$).

Noting that Leontovitch and Debye approximations (Table 4) lead to

$$\eta_{a,P}^S \Big|_{\frac{k_x}{k_0}=0} = \eta_a^{TEM} \sim \eta_{a,C}^S \Big|_{\frac{q}{k_0 a}=0}, \tag{8}$$

where η_a^{TEM} is expressed as [4]

$$\eta_a^{TEM} \sim \frac{2\Re\left\{\frac{Z_1}{Z_0}\right\}\left(1-\Re\left\{\frac{Z_1}{Z_0}\right\}\right)}{1-\Re\left\{\frac{Z_1}{Z_0}\right\}-\left(1-2\Re\left\{\frac{Z_1}{Z_0}\right\}\right)\cos^2\left(k_0 d+\Im\left\{\frac{Z_1}{Z_0}\right\}\right)}. \tag{9}$$

This results in an asymptotic common lower bound η_a^{TEM} for both models in (7) and renders a tight asymptotic common lower bound for the line-source power absorption efficiencies $\eta_{a,P}^L$ and $\eta_{a,C}^L$ associated with the planar and the cylindrical models, i.e.,

$$\eta_{a,P}^{L}=\frac{\int_{k_x}\mathcal{P}_a(k_x)\frac{dk_x}{|\beta_0|}}{\int_{k_x}\mathcal{P}_s(k_x)\frac{dk_x}{|\beta_0|}}=\frac{\int_{k_x}\mathcal{P}_s(k_x)\eta_{a,P}^{S}\frac{dk_x}{|\beta_0|}}{\int_{k_x}\mathcal{P}_s(k_x)\frac{dk_x}{|\beta_0|}}\geq\eta_a^{TEM}, \tag{10}$$

and

$$\eta_{a,C}^{L}=\frac{\sum_{q=-\infty}^{\infty}\mathcal{P}_{a,q}\left|H_q^{(2)}(k_0\rho')\right|^2}{\sum_{q=-\infty}^{\infty}\mathcal{P}_{s,q}\left|H_q^{(2)}(k_0\rho')\right|^2}=\frac{\sum_{q=-\infty}^{\infty}\mathcal{P}_{s,q}\eta_{a,C}^{S}\left|H_q^{(2)}(k_0\rho')\right|^2}{\sum_{q=-\infty}^{\infty}\mathcal{P}_{s,q}\left|H_q^{(2)}(k_0\rho')\right|^2}\geq\eta_a^{TEM} \tag{11}$$

respectively.

Finally, in the limit of zero curvature as $k_0a\to 0$, the cylindrical model is asymptotically reduced into the planar model, i.e.,

$$\eta_{a,C}^{L}\sim\eta_{a,P}^{L}, \tag{12}$$

It is readily noted that while the asymptotic result in (8) is valid if Leontovitch and Debye approximations can be applied, for the validity of (12) requires, in addition, that $a\ \rho'\to 1$ (or equivalently $d\ a\to 0$).

Calculations based on Eq. (5) and Tables 2-3 are now carried out for magnetic line-source excitation (Table 1) utilizing FCC guidelines [14] for evaluation of biological tissues parameters at cellular frequencies (human brain parameters at 900 MHz: $\sigma=0.7[S/m]$, $\varepsilon_1=45\varepsilon_0$). Fig. 3 reveals that the cylindrical model's results correlate well with Eqs. (7)-(12). Furthermore, as expected, the power absorption efficiencies $\eta_{a,C}^{L}$ for the cylindrical model is tightly bounded from above and bellow by the power absorption efficiencies associated with the planar model excited by surface and line magnetic currents (Table 1), respectively, for a broad range of k_0a values, i.e.,

$$\eta_a^{TEM}\leq\eta_{a,C}^{L}\leq\eta_{a,P}^{L},\qquad k_0a>1. \tag{13}$$

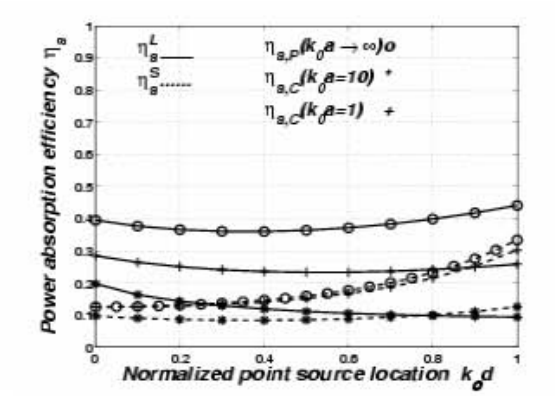


Figure 3: Curvature effect on efficiencies and bounds: FCC parameters at 900MHz [14], $\sigma=0.7[S/m]$, $\varepsilon_1=45\varepsilon_0$.

In conclusion, the power absorption efficiency for the cylindrical model is universally bounded by the planar model efficiencies for both excitations (Table 1), namely, the planar and the line magnetic current sources. Furthermore, as the curvature of the absorbing medium approaches zero, the power relations for the cylindrical model are asymptotically reduced to the results associated with the planar model.

References

[1] T. B. A. Senior, Impedance Boundary Conditions for Imperfectly Conducting Surfaces, *Appl. Sci. Res.*, Sect. B 8, 1959, 418-436.

[2] G. Tyras, *Radiation and Propagation of Electromagnetic Waves*, (New York: Academic, 1969).

[3] D. F. Soldea, D. Razansky, and P. D. Einziger, Plane-Wave Model for Electromagnetic Power Absorption in Biological Tissues, *J. Appl. Phys.*, 94(3), 2003, 2053-2059.

[4] D. Razansky, D. F. Soldea, and P. D. Einziger, Bounds Estimates and Resolution for Power Absorption in 2D Highly-Lossy Configurations - *J. Appl. Phys.*, 95(12), 2004, 8298-8308.

[5] D. Razansky, D. F. Soldea, and P. D. Einziger, Transmission-Line Model for Estimation of Cellular Handset Power Absorption in Biological Tissues- *IEEE Trans. on Electromagn. Compat.*, 47(1), 2005, 61-67.

[6] R.W. P. King, Electric Currents and Field Induced in Cells in the Human Brain by Radiation from Hand-Held Cellular Telephones, *J. Appl. Phys.*, 87(2), 2000, 893-900.

[7] G. Lazzi, O. P. Gandhi, S. Ueno, Guest Editorial, *IEEE Trans. Microwave Theory and Tech.*, 52(8), 2004, 1853 - 1855.

[8] A. J. Fenn, G. L. Wolf, and R. M. Fogle, An adaptive microwave phased array for targeted heating of deep tumours in intact breast: animal study results, *Int. J. Hyperthermia*, 15(1), 1999, 45-61

[9] D. Razansky, P. D. Einziger, and D. R.Adam *Phys. Rev. Lett.*, 93, 2004, 083902.

[10] D. Razansky, P. D. Einziger, and D. R.Adam *Phys. Rev. Lett.*, 95, 2005, 018110.

[11] M. Specht, J. D. Pedarning, W. M. Hechkl, and T. W. Hanisch, *Phys. Rev. Lett.*, 68, 1992, 476.

[12] A. Shtrom, D. F. Soldea, D. Razansky, and P. D. Einziger, Curvature effect for electromanetic power absorption in biological tissues, *Proc. of the 24th IASTED International Multi-Conference on Biomedical Engineering*, Innsbruck, Austria, Feb. 15-17, 2006, 339-343.

[13] M. Abramowitz and I. A. Stegun, *Handbook of Mathematical Functions*, (New York: Dover, 1972).

[14] Federal Communications Commission, Evaluating Compliance with FCC Guidelines for Human Exposure to Radiofrequency Electromagnetic Fields, Supplement C, *OET Bulletin 65*, Ed. 97-01.

RECOGNITION AND ENGULFMENT OF THE APOTOTIC CELLS: INFLUENCE OF THE EXPOSURE TO MODERATE-INTENSITY STATIC MAGNETIC FIELD

LUCIANA DINI, PATRIZIA TARANTINO, BERNADETTE TENUZZO, MAJDI DWIKAT and ALESSANDRA QUARTA

DEPARTMENT OF BIOLOGICAL AND ENVIRONMENTAL SCIENCE AND TECHNOLOGY; UNIVERSITY OF LECCE; LECCE, ITALY

ABSTRACT

Phagocytosis of the apoptotic cells requires distinguishing features on the surface of dead cells, recognition and tethering molecules, as well as the cytoskeletal and other cellular machinery involved in engulfment.

If the details of the interaction between apoptotic cells and phagocytes are still far to be fully understood, even more obscure are the external factors able to modulate the phagocytosis. We have hypothesized that any factors influencing cell surface molecules expression (phagocyte and /or apoptotic cell) can in turn affect recognition of apoptotic cells. This is indeed the case of static magnetic field of moderate intensity that alters the surface of cells after 24 h of continuous exposure.

Therefore, the recognition of apoptotic lymphocytes by liver sinusoidal cells under exposure to 6 mT static magnetic field to define at which extent static magnetic fields are able to modulate this specific type of phagocytosis was studied.

Carbohydrate expression on lymphocyte surfaces was extensively affected by exposure to static magnetic field irrespective of the cell status, i.e. normal or apoptotic. These modifications are responsible of the altered recognition of apoptotic lymphocytes by the sinusoidal liver cells. In particular, the exposure to static MF has been found to be an extremely critical factor for the recognition of not only apoptotic lymphocytes, but especially for control ones.

INTRODUCTION

The interest in the biological effects of non-ionizing electromagnetic fields (EMFs) on the whole organism, as well as on cellular systems, has considerably increased in recent years in consideration of their increased production (from the generation and transmission of electricity, to domestic appliances and industrial equipment, to telecommunications and broadcasting) and of possible health risk for humans. Findings on the effects of (E)MFs exposure on humans are often contradictory and, therefore, difficult to interpret. No direct evidence of tumorigenicity have ever been demonstrated, however, epidemiological studies have associated (E)MFs exposure with increased incidence of cancer. The multiplicity of experimental conditions (i.e., in vitro or in vivo models, intensity and type of field, oscillatory or static, time of exposure, metabolic state of the cells, etc) makes contradictory the data on the biological effects of (E)MFs. Many researches have indicated plasma membrane as the primary site of action of (E)MFs (Santoro et al., 1997). Indeed, the effects on plasma membrane have been described at different levels: on the electrochemical balance of the membrane (Panagopouls et al., 2000), on its surface (Paradisi et al., 1993), on the distribution of membrane proteins (Bersani et al., 1997) and membrane receptors, on the cell-cell and cell-matrix junctions (Somosy, 2000), on lipid peroxidation and generation of reactive oxygen species (ROS) (Ishisaka et al., 2000; Jelenkovic et al., 2006), on DNA damage (Fiorani et al., 1992; Miyakoshi 2005), on the sugar residues on cell membrane (Bordiushkov et al., 2000; Chionna et al. 2003b) and on trans-membrane fluxes of different ions especially calcium (Thompson et al., 2000; Cho et al., 1999 Lyle et al., 1997). As a consequence, cellular processes (physiology and metabolism, i.e. apoptosis, cellular shape, cytoskeleton polymerization) are influenced (Fanelli et al., 1999; Teodori et al., 2002a, b; Chionna et al., 2003a, 2005). In turn, modulation of apoptosis can favor the development of many diseases (Kountouras et al., 2004; Nikitakis et al., 2004).

In particular, apoptosis is an important and widespread process aimed to protect organism by the silent demise of damaged and/or aged cells. Apoptotic cells are usually cleared by phagocytosis *in vivo* with a rapid and efficient process able to remove damaged cells and components by inhibiting inflammation (Savill and Fadok, 2000). The initial event in phagocytosis is the recognition of the target. Successful engulfment requires that apoptotic cells expose at least one "eat-me" signal on their surface (Savill and Fadok, 2000). Apoptosis leads to disruption of the normal phospholipid asymmetry of the plasma membrane, that generates ligands on the cell surface (Williamson and Schleger, 2002), facilitating recognition by specific receptors on the phagocytes. Several *in vitro* study, starting from the pioneering work of Savill et al. (1990), which identified macrophage vitronectin receptor (αvβ3 integrin) as the first receptor to recognize and engulf apoptotic cells, have characterized several recognition systems, mainly by inhibitory studies of the phagocytic process. Table I summarizes the various "eat-me" signals, so far identified, capping the apoptotic cells, that are recognized simultaneously or alternatively by distinct phagocyte receptor molecules.

Table I:*Redundancy in apoptotic cell surface determinants and phagocytes receptors*.

	Present on	
Epitopes and/or receptor	Apoptotic cells surface	Phagocyte surface
phosphatidylserine (PS)	yes	yes
CD31	yes	yes
ATP-binding cassette transporter (ABC1)	yes	yes
phosphatidylserine receptor (PSR)	no	yes
C1q/Mannose Binding Lectin (MBL)	no	yes
calreticulin and CD91	no	yes
CD14	no	yes
αvβ3/αvβ5	no	yes
Scavenger receptors (SRA,CD68,LOX1,CD36)	no	yes
CD11/CD18	no	yes
Lectins	no	yes
Ox-LDL	yes	no
ICAM 3	yes	no
MER	no	yes
αvβ3 integrin	no	yes
β2-GPI receptors	no	yes
bridging molecules:		
Milk Fat Globule Epidermal growth factor 8, (MF-GE8); Growth Arrest Specific gene 6, (Gas6); trombospondin (TSP)		

The same "eat-me" ligand can be recognized by different receptors or bridging molecules, so that recognition possibilities are widely amplified. This redundancy aims to assure maximum clearance efficiency and explains the inability of some individual deletions to efficiently impaired apoptotic cell clearance *in vivo*.

In a wide range of phagocytes, both professional and non-professional, charbohydrate changes on the surface of apoptotic cells are important in triggering recognition (Duvall et al., 1985; Dini et al., 1992; Dini, et al.1993). Initially it has been suggested that healthy hepatocytes ingested apoptotic ones via the asiaologlycoproteins receptor, that is exclusively present on the parenchymal liver cells (Dini et al., 1992). Galactose and mannose- specific recptors of sinusoidal liver cells have been also found play a role in the recognition and engulfment of apoptotic cells, mostly blood circulating (Dini, et al. 1995; Falasca, et al. 1996; Dini and Carlà, 1998), likely in cooperation with other hepatic carbohydrate-specific receptors. Indeed, the mannose receptor of macrophages and liver endothelial cells is the best characterized member of a family of surface lectin receptors that mediates binding and internalization of mannose and fucose (Duvall et al., 1985; Dini et al., 1992; Dini, et al.1993; Dini et al., 1995). CD14, a multifunctional receptor known originally for its role as the lipopolysaccharide (LPS) receptors (Gregory, 2000), could bind the carbohydrate groups that are exposed during the apoptosis.

The overall environmental generation of (E)MFs is due to both natural and artificial sources. Thus, many cell functions can be influenced by the accidental or intentional exposure to (E)MFs. It is likely

that recognition of apoptotic cells could be affected by any environmental factors able to modulate cell surface molecules expression, irrespectively on phagocyte and /or apoptotic cells. Among all the possible factors present in the environment static magnetic field of moderate intensity (static MF 6 mT of intensity) are also included. While it has been reported that static MF can alter surface of cells after 24 h of continuous exposure (Chionna et al. 2003b; 2005), scarce and very contradictory are the data of literature regarding the effects of (E)MFs on phagocytosis (Flipo et al. 1998; Simko et al. 2001).

Aim of the present work has been the study of the *in situ* liver recognition of normal or apoptotic lymphocytes that have been exposed for up to 24 h to 6 mT static MF, to define at which extent static MF are able to modulate this specific type of phagocytosis. In particular, liver is the main site for apoptosis of blood cells, is for lymphocytes either a battlefield or a graveyard (Sun and Shi, 2001; Crispe et al., 2000).

Characterization of cell surface of isolated human lymphocytes: apoptotic versus static MF exposed

Human lymphocytes cells were obtained after Ficoll gradient separation of buffy coats from blood donations of non-smoker healthy males, aged 25–45. They were separated from monocytes by double adherence to plastic. During and after the treatments, they were maintained at a cell density of 1×10^6 cells/ml in complete culture medium at 37 °C supplemented with 10% inactivated fetal calf serum (FCS), 2 mM l-glutamine, 100 IU/ml penicillin and streptomycin in a humidified atmosphere of 5% CO_2; cells were used on the first day of explant. Cell viability was more than 95% at the end of the isolation procedure and it was reduced of about 55 and 70% when cells were induced to apoptosis by using heat shock at 43 °C for 1 h followed by 4 h recovery in fresh medium or cycloheximide (CHX) 10^{-2} M for up to 24 h. The exposure to static MF of 6 mT of intensity, up to 24 h, did not induce any reduction of the cell viability nor modification of cell growth (Fig. 1). Static MF was produced by Neodymium magnetic disks (10 mm in diameter and 5mm in height) of known intensity supplied by Calamit L.td (Milano, Italy) placed under the culture Petri dishes. The intensity of the field generated by the magnet was checked by means of a gaussmeter with a range of operating temperature of 0°C to 50°C and an accuracy (at 20°C) of $\pm$ 1% (Hall-effect gaussmeter, GM04 Hirst Magnetic Instruments Ltd, UK). The laboratory areas between incubators, worktops and tissue culture hood measured 0.08 μT to 0.14 μT (50 Hz) magnetic fields. In the room the background flux density was 10 μT (static) and the local geomagnetic field was approximately 43 μT.

However, when apoptosis was induced under exposure to static MF, the percentage of dead cell was reduced of about 15-20% (Fig. 1). Morphological observation confirmed these results. Indeed, exposure to static MF affected cell shape and surface. Microvilli of control cells became lamellar and cells was more elongated. The surface of lymphocytes induced to apoptosis under exposure was less smooth than not exposed ones (Chionna et al. 2003a).

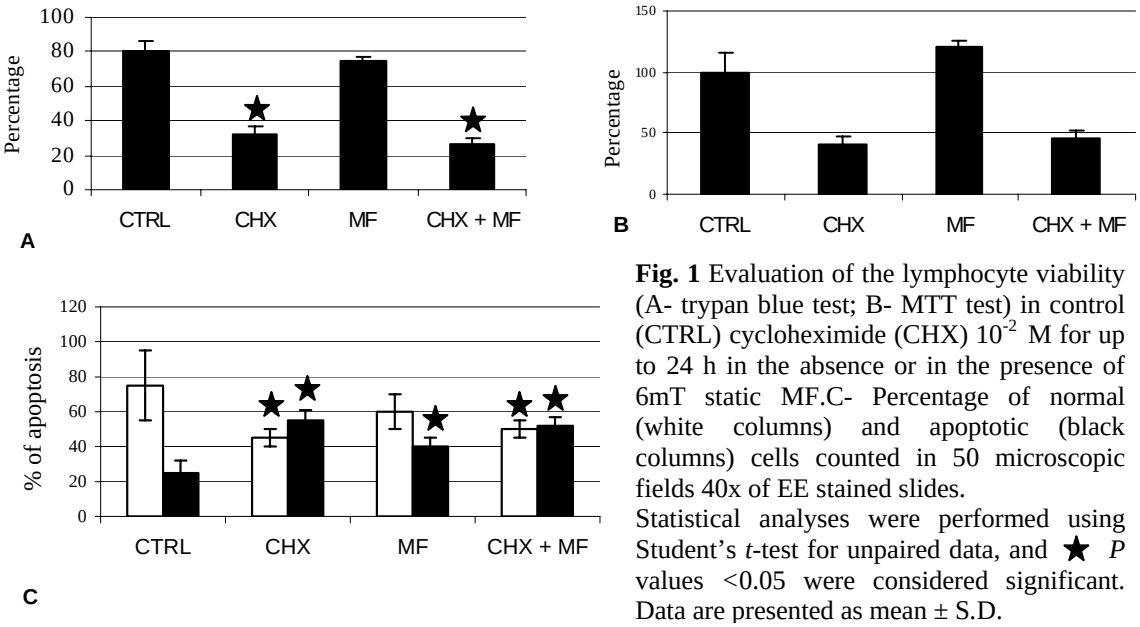


Fig. 1 Evaluation of the lymphocyte viability (A- trypan blue test; B- MTT test) in control (CTRL) cycloheximide (CHX) 10^{-2} M for up to 24 h in the absence or in the presence of 6mT static MF.C- Percentage of normal (white columns) and apoptotic (black columns) cells counted in 50 microscopic fields 40x of EE stained slides.

Statistical analyses were performed using Student's *t*-test for unpaired data, and ★ *P* values <0.05 were considered significant. Data are presented as mean ± S.D.

The liver phagocytosis of apoptotic lymphocytes is mediated by carbohydrate-specific receptors (Dini 2005). In fact, the cell surface of apoptotic lymphocytes express normally hidden sugar moieties like

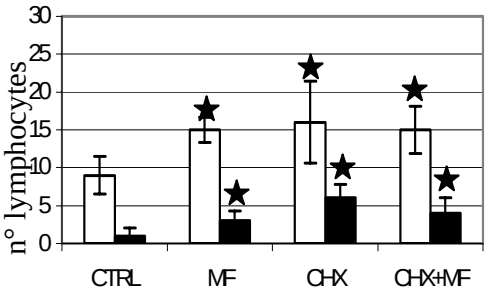
D-galactose, Mannose, N-acetyl-Dgalactosamine, N-acetyl-Dglucosamine, Fucose. Cells, fixed with 4% formalin in phosphate buffer pH 7.4, 5 min, were labelled with lectin-FITC conjugates, i.e. Concanavalin-A (Con-A) (D-mannose) (40 μg/ml) and Ricinus communis (D-galactose) (2 μg/ml), 30 min in the dark.
Both the apoptotic treatment and the exposure to 6 mT static MF influenced the sugar expression; in addition exposure to static MF modified fluorescence pattern and intensity with respect to the corresponding non exposed cells. In table II are summarized the semiquantitative evaluation of different carbohydrate exposure on cell surfaces of normal, apoptotic and static MF exposed lymphocytes, analyzed with fluorescence microscopy. The carbohydrates whose expression is enhanced after exposure are mannose/D-glucosammine and galactose/D-galactosamine, while the fluorescence pattern resulted modified for all lectins.

Table II Semiquantitiative evaluation of FITC-conjugate lectins for the detection of carbohydrate residues on the cell surfaces of control (CTRL), apoptotic human lymphocytes in the presence or in the absence of static MF

Lectins	CRTL	CTRL+MF	Apoptotic	Apoptotic+MF
Con-A	-	+	++	+
Ricinus Communis	-	++	+++	++

Liver recognition and internalization of lymphocytes
The quantification of adhesion and internalization of the in situ injection of normal, apoptotic and static MF exposed lymphocytes to mouse liver sinusoidal walls is reported in fig. 2. Male Swiss mice, weighting 15-20 g were maintained on a standard laboratory diet and free water access. Before surgery, animals were anaestethized by an i.p. injection with Farmotal (barbiturate anaestethic) (Farmitalia, Italy), 10 mg/100g body weight. All animals received humane care according to the criteria outlined by the national law. For each set of experiments at least three animals were used. Livers were perfused in a non-recirculating system at a flow rate of 1ml/min. $1x10^6$ lymphocytes labelled with Hoechst 33342 were injected into the liver circulation (total volume 10 ml). Lymphocytes used in the different experiments were control, apoptotic, control static MF exposed and induced to apoptosis under static MF. The livers were then extensively washed with culture medium to remove unbound cells. Livers, fixed in 4% paraformaldehyde in phosphate buffer, were processed for routine light microscopy or for cryosectioning. The adhesion of lymphocytes to the sinusoidal wall was evaluated by light and fluorescent microscopy of liver sections. The adhesion specificity was tested in parallel inhibition experiments by adding 80 mM (final concentration) of a sugar cocktail (N-acetyl-D-galactosamine, Mannose, fucose, N-acetilglucosammine) into the perfusion tube before adding apoptotic lymphocytes. To allow internalization warmed solution (37°C) were used. The concentration of lymphocytes used for all experiments was at saturation point, as evaluated by the presence of apoptotic lymphocytes in the medium collected from the liver.
Liver cells were very active in blocking apoptotic lymphocytes, leaving away normal one (less than 6 % of injected cells were bound to sinusoids). Apoptosis was estimated by morphological analysis at the optical level. Light microscopic analysis of apoptosis was done on haematoxylin/eosin stained cells on slides. Haematoxylin-eosin slides were examined for the scoring of cells undergoing apoptosis, by counting in 50 to 100 high-power microscopic fields (x40). Approximately 300 nuclei per slides were counted. The number of apoptotic cells was expressed as number per microscopic field 40x. Slides were also observed for the presence anomalies in the morphologies (normal or altered shape).
Apoptotic lymphocytes were retained by sinusoidal liver cells at high degree, and when internalization was allowed (i.e. perfusion at 37°C), they were found inside the cells. Worth noting, control non exposed lymphocytes were never phagocyted. Surprisingly, when normal lymphocytes were exposed for 24 hr to static MF, they were retained by sinusoidal walls (three times with respect to control) (fig.2) and internalized when allowed.
The percentage of lymphocytes induced to apoptosis under exposure to static MF bound to sinusoidal liver cells was higher than the apoptotic ones. Correspondingly the number of internalized apoptotic lymphocytes was increased. The induction of apoptosis and static MF exposure had a synergic effect. The recognition of apoptotic lymphocytes was, in all cases, specific as indicated by the inhibition experiments. In fact the clearance of apoptotic lymphocytes was mediated by specific receptors, most likely mannose and galactose, able to recognize the surface modifications. Indeed, liver periportal

sinusoidal tracts express higher amount of mannose and galactose-specific receptors than perivenous sinusoidal tracts, thus leading the periportal liver sinusoids to recognize and internalize more apoptotic lymphocytes than the corresponding perivenous cells (Fig.2). Worth noting, the control static MF - exposed cells were recognized at the same extent in the perivenous and periportal tract of the liver sinusoids. The sugar inhibition experiments indicated a synergic recognition between lectin like receptor and not yet known receptor, since the reduction of binding was only partial prevented (Fig. 2).



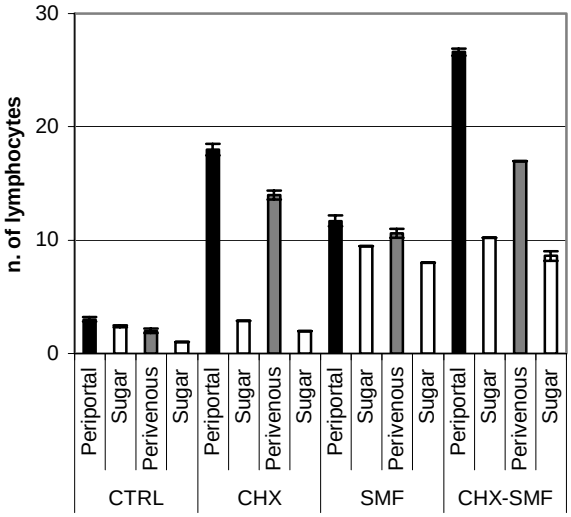


Fig. 2 Number of control or CHX 10^{-2} M for up to 24 h treated lymphocytes in the absence or in the presence of 6 mT static MF for 24 h, adhering (white columns) or internalized (black columns) by liver sinusoidal cells.Statistical analyses were performed using Student's *t*-test for unpaired data, and ★ *P* values <0.05 versus CRTL were considered significant. Data are presented as mean ± S.D.

Analysis of membrane proteins of static MF exposed lymphocytes

The protein pattern of membrane of normal, apoptotic and static MF exposed lymphocytes is reported in fig. 3. Western blot analysis were performed according to Towbin et al. (1979) (Fig.). Specific lectins conjugated to biotin were used: lectin from Concanavalin A specific for α-Mannose and α-glucose residues (at a concentration of 50µg/ml), lectin from *Helix pomatia* specific for N-acetyl-α -D-galactosaminyl residues (at a concentration of 50µg/ml), lectin from *Triticum vulgaris* specific for N-acetyl-β-D-glucosaminyl residues and N-acetyl-β-D-glucosamine oligomere, (at a concentration 50µg/ml), and lectin from *Ulex Europaeus* specific for L-Fucose residues (at a concentration 30µg/ml) (Sigma-Aldrich, Saint Louis, MO, USA). Specific binding of the lectins was detected using streptavidin conjugated to peroxidase (1:1,500 dilution) and visualized using 3-3' diaminobenzidine (DAB) as a substrate in the presence of H_2O_2. Quantification of the glycoprotein bands was performed by using a Biorad Model GS 700 Imaging densitometer.

Differences between exposed and non exposed cells and between control and apoptotic ones have been detected. Apoptosis as well as exposure to static MF induced modifications in the protein profile of cells. In particular, from gel electrophoresis three bands underwent major modifications:130, 95 and 45-43 kDa, while a fourth band was only found in control exposed cells, 60 kDa. The control exposed and the apoptotic non exposed lymphocytes showed an increment of the band of 43KDa. Conversely, the bands of 95 and 130 KDa increased in the presence of static MF while decreased with the CHX treatment. The intensity of the 45KDa band decreased with the treatments respectively with the incubation of CHX, exposure to static MF and CHX incubation in presence of static MF (Fig. 3).

By using different lectins (Concanavalin-A, Ulex europaeus and Triticum vulgaris) the expression of glycidic residues of the proteins was evaluated. The western blots for α-Mannose and α-glucose (Con A) has shown 6 different bands (Fig.5). The 100 KDa α band was modified (+8% versus control) only in the samples incubated with CHX under static MF. The 100 KDa β band was modified at the same extent (- 15%) in both samples exposed to static MF or CHX treated. CHX incubation reduced of about 10% the intensity of the 70 KDa γ band with respect to control. Similar pattern (-8%) was found for 65 KDa δ band,while only the samples exposed to static MF showed a decrement (-9%) of 55KDa ε band. The 30 KDa ζ band was unchanged. The western blots for α-L-Fucose (Ulex europaeus) has shown that the majority of proteins belong to the low molecular weight. Modifications of optical densitometry

with the relative increment or decrement given in percentage with respect to control are reported in fig. 4. The western blots for N–acetyl-D-glucosammine and N–acetyl-neuroaminic (Triticum vulgaris) has shown that the majority of proteins belong to the high molecular weight. Optical densitometry with the relative percentage increments with respect to control are reported in fig.4.

In the present work data have been shown on the strong and reproducible effects that the exposure to static MF exerts on the process of liver phagocytosis of apoptotic lymphocytes.
Liver clearance of apoptotic lymphocytes is a complex mechanism that can be influenced at least at three different levels: phagocyte receptors, apoptotic cell quality and static MF exposure. On the side of the phagocyte receptors, in general, the efficiency of phagocytosis is proportional to the number of expressed receptors. In the liver this aspect is particular evident, since the receptors involved in the recognition of apoptotic cells are modulated in relation to the type of the cells (i.e. Kupffer, endothelial cell, hepatocytes) (Dini and Kolb-Bachofen, 1989), to the physiological or pathological status of the organ and to the cell localization inside the lobule (Dini et al., 2002; Dini, 2000; Dini and Carlà, 1998). With respect to this latter aspect, the efficiency of recognition and internalization is higher in the periportal tracts of the liver lobule, than in the perivenous ones, according to the number of carbohydrate specific receptors.

	treatments			
	ctrl	chx	mf	chx +mf
43kDa	0	0	0.033	0.065
45 kDa	1.23	0.81	0.35	0.76
95 kDa	0.084	0.056	0.11	0.085
130 kDa	0	0	0.064	0.058

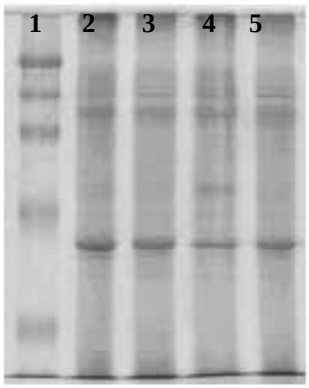


Fig. 3 SDS-PAGE of membrane proteins from control (CRTL), CHX treated lymphocytes in the absence or in the presence of 6 mT static MF for 24 h. Lane 1 Marker; lane 2 control; lane 3 CHX 10^{-2} M for up to 24 h; lane 4 CTRL + static MF for 24 h; lane 5 CHX 10^{-2} M for up to 24 h + static MF for 24 h.

On the side of the edible cells, the quality of apoptotic cells can determine the efficiency of clearance by the liver (Chionna et al., 2003a). It is known that the step in the process of apoptosis (i.e. early, mature or late apoptosis) has influence on the efficiency of removal since the modification of the cell surface changes accordingly with the progression through the apoptotic program (Chionna et al., 2003a). A hierarchy of the expression of specific epitopes on the cell surface of apoptotic lymphocytes has been reported (Chionna et al., 2003a). Therefore, the cell surface of dying cells is progressively changing leading to widely amplified possibilities of a safe recognition and to modulation in the rate of recognition and engulfment. The third level is given by the perturbation exerted by exposure to static MF of moderate intensity. In previous works (Chionna et al., 2003b, 2005; Dini and Abbro 2005;Tenuzzo et al. 2006) we have described the interference of static MF with the process of apoptosis, with cell shape and surfaces, with Calcium ions concentrations, cytoskeleton, differentiation and in the present work, on the liver clearance of normal and apoptotic lymphocytes. Our data confirm those in the literature indicating that cell membranes are the preferential site for the action of the (E)MF (Panagopouls et al., 2000; Paradisi et al., 1993; Bersani et al., 1997; Somosy, 2000).

By using two different experimental approaches, lectin cytochemistry and western blotting of glycoproteins, the modifications of the sugars moieties and/or the glycoproteins of membranes were shown. Apparent discrepancies between lectin cytochemistry and western blots analysis can be due to the labeling of glycolipids of the plasma membranes with cytochemistry methods.
The identification of the (glyco)proteins whose amount has been modified by the exposure to static MF is currently under inestigation. Many of the possible candidate belongs to the transduction pathways and to the adhesion molecules: they are, therefore, molecules that can be involved in the process of

recognition, cell-cell adhesion and the intracellular pathways; processes that are all important for the recognition and engulfment. Indeed, it is not possible to define if the modifications in the cell proteins are due to conformational changes, to transductional or transcriptional modifications or to a synergic effects of all these factors.

	treatments			
	chx e mf	**mf**	**chx**	**ctrl**
Band α	0.334	0.324	0.314	0.307
	+8%	+5%	+2%	
Band β	0.390	0.321	0.326	0.384
	+2%	-16%	-15%	
Band γ	0.381	0.359	0.339	0.376
	+1%	-4%	-10%	
Band δ	0.459	0.408	0.393	0.429
	+7%	-5%	-8%	
Band ε	0.416	0.357	0.374	0.392
	+6%	-9%	-5%	
Band ζ	0.448	0.407	0.414	0.424
	+6%	-4%	-2%	

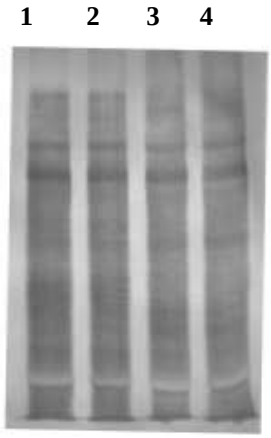


Fig. 4 Western blot assays and O.D. of ConA expression on membrane glycoproteins of isolated human lymphocytes. Lane 1 CHX 10^{-2} M for up to 24 h + static MF for 24 h; lane 2 CTRL + static MF for 24 h; lane 3 CHX 10^{-2} M for up to 24 h; lane 4 control .

Ulex Europeous

	treatments			
	ctrl	chx	mf	chx +mf
Band α	0.398	0.1	0	0
		-79%	-100%	-100%
Band β	0.5	0.1	1.08	1.12
		-80%	+100%	+100%
Band γ	0.64	0.94	0.96	1.35
		+47%	+50%	+100%
Band δ	0	0	0	0

Triticum Vulgaris

	treatments			
	ctrl	chx	mf	chx +mf
Band α	0.643	0.801	0.819	0.836
		+21%	+27%	+30%
Band β	0.7	1..0	1.31	1.26
		+42%	+87%	+80%
Band γ	0.41	0.23	0.43	0.498
		-43%	+5%	+21%
Band δ	0.098	0	0	0
		-100%	-100%	-100%

Fig. 5 Optical Density values of one representative western blot of Ulex Europeous and Triticum vulgaris expression in isolated human lymphocytes in control and CHX 10-2M for 24 h treated in the absence or in the presence of 6 mT static MF.

To date, the very few data that have been published on the effects of static MF on gene expression are confusing and, none of them is referring to genes regulating the apoptotic program. Indeed, some studies obtained by using electromagnetic fields at diverse intensities, i.e. ELF and EMF, reported effects on gene expression, particularly at the transcriptional level, after exposure to ELF and EMF of human HL60 (Goodman et al., 1992). Several specific transcripts, i.e. actin, tubulin, H2B histone, c-myc, increased their expression by two to three fold after 20 min of exposure (De Mattei et al., 2005). Conversely, in other reports (Hirose et al., 2003) the exposure to homogeneous static MF at 10 T was unable to affect the expression of c-Jun, c-Fos and c-Myc, while the inhomogeneous static MF at 6T significantly increased c-Jun expression but only at the long-time exposure.

The most intriguing data that has been here shown is the ability of sinusoidal liver cells to retain and to internalize normal exposed lymphocytes. One possible reason of this recognition can be the modifications exerted by static MF on the surface of lymphocytes that share changes with apoptotic cells, thus leading to the removal of control exposed cells via receptors used for the clearance of apoptotic lymphocytes.
It is worth noting to mention that the process of recognition and engulfment of the apoptotic cells has same peculiarity that makes the process of phagocytosis of apoptotic cells different from the phagocytosis of microrganisms or debris (Krysko et al., 2003). In fact, in non-pathological conditions, an efficient clearance is assured by the redundant interaction between apoptotic cell ligands and multiple molecules present on the engulfing cell surface. The apoptotic cell engulfment appears to activate signals able to suppress release of pro-inflammatory cytokines, thus pro-inflammatory responses are not elicited. The phagocytosis of apoptotic cells prevents inflammation (Maderna and Godson, 2003). Therefore, it should be further investigated if the removal of static MF exposed lymphocytes share the characteristic of the phagocytosis of apoptotic cells.

SUMMARY

In summary, evidences of the perturbation exerted by the exposure to 6 mT static MF of human isolated lymphocytes have been reported. In particular, the static MF exposure impaired the apoptotic rate and gave rise to modifications of the cell surface in normal exposed cells similar to the cell surface modifications achieved during the apoptotic program. The cell surface modifications of apoptotic cells are important for their fast and silent removal by professional and amateur phagocytes. Interestingly, the same liver receptorial systems are also used for the recognition of control exposed lymphocytes. The pathological and/or physiological implications are not yet understood and need to be further investigated.
Data showed that the recognition of apoptotic lymphocytes by the sinusoidal liver cells is affected by the exposure to static MFs. Interestingly, exposure to static MFs has been found to be an extreme critical factor not only for the recognition of apoptotic lymphocytes but also for control ones. The imp'lication for human health needs to be deeply investigated.

REFERENCES

Bersani F., Marinelli F., Ognibene A.., Matteucci A.., Checchi S., Santi S., Squarzoni S., Maraldi N.M., 1997**.** Intramembrane protein distribution in cell cultures is affected by 50 Hz pulsed magnetic fields. Bioelectromagnetics 18, 463--469.

Bordiushkov IuN., Goroshinskaia IA.., Frantsiiants EM., Tkacheva GN., Gorlo EI., Neskubina IV.2000. Structural-functional changes in lymphocyte ans erythrocyte membranes after exposure to alternating magnetic field. Vopr Med Khim. 46,72-80. Russian.

Chionna A., Dwikat M., Panzarini E., Tenuzzo B., Carlà EC., Verri T., Pagliara P., Abbro L., Dini L. 2003b. Cell shape and plasma membrane alterations after static magnetic fields exposure European Journal of Histochemistry 47, 299-308.

Chionna A., Panzarini E., Pagliara P., De Luca A., Caforio S., Abbro L., Dini L. 2003a. Hepatic clearance of Apoptotic lymphocytes: simply removal of waste cells? Europ.J.Histochem.47, 97-104

Chionna A., Tenuzzo B., Panzarini E., Dwikat M., Abbro L., Dini L. 2005. Time-dependent modifications of Hep G2 cells during exposure to Static Magnetic Fields. Bioelectromagnetics. 26, 275-286.

Cho MR., Thatte HS., Silvia MT., Golan DE. 1999. Transmembrane calcium influx induced by an electric field. Faseb Journal 13, 677--683.

Crispe IN., Dao T., Klugewitz K., Mehal W.Z., Metz D.P. 2000. The liver as a site of T-cell apoptosis: graveyard, or killing field? Immunol. Rev. 174, 47-62.

De Mattei M., Gagliano N., Moscheni C., Dellavia C., Calastrini C., Pellati A., Gioia M., Caruso A., Stabellini G. 2005. Changes in polyamines, c-myc and c-fos gene expression in osteoblast-like cells exposed to pulsed electromagnetic fields. Bioelectromagnetics 26, 207-214.

Dini L., Kolb-Bachofen V. 1989. Preclustered receptor arrangement is a prerequisite for galactose-specific clearance of large particulate ligands in rat liver. Exp Cell Res.184, 235-40.

Dini L., Abbro L. 2005. Bioeffects of moderate-intensity static magnetic fields. Micron 36,195-217.

Dini L., Autori F., Lentini A., Oliverio S., Piacentini M., 1992. The clearence of apoptotic cells in the liver is mediated by the asialoglycoprotein receptor. Febbs Letters 296, 174--178.

Dini L., Carlà EC., 1998. Hepatic sinusoidal endothelium heterogeneity with respect to the recognition of apoptotic cells. Experimental Cell Research 240, 388--393.

Dini L., Falasca L., Lentini A., Mattioli P., Piacentini M., Piredda L., Autuori F. 1993. Galactose-specific receptor modulation related to the onset of apoptosis in rat liver., Eur. J. Cell Biol. 61, 329-337.

Dini L., Lentini A., Diez Diez G., Rocha M., Falasca L., Serafino L., Vidal-Vanaclocha F. 1995. Phagocytosis of apoptotic bodies by liver endothelial cells., J. Cell Sci 108, 967-973.

Dini L., Pagliara P., Carlà E.C., 2002. Phagocytosis of apoptotic cells by liver: a morphological study. Microscopy Research Techniques 57, 530--540.

Dini, L., 2000. Clearance of apoptotic lymphocytes by human Kupffer cells. Phagocytosis of apoptotic cells in the liver: role of lectin receptors and therapeutic advantages In: Cameron R.G., Feuer G. (Eds), Handbook of experimental pharmacology. Apoptosis and its modulation by drugs. Springer-Verlag Berlin Heidelberg, vol. 142 pp. 319--341.

Duvall E., Wyllie A.H., Morris R.G. 1985. Macrophage recognition of cells undergoing programmed cell death (apoptosis)., Immunology 56, 351-358.

Falasca L., Serafino L., Balabaud C., Dini L. 1996. Human Kupffer cell recognition and phagocytosis of apoptotic peripheral blood lymphocytes., Exp. Cell Res. 224, 152-162.

Fanelli C., Coppola S., Barone R., Colussi C., Gualandi G., Volpe P., Ghibelli L. 1999. Magnetic fields increase cell survival by inhibiting apoptosis via modilation of Ca++ influx Faseb J 13, 95-102.

Fiorani M., Cantoni O., Sestili P., Conti R., Nicolini P., Vetrano F., Dacha M. 1992. Elecrtic and /or magnetic field effects on DNA structure and function in cultured human cells. Mut Res 282, 25-29.

Flipo D., Fournier M., Benquet C., Roux P., Le Boularie C., Pinsky C., La Bella F.S., Krzystyniak K. 1998. Increased apoptosis, changes in intracellular Ca^{2+}, and functional alterations in lymphocytes and macrophages after in vitro exposure to static magnetic field. Journal of Toxicology and Environmental Health 54, 63--76.

Goodman R., Wei L.-X., Bumann J., Henderson AS. 1992. Exposure of human cells to electromagnetic fields: Effect of time and field strength on transcript levels. J. Electro. Magnetobiol, 11. 19–28.

Gregory C.D. 2000. CD14-dependent clearance of apoptotic cells: relevance to the immune system. Curr Opin Immunol.12, 27-34. Review.

Hirose H., Nakahara T., Zhang QM., Yonei S., Miyakoshi J. 2003. Static magnetic field with a strong magnetic field gradient (41.7 T/m) induces c-Jun expression in HL-60 cells. In vitro cell dev boil anim 39, 348-352.

Ishido M., Nitta H., Kabuto M. 2002. The mechanim of biologicalmagnetic field effects on oncostatic actions of melatonin. RIKEN Review No.44, 72-74.

Ishisaka R., Kanno T., Inai Y., Nakahara H., Akiyama J., Yoshioka T., Utsumi K. 2000. Effects of a magnetic fields on the various functions of subcellular organells and cells. Pathophysiol 7, 149-152.

Jelenkovic A.., Janac B., Pesic V., Jovanovic DM., Vasiljevic I., Prolic Z. 2006. Effects of extremely low-frequency magnetic field in the brain of rats. Brain Res Bull. 68, 355-360.

Kountouras J., Zavos C., Chatzopoulos D. 2004. Induction of apoptosis as a proposed pathophysiological link between glaucoma and Helicobacter pylori infection. Medical Hypotheses 62, 378–381.

Krysko DV., Brouckaert G., Kalai M., Vandenabeele P., D'Herde K. 2003. Mechanisms of internalization of apoptotic and necrotic L929 cells by a macrophage cell line studied by electron microscopy. J Morphol 258, 336-345.

Lyle DB., Fuchs TA., Casamento JP., Davis CC., Swicord ML. 1997. Intracellular calcium signaling by Jurkat T-lymphocytes exposed to 60 Hz magnetic field. Bioelectromagnetics 18, 439-445.

Maderna P., Godson C. 2003.Phagocytosis of apoptotic cells and the resolution of inflammation. Biochim Biophys acta 1639, 141-151.

Miyakoshi J. 2005. Effects of static magnetic fields at the cellular level. Prog Biophys Mol Biol. 87, 213-223.

Nikitakis NG., Sauk JJ., Papanicolaou SI. 2004. The role of apoptosis in oral disease: Mechanisms; aberrations in neoplastic, autoimmune, infectious, hematologic, and developmental diseases; and therapeutic opportunities. Oral Surg Oral Med Oral Pathol Oral Radiol Endod. 97, 476-490.

Panagopoulos DJ., Karabarbounis A., Margaritis LH. 2002. Mechanism for action of electromagnetic fields on cells. Biochem Biophys Res Commun. 298, 95-102.

Panagopoulos DJ., Messini N., Karabarbounis A., Philippetis AL., Margaritis LH. 2000. A mechanism for action of oscillating electric fields on cells. Biochemical Biophysical Research Communication 273, 634--640.

Paradisi S., Donelli G., Santini, M.S., Straface E., Malorni W., 1993. A 50 Hz magnetic field induces structural and biophysical changes in membranes. Bioelectronmagnetics 14, 247--255.

Rosen AD. 2003. Mechanism of action of moderate-intensity static magnetic fields. Biochem Biophys Acta 1282: 149-155.

Santoro N., Lisi A., Pozzi D., Pasquali E., Serafino A., Grimaldi S. 1997. Effect of extremely low frequency (ELF) magnetic field exposure on morphological and biophysical properties of human lymphoid cell line (Raji). Biochem. Biophys. Acta 1357:281-290.

Savill J., Dransfield I., Hogg N., Haslett C. 1990. Vitronectin receptor-mediated phagocytosis of cells undergoing apoptosis., Nature, 343, 171-173.

Savill J., Fadok V. 2000. Corpse clearance defines the meaning of cell death., Nature 407, 784-788. Review

Simko M., Droste S., Kriehuber R., Weiss DG. 2001. Stimulation of phagocytosis and free radical production in murine macrophages by 50 Hz electromagnetic fields, European Journal of Cell Biology 80, 562--566.

Somosy Z. 2000. Radiation response of cell organelles. Micron. 31, 165-181.

Sun EW., Shi YS., 2001. Apoptosis: the quiet death silences the immune system., Pharmacol. Therap. 92, 135-145.

Tenuzzo B., Chionna A., Panzarini E., Lanubile R., Tarantino P., Di Jeso B., . Dwikat M, Dini L. 2006. Biological effects of 6mT Static Magnetic Fields on induction of apoptosis: a comparative study in different cell types Bioelectromagnetics in press

Teodori L., Gohde W., Valente MG., Tagliaferri F., Colett D., Perniconi B., Bergamaschi A., Cerella C., Ghibelli L. 2002a. Static magnetic fields affect calcium fluxes and inhibit stress-induced apoptosis in human glioblastoma cells. Cytometry 49, 143-149.

Teodori L., Grabarek J., Smolewski P., Ghibelli L., Bergamaschi A., De Nicola M., Darzynkiewicz Z. 2002b. Exposure of cells to static magnetic fields accelerates loss of integrity of plasma membrane during apoptosis. Cytometry 49, 113-118.

Thompson CJ., Yang YS., Anderson V., Wood AW. 2000. A cooperative model for Ca(++) efflux windowing from cell membranes exposed to electromagnetic radiation, Bioelectromagnetics 21, 455--464.

Towbin H., Staehelin T., Gordon J. 1979. Electrophoretic transfer of proteins from polyacrilamide gels to nitrocellulose sheets: procedure and some applications. Proc Natl Acad Sci USA 76: 4350-4354.

Williamson P., Schleger RA 2002 Transbilayer phospholipid movement and the clearance of apoptotic cells.. Biochim. Biophys. Acta 1585, 53-63.

EFFECTS OF HYDROGEN PEROXIDE AND ADP-RIBOSE ON THE ACTIVATION OF TRPM2 CATION CHANNELS

MUSTAFA NAZIROĞLU

Department of Biophysics,, Faculty of Medicine, Suleyman Demirel University, Isparta, Turkey (mnaziroglu@med.sdu.edu.tr)

***Abstract*:**
It is well known that microwaves from cellular phones or other sources may affect biological systems by increasing free radicals, which may enhance lipid peroxidation levels of the cells, thus leading to oxidative damage. Hydrogen peroxide (H_2O_2) produces during oxidative stress. The Na^+- and Ca^{2+}-permeable melastatin related transient receptor potential channel TRPM2 cation channels can be gated either by adenosine diphosphoribose **(**ADP-ribose) in concert with Ca^{2+} or by H_2O_2, an experimental model for oxidative stress, binding to the channel's enzymatic Nudix domain. Since the mechanisms that lead to TRPM2 gating in response to ADP- ribose and H_2O_2 are not understood, we tested the effects of various antioxidants on ADP-ribose, NAD^+ and H_2O_2-induced TRPM2 currents.

Chinese hamster ovary (CHO) cells were transfected with cDNA coding for TRPM2. Cells were studied with the conventional whole-cell patch clamp technique. The intracellular solution used EDTA (10 mM) as chelator for Ca^{2+} and heavy metal ions. H_2O_2 (10 mM) was added extracellularly although the ADP- ribose (0.3 mM) and NAD^+ (1 mM) were applied intracellularly (i.e. through the pipette).

Non-selective cation currents in whole cell experiments were consistently induced by ADP- ribose, NAD^+ and H_2O_2. The time cause of ADP- ribose and NAD^+ was characterized by a delay of 0.6-3.0 min and a slow current induction to a plateau although the time cause of H_2O_2 was characterized by a delay of 2-5 min and it didn't reach a slow current induction to a plateau

These results demonstrated that all three agonists, H_2O_2, ADP- ribose and NAD+, are capable of activating TRPM2. The three agonists are likely to interact directly with TRPM2 channels, consistent with the idea that they bind to the nudix domain**.**

Introduction

Daily exposures to various types of magnetic fields are increasing in human environment. Extremely low frequency microwaves (MW) from power lines and public transportation systems, high- frequency MW from mobile phones and computers, and strong MW from magnetic resonance imaging in medical diagnosis are the most familiar sources of exposure. Possible biological effects due to exposure various types of MW have become of considerable public interest and concern (McCann et al., 1993; Murphy, 1993).

Reactive oxygen substances (ROS) and lipid peroxides are produced by a free radical chain reaction, which can also be initiated by ROS. The ROS, i.e. singlet oxygen, superoxide anion radical, perhydroxyl radical and hydroxyl radical, contribute to tissue damage (Halliwell and Gutteridge, 1999). ROS also cause injury by reacting with biomolecules such as lipids, proteins and nucleic acids as well as by depleting enzymatic and/or nonenzymatic antioxidants in the brain (Baydaş et al., 2003, Koylu et al., 2006). ROS and/or free radicals may be involved in the action of MW on biological system (Irmak et al., 2002; Ilhan et al., 2004; Koyu et al., 2005; Koylu et al., 2006). Antioxidant treatments in animals and humans could be beneficial in preventing or reducing some complications of low frequency MW (Ilhan et al., 2004; Koyu et al., 2005; Koylu et al., 2006).

Transient receptor potential (TRP) channels were first described in *Drosphila*, where photoreceptor carrying *trp* gene mutations exhibit a transient voltage response to continuous light (Clapham, 2003). These are subdivided into three major subgroups, namely, the vanilloid receptor family, the short TRP channels and melastatin (or long) TRP channels (Kolisek et al., 2005). We have become particularly interested in one member of latter family, known as TRPM2, for a number of reasons a potential role in cell death resulting from oxidative stress (Wehage et al., 2002).

Although TRPM2 is dominantly expressed in brain, it is also detected many other tissues, including bone marrow, spleen, heart, leukocytes, liver, and lung. Native TRPM2 currents have been recorded from U937 monocyte cell line (Perraud et al., 2001), neutrophils (Heiner et al., 2003), and CRI-G1 insulinoma cells (Togashi et al., 2006) where ADP- ribose induces large cation currents that closely match those mediated by

heterologously expressed TRPM2. The Intracellular Ca^{2+} appears to be an important modulator and cofactor of TRPM2, as elevated intracellular Ca^{2+} can significantly increase the sensitivity of TRPM2 toward ADP- ribose (Wehaga et al., 2002; Hara et al., 2002; Kolisek et al., 2005). The channel in human embryonic kidney (HEK)-293 cells can also be gated by H_2O_2, a model substance used as paradigm for oxidative stress (Wehaga et al., 2002; Fonfria et al., 2004; Kolisek et al., 2005). There are conflict reports on the mechanism of H_2O_2- mediated gating of TRPM2. The mechanism has been proposed to be direct or independent ADP-ribose (Wehaga et al., 2002; Hara et al., 2002; Heiner et al., 2003; Kolisek et al., 2005). More recent evidences suggest an indirect mechanism, because H_2O_2- releases ADP- ribose from mitochondria (Fonfria et al., 2004; Kolisek et al., 2005). However, molecular mechanisms of H_2O_2 gates the TRPM2 channels cells are unclear and warrant further studies.

The molecular mechanism by oxidative stress leads to opening of TRPM2 channels need to be elucidated in detail. To study the role of TRPM2 in oxidative stress we used an experimental model, H_2O_2, was applied to TRPM2- transfected cells. Furthermore, the present study was aimed at elucidating the role of the ADP- ribose and NAD+ for gating TRPM2 channels in the chinese hamster ovary (CHO) transfected cells.

Material and methods

Cell culture and transfection

CHO cells were obtained from A.T.C.C. (Rockville, MD, U.S.A.). The cells were cultured in Ham's medium (1 x) (Biochrom, Berlin, Germany), supplemented with 10% (v/v) fetal calf serum (Biochrom), 1 mM sodium-pyruvate (Sigma) and 4 mM L-glutamine (Biochrom, Berlin, Germany). Penicillin (50 U/ml)- streptomycin (50 mg/ml) combination in single- cell experiments was added to the medium. Cells were plated onto Poly-Lysin (0.1 µg/µl, Sigma) coated glass coverslips for 24 h and then transiently transfected with one of the described pcDNA3-EGFP-channel-vector constructs (5 µg) and TransFast Transfection Reagent (7.5 µl; Promega, Mannheim, Germany). As controls, cells were transfected with 2.5 µg „empty" vector-construct and 3.75 µl TransFast Transfection Reagent. Electrophysiological studies were carried out 24-48 h after transfection in cells visibly positive for EGFP.

Electrophysiology

Patch clamp techniques have been described in detail elsewhere (Wehage te al., 2002; Nazıroğlu et al., 2006). Transfected cells were studied with the patch-clamp technique in the whole-cell mode, using a EPC 9 equipped with a personal computer with Pulse and X chart software (HEKA, Lamprecht, Germany). The standard extracellular bath solution contained (in mM) 140 NaCl, 1.2 $MgCl_2$, 1.2 $CaCl_2$, 5 KCl, 10 HEPES, pH adjusted with KOH to 7.4. For Na^+ free solutions, Na^+ was replaced by NMDG (150 mM) and the titration was performed with HCl. For the NMDG solutions with Ca^{2+}, NMDG was partly replaced with $CaCl_2$ (11.2 mM), preserving an osmolarity of about 300 mosmol/l. The noise level in all experiments was minimised by coating the patch electrode tip with agarose (GibcoBRL, paisley, Scotland). The pipettes for whole cell recordings were filled with a solution composed of (in mM) 145 Cs-glutamate, 8 NaCl, 2 $MgCl_2$, 10 EGTA, 10 HEPES, pH 7.2 (adjusted with CsOH). In some experiments, the pipette solution additionally contained ADP-ribose (0.3 mM) or NAD^+ (final concentration 1 mM, added to the pipette solution from a stock of 70 mM in ethanol). Heavy metal concentration of internal buffer affected activation of the channels by H_2O_2. In whole cell experiments, the pipette solution added 10 mM EDTA for EGTA. Cells were held at a potential of –60 mV, and current-voltage (I-V) relations were obtained from voltage ramps from –90 to +60 mV applied over 400 ms. ADP-ribose, NAD^+ and H_2O_2 and all other chemicals were obtained from Sigma.

Data are expressed as mean ± SD. Statistical significance between groups were assessed with Student's t-test. A $p < 0.05$ value was considered significant.

Results

In a previous study (Wehage te al., 2002), authors have characterized TRPM2 currents in TRPM2-transfected HEK-293 cells. The currents were consistently activated by intracellular ADP-Ribose and also by extracellular H_2O_2, but the latter stimulus was effective in only about 25 % of the experiments. A further stimulus of TRPM2 channels, intracellular $NAD^{+,}$ failed in HEK-293 cells. In a further study, we have transfected TRPM2 channels into CHO cells and could stimulate them also with NAD^+; however, no stimulation with H_2O_2 was possible. In the present experiments, we again chose CHO cells but changed the intracellular buffer that used now EDTA rather than EGTA as chelator for Ca^{2+} and probably contaminating

heavy metal ions. Moreover, we chose an intracellular Ca^{2+} concentration calculated to be in the range of 1 µM. Using these conditions, we were able to evoke TRPM2 currents consistently with either of the three stimuli, intracellular ADPR (0.3 mM), intracellular NAD (1 mM), and extracellular H_2O_2 (10 mM) (Figures. 1A and B, 2A and 2B). The currents were non-selective cation currents with a reversal potential close to 0 mV, as previously found to be typical of TRPM2 currents, and were readily blocked in the inside direction when the Na^+ in the bath was replaced by the large impermeant cation $NMDG^+$. No such currents were ever observed when cells were studied that were transfected with a vector only but not with TRPM2; such negative control data were obtained on every experimental day studying TRPM2.

The values for the current densities were 1.87 ± 0.98 pF^{-1} (n=4) and (- 60 mV holding potential) in the absence of NAD^+ and ADP- ribose, 29.16 ± 10.57 pF^{-1} (n=5) and 31.45 ± 23.16 pF^{-1} (n=5) in the presence of NAD^+ and ADP-ribose in the patch- pipette, respectively (Figure 3). The times elapsed before the full response to ADP- ribose and NAD^+ occurred varied between 0.6 -3.0 min. This variability is probably caused by variable diffusion times of ADP- ribose and NAD^+ from pipette bath into cytosol and by metabolism of ADP- ribose and NAD^+ to products that do not active TRPM2 (Perraud et al., 2001; Wehega et al., 2002); metabolism is expected to delay activation of TRPM2 particularly when diffusion is already slow.

The ADP- ribose- and NAD^+ induced inward currents was abolished when extracellular Na^+ was substituted with the large impermeable cation NMDG ((Figures. 1A and B, 2A and 2B). When Ca^{2+} (10 mM) was added to NMDG, a small inward current was restituted (Figures 1B, C and 2B, C). These data indicate that TRPM2 enables non- selective cation currents carried mainly Na^+, but to a small part also by Ca^{2+}, in inward direction and carried by Cs^+ in the autward direction under our experimental conditions. Our results with TRPM2 are essentially identical reports (reviewed in Kuhn et al., 2005).

Figure 1. Stimulator role of intracellular ADP-ribose on the currents of TRPM2 channel. The time where the whole cell period where the normal bath solution (140 nM Na^+) was exchanged to a solution with NMDG as main cation (150 mM, no Ca^{2+} present). The holding potential was –60 mV. **A**. Original recordings from control cell. **B**. Ca^{2+} selectively of TRPM2. A cell expressing TRPM2 currents stimulated with ADP-ribose (0.3 mM) in the pipette. **C**. Current voltage relationships of ADP- ribose currents through TRPM2 in presence of various extracellular cation (same experiments as in panels B).

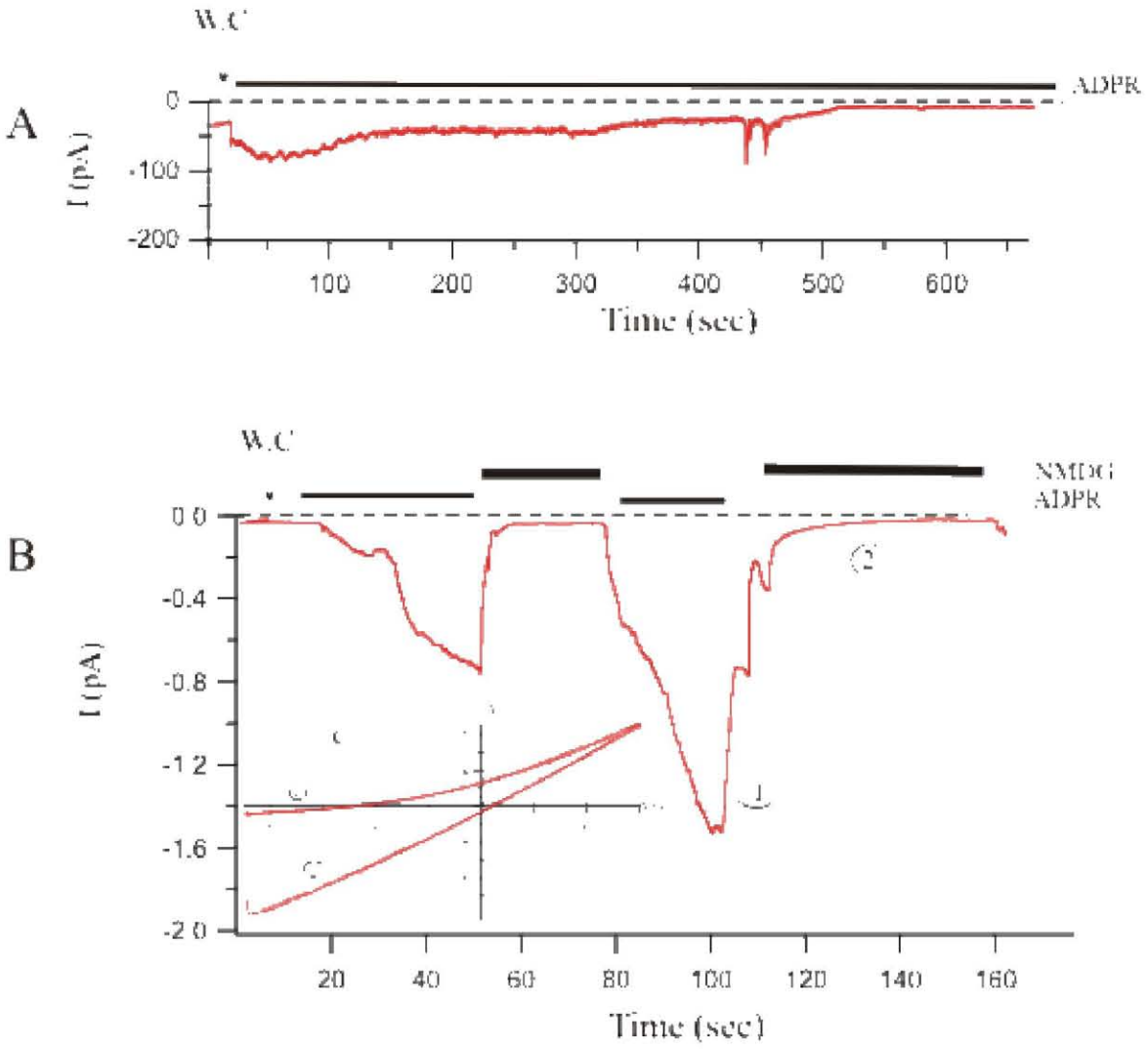


Figure 2. Stimulator role of intracellular β-NAD^+ on the currents of TRPM2 channel. The time where the whole cell period where the normal bath solution (140 nM Na^+) was exchanged to a solution with NMDG as main cation (150 mM, no Ca^{2+} present). The holding potential was –60 mV. **A**. Original recordings from control cell. **B**. Ca^{2+} selectively of TRPM2. A cell expressing TRPM2 currents stimulated with β-NAD^+ (1 mM) in the pipette. **C**. Current voltage relationships of β-NAD^+ currents through TRPM2 in presence of various extracellular cation (same experiments as in panels B).

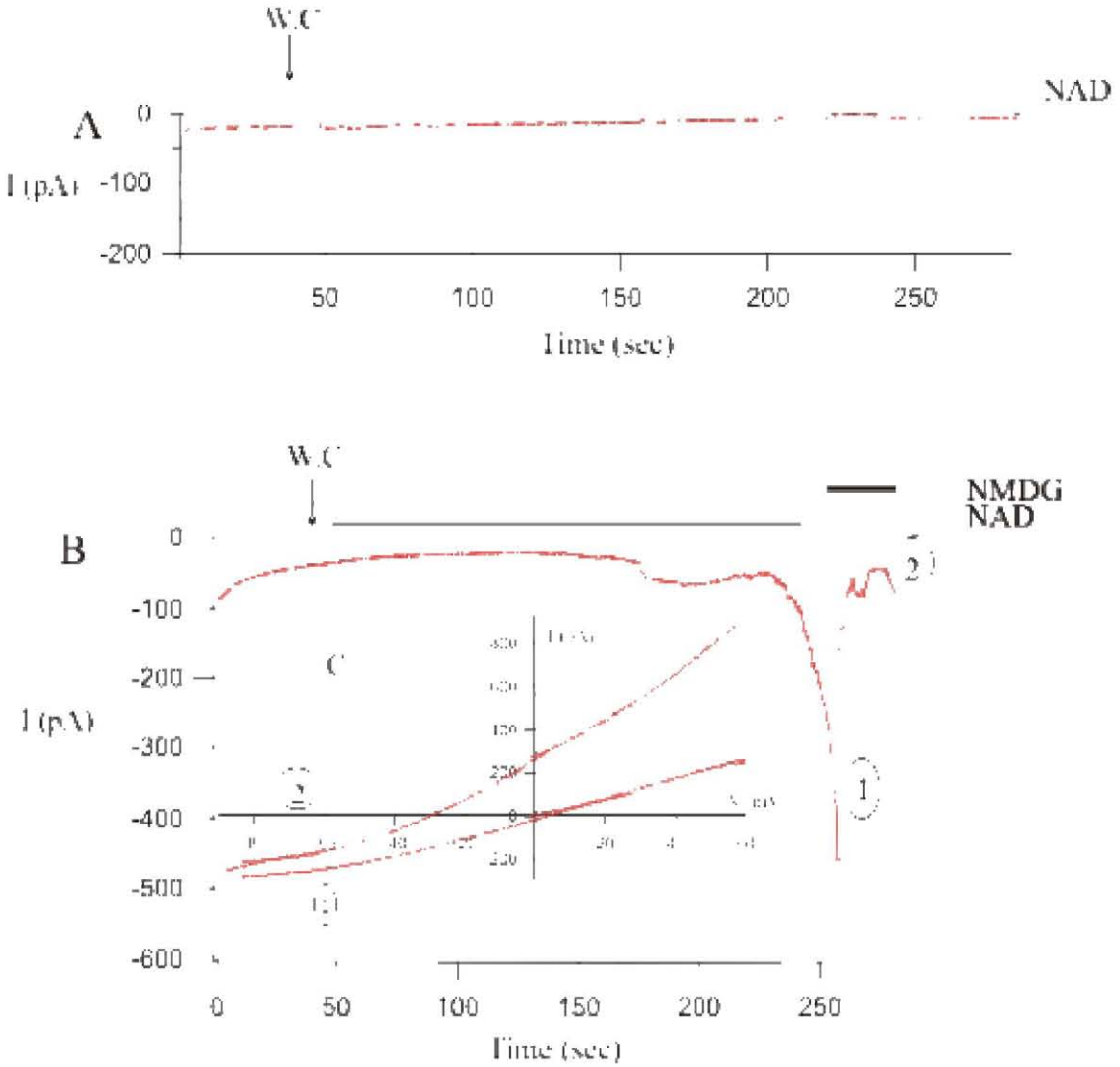
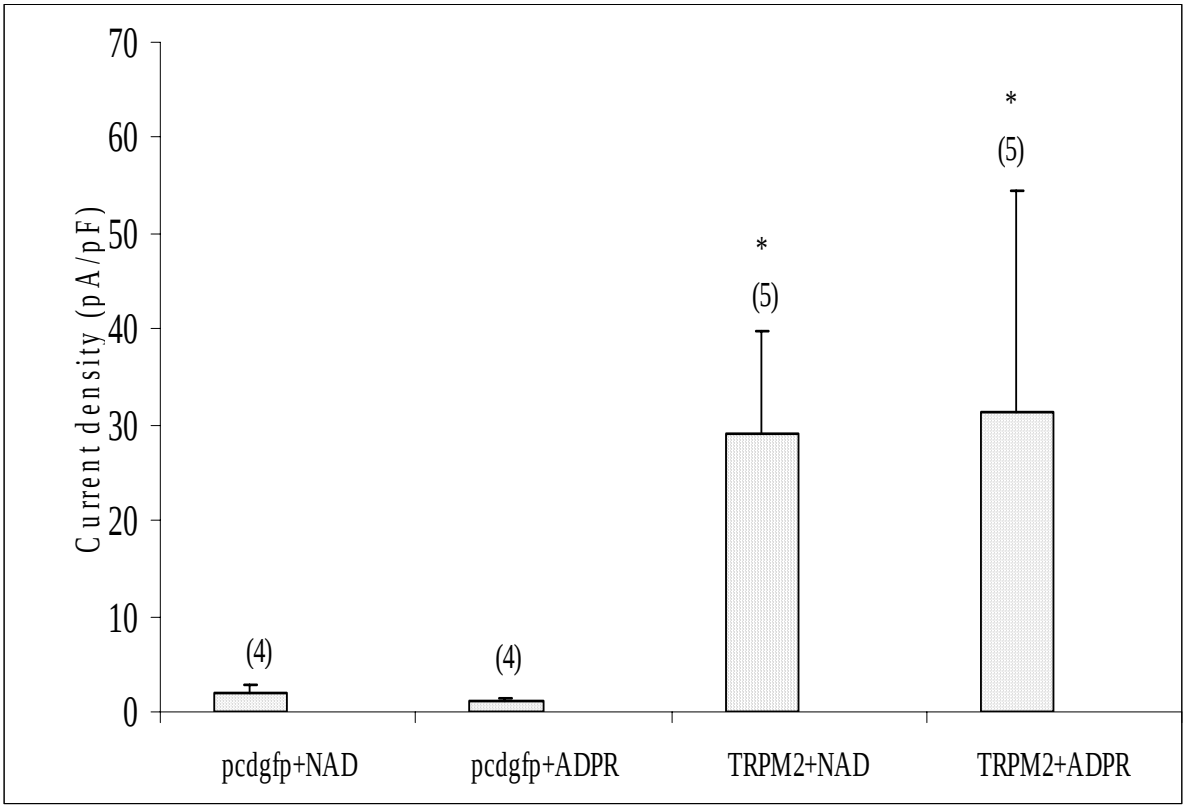


Figure 3. Stimulation of TRPM2 with intracellular β-NAD$^+$ (1 mM) and ADP-Ribose (0.3 mM). For each of the two applicants studied and for pcdfgp (control- transfected cells), the initial current density (current amplitude at –60 mV, divided by the cell capacitance, a measure of cell size as well as maximal current density after dialysis with β-NAD$^+$ and ADP-Ribose was allowed. The numbers of parentheses indicate the number of cells studied; significant stimulation of currents is indicated with *asterisk*. (mean ± SD).

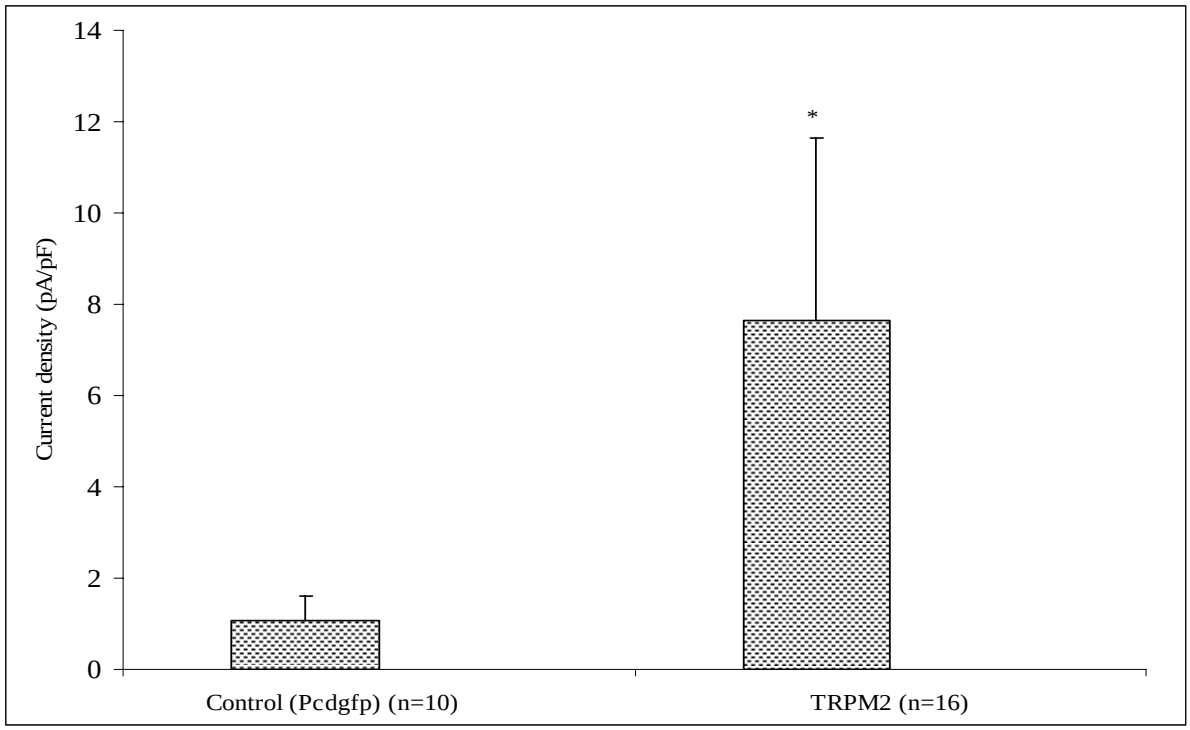


Activation of TRPM2 currents by H_2O_2

It has been well established that mitochondria produce most of the endogenous ROS, including H_2O_2, through oxidative stress. It is therefore rational to propose that the exogenously or endogenously produced ROS via oxidative stress could impair TRPM2 channel function. As a model of oxidative stress, we tested the effects of extracellular H_2O_2 on the TRPM2 channels. H_2O_2 was added to the bath to a final concentration of 10 mM. After a delay of 2-5 min, an inward current developed gradually that was blocked by NMDG and was partly carried by Ca^{2+}. After was-out of H_2O_2, the current initially increased further but then declined almost the base-line levels although a small NMDG- sensitive currents was still present (data were not shown). Re addition of H_2O_2 led to a second current rise. When the cell were exposed to H_2O_2 over more extended times than in Figure 3, the inward currents did not reach a plateau after even 15 min (data were not shown). These data suggest a participation of ROS in the TRPM channel regulation by oxidative stress.

Stimulation currents with H_2O_2 after a characteristic delay was consistently observed more then 16 cells expressing TRPM2. The mean increase in current density was –3.8- to -13.2 (Figures 4). The time elapsed before the full response to H_2O_2 occurred varied between 2-5 min.

Figure 4. Stimulation of TRPM2 with extracellular H_2O_2 (10 mM). For each of the two applicants studied and for pcdfgp (control- transfected cells), the initial current density (current amplitude at –60 mV, divided by the cell capacitance, a measure of cell size as well as maximal current density after dialysis with H_2O_2 was allowed. The numbers of parentheses indicate the number of cells studied; significant stimulation of currents is indicated with *asterisk*. (mean ± SD).



Discussion

The present study was examined effects of H2O2, ADP- ribose and NAD+ on activation of TRPM2 channel. The present study found that the non- selective cation channel currents induced by H_2O_2, ADP- ribose and NAD+.

NAD+ has been reported to stimulate TRPM2 (Sano et al., 2001; Hara et al., 2002). We saw the activation of TRPM2 by NAD+, which support the idea that this substance activates TRPM2 directly. TRPM2 contains as a characteristics structural feature a Nudix domain in its C- terminal cytosolic tail (Perraud et al., 2001). A nudix domain is a consensus region that has been known for a class of pyrophosphatases that degrade nucleoside diphosphates (Heiner et al., 2003). Indeed, the nodix domain of TRPM2 cleaves ADP- ribose, a breakdown product of NAD+ and cyclic ADP- ribose, representing an intacellular second messenger stimulating calcium release mediated by ryanodine receptors. While ADP- ribose is hydrolyzed by TRPM2, it is also activates TRPM2 and induces TRPM2 currents during infusion of ADP- ribose by the patch pipette (Harteneck, 2005). NAD+ has been reported that to stimulate TRPM2 (Hara et al., 2002).

Activation of TRPM2 by H2O2 has been reported from two approaches. One group suggested to gate the channel independently of ADP- ribose (Fonfria et al., 2004; Perraud et al., 2005) and the activation of TRPM2 by H_2O_2 is probably linked to the activity of the poly(ADP- ribose) polymerase (PARP-1), an enzyme transferring multiple ADP- ribose groups to proteins. Evidence for this intracellular pathway resulting in TRPM2 activation has been confirmed by the use of the inhibitors of poly(ADP- ribose) polymerase (PARP-1), which were able to interfer with the hydrogen peroxide induced TRPM2 activation (Reviewed in Harteneck, 2005). However, although evidence has been presented to indicate that PARP- 1 is present in mitochondria, H_2O_2 have also both been suggested to have direct effects on mitochondria (Halliwel and Gutteridge, 1999), such that the interpretation of their capacity to induce DNA damage and active PARP-1 may not be justified. In addition, PARP-1 inhibitors are known to be promiscuous within PARP family because of their structural mimicry of nicotinamide (Ferrais et al., 2003), and the concentrations required to inhibit oxidant mediated TRPM2 gating are well above those required to inhibit PARP-1 *in vitro*, precluding an unambiguous interpretation of the in cell or *in vivo* targets of these compounds. Finally, it is not obvious, at least to these authors, why PARP-1 activation should be connected to activation of a plasma membrane channel (Perraud et al., 2005).

Another group has shown H_2O_2- induced opening of TRPM2 channel directly (Hara et al. (2002; Wehaga et al., 2002; Karft et al., 2003). Indeed, currents through TRPM2 as well as increase in free Ca2+ were consistently observed. In both and TRPM2- transfected HEK-293 cells, authors current responses in whole cell configuration, which also raises the possibility of a direct effect of H_2O_2 on TRPM2 channels. Experiments on COOH- terminal truncated TRPM2 channels, lacking the ADP- ribose pyrophosphatase domain, revealed a loss of ADP- ribose- mediated gating but a retention of H_2O_2- induced activation (Wehaga et al., 2002; Karft et al.,

2003). This observation strongly supports the hypothesis of independent gating mechanisms by H_2O_2 and ADP-ribose.

According to results of current study, the H_2O_2- mediated activation of TRPM2 appears to result from a direct gating mechanism, because TRPM2 activation by H_2O_2 was relatively rapid in whole cell recordings. After adding H_2O_2 to bath, cell in whole cell records was washed by extracellular buffer and then H_2O_2 was given again. The channel was activated again by second administration of H_2O_2. From, this, we can also conclude that H_2O_2- induced, single channel activity observed in excised membrane patches is likely caused by a direct gating mechanism.

Conclusions

These results demonstrated that all three agonists, H_2O_2, ADP- ribose and NAD+, are capable of activating TRPM2. The three agonists are likely to interact directly with TRPM2 channels, consistent with the idea that they bind to the nudix domain (Hara et al. (2002; Wehaga et al., 2002; Karft et al., 2003). However, there remains insufficient evidence to suggest that three agonists are likely to interact directly with TRPM2 channels. Further studies including inside out and cell attached records are necessary to conclude definitively the conclusions.

Acknowledgment

The study was performed in Physiology Institute of RWTH- Aachen (Germany). Prof. Dr. Mustafa NAZIROGLU was supported for the study by an Alexander Humboldt Foundation (AvH) Research Fellowship. We thanks Ilinca Ionescu and Eberhard Jungling for expert technical assistance. Correspondence address is Department of Biophysics Medical (TIP) Faculty, Suleyman Demirel University Posta Kutusu 68 Cunur, TR-32260 Isparta- TURKEY. Tel: +90 246 2113310 Fax: +90 246 2371165 mnaziroglu@med.sdu.edu.tr

References

Baydaş G, Kutlu S, Nazıroğlu M, Canpolat S, Sandal S, Özcan M, Keleştimur H. Inhibitory effects of melatonin on lipid peroxidation induced by intracerebroventricularly administered homocysteine. *J Pineal Res* 2003; **34**: 36-39.

Clapham DE. TRP channels as cellular sensors. *Nature* 2003; **426**: 517-24.

Ferraris D, Ficco RP, Dain D, Ginski M, Lautar S, Lee-Wisdom K, Liang S, Lin Q,Lu MX, Morgan L, Thomas B, Williams LR, Zhang J, Zhou Y, Kalish VJ.Design and synthesis of poly(ADP-ribose) polymerase-1 (PARP-1) inhibitors. Part4: biological evaluation of imidazobenzodiazepines as potent PARP-1 inhibitors for treatment of ischemic injuries. *Bioorg Med Chem* 2003; **11**: 3695-707.

Fonfria E, Marshall, Benham CD, Boyfield I, Brown JD, Hill K, Hughes JP, Skaper SD, McNultym S. TRPM2 channel opening in response to oxidative stress is dependent on activation of poly(ADP-ribose) polymerase. *Br J Pharmacol* 2004; **143**: 186-92.

Halliwell B, Gutteridge JMC. Free radicals, other reactive species and disease. In Free Radicals in Biology and Medicine, 3rd ed.; Halliwell, B., Gutteridge, J.M.C., Eds.; Oxford University Press: New York, 1999, pp 639-645.

Hara Y, Wakamori M, Ishii M, Maeno E, Nishida M, Yoshida T, et al. LTRPC2 Ca^{2+}-permeable channel activated by changes in redox status confers susceptibility to cell death. *Mol Cell* 2002; **9**: 163-73.

Heiner I, Eisfeld J, Luckhoff A. Role and regulation of TRP channels in neutrophil granulocytes. *Cell Calcium* 2003; **33**: 533-40.

Ilhan A, Gurel A, Armutcu F, Kamisli S, Iraz M, Akyol M, Ozen S. Ginkgo biloba prevents mobile phone-induced oxidative stress in rat brain. *Clin Chim Acta* 2004; **340**:153-162.

Irmak MK, Fadillioglu E, Gulec M, Erdogan H, Yagmurca M, Akyol O. Effects of electromagnetic radiation from a cellular telephone on the oxidant and antioxidant levels in rabbits. Cell Biochem Funct 2002; **20**: 279-283.

Kolisek M, Beck A, Fleig A, Penner R. Cyclic ADP-ribose and hydrogen peroxide synergize with ADP-ribose in the activation of TRPM2 channels. *Mol Cell* 2005; **18**: 61-9.

Koliwad SK, Elliott SJ, Kunze DL. Oxidized glutathione mediates cation channel activation in calf vascular endothelial cells during oxidant stress. *J Physiol* 1996; **495**: 37-49.

Köylü H, Mollaoglu H, Ozguner, F., Nazıroğlu, M., Delibaş, N. Melatonin Modulates 900 MHz Microwave-Induced Lipid Peroxidation Changes in Rat Brain. *Toxicol Ind Health* 2006; **22**: 211-16.

Koyu A, Nazıroğlu M, Ozguner F, Yılmaz HR, Uz E, Cesur G. Caffeic acid phenethyl ester modulates 1800 MHz microwave-induced oxidative stress in rat liver. *Electromag Biol Med* 2005; **24**: 135-42.

Kuhn FJ, Heiner I, Luckhoff A. TRPM2: a calcium influx pathway regulated by oxidative stress and the novel second messenger ADP-ribose. *Pflugers Arch* 2005; **451**:212-219.

Kraft R, Grimm C, Grosse K, Hoffmann A, Sauerbruch S, Kettenmann H, Schultz G, Harteneck C. Hydrogen peroxide and ADP-ribose induce TRPM2-mediated calcium influx and cation currents in microglia. *Am J Physiol Cell Physiol* 2004; **286**: C129-37.

McCann J, Dietrich F, Rafferty C, Martin AO. A critical review of the genotoxic potential of electric and magnetic fields. *Mutat Res* 1993; **297**: 61-95.

Mendez F, Penner R. Near-visible ultraviolet light induces a novel ubiquitous calcium- permeable cation current in mammalian cell lines. *J. Physiol* 1998; **507**: 365-377.

Murphy JC, Kaden DA, Warren J, Sivak A. International Commission for Protection Against Environmental Mutagens and Carcinogens. Power frequency electric and magnetic fields: a review of genetic toxicology. *Mutat Res* 1993; **296**: 221-40.

Nazıroğlu M, Lückhoff A, Jungling E. Antagonist effect of flufenamic acid on TRPM2 cation channels activated by hydrogen peroxide. Cell Biochem Funct. 2006 (in press).

Perraud AL, Fleig A, Dunn CA, Bagley LA, Launay P, Schmitz C, Stokes AJ, Zhu Q, Bessman MJ, Penner R, Kinet JP, Scharenberg AM. ADP-ribose gating of the calcium-permeable LTRPC2 channel revealed by Nudix motif homology. *Nature*, 2001; **411**, 595-99.

Sano Y, Inamura K, Miyake A, Mochizuki S, Yokoi H, Matsushime H, Furuichi K.Immunocyte Ca^{2+} influx system mediated by LTRPC2. *Science*. 2001 17; **293 (5533)**: 1327-30.

Togashi K, Hara Y, Tominaga T, Higashi T, Konishi Y, Mori Y, Tominaga M. TRPM2 activation by cyclic ADP-ribose at body temperature is involved in insulin secretion. *EMBO J* 2006; **25** : 1804-15.

Wehage E, Eisfeld J, Heiner I, Jüngling E, Zitt C, Lückhoff A. Activation of the cation channel long transient receptor potential channel 2 (LTRPC2) by hydrogen peroxide. A splice variant reveals a mode of activation independent of ADP- ribose. *J Biol Chem* 2002; **277**: 23150-6.

Appendix: TRMP2 cation channels; Oxidative injury; electromagnetic fields;

3-DIMENSIONAL ITERATIVE FORWARD MODEL FOR MICROWAVE IMAGING

OLEKSIY S. KIM and PETER MEINCKE

ØRSTED•DTU, ELECTROMAGNETIC SYSTEMS
TECHNICAL UNIVERSITY OF DENMARK
ØRSTEDS PLADS, BUILDING 348, DK-2800 KGS. LYNGBY, DENMARK
(osk@oersted.dtu.dk)

Abstract
The efficient solution of a forward scattering problem is the key point in nonlinear inversion schemes associated with microwave imaging. In this paper the solution is presented for the volume integral equation based on the method of moments (MoM) and accelerated with the adaptive integral method (AIM). The proposed technique differs from the usual well-known MoM and AIM in the way the matrices are computed and stored. It is shown that the MoM matrix can be split in parts, which are independent of the material parameters of the scattering object. Then, provided with the actual values of the object parameters, the matrix is promptly restored in each iteration of the nonlinear inversion process. The coefficients of the multipole expansion of the basis functions in AIM are also computed irrespective of the object properties, so that the far-field contribution is computed on-the-fly via FFT in each iteration of the forward solution. Thus, the presented technique allows us to avoid the time-consuming procedure of the MoM matrix filling in each inversion iteration. Furthermore, the forward solution from the previous inversion iteration can be utilized in the next one as an initial guess, thus reducing the solution time for the forward model.

Introduction
Nonlinear inversion schemes applied in microwave imaging involve the solution of a forward scattering problem, which takes the major part of the overall solution time. Therefore, it is of great importance to make the forward model fast and efficient to ensure the rapid convergence of the imaging procedure.

If a single-frequency inversion technique is utilized, it implies a frequency-domain forward scattering model. The volume integral equation (VIE) technique or the finite element method (FEM) can be applied in this case. The VIE solution converges much faster than FEM [1]. However, its memory demand is also significantly higher. The FEM generates a sparse matrix, while the method of moments (MoM) applied to transform the integral equation into a system of linear equations yields a matrix with a very high fill-in. The large memory requirements of MoM for integral equations can be a bottleneck for imaging of dense inhomogeneous dielectric objects. To overcome this difficulty an accelerated MoM solver, such as the multilevel fast multipole method (MLFMM) or the adaptive integral method (AIM), can be applied.

In this paper, we present the solution for the volume integral equation by the method of moments accelerated with the adaptive integral method. The proposed technique differs from the usual well-known MoM and AIM in the way the matrices are computed and stored.

Nonlinear inversion process involves an iteration procedure, in which a forward problem is solved in each iteration with a relatively small variation of the material parameters of the object under investigation. To improve the efficiency of the algorithm the forward solution can take advantage of the solution from the previous iteration. First of all, the time consuming MoM matrix filling process can be almost eliminated if the matrix is split into parts independent of the material parameters of the scattering object. These parts can be computed only once and stored in computer memory or on a hard disk. Then, provided with the actual values of the object parameters, the matrix is promptly restored in each iteration of the nonlinear inversion process. Thus, a significant saving in the computational time can be achieved as compared to the case when the MoM matrix is

computed from scratch in each iteration. Furthermore, the forward solution from the previous inversion iteration can be utilized in the next one as an initial guess, thus reducing the solution time for the forward model.

Method of Moments for Volume Integral Equation

The volume integral equation represents the total electric field $\bar{E}(\bar{r})$ in the volume V as a sum of the incident $\bar{E}^i(\bar{r})$ and the scattered $\bar{E}^s(\bar{r})$ electric fields as

$$\bar{E}(\bar{r}) = \bar{E}^i(\bar{r}) + \bar{E}^s(\bar{r}), \qquad \bar{r} \in V. \tag{1}$$

The scattered electric field $\bar{E}^s(\bar{r})$ can be written in terms of the magnetic vector potential $\bar{A}(\bar{r})$ and scalar potential $\Phi(\bar{r})$ as

$$\bar{E}^s(\bar{r}) = -j\omega\bar{A}(\bar{r}) - \nabla\Phi(\bar{r}), \tag{2a}$$

$$\bar{A}(\bar{r}) = \mu_b \int_V G(\bar{r},\bar{r}')\bar{J}(\bar{r}')dv', \tag{2b}$$

$$\Phi(\bar{r}) = \frac{1}{\varepsilon_b}\int_V G(\bar{r},\bar{r}')\rho(\bar{r}')dv', \tag{2c}$$

where $G(\bar{r},\bar{r}')$ is the free space Green's function and $\bar{J}(\bar{r})$, $\rho(\bar{r})$ are the unknown induced electric volume current and charge densities, respectively. In (2), ε_b is the permittivity and μ_b is the permeability of the background medium. It is noted that the VIE is more conveniently solved with respect to the electric flux density $\bar{D}(\bar{r})$ because its normal component is continuous across the boundary between two different dielectric materials. The substitution in variables is carried out as

$$\bar{J}(\bar{r}) = j\omega K(\bar{r})\bar{D}(\bar{r}) == j\omega\frac{\varepsilon(\bar{r})-\varepsilon_b}{\varepsilon(\bar{r})}\bar{D}(\bar{r}). \tag{3}$$

To discretize the VIE in (1) the scattering object is divided into cells using curvilinear hexahedral elements. Then, the unknown function $\bar{D}(\bar{r})$ is expanded locally in each cell in terms of the higher-order hierarchical Legendre basis functions $\overline{f_n}(\bar{r})$ [2]. Finally, the Galerkin's testing is employed to transform the VIE in (1) into a system of linear equations. Assuming the dielectric permittivity $\varepsilon(\bar{r})$ to be constant within each cell and taking into account that $\rho(\bar{r}) = j\omega^{-1}\nabla\cdot\bar{J}(\bar{r})$, an element z_{mn} of the resulting MoM matrix $[Z]$ can be written as

$$\begin{aligned} z_{mn} &= \frac{\left\langle \overline{f_m}(\bar{r}), \overline{f_n}(\bar{r})\right\rangle}{\varepsilon_l} + K_l\left\{-\omega^2\mu_b\left\langle \overline{f_m}(\bar{r}), \int_{V_l} G(\bar{r},\bar{r}')\overline{f_n}(\bar{r}')dv'\right\rangle\right. \\ &\left. -\frac{1}{\varepsilon_b}\left\langle f_m(\bar{r}), \nabla\left(\int_{V_l} G(\bar{r},\bar{r}')\left[\nabla'\cdot\overline{f_n}(\bar{r}')\right]dv' - \int_{S_l} G(\bar{r},\bar{r}')\left[\overline{f_n}(\bar{r}')\cdot\overline{dS'}\right]\right)\right\rangle\right\} \\ &= \frac{z'_{mn}}{\varepsilon_l} + K_l z''_{mn}, \end{aligned} \tag{4}$$

where $\langle\cdot,\cdot\rangle$ is the inner product, and the subscript l denotes the cell, in which the function $\overline{f_n}(\bar{r})$ is defined. The surface integral in (4) is taken "just inside" the surface of the cell l. It is seen that both z'_{mn} and z''_{mn} are independent on the material parameters of the object. However, the expression (4) is valid only for a subset of the higher-order hierarchical Legendre basis functions $\overline{f_n}(\bar{r})$, namely those that are defined within one cell. For the basis functions that span two neighbor cells (rooftop, for instance), so that $\overline{f_n}(\bar{r}) = \overline{f_n^-}(\bar{r}) + \overline{f_n^+}(\bar{r})$, the expression (4) can be modified as

$$\begin{aligned} z_{mn} &= \frac{\left\langle \overline{f_m}(\bar{r}), \overline{f_n^-}(\bar{r})\right\rangle}{\varepsilon_l^-} + \frac{\left\langle \overline{f_m}(\bar{r}), \overline{f_n^+}(\bar{r})\right\rangle}{\varepsilon_l^+} + K_l^- z''^-_{mn} + K_l^+ z''^+_{mn} \\ &= \frac{z'^-_{mn}}{\varepsilon_l^-} + \frac{z'^+_{mn}}{\varepsilon_l^+} + K_l^- z''^-_{mn} + K_l^+ z''^+_{mn}. \end{aligned} \tag{5}$$

Again, the expressions for $z'^{\pm}_{mn}$ and $z''^{\pm}_{mn}$ do not contain the material parameters of the scattering object. Consequently, the matrices $[Z''^{-}]$ and $[Z''^{+}]$ can be precomputed and stored for the subsequent iterations of the nonlinear inversion process. The first two terms in (5) do not require precomputation. They can be computed "on the fly", since no time-consuming Green's function calculations are involved.

Adaptive Integral Method for Volume Integral Equation

The adaptive integral method accelerates the solution of the VIE by separating elements of the MoM matrix $[Z]$ responsible for near- and far-interactions [3], as

$$[Z] = [Z^{near}] + [Z^{far}]. \tag{6}$$

The near-field elements $[Z^{near}]$ constitute a relatively small part of the full matrix. They are computed explicitly and stored in a sparse matrix format. The far interactions are accounted implicitly in the matrix-vector product $[Z^{far}][X]$, where $[X]$ is the unknown solution vector in each iteration of the iterative solution of the MoM matrix system. The following procedure makes it possible to apply the FFT to speed up the matrix-vector multiplication.

The induced volume current and charge densities are represented by point-like sources located at nodes of a regular rectangular grid enclosing the scattering object. Mathematically, it is equivalent to the expansion of the components of the functions $\overline{f_n}(\bar{r})$ and $\nabla \cdot \overline{f_n}(\bar{r})$ in terms of Dirac delta-functions as

$$f_\alpha(\bar{r}) \cong \sum_{\bar{u} \in C_\alpha} \Lambda_{\alpha\bar{u}} \delta(\bar{r} - \bar{u}), \tag{7}$$

where f_α denotes f_{nx}, f_{ny}, f_{nz}, or $\nabla \cdot \overline{f_n}$, and C_α is a cube of $(M+1)^3$ nodes. The coefficients $\Lambda_{n\bar{u}}$ are chosen so that the expansion (7) reproduces the far field radiated by the current element $\overline{f_n}(\bar{r})$. This can be achieved in different ways, depending on approximation criteria established. Here, we use a multipole expansion described in [3].

To make the expansion (7) consistent with the representation (5) for the rooftop basis function, we can similarly write

$$f_\alpha(\bar{r}) = f^-_\alpha(\bar{r}) + f^+_\alpha(\bar{r}) \cong \sum_{\bar{u} \in C^-_\alpha} \Lambda^-_{\alpha\bar{u}} \delta(\bar{r} - \bar{u}) + \sum_{\bar{u} \in C^+_\alpha} \Lambda^+_{\alpha\bar{u}} \delta(\bar{r} - \bar{u}). \tag{8}$$

Thus, the elements of the matrix $[Z^{far}]$ can be approximated as

$$z^{far}_{\beta\alpha} \cong K_l^- \sum_{\bar{v} \in C_\beta} \sum_{\bar{u} \in C^-_\alpha} \Lambda_{\beta\bar{v}} G(\bar{v} - \bar{u}) \Lambda^-_{\alpha\bar{u}} + K_l^+ \sum_{\bar{v} \in C_\beta} \sum_{\bar{u} \in C^+_\alpha} \Lambda_{\beta\bar{v}} G(\bar{v} - \bar{u}) \Lambda^+_{\alpha\bar{u}}. \tag{9}$$

In (9), we assume that constants, such as ω, ε_b, μ_b, are included in the corresponding coefficients Λ. Based on the expression (9) it can be observed that the matrix vector-product $[Z^{far}][X]$ can be effectively computed by FFT's.

The coefficients $\Lambda^{\pm}$ are independent of the material parameters of the scattering object, and therefore calculated once they can be reused throughout the nonlinear inversion process.

Forward Solution Procedure in the context of the Nonlinear Inversion Process

The computational procedure for the solution of the forward scattering problem in the context of the nonlinear inversion process is as follows:

1. Set initial values for the material parameters of the object under investigation.
2. Discretize the object.
3. Set the expansion order for the unknown function $\overline{D}(\bar{r})$ in each cell according to its electrical size.
4. Specify a regular rectangular grid enclosing the scattering object and compute the coefficients $\Lambda^{\pm}$.
5. Compute the terms $z''^{\pm}_{mn}$ for the elements of $[Z^{near}]$ and store them in a sparse matrix format.
6. Reconstruct the matrix $[Z^{near}]$ using the precomputed $z''^{\pm}_{mn}$ and actual material parameters of the object (Equation (5)).

7. Solve the MoM matrix system using an iterative solver. The product $[Z^{far}][X]$ is calculated by FFT's in each iteration using the precomputed $\Lambda^{\pm}$.
8. If necessary update the material parameters of the object and return to step 6.

It should be noted that the procedure presented above is valid only for a reasonable variation of the material parameters of the object (within 10-20%). Otherwise, to avoid over- or under-discretization the procedure should be repeated starting from step 3. If our method of moments solution were based on low-order basis functions (pulse, RWG, etc.) the procedure should have been repeated starting from step 2.

Numerical Results

To verify the proposed technique, we consider scattering by a solid dielectric cube with the side length $1.4\lambda_0$. The cube is made of lossless dielectric with the relative permittivity $\varepsilon_r = 4.0$, except its central slice of width $0.28\lambda_0$ (see Fig. 1). The relative permittivity of the slice is varied from $\varepsilon_r = 4.1 - j0.05$ to $\varepsilon_r = 5.1 - j0.55$ in 11 cycles, which represent the iterations of a nonlinear inversion process. An x-polarized plane wave illumination is considered. The object is discretized with 1000 identical cells, and the second expansion order is utilized to expand the unknown electric flux density in each cell. The discretization yields 25200 unknowns, which would require about 4.7 GB of computer memory to store the full MoM matrix. For the modified MoM and AIM techniques presented in this paper the memory requirement is 510 MB.

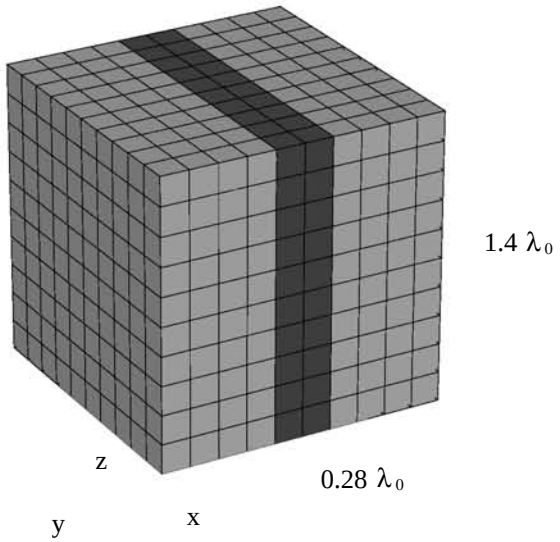


Fig.1. Solid dielectric cube with a central slice made of different dielectric material.

In the numerical experiments the Generalized Minimal Residual (GMRES) iterative solver with restarts after 30 iterations is employed. The time to fill the MoM matrix and the number of iterations to convergence to a relative residual error of 10^{-5} is summarized in Table 1 for all 11 cycles. In the first cycle all necessary calculations to precompute the data for the subsequent cycles are carried out, i.e., steps 1-5 of the solution procedure described in the previous section. Then steps 6-8 follow. In the subsequent cycles only steps 6-8 are involved. It is seen that a significant saving in time in cycles 2-11 is achieved by eliminating the matrix filling process and reusing precomputed result from the first cycle. The matrix reconstruction at the step 6 is extremely fast. Moreover, the number of iterations to converge is also decreased by employing as an initial guess the solution vector from the previous cycle.

Table 1. MoM matrix filling time and the number of iterations to converge.

Cycle	1(setup)	1	2	3	4	5	6	7	8	9	10	11
Permittivity	4.1-*j*0.05	4.1-*j*0.05	4.2-*j*0.10	4.3-*j*0.15	4.4-*j*0.20	4.5-*j*0.25	4.6-*j*0.30	4.7-*j*0.35	4.8-*j*0.40	4.9-*j*0.45	5.0-*j*0.50	5.1-*j*0.55
Filling time, sec	33547	15	15	15	15	15	15	15	15	15	15	15
Iterations	–	1559	1000	965	934	908	885	861	840	822	805	789

The configuration of the cycle 11 is also simulated from scratch using the classical MoM accelerated with the AIM. In Fig. 2, the obtained bistatic radar cross section (RCS) is compared to the result of the cycle 11. As expected, no difference is observed, which illustrates the correctness of the derivation and implementation of the presented technique.

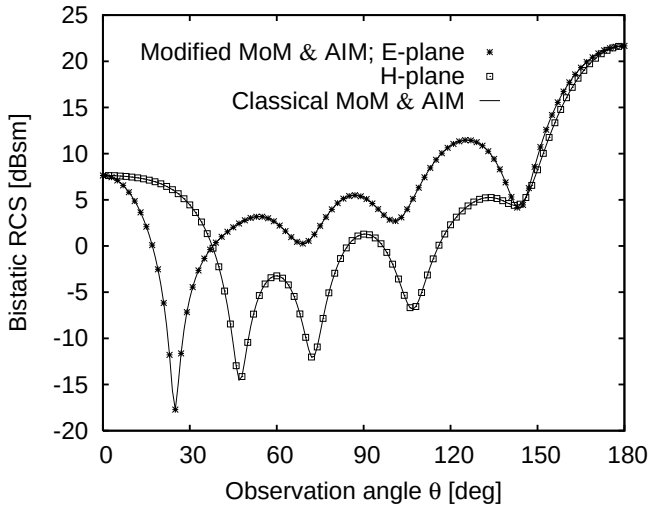


Fig.2. Bistatic RCS of the dielectric cube with a central slice made of dielectric with $\varepsilon_r = 5.1 - j0.55$.

Conclusions

The formulation for the classical method of moments for the volume integral equation, which is employed to solve the forward scattering problem, is modified so that the time consuming matrix filling procedure is moved to the setup phase of a nonlinear iterative inversion process. This is accomplished by splitting the MoM matrix in parts, which are independent of the material parameters of the scattering object. Once computed in the setup phase these parts are stored in the memory or on a hard disk. Then, provided with the actual values of the object material parameters, the matrix is promptly restored in each iteration of the nonlinear inversion process. Similar modifications are made in the adaptive integral method, which is applied to accelerate the MoM solution as well as to reduce its memory demands. The given numerical results show that the present technique allows the forward model to be solved fast and efficiently in each iteration of a nonlinear inversion process.

Acknowledgments

The Danish Technical Research Council is acknowledged for supporting this work.

References

1. Volakis J.L., Sertel K., Jorgensen E., Kindt R.W., “Hybrid finite element and volume integral methods for scattering using parametric geometry”, *Computer Modeling in Engineering & Sciences*, vol. 5., no. 5, pp. 463-476, 2004.

2. Kim O.S, Jørgensen E., Meincke P., Breinbjerg O., “Method of moments solution of volume integral equations using higher-order hierarchical Legendre basis functions”, *Radio Sci.*, 39, RS5003, doi:10.1029/2004RS003041.

3. Bleszynski E., Bleszynski M., Jaroszewicz T., “AIM: adaptive integral method for solving large-scale electromagnetic scattering and radiation problems”, *Radio Sci.*, vol. 31, no. 5, pp. 1225-1251, 1996.

USING COMPUTER PROGRAMS TO EVALUATE EFFICIENCY OF DIFFERENT SHIELDS CONFIGURATION

KUREK KRZYSZTOF[1)], GRYZ KRZYSZTOF[2)], KARPOWICZ JOLANTA[2)], KUREK ALICJA[1)], SMALCERZ ALBERT[1)], ZRADZIŃSKI PATRYK [2)]

[(1)] SILESIAN UNIVERSITY OF TECHNOLOGY, DEPARTMENT OF ELECTROTECHNOLOGY, 8 KRASIŃSKIEGO STR., 40-019 KATOWICE, POLAND
[(2)]CENTRAL INSTITUTE FOR LABOUR PROTECTION-NATIONAL RESEARCH INSTITUTE, 16 CZERNIAKOWSKA STR, 00-701 WARSAW, POLAND

Abstract
The issue of limiting negative influence of effect of electromagnetic fields from induction heating devices using electromagnetic shields has been presented in the paper. The effectiveness of shielding for fields of different frequencies has been examined considering the material, thickness and size of shields as well as multilayer systems. The research was conducted applying computer simulation method using Flux3D and CST EM Studio programs and subsequently experimentally verified at laboratory stand. The satisfactory similarity of simulation and experimental results allows for using the simulation method in designing shields for industrial use.

Introduction
Induction as well as magnetohydrodynamic (MHD) heating devices are commonly used in industry especially in metallurgy and machine building. Conversion of energy into heat or generation of electrodynamic forces moving liquid metal happens through electromagnetic fields of low frequencies of 50 and 60 Hz, medium ones of around 30 kHz and high ones of up to around 400 kHz. Because of it the supplying sources of induction or MHD devices have negative influence on the surrounding environment. One of the technical means most often used for limiting electromagnetic radiation is electromagnetic shielding. Technical surroundings in industrial environment very frequently cause unexpected distribution of field around the devices, which makes proper design and production of effective shielding a very complicated issue. Usually adequate experience is required as well as suitable research methods need to be applied. In the authors' opinion a computer simulation method is very useful to achieve these aims provided that it is properly experimentally verified [1,2].
The multivariant calculations in the paper have been carried out applying programs using the finite elements and boundary integrals method for calculations of magnetic field intensity in front and behind the shield, since in case of induction or MHD devices these are the real risks. Different shield structures: single-layer and double-layer have also been examined taking into consideration the material they have been made from, their size and positioning in relation to the measuring point. The calculations have been performed for the frequency range most often used in induction heating and metallurgical MHD devices.

Simulation results
The simulation calculations have been made in a system (Fig.1) consisting of an inductor loaded with a charge being a field source and a shield placed between the inductor and the points in space in which the field intensity have been calculated. Flux3D computer programs were used for calculation basing on Maxwell's equations solution applying finite elements method and respectively CST EM Studio using boundary integrals method. Physical properties of materials being subject of simulation have been put into Table 1.
Shielding effectiveness has been calculated in accordance with the relation [3]:

$$S_H = 20\,lg\,\frac{H}{H_S}$$

where: H – magnetic field intensity in a system without a shield, H_S - magnetic field intensity in a system with a shield.

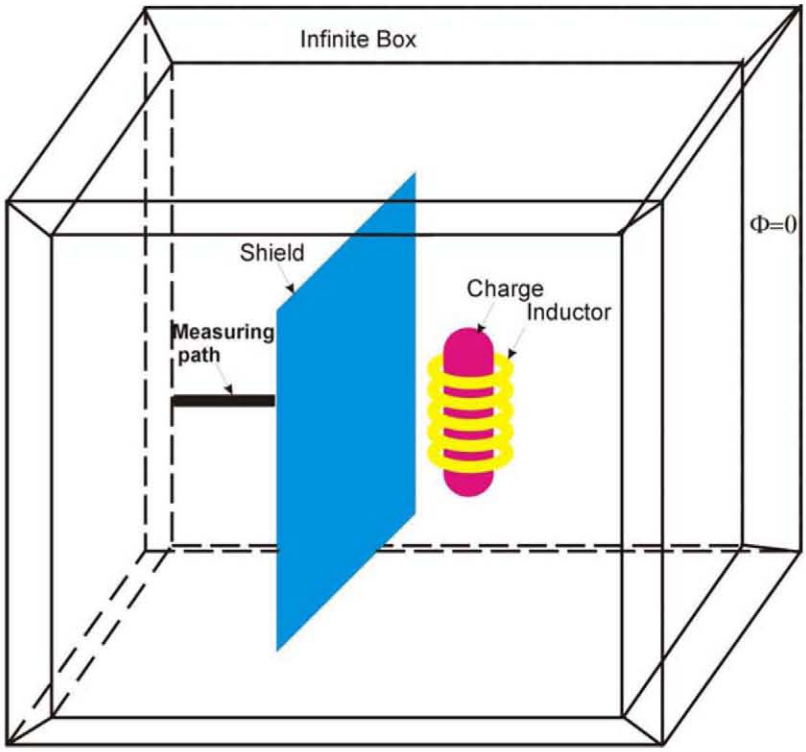


Fig.1. 3D calculation model for simulation of shielding effectiveness of induction devices

The influence of the shield's material, its thickness, structure, existence of one or two layers and the placing between source and a measuring point on shielding effectiveness has been examined with certain supplying parameters. The simulation results are shown in Figures 2-5.

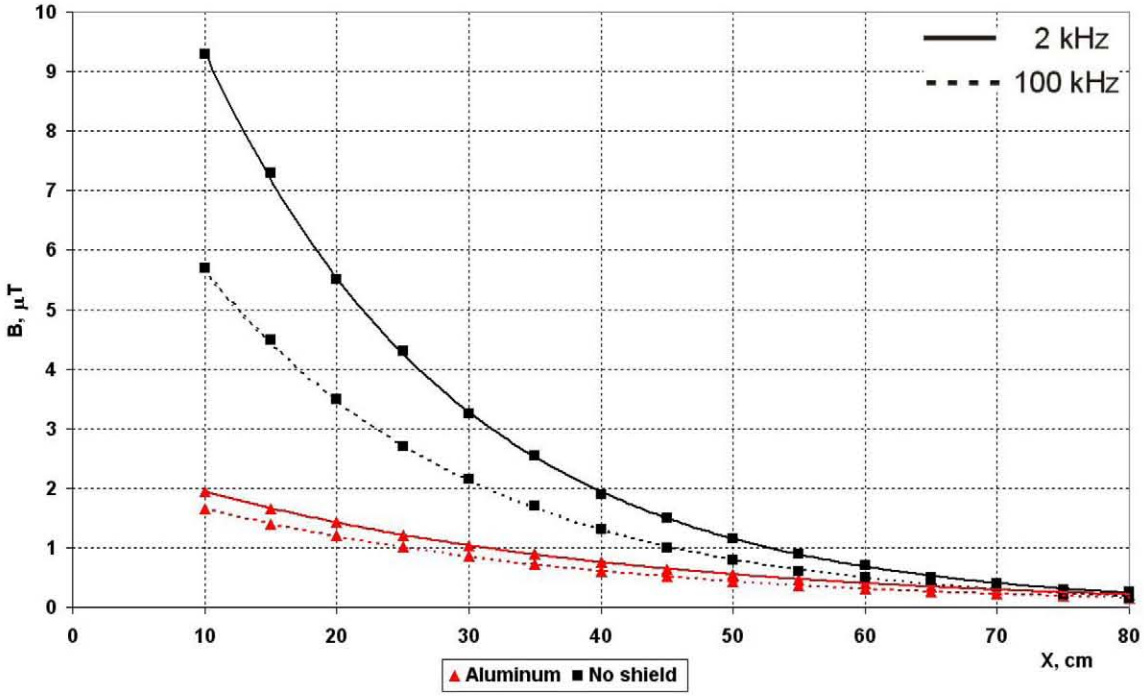


Fig. 2. Effect of using shield on magnetic induction value on measuring path outside shield

Using an electromagnetic shield (Fig.2) leads to a rapid four times decrease of magnetic induction value in places outside the shield especially in its nearest proximity, since with moving away from the source the field weakens in a natural way.

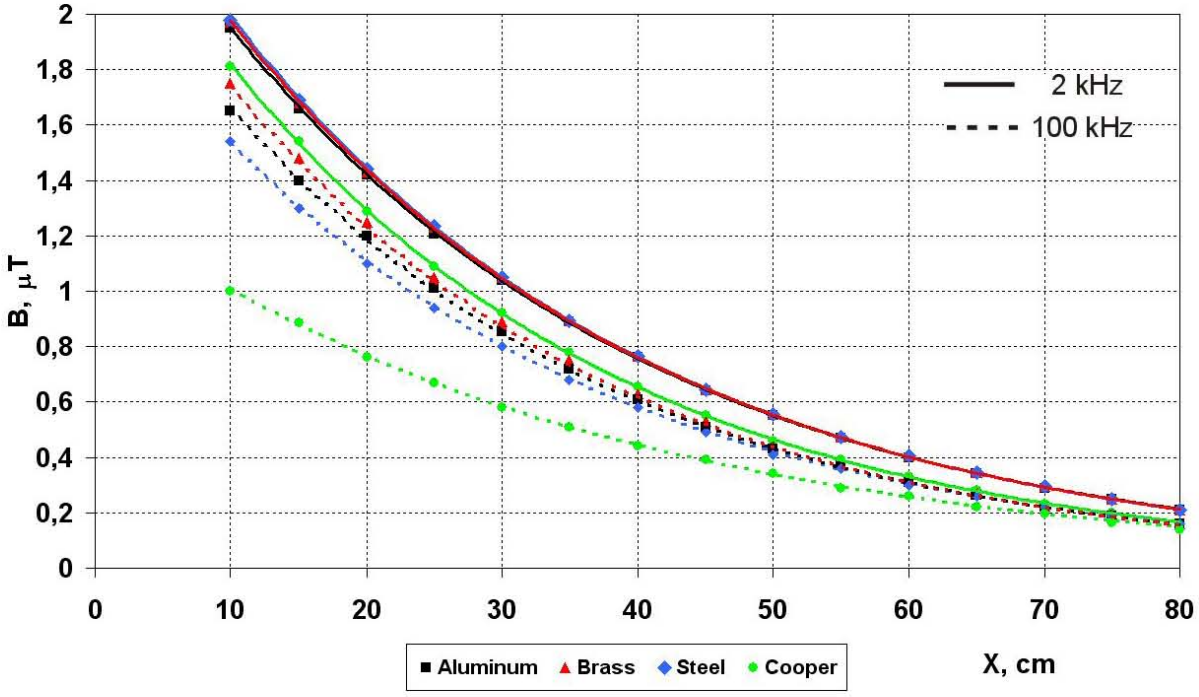


Fig.3. Calculated magnetic induction values for shields made of various materials

The materials of high conductivity and possibly of high magnetic permeability (ferromagnetics) have the best shielding properties (Fig.3) by certain shield thickness. One has to however bear in mind that using ferromagnetics as shields is limited and near the sources with medium and high frequencies even impossible due to their quick heating leading to melting in places. While choosing the material its costs also have to be considered. This makes using of copper very problematic and therefore aluminum and non-magnetic steel are used far more often

Tab. 1. Physical properties of materials

Material	Conductivity, MS/m	Magnetic permeability
Aluminum	33	1
Brass	25	1
Steel	4,3	1000
Copper	55	1

Figure 4 indicates that the shield should not be to thin (0,5 mm) in relation to the depth of electromagnetic field penetration

$\delta = \frac{2}{\mu\gamma\omega}$, where μ - magnetic permeability of the shield, γ – electrical conductivity of the shield, ω – pulsation of the coil current ($\omega = 2\pi f$). Nevertheless further increase of its thickness to over 2 mm is purposeless since the production costs grow significantly with slight decrease of induction value.

On the other hand the course of curves shown in Figure 5 indicates that application of double-layer structures (two different materials) is reasonable only for a system conductor (Cu or Al) – ferromagnetic. It seems that this has to be subject of further research.

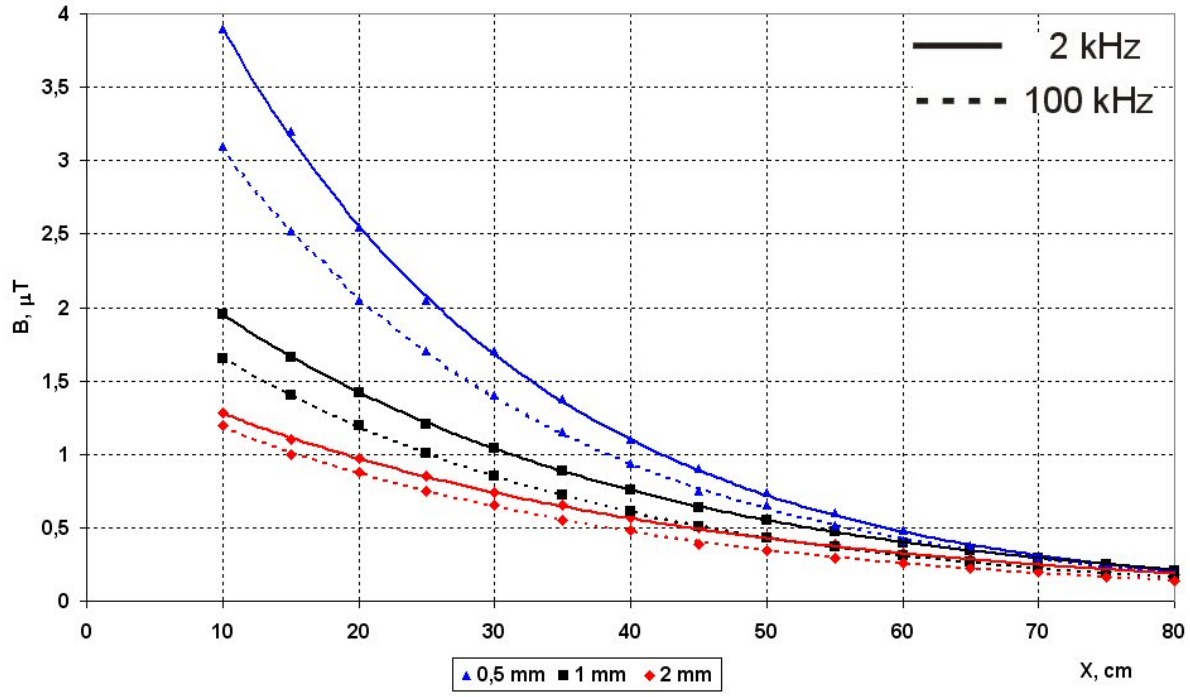


Fig.4. Calculated values of magnetic induction for aluminum shields of various thicknesses

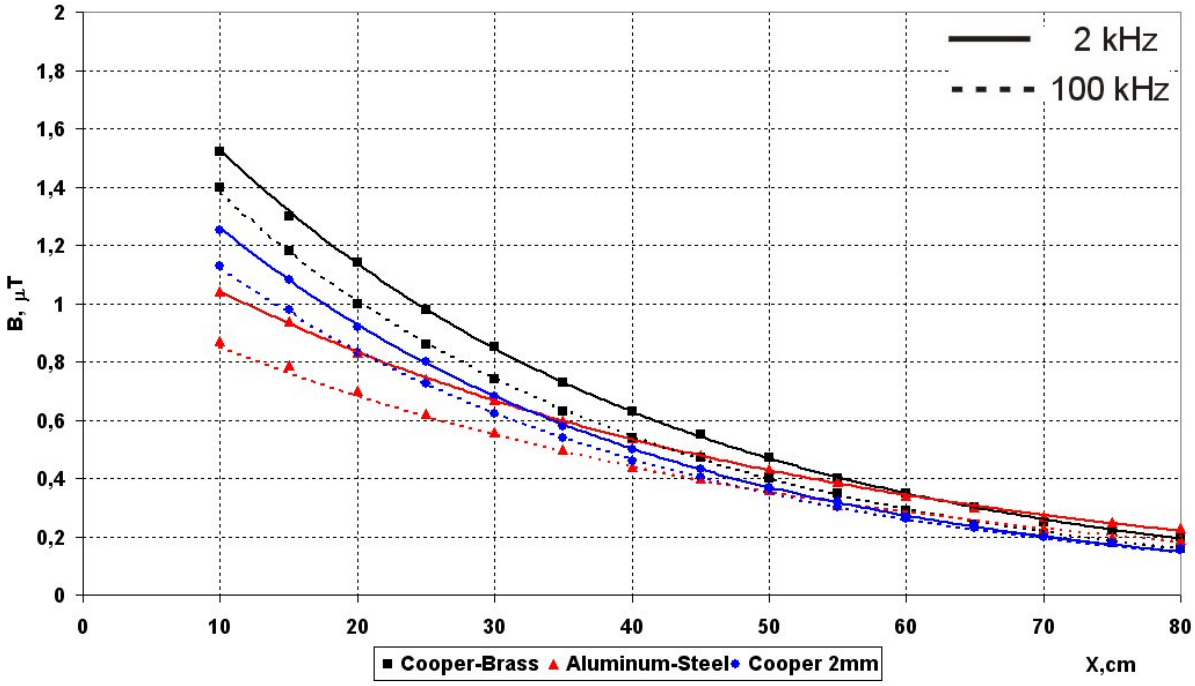
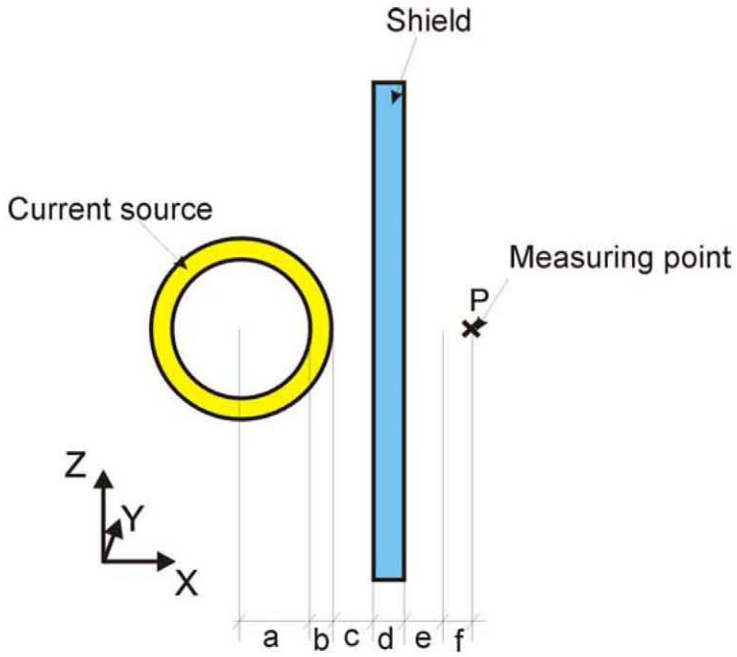


Fig. 5. Calculated values of magnetic induction for double-layer shields in relation to single-layer shield made of copper with same thickness as double-layer shields

Experimental verification

The carried out simulation research was experimentally verified in the laboratory of Electromagnetic Risks Workroom in the Central Institute of Work Protection. The examinations have been performed in the system as in Figure 6 and covered determination of frequency characteristics of shielding effectiveness for metal shielding structures, comprising of various combinations of sheet metal. The frequency characteristics have been determined for electromagnetic fields' frequency of 20 to 100 kHz. The Helmholtz's coils were used as electromagnetic field source during examinations. The supplying system consisted of a HAMEG HM8130 generator, PA-300S power supplier, H/PA-300S adjusting system. The stability of the generated magnetic field

was monitored with excitation check using HP 34401A voltmeter. The shielding effectiveness was determined on the basis of magnetic induction measurements using Narda ELT-400 meter (S/N K-0036) with 1Hz-400kHz probe (S/N K-0042), applied in a RMS 320μT, LowCut 1Hz working mode. Comparison of shielding effectiveness results obtained from simulation and measurements has been shown in Figure 7 and 8.



a	b	c	d	e	f
mm	mm	mm	mm	mm	mm
150	20	10	10	50	50

Fig.6. Measuring system for experimental verification of shielding effectiveness

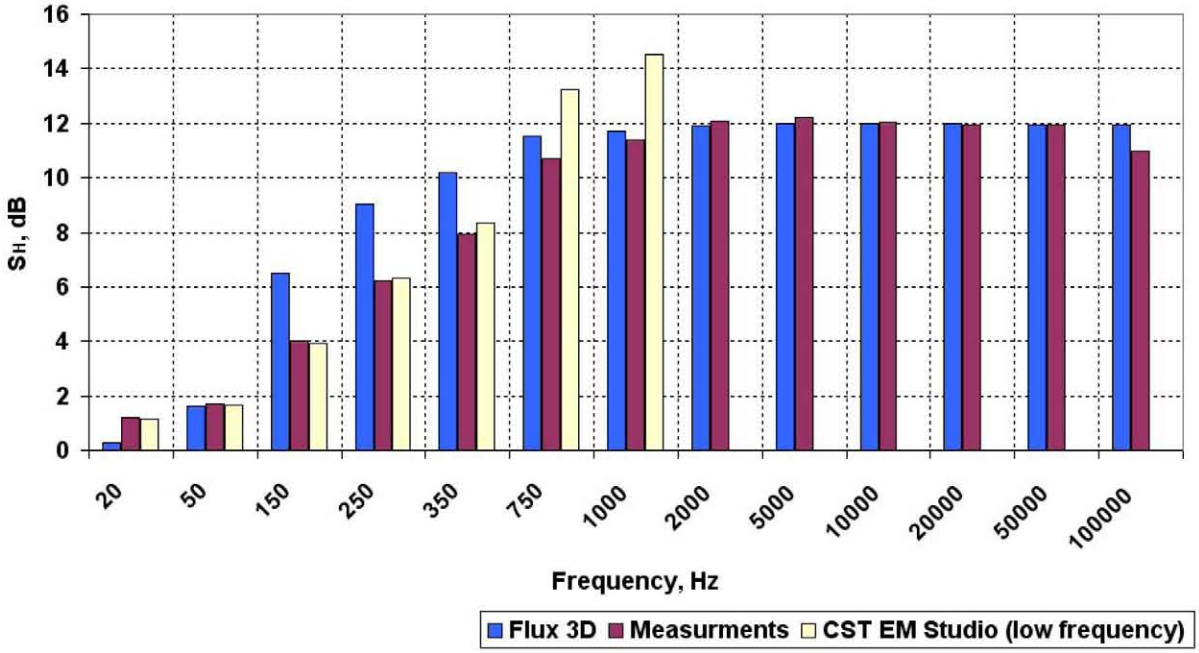


Fig.7. Comparison of shielding effectiveness results obtained from simulation (Flux3D, CST Studio) and measurements for shield made of sheet copper of 1 mm thickness

The presented comparison show that the calculation carried out using Flux3D program for medium and high frequencies > 750 Hz are very similar to experimental results (Fig.7) for single-layer shield and a little less so for

double-layer shield (Fig.8). In both cases good conformity of CST Studio and experimental results has been obtained for low frequencies < 250 Hz.

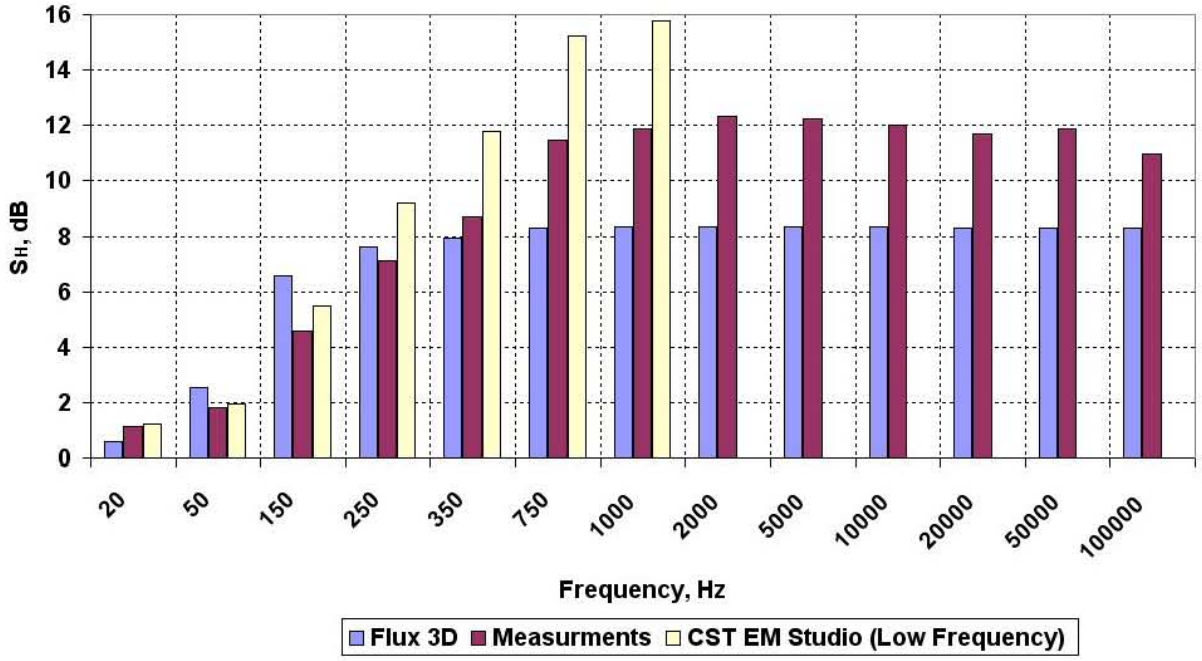


Fig.8. Comparison of shielding effectiveness results obtained from simulation (Flux3D, CST Studio) and measurements for double-layer shield made of sheet copper of 1 mm thickness and made of brass of 1 mm thickness

Summary

Usability of computer simulation method for research on shielding effectiveness and consequently on limitation of electromagnetic radiation levels around induction devices has been presented in the paper. The carried out examinations proved that that for frequency ranges applied in induction heating the best results of shielding effectiveness were obtained for copper shields of thicknesses up to 2 mm. Only slightly worse results were obtained for aluminum, but considering the cost of both materials, the latter will be much more frequently used. Interesting results have been obtained for double-layer systems especially for aluminum-steel, however this requires further research in order to select the optimum sort of sheet steel and thickness of both layers.

Application of computer simulation may be a basic tool in the design process of electromagnetic shields in industry installations.

Acknowledgments

This paper was supported by the State Committee for Scientific Research under research grants number 3 T08B 051 29 and 3 T08B 033 27.

References

1. Kurek K., Smalcerz A.: Methods of reduction of electromagnetic radiation around the induction devices, Workshop Warsaw, 2005, pp. 53-57 s. VI
2. Kurek K., Smalcerz A.: Electromagnetic fields exposure around induction heaters and methods of its limitation, International Conference on Electromagnetic Fields, Health and Environment, EHE'06, Funchal, Madeira, Portugal, April, 2006 pp. 1.93-1.98
3. Korniewicz H.: Ekranowanie źródeł pól elektromagnetycznych 0,1-300 MHz. Prace CIOP 1984, Polish pp.3-26

NEW FEATURES IN THE IEEE C95.1-2005 RF EXPOSURE STANDARD

C-K. CHOU[1], JOHN A. D'ANDREA[2], RICHARD A. TELL[3], J. PATRICK REILLY[4], ELEANOR R. ADAIR[5], MAYS L. SWICORD[6], SAKARI LANG[7], JOHN J. DEFRANK[8], RONALD C. PETERSEN[9]

[1]MOTOROLA LABS, CK.CHOU@MOTOROLA.COM
[2]NAVAL HEALTH RESEARCH CTR., JOHN.DANDREA@NAVY.BROOKS.AF.MIL
[3]RICHARD TELL ASSOCIATES, RTELL@RADHAZ.COM
[4]METATEC ASSOCIATES, JPREILLY@IEEE.ORG
[5]INDEPENDENT CONSULTANT, EADAIR@COMCAST.NET
[6]MOTOROLA LABS, MAYS.SWICORD@MOTOROLA.COM
[7]NOKIA CORPORATION, SAKARI.LANG@NOKIA.COM
[8]USACHPPM, JOHN.DEFRANK@AMEDD.ARMY.MIL
[9]R C PETERSEN ASSOCIATES, R.C.PETERSEN@IEEE.ORG

Abstract
C95.1-2005 "IEEE Standard for Safety Levels with Respect to Human Exposure to Radio Frequency Electromagnetic Fields, 3 kHz to 300 GHz" was approved on October 5, 2005 and published on April 19, 2006. This revision (of C95.1-1991) is based on an evaluation of the scientific literature through 2003. The recommendations are intended to protect people of all ages against established RF adverse health effects. Major changes (compared with the 1991 standard) are: 1) The maximum permissible exposure values of the lower tier are harmonized with other standards between 30 MHz and 100 GHz. 2) The upper frequency for the basic restriction on whole-body averaged SAR has been reduced from 6 to 3 GHz. 3) The BRs on peak spatial-average SAR have been changed from 1.6 W/kg and 8 W/kg for the lower and upper tiers to 2 W/kg and 10 W/kg, respectively, and the corresponding averaging mass from 1 to 10 g of tissue in the shape of a cube. For the extremities (including forearms and lower legs) and pinnae, the permitted peak SAR averaged over 10 g of tissue is now 20 W/kg for the upper tier and 4 W/kg for the lower tier. 4) The averaging times for both the upper and lower tiers have been changed to more realistic values for frequencies above 3 GHz.

Introduction

The purpose of IEEE Std. C95.1-2005 [1] is to provide exposure limits (basic restrictions and derived limits) to protect against established adverse effects to human health associated with exposure to RF electric, magnetic and electromagnetic fields over the frequency range of 3 kHz to 300 GHz. This standard is a revision of IEEE Std C95.1-1991 (1999 edition) [2] and IEEE Std C95.1b-2004 [3]. In revising the standard, findings of studies published between 1950 and December 2003[1] were considered, including those studies that involve low level exposures where increases in temperature could not be measured or were not expected. New insights gained from improved experimental and numerical methods and a better understanding of the effects of acute and chronic RF electromagnetic field exposures of animals and humans are included. A lack of credible scientific and medical reports showing adverse health effects for RF exposures at or below corresponding exposure limits in past standards supports the protective nature of the standards. This standard for the first time includes guidance on the necessity of an RF exposure control program (C95.7-2005) [4].

Below 100 kHz, the effect being minimized is aversive or painful electrostimulation. Above 100 kHz there can be a sensation of heating, which is not considered adverse. The limits in this standard may not prevent such

[1] Although the literature cutoff date was December 2003, several papers published in 2004 and 2005 were included.

thermal sensations; they are designed to protect against adverse health effects resulting from tissue heating, the only established mechanism relating to adverse effects of exposure to RF energy at frequencies above 100 kHz.

The standard consists of two main parts. The normative part includes an overview of the document (scope, purpose, and introduction), references, definitions, and recommendations. The informative part is comprised of 7 Annexes, with the first three explaining the revision process, summary of literature, and rationale of the revision. Examples of practical applications are shown in Annex D. The last three annexes are glossary, literature database (with 1143 references) and bibliography. This paper summarizes the 250 page standard, with emphasis on the new features. For details, especially on the literature summary of about 1300 peer reviewed papers (Annex B) and rationale of all changes (Annex C), please refer to the original standard [1].

Recommendations

The recommendations are expressed in terms of basic restrictions (BRs) and maximum permissible exposure (MPE) values (sometimes called reference levels, or investigation levels). The BRs are limits on internal fields, specific absorption rate (SAR), and current density; the MPEs, which are derived from the BRs, are limits on external fields and induced and contact current. The recommendations, which protect against effects associated with electrostimulation and tissue and whole body heating, are intended to apply to all human exposures except for exposure of patients by, or under the direction of, physicians and medical professionals.

BRs and MPEs for frequencies between 3 kHz and 100 kHz

Table 1 lists basic restrictions for particular areas of the body in terms of the electric field within the biological tissue (*in situ*). Two parameters are listed in the table: the rheobase *in situ* field, E_0, and a strength-frequency parameter, f_e. Limits are determined from Table 1 as:

$$E_i = E_0 \text{ for } f \leq f_e$$

$$E_i = E_0 (f/f_e) \text{ for } f \geq f_e$$

Where E_i is the maximum allowed induced in situ electric field.

Table 1 – BRs applying to various regions of the body

		Action Level[a]	**Persons in Controlled Environments**
Exposed tissue	f_e (Hz)	E_0 (rms) (V/m)	E_0 (rms) (V/m)
Brain	20	5.89×10^{-3}	1.77×10^{-2}
Heart	167	0.943	0.943
Extremities	3350	2.10	2.10
Other tissues	3350	0.701	2.10

[a] Within this frequency range the term "action level" is equivalent to the term "general public".

Table 2 lists the MPEs for the magnetic field (flux density, *B*, and magnetic field strength, *H*) for exposure of the head and torso. The averaging time for an rms measurement is 0.2 second.

Table 2 – MPE for exposure of head and torso: f = 3 kHz to 5 MHz

Frequency range (kHz)	Action Level		Persons in Controlled Environments	
	B_{rms} (mT)	H_{rms} (A/m)	B_{rms} (mT)	H_{rms} (A/m)
3.0 – 3.35	0.687/f	547/f	2.06/f	1640/f
3.35 – 5000	0.205	163	0.615	490
NOTE—f is expressed in kHz.				

The MPEs for the limbs (entire arms and legs) are listed in Table 3.

Table 3 – MPE for the limbs: f = 3 kHz to 5 MHz

Frequency range (kHz)	Action Level		Persons in Controlled Environments	
	B_{rms} (mT)	H_{rms} (A/m)	B_{rms} (Mt)	H_{rms} (A/m)
3.0 – 3.35	3.79/f	3016/f	3.79/f	3016/f
3.35 – 5000	1.13	900	1.13	900
NOTE—f is expressed in kHz.				

Table 4 lists MPEs in terms of the undisturbed (absent a person) external electric field, E.

Table 4 – Electric field MPE – whole body exposure: f = 3 kHz to 100 kHz

	Action Level	Persons in Controlled Environments
Frequency range (kHz)	E (rms) (V/m)	E (rms) (V/m)
3 kHz to 100 kHz	614	1842

The limits in Table 5 protect against adverse electrostimulation effects.

Table 5 – RMS induced and contact current limits for continuous sinusoidal waveforms, f = 3 kHz to 100 kHz

Condition	Action Level (mA)	Persons in Controlled Environments (mA)
Both feet	0.90f	2.00 f
Each foot	0.45f	1.00 f
Contact, grasp[a]	--	1.00 f
Contact, touch	0.167f	0.50 f
NOTE 1— f is expressed in kHz. NOTE 2—Limits apply to current flowing between the body and a grounded object that may be contacted by the person. NOTE 3—The averaging time for determination of compliance is 0.2 s.		

[a] The grasping contact limit pertains to controlled environments where personnel are trained to make grasping contact and to avoid touch contacts with conductive objects that present the possibility of painful contact.

BRs and MPEs for frequencies between 100 kHz and 3 GHz

The whole-body-average BRs shown in Table 6 are based on established adverse health effects associated with heating of the body during whole-body exposure. Consistent with the approach used in the prior standard to derive exposure limits, a traditional safety factor of ten (10) has been applied to the established SAR threshold for such effects, yielding an SAR of 0.4 W/kg averaged over the whole body. In the absence of an RF safety program, the BRs of the lower tier (action level) may also be used for the general public. Applied to members of the general public, the lower tier provides more assurance that continuous, long-term exposure of all individuals in the population, will be without risk of adverse effects. The localized exposure BRs shown in Table 6 are established to protect against excessive temperature rise in any part of the body that might result from localized or non-uniform exposure. When averaging SAR over a 10-g volume of tissue in the extremities and the pinnae, only SAR values for that tissue may be considered. If any cubic volume contains tissue from both the body and the extremities or pinna, each must be considered separately.

Table 6 – BRs for frequencies between 100 kHz and 3 GHz

		Action Level [a] SAR[b] (W/kg)	Persons in Controlled Environments SAR[c] (W/kg)
Whole-body exposure	(Whole-Body Average— WBA)	0.08	0.4
Localized exposure	(Local peak spatial-average)	2[c]	10[c]
Localized exposure	(Extremities[d] and pinnae)	4[c]	20[c]

[a] BR for the general public when an RF safety program is unavailable.

[b] SAR is averaged over the appropriate averaging times as shown in Table 8 and Table 9.

[c] Averaged over any 10 g of tissue (defined as a tissue volume in the shape of a cube)[2].

[d] The extremities are the arms and legs distal from the elbows and knees, respectively.

[2] The volume of the cube is approximately 10 cm^3.

Contact and induced current limits, 100 kHz to 110 MHz

In the transition region of 100 kHz to 5 MHz, two sets of contact and induced current limits apply. The limits in Table 5 protect against effects associated with electrostimulation and the limits in Table 7 protect against effects associated with tissue heating. Contact and induced current shall both be limited as specified in Table 7.

Table 7 – RMS induced and contact current limits for continuous sinusoidal waveforms, *f* = 100 kHz to 110 MHz

Condition	Action Level [a] (mA)	Persons in Controlled Environments (mA)
Both feet	90	200
Each foot	45	100
Contact, grasp[b]	-	100
Contact, touch	16.7	50
NOTE 1—Limits apply to current flowing between the body and a grounded object that may be contacted by the person. NOTE 2—The averaging time for determination of compliance is 6 minutes.		

[a] MPE for the general public in absence of an RF safety program.

[b] Grasping contact limit pertains to controlled environments where personnel are trained to make grasping contact and to avoid touch contacts with conductive objects that present the possibility of painful contact

BRs for frequencies between 3 GHz and 300 GHz

BRs to protect against adverse effects associated with heating are established for incident power density for frequencies between 3 GHz and 300 GHz. Such restrictions are derived with consideration of adverse effects thresholds (based on the literature review and evaluation), their distribution among the population, and safety factors. The BRs for frequencies between 3 GHz and 300 GHz are the same as the corresponding MPEs shown in Table 8 and Table 9, and are considered appropriate for all human exposure.

Table 8 – MPE for the upper tier (people in controlled environments)

Frequency range (MHz)	**RMS electric field strength (E)[a] (V/m)**	**RMS magnetic field strength (H)[a] (A/m)**	**RMS power density (S) E-field, H-field (W/m^2)**	**Averaging time $\|E\|^2$, $\|H\|^2$ or *S* (min)**
0.1–1.0	1842	16.3 / f_M	(9000, 100 000 / f_M^2)[b]	6
1.0–30	1842/ f_M	16.3 / f_M	(9000 / f_M^2, 100 000 / f_M^2)	6
30–100	61.4	16.3 / f_M	(10, 100 000 / f_M^2)	6
100–300	61.4	0.163	10	6
300–3000	—	—	f_M / 30	6
3000–30 000	—	—	100	19.63 / $f_G^{1.079}$
30 000–300 000	—	—	100	2.524 / $f_G^{0.476}$

NOTE—f_M is the frequency in MHz, f_G is the frequency in GHz.

[a] For exposures that are uniform over the dimensions of the body, such as certain far-field plane-wave exposures, the exposure field strengths and power densities are compared with the MPEs in the Table. For non-uniform exposures, the mean values of the exposure fields, as obtained by spatially averaging the squares of the field strengths or averaging the power densities over an area equivalent to the vertical cross section of the human body (projected area), are compared with the MPEs in the Table.

[b] These plane-wave equivalent power density values are commonly used as a convenient comparison with MPEs at higher frequencies and are displayed on some instruments in use.

Table 9 – Action level (MPE for the general public when an RF safety program is unavailable)

Frequency range (MHz)	RMS electric field strength (E)[a] (V/m)	RMS magnetic field strength (H)[a] (A/m)	RMS power density (S) E-field, H-field (W/m^2)	Averaging time $\|E\|^2$, $\|H\|^2$ or S [b] (min)	
0.1–1.34	614	$16.3 / f_M$	$(1000, 100\,000 / f_M^2)$ [c]	6	6
1.34–3	$823.8 / f_M$	$16.3 / f_M$	$(1800/ f_M^2, 100\,000 / f_M^2)$	$f_M^2 / 0.3$	6
3–30	$823.8 / f_M$	$16.3 / f_M$	$(1800/ f_M^2, 100\,000 / f_M^2)$	30	6
30–100	27.5	$158.3 / f_M^{1.668}$	$(2, 9\,400\,000 / f_M^{3.336})$	30	$0.0636 f_M^{1.337}$
100–400	27.5	0.0729	2	30	30
400–2000	—	—	$f_M / 200$	30	
2000–5000	—	—	10	30	
5000-30 000	—	—	10	$150 / f_G$	
30 000-100 000	—	—	10	$25.24 / f_G^{0.476}$	
100 000-300 000	—	—	$(90 f_G - 7000)/200$	$5048/[(9 f_G - 700) f_G^{0.476}]$	
NOTE—f_M is the frequency in MHz, f_G is the frequency in GHz.					

[a] For exposures that are uniform over the dimensions of the body, such as certain far-field plane-wave exposures, the exposure field strengths and power densities are compared with the MPEs in the Table. For non-uniform exposures, the mean values of the exposure fields, as obtained by spatially averaging the squares of the field strengths or averaging the power densities over an area equivalent to the vertical cross section of the human body (projected area), are compared with the MPEs in the Table.

[b] The left column is the averaging time for $|E|^2$, the right colum is the averaging time for $|H|^2$. For frequencies greater than 400 MHz, the averaging time is for power density S.

[c] These plane-wave equivalent power density values are commonly used as a convenient comparison with MPEs at higher frequencies and are displayed on some instruments in use.

RF safety programs

Throughout the RF spectrum applicable to this standard, the MPEs apply to exposure of people, i.e., compliance with this standard is determined by whether or not exposures of people to RF fields, currents and voltages exceed the applicable MPEs. Where there may be access to RF fields, currents, and/or voltages that exceed the lower tier (Action Level) of this standard, an RF safety program such as detailed in IEEE Std C95.7-2005 [4] shall be implemented to ensure that exposures do not exceed the MPEs or BRs for persons in a controlled environment.

Similarities and differences between this standard and IEEE Std C95.1-1991

Similarities:

a) All relevant reported biological effects at either low ("non-thermal") or high ("thermal") levels were evaluated. Research on the effects of chronic exposure and speculations on the biological significance of low-level interactions have not changed the scientific basis of the adverse effect level.

b) WBA and peak spatial-average SAR remain the basic restrictions of exposure over much of the RF spectrum. The whole body average SAR values remain the same as in IEEE Std C95.1-1991, i.e., 0.4 and 0.08 W/kg.

c) The MPE for exposures in controlled environments remain the same as in IEEE Std C95.1-1991.

d) The averaging time remains six minutes for frequencies below 3 GHz for effects associated with tissue heating. For electrostimulation effects, the averaging time is 0.2 s for an rms measurement. Peak electrostimulation limits apply to instantaneous values within the applicable bandwidth.

Differences:

a) IEEE Std C95.1-1991 contains two tiers; an upper tier for "exposures in controlled environments" and a lower tier for "exposures in uncontrolled environments." In this standard, two tiers have also been set. As in the 1991 standard, an upper tier has been set for exposure of persons in controlled environments. While the weight of scientific evidence supports the conclusion that no measurable risk is associated with RF exposures less than the upper tier of this standard, it is impossible to scientifically prove absolute safety (the null hypothesis). Thus a lower tier has been set with an extra margin of safety that applies to all other individuals. The lower tier, called an "action level," recognizes public concerns, takes into account uncertainties in laboratory data and in exposure assessment, and supports the process of harmonization with other standards, e.g., the NCRP recommendations [6] and the ICNIRP guidelines [7]. For practical purposes, the lower tier may be used for the general public or as an action level, above which an RF safety program shall be implemented to protect against exposures that exceed the upper tier.

b) The upper frequency boundary over which whole body average SAR is deemed to be the basic restriction has been reduced from 6 GHz to 3 GHz.

c) The long-term MPEs for the lower tier are different from those in IEEE Std C95.1-1991 and are in general more restrictive between 300 MHz and 300 GHz.

d) The peak spatial-average SAR values have been changed from 1.6 W/kg and 8 W/kg for lower and upper tiers to 2 W/kg and 10 W/kg, respectively.

e) The averaging mass for determining the peak spatial-average SAR has been changed from 1 g of tissue in the shape of a cube to 10 g of tissue in the shape of a cube.

f) Although implicit in previous versions of IEEE Std C95.1, the present standard explicitly relies on "basic restrictions".

g) The standard now requires the development and implementation of an RF safety program in controlled environments.

h) The averaging time for both the upper and lower tiers has been changed for frequencies above 3 GHz.

i) The upper frequency at which maximum induced and contact currents are specified is now 110 MHz compared with 100 MHz in the previous standard.

j) The frequency at which the upward ramp begins for the relaxation of the power density limits for localized exposure has been changed from 6 GHz to 3 GHz.

k) In recognition of the differing impact of exposure to particular frequencies, the standard provides sections devoted to three frequency bands: 3 kHz to 5 MHz, 100 kHz to 3 GHz and 3 GHz to 300 GHz. The limits in the first band minimize adverse effects associated with electrostimulation. This overlaps the second band where the limits also protect against effects associated with heating. The limits in the third band protect against effects associated with heating. Differences within each of those bands are provided below.

Features:

a) **3 kHz to 5 MHz** – The standard defines basic restrictions (BR) in terms of the *in situ* (within biological tissue) electric fields for different regions of the body. Magnetic field MPEs are specified for the arms and legs and for the head and torso, but compliance with the standard can be demonstrated for uniform sinusoidal magnetic fields by showing that either the *in situ* electric field BR or the magnetic field MPE is satisfied. If the magnetic field is not constant over the head and torso, it is sufficient to demonstrate that the basic restrictions are satisfied, or that the spatial peak of the magnetic field MPE is not exceeded. Based on current knowledge of adverse effects on humans within this frequency range, the whole body electric field MPE for the controlled environment has been increased. Similarly, the magnetic field MPEs, with separate requirements for body portions as noted above, have been increased for both the general public and controlled environments and have been made frequency dependent. Averaging time for an RMS measurement is 0.2 second. Formulas have been included for determining maximum permitted peak electric fields for both *in situ* and environmental considerations.

b) **100 kHz to 3 GHz** – In this frequency range where SAR is the controlling criterion, the revised standard confirms the presumed threshold whole body average SAR of 4 W/kg for potentially adverse effects. Localized exposure restriction criteria (peak spatial-average SAR) have been changed for both the upper and lower tiers. Peak spatial average SAR for any body tissue including the hands, wrists, forearms, feet, ankles, lower legs and pinnae, is required to be determined over 10 g of tissue in the shape of a cube. Peak spatial average SAR for the 10-g sample is to be no greater than 10 W/kg for the upper tier and 2 W/kg for the lower tier. For the hands, wrists, forearms, feet, ankles, lower legs and pinnae, the permitted peak spatial average remains as specified previously in 10 g of tissue, *i.e.*, 20 W/kg for the upper tier and 4 W/kg for the lower tier. The contact current limits for the frequency range of 100 kHz to 110 MHz have been subdivided into touch and grasping conditions, with the grasping condition confined to the controlled environment. The permissible touch contact current has been reduced for both the controlled environment and the general public. The lower part of this frequency range, i.e., 100 kHz to 5 MHz, is a transition region where the limits protecting against electrostimulation and the limits protecting against effects associated with heating must be met.

c) **3 GHz to 300 GHz** – In this frequency range, the interactions become quasi-optical, and the MPEs are expressed in terms of incident power density and exposure duration. The principal change in the standard has been in the MPE frequency dependence above 300 MHz for the lower tier (general public).

Summary

IEEE C95.1-2005 provides recommendations to protect against established adverse effects in human beings exposed to electromagnetic fields in the frequency range from 3 kHz to 300 GHz. Similarities and differences from the IEEE C95.1-1991 (and its two amendments) are discussed. A notable revision to the new standard is the recommendation of peak spatial average SAR of 2 and 10 W/kg averaged over 10 g tissue for the lower and upper tier limits, respectively. This revision resolves a major harmonization issue with other RF standards and guidelines. Cooperative efforts should be continued to achieve internationally harmonized exposure limits.

References

[1] IEEE C95.1-2005, "IEEE Standard for Safety Levels with Respect to Human Exposure to Radio Frequency Electromagnetic Fields, 3 kHz to 300 GHz".

[2] IEEE C95.1-1991, "IEEE Standard for Safety Levels with Respect to Human Exposure to Radio Frequency Electromagnetic Fields, 3 kHz to 300 GHz", (1999 edition).

[3] IEEE C95.1b-2004, "IEEE Standard for Safety Levels with Respect to Human Exposure to Radio Frequency Electromagnetic Fields, 3 kHz to 300 GHz - Amendment 2: Specific Absorption Rate (SAR) Limits for the Pinna)".

[4] IEEE C95.7-2005, "Recommended Practice for Radio Frequency Safety Programs".

[5] IEEE C95.6-2002, "IEEE Standard for Safety Levels with Respect to Human Exposure to Electromagnetic Fields, 0 to 3 kHz".

[6] NCRP, Biological Effects and Exposure Criteria for Radiofrequency Electromagnetic Fields. Bethesda: NCRP Report no. 86, National Council on Radiation Protection and Measurements, Bethesda, MD, 1986

[7] ICNIRP (International Commission on Non-Ionizing Radiation Protection), "Guidelines for limiting exposure to time-varying electric, magnetic, and electromagnetic fields (up to 300 GHz)," *Health Physics*, vol. 74, pp. 494 - 522, 1998

EXPERIMENTAL DOSIMETRY FOR THE UK MOBILE TELECOMMUNICATIONS AND HEALTH RESEARCH PROGRAMME

BENJAMIN LOADER
NATIONAL PHYSICAL LABORATORY,
HAMPTON ROAD, TEDDINGTON MIDDLESEX, UK, TW11 0LW

Abstract
This paper presents a review of the dosimetry in the UK Mobile Telecommunications and Health Research (MTHR) programme. It describes the exposure systems used in the human volunteer studies, their output characteristics, and the rationale behind their specifications. It also describes how traceability to national standards was established for the *in vitro* studies. Problems encountered during the development of these systems are also presented.

Introduction
The Link Mobile Telecommunications and Health Research Programme (MTHR) resulted from the publication of the report by the Independent Expert Group on Mobile Phones [1]. The MTHR has funded research in the UK to a value of £8.8 million to investigate the impact of mobile telecommunications on health. In determining the research priorities, the programme has sought to take into account public concerns about mobile communications technology as well as other research conducted nationally and internationally. To date, MTHR has funded twenty projects, and another six projects have been funded as an adjunct to the programme by the UK Department for Trade and Industry or the Home Office. Effective and accurate dosimetry is essential if meaningful conclusions are to be drawn from these studies. Under the programme, the National Physical Laboratory (NPL) has provided dosimetry support to the research projects. This support has included advice regarding the specification of exposure systems, independent verification that the systems used meet these specifications, and calibration to provide traceability to National Standards. Staff at NPL have also measured and characterised other aspects of the systems' performance, such as the low frequency magnetic fields that they emit [2].

For dosimetry purposes, the studies fall into the following categories: human volunteer studies on handset exposure, human volunteer studies on base station exposure, *in vitro* studies, in *vivo* studies, and epidemiology. This paper considers the exposure systems used for the human volunteer and *in vitro* studies. It provides a description of the devices used for generating the exposures, the rationale behind the choice of signal characteristics and exposure levels, and problems that were encountered during their development. The paper also examines how traceability to National Standards was established for exposures in the *in vitro* studies, and how the systems were characterised at NPL.

1. Human-volunteer studies
Handset exposure. During typical phone use there is a wide variation in exposure. This is dependent on the phone type, radio reception conditions, pattern of speech or type of data sent, the way the phone is held, and whether it is used in the left or right hand. Along with the RF signals, the phone will generate low frequency magnetic fields caused by the pulsed nature of the battery currents and static magnetic fields caused by the earpiece in the phone. Movement of the phone may modulate such static fields during use. There will be some heating of the skin in the region of the phone because the circuits dissipate heat and the use of the phone may also affect the subject's posture. All of these factors could potentially affect the outcomes of human volunteer studies. It would be impossible to encompass all possible variations in exposure conditions within a single experiment. Practical considerations limit the duration of test sessions for human volunteer studies, and therefore the number of exposure conditions that can be tested. Whilst a system could be designed to generate uniform exposure to cover all possible regions exposed during phone use, such a system would not give realistic patterns of exposure, and in particular, any effects due to the field gradients in the head would not be apparent.

MCL (www.mcluk.org), in collaboration with the Department of Electronics at York University, developed the handsets that were used for all the human volunteer studies on handset exposure within the MTHR programme (Fig. 1). These handsets are designed to give accurate and reproducible exposures representative of those from GSM [3] or TETRA [4] phones, and to facilitate double-blind experiments. The handsets are battery powered, to allow free movement of the subjects during the tests and also to avoid coupling effects that occur if a cable connects the antenna to the signal source. They can operate for approximately one hour before the batteries need

charging and there is an audible low battery warning. They operate as "stand alone" transmitters without the requirement for an operational network.



Three modes of exposure were used for the MTHR studies; pulsed mode (GSM or TETRA), continuous wave (CW) mode, which produces an unmodulated signal with the same frequency and average power as the pulsed mode, and sham mode. CW mode was included to determine whether any observed effects are due to the pulsed nature of mobile phone signals. Selection of the mode of operation is by two 16-position rotary switches, the codes for each mode being assigned randomly for each handset and held by the manufacturer. This facilitates double blind experiments. The characteristics of the output from the handsets in each mode are shown in Table 1.

Figure 1: Picture of the MTHR handsets. Front and rear view. The antenna is angled slightly towards the head to increase specific absorption rate (SAR) level. Visible are two rotary mode switches and RF test connector used to check correct operation prior to test sessions.

Table 1: Comparison of exposure modes.

Output characteristics	**Mode**		
	GSM or TETRA	**CW**	**Sham**
RF exposure level	1.4 Wkg^{-1}	1.4 Wkg^{-1}	0.002 Wkg^{-1}
Pulse modulation of signals	Yes	No	No
Low frequency magnetic fields	Yes	No	No
Static magnetic field	Yes	Yes	Yes
Heat dissipation from circuits in phone	Yes	Yes	Yes

The characteristics of the modulation for the GSM and TETRA modes are given in Table 2. The transmission frequency was chosen to be 888 MHz for the GSM handset and 381 MHz for the TETRA phone. The GSM handset frequency is just outside the normal operating band of the GSM system, and this is to avoid interference with operational networks. Signal modulation gives rise to a low frequency magnetic field, which is the case for a real phone, and these are shown in Fig. 2. In the sham mode, the CW signal is generated and a switch diverts the signal to an internal load so that the antenna does not transmit it. This gives the same battery life and operating temperature as the transmitting modes, which is a requirement for double blinding. The sham mode therefore produces the same static magnetic field as the CW mode. The circuit boards within the handset also radiate electromagnetic fields in the sham mode and this, rather than the performance of the RF switch used, limits the degree of isolation that can be achieved. In the "sham" mode the exposure level is reduced by at least 20 dB compared to the exposed modes. The field level in air at 10 cm from the handset is between 0.5 Vm^{-1} and 1 Vm^{-1} for the sham mode, compared to 13 V/m for the CW exposed mode.

Table 2: Main characteristics of GSM & TETRA signals.

GSM		TETRA	
Handset characteristics	Included in MTHR handset	Handset characteristics	Included in MTHR handset
GSM 900	Yes	Voice plus data mode (V + D)	Yes [2]
GSM 1800	No	Direct mode (DMO)	No
GSMK mask for pulse shape (GSM)	Yes	Packet data optimised mode (PDO)	No
PSK modulation (GSM)	Yes	DQPSK modulation [3]	Yes
Super- and Hyper-frame structures.	Yes	Hyper and Multi-frame structure	Yes
Variation in slot transmit power (adaptive power control)	No	Variation in slot transmit power (adaptive power control)	No
GSM DTX mode[1]	No[1]	Correct pulse shape	Yes
Frequency hopping	No	Frequency hopping	No
Multi-slot operation	No	Multi-slot operation	No

Notes:

1. The handsets have this capability, but it was not used for the MTHR trials. Discontinuous Transmission (DXT) mode will alter the low frequency magnetic fields produced by the handset.
2. V + D is the most common mode of operation for TETRA. Only voice communication is included.
3. DQPSK = Π/4 Differential Quaternary Phase Shift Keying.

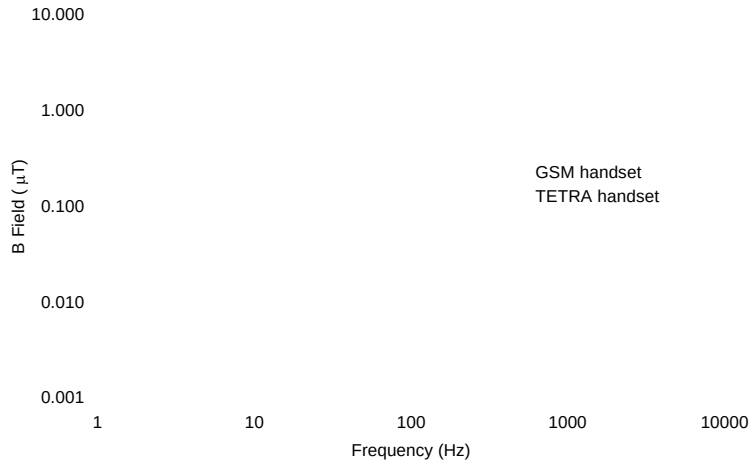


Figure 2. Magnetic field from MTHR handsets in GSM and TETRA "exposed" mode [2].

SAR is the specific absorption rate of RF energy in tissues in watts per kilogram (Wkg^{-1}). The target level for the GSM, CW and TETRA exposures was chosen as 1.4 Wkg^{-1} averaged over a 10 g mass. This is the highest level that ensures volunteers will not be exposed above the ICNIRP limit of 2 Wkg^{-1} for public exposure, allowing for the uncertainty of the dosimetry. Most available GSM handsets are designed to comply with IEEE limit [5] of 1.6 Wkg^{-1} averaged over a 10 g mass, so this level is representative of GSM phones. TETRA handsets with 1 W peak power produce similar SAR levels to GSM phones when used in voice communication mode [6, 7]. However, TETRA handsets having 3 W peak power can produce higher SAR levels [7]. The SAR from each handset was measured to an accuracy of ± 30 % by an accredited test laboratory and was checked and adjusted periodically during the studies. The handsets incorporate a test mode that allows the modulated or CW signal to be measured with a power meter prior to each test session, to confirm that the handset is operating correctly. Fig. 3 shows the measured SAR distribution from the GSM handset. The 10 g averaged SAR from the antenna is 1.4 Wkg^{-1}. The 10 g averaged SAR in the region of the body of the handset is 0.4 Wkg^{-1}.

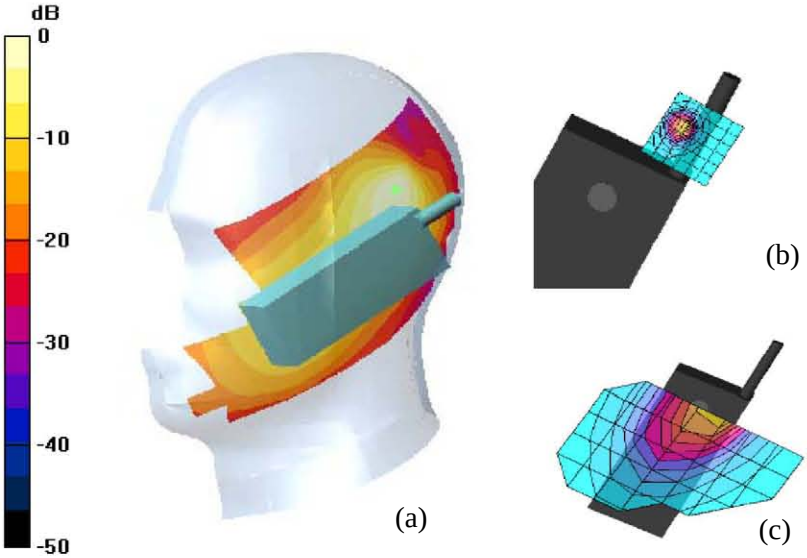


Figure 3. SAR distributions from the MTHR GSM handset (reproduced courtesy MCL Ltd). (a) Position of the handset for left hand exposures. (b) SAR distribution from antenna. (c) SAR distribution from circuits in the handset.

Both left hand and right hand use of the phone were considered in the studies. The phone was positioned in the "cheek position" defined in [8] when used on the left-hand side of the head. When used on the right-hand side of the head, it was shifted upwards from this position by 4 cm. This ensures that the position of the maximum SAR relative to the ear remains the same for both sides of the head, even though the antenna is not located symmetrically on the handset. The region of brain exposed may affect whether a particular effect is detected.

From switch on to the point the low battery audible warning activates, there is a gradual reduction in the power radiated by the handset, as shown in Fig. 4. Note that during all sessions, the handsets are switched on three minutes prior to beginning the tests.

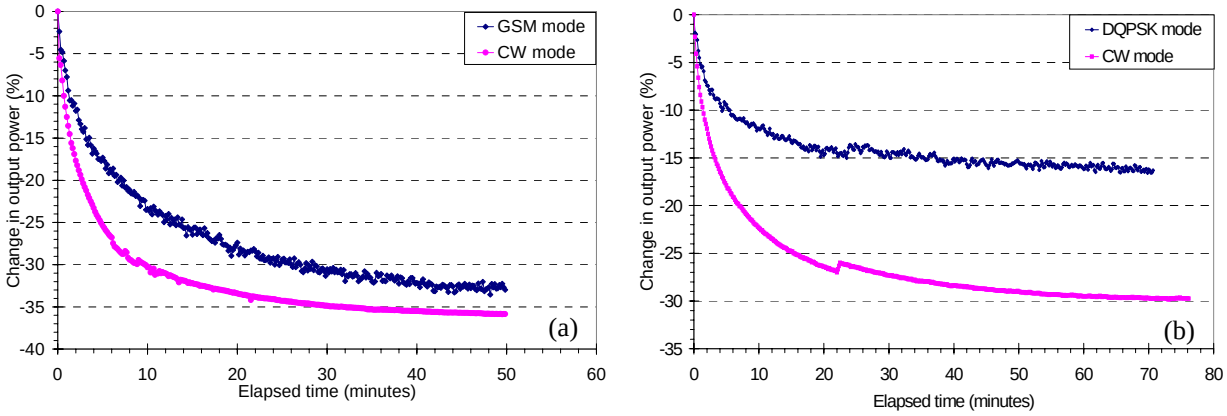


Figure 4. Change in radiated power versus time from switch on. (a) GSM handset, (b) TETRA handset

Achieving double blinding for the handsets was quite challenging. Each mode of operation must discharge the battery at the same rate, must result in the same degree of heating of the handset, and produce no audible or visual indications. Initial trials of the handsets showed that they got hotter in CW mode than modulated mode, and subjects were able to detect this difference. Adding an additional resistor to generate heat in the pulsed mode rectified this, but meant the handsets may get slightly hotter than is the case for a normal phone. In very quiet environments, some subjects were able to hear a clicking noise from the battery when the handset was in pulsed modes. Some low-level background noise was necessary to mask this sound during the experiments.

Studies look for differences in a measurable response resulting from the different exposure modes. Given the nature of the three exposure conditions from the MTHR handsets, studies using the handsets would show: *1. Effects that are due to GSM or TETRA signals from the handset in the presence of static magnetic fields, low frequency magnetic fields and contact heating that is typical of a real phone. 2. Effects arising from a CW signal whose severity increase with exposure level*. However, the following are not tested, since these are present in both the exposed and sham conditions: *1. Effects due to CW signals with a threshold that is below the sham level and whose severity does not increase with exposure level. 2. An effect arising solely from the static magnetic field of the handset. 3. Effects caused solely by the very slight heating of the head that occurs through contact with the warm phone.*

Base Station exposure. Base stations may have multiple traffic and control channels. The control channels always have full slot occupancy and maximum power level. The traffic channels have variable slot occupancy, and some designs have variable power level for the bursts (down-link power control). The inter-slot guard period that separates bursts are synchronised between channels. In real-life situations, the signal is reflected and attenuated by buildings and structures. As a person moves through the field, the amplitude of the signal may increase and decrease (fading multi-path). They will be exposed to many different radio signals simultaneously. The height of the antenna and the elevation pattern mean exposure may not decrease with distance from the antenna. Base stations may generate electromagnetic fields other than the transmitted signals, but these emissions are limited by the GSM specifications [3].

The base station exposure system used by MTHR was developed by Red-M Ltd [9], and installed at the University of Essex in an absorber-lined screened room supplied by NPL. The system provides three exposure modes; GSM mode, UMTS mode and sham mode. The sequence of exposure for each test session is determined by a test code that is assigned to each volunteer in the study, and these are randomised. This facilitates double blinding of the studies. In addition there is an open provocation mode. Fading multi-path effects were not simulated in the exposure system. Whilst fading multi-path simulators to represent different environments are available, this would have added considerably to the cost of the exposure system, and the choice of which environment to simulate would be difficult. The system uses a Rhode and Schwarz SMU 200A digital signal generator. For GSM mode, the amplitude-quadrature (I/Q) data of the traffic and control channels is generated externally and sent to the modulation inputs of the signal generator. An external circuit then adds the inter-slot guard period to give the correct pulse shape. As a result the data sent is not synchronised to the bursts. For UMTS, the signal generator generates the signal internally. In the sham mode the modulation and RF output

from the signal generator are turned off. The signals are amplified before being transmitted by a vertically polarised log periodic dipole array (LPDA) located inside the screened room. The antenna is at a distance of 5 m from the subject and is concealed behind a curtain. Forward and reverse power to the antenna are monitored prior to test sessions to confirm correct operation of the system. To reduce the field level that is present in the sham mode, the signal generator and amplifier are located outside the screened room used for the exposures. The system is calibrated every six months during the study to ensure that its output remains stable.

The total power density in the GSM mode and also the UMTS signal is 10 mWm^{-2} ± 30%. The choice of this exposure level was based on a detailed survey of seventeen macro-cellular base station sites in the UK, which found a maximum power density of 8.3 mWm^{-2} [10]. Exposure to members of the public from Microcell and Picocell base stations may exceed 100 mWm^{-2} [11], so this does not represent a maximum exposure for all types of base station. The variation in power density over the region occupied by the seated volunteer (a 1 m by 0.9 m plane orthogonal to the antenna boresight) is no more than ± 3.2 dB. The power density in the sham mode is 54 dB lower than for the transmit mode, and is a CW signal.

The GSM signal is representative of a GSM macro-cell base station without downlink power control on the traffic channels. The main characteristics of the GSM signal are given in Table 3. The pulse shape and inter-slot guard interval, Fig. 5(a), conform to the GSM specifications [3]. There are two traffic channels, one at 886.8 MHz and one at 1877 MHz, and two broadcast channels, one at 888.8 MHz and 1879 MHz and these signals are transmitted simultaneously. The broadcast channels have all eight slots in the frame continuously transmitted at a constant power level. The traffic channels have constant pulse amplitude but variable slot occupancy, the slot occupancy being generated stochastically, Fig. 5(b). The peak amplitude of the signal at the four frequencies are approximately equal.

Table 3: Main characteristics of GSM signals from the base station exposure system.

GSM base station	Included in MTHR exposure system
GSM 900 band	Yes
GSM 1800 band	Yes
Traffic channel	Yes
Control channel	Yes
Variations in slot transmit power on traffic channels (downlink power control).	No
PSK modulation	Yes
GSMK mask for pulse shape	Yes
Variable slot occupancy for traffic channel	Yes -this is generated stochastically
EMC emissions from base station	No
Fading multi-path effects	No

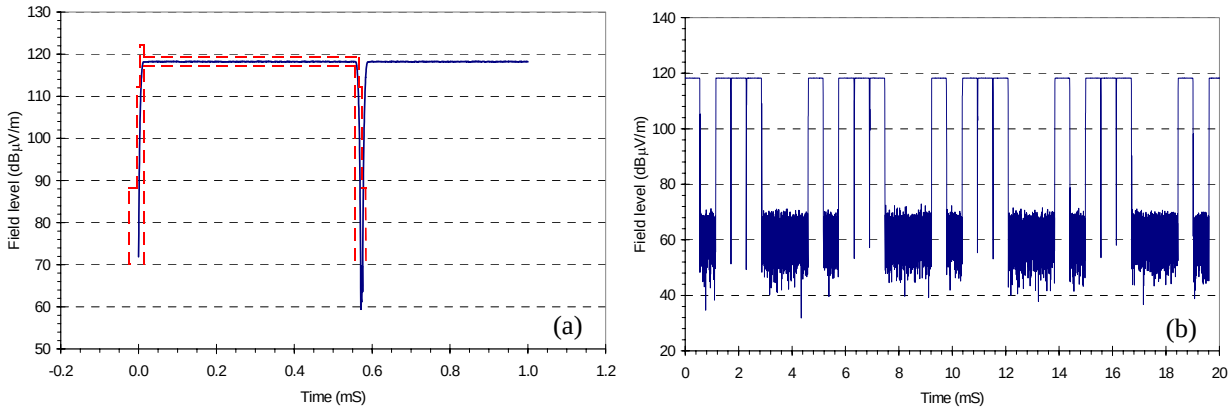


Figure 5. GSM 900 Traffic Channel: (a) Single pulse, dashed-line shows pulse limits from GSM specifications [3], (b) Multiple pulses, showing slot occupancy within the GSM fames.

The UMTS mode is based on test mode 1 specified in the 3GPP standard [12] and is representative of a realistic traffic scenario with high peak to average ratio. It is a single channel with 5 MHz bandwidth, as shown in Fig. 6. The signal was decoded using an Agilent PSA spectrum analyser, and the results are shown in Table 4

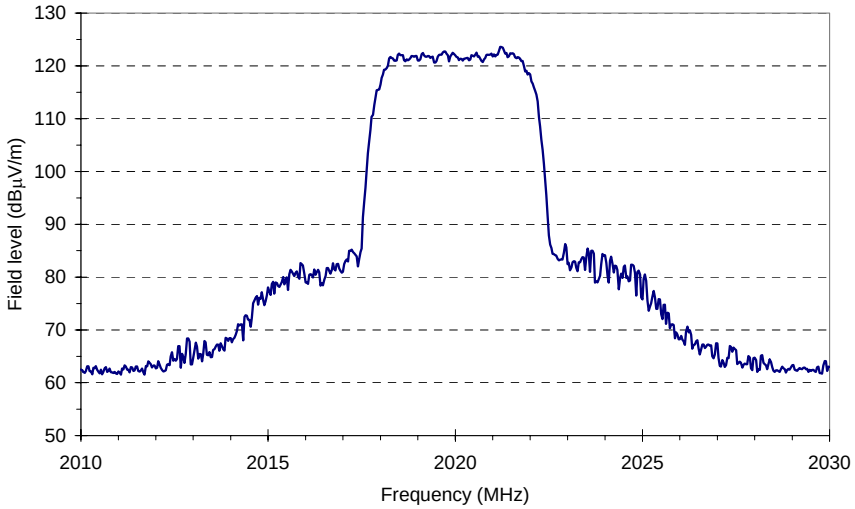


Figure 6. Peak amplitude versus frequency for UMTS signal.

Table 4. Composition of UMTS signal

Signal component	Level [1]
Common Pilot Channel (CPICH)	-24.009 dBc
Primary Synchronisation Channel (PSCH)	-43.09 dBc
Secondary Synchronisation Channel (SSCH)	-43.82 dBc
Number of active channels	none
Maximum power for inactive channel	-21.762 dBc
Average power for inactive channel	-27.093 dBc

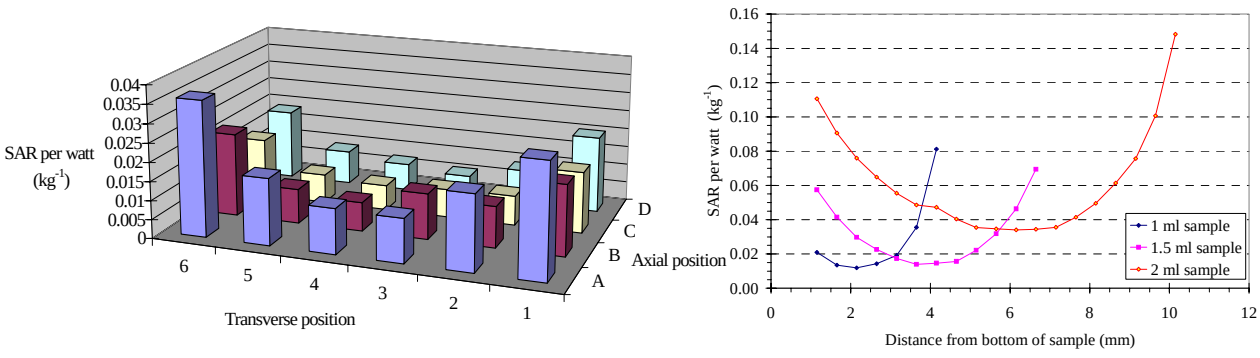
Note.
1. $$dBc = 10\log_{10}\left(\frac{channel\ \ power(W)}{Power\ at\ centre\ carrier\ \ frequency\ (W)}\right)$$

2. Exposure systems for in vitro studies.
Great care must be taken when designing and calibrating experimental exposure systems, and the scale of this task should not be underestimated when planning a study. As well as establishing known and accurate exposure levels with suitable signal characteristics, all other environmental factors must be considered and relevant parameters monitored during the experiments. A high efficiency at inducing SAR is desirable, since any power losses within the exposure device are likely to cause heating in the samples in addition to the heating due to their dielectric losses. Transverse Electromagnetic (TEM) cells [13], which are widely used for generating exposures, generally have a low efficiency for inducing SAR in small samples. Sample containers should not be placed directly on the conductors of the TEM line, as this allows thermal conduction to occur. For matched systems, heat may be transferred from the termination, and this should be remote from the exposure set up. For exposure systems used in incubators, there should be sufficient airflow to ensure the samples are at the same temperature as the incubator. In this respect open-sided transmission lines are better than closed TEM cells. It is essential to measure the heating of the biological samples that occurs during the exposure, and assess the effect that this will have. Where such heating occurs, rate of temperature rise measurements will over-estimate the SAR arising from absorption of RF energy. Systems with high VSWR may give higher efficiencies, but uncertainty in the position of the standing wave will lead to large uncertainties in the exposure. The position of the standing wave is dependent on the complex impedance of the source and termination. Determining the level at which samples should be exposed for a particular experiment is difficult. Whilst SAR measurements in homogeneous phantoms can be used to determine conservative estimates for the maximum 1 g or 10 g averaged SAR from a device, they cannot predict the SAR level in a particular biological tissue within a person or animal exposed to electromagnetic fields, and this can usually only be determined by computer simulations.

Calibrating *in vitro* exposure systems is difficult, and dosimetry may rely heavily on computer simulations. Systems that operate at 37°C, should be characterised at this temperature, as the conductivity of the samples, and therefore the energy absorption, will change with temperature. For multi-well plates the exposure will not be the same for all the wells. This should be taken into account when designing the experimental protocol. Uniformity of exposure may be enhanced by filling the regions between the wells with dielectric material having similar permittivity to the samples. Non-uniformity of samples and meniscus effects add to exposure uncertainty [14]. Whilst it is possible to measure the SAR in the media containing cells or organisms, the measurement techniques generally have insufficient resolution to determine the SAR within the biological material of interest. There is a clear need to develop techniques of dosimetry with much higher spatial resolution for this purpose (micro-dosimetry).

Two types of system were used to generate exposures for the in-*vitro* studies in the MTHR programme; a TEM cell for use in incubators (University of Nottingham) and open-sided transmission lines for use in microscope systems (Babraham Institute, Cambridge). The systems were calibrated at NPL to provide exposures that were traceable to National Standards. The method of calibration is to use a 1.4 mm diameter electric field probe to compare the electric field within the exposed samples with a known electric field in the same material generated within a matched waveguide system [15]. This may require several litres of sample at 900 MHz for the measurement in the matched waveguide. The measurement in the exposure system must be performed using a higher input power than is used for the experiments, and the results scaled to the correct power level. This is because the small size of the E-field probe yields poor sensitivity. A sample depth of at least 5 mm is necessary to avoid errors. For these systems, the field strength in the air above the sample is much higher than the field in the sample itself, and the probe will over-read if the sensors are not immersed sufficiently in the sample. Accuracy is improved by using the same power sensor to determine the input power to the waveguide and the exposure system. The material density must be measured to determine the SAR level, but the conductivity of the material is not used in the calculation using this method. The temperature rise in the samples was measured using a SPEAG TV1V3 temperature probe for different power levels.

The system used by the University of Nottingham for previous studies into effects of RF exposures on nematodes [16, 17, 18] has a twenty-four well *petri* dish located within the TEM cell. The exposure system is placed inside an incubator. As part of the MTHR programme, the performance of this system was assessed at NPL. Fig. 7(a) shows the measured SAR value at the centre of a 1 ml sample of K-medium (permittivity 78.30 – 22.96 j at 900 MHz and 22.5ºC) for each of the wells in the *petri* dish. There is considerable variation in the SAR level between wells in the *petri* dish. The SAR level averaged across all the wells was 0.0141 Wkg^{-1} for 1 W at input power, so the system has relatively low efficiency at inducing power absorption in the samples. It is important to note that the SAR was measured in the K-media used to support the nematodes, and not within the nematodes. The variation in SAR with sample volume and probe height is shown in Fig. 7(b). Note that the probe is over-reading as it comes into proximity of the surface of the sample because the field in air above the sample is much higher than the field within the sample.



(a) (b)

Figure 7. (a) Variation in SAR level for different wells in a multi-well petri-dish, (b) Variation in SAR with probe height for different sample volumes.

The temperature rises at the centre of the samples were measured at NPL in a temperature controlled laboratory. Cycling the power on and off allowed heating due to the RF power to be distinguished from any changes in the ambient temperature. It became apparent that the power loss in the TEM cell was giving rise to additional heating of the samples, and this was not predicted from SAR calculations. To reduce this loss, the following modifications were made to the system; the foam filler that originally filled the lower chamber of the TEM cell was removed; the BNC connectors used at either end of the TEM cell were replaced with APC3.5 connectors (BNC connectors are for frequencies up to 500 MHz); the TEM cell was silver-plated. The results of the sample temperature measurements before and after modification are shown in Fig. 8 and in Table 5. The temperature measurements were repeated with the system in the incubator used for the experiments and the results confirmed. Previously reported effects from the studies could not be replicated once the unwanted sample heating caused by the exposure system was reduced in this way [19]. It is probable that the nematodes used for the studies were sensitive to the temperature changes that were occurring in the original exposure system.

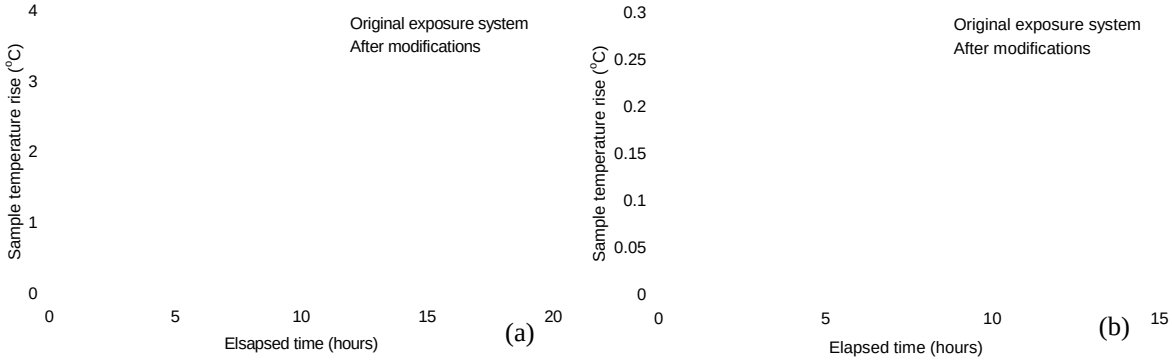


Figure 8. Temperature rises in samples for; (a) an input power of 10 W, (SAR level 0.14 Wkg^{-1}) and (b) an input power of 1 W (SAR level 0.014Wkg^{-1}) before and after modification of the exposure system.

Table 5: Performance of exposure system before and after modification.

Parameter	Original exposure system	After modification
Power loss at 900 MHz	8.47%	1.09%
Sample Temperature rise for 1 W input power	0.25ºC	0.12ºC
Sample temperature rise for 10 W input power	3.6ºC	1.4ºC
Average SAR level in samples for 1 watt input power.	0.014 Wkg^{-1}	(0.014 Wkg^{-1})

The system used by Babraham Institute [20, 21] is shown in Fig. 9. An inner conducting plate, and two outer conducting plates form an open-sided TEM transmission line. The sample is placed on the lower conductor directly above an aperture, and this allows it to be viewed with a microscope during exposure. Table 6 gives the measured SAR levels for 1 watt input power at five positions (Fig. 10) in HEPES and DMEM. The measurements were made at 22.2°C. This is because the National Standard for SAR is controlled at this temperature. However, the exposure system is normally used in an incubator at 37°C. The dielectric properties for these materials at 22.2°C and 37°C are given in Table 7. The SAR levels in the sample will be proportional to the conductivity, so the measured SAR values must be adjusted to account for temperature. The efficiency at inducing SAR in the samples is twenty times that of the Nottingham system, due to the smaller separation of the conductors, and no significant sample heating occurs.

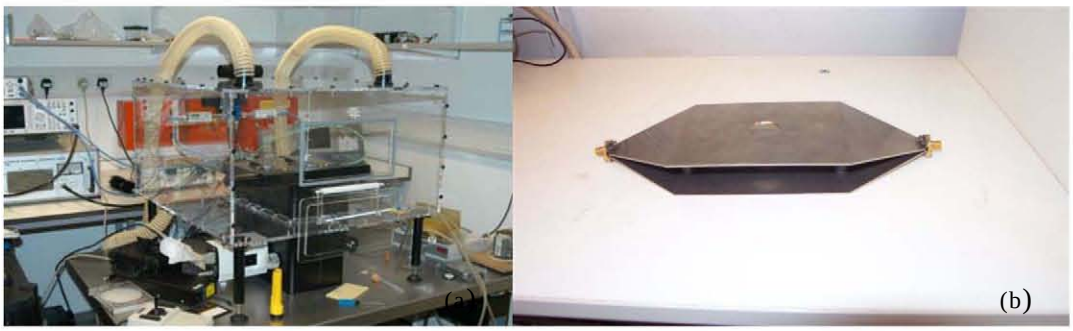


Figure. 9: Exposure system used at Babraham Institute (Courtesy Rod O'Connor, Babraham Inst.). (a) Enclosure for environmental control. (b) TEM-line used to generate RF exposures to samples.

Table 6: SAR levels per watt measured in different growth media at 22.2°C

	SAR (Wkg^{-1}) per watt	
Position	HEPES	**DMEM**
Centre	0.49	0.57
Left	0.56	0.71
Right	0.52	0.69
Front	0.51	0.68
Back	0.57	0.64
Average	**0.53**	**0.66**

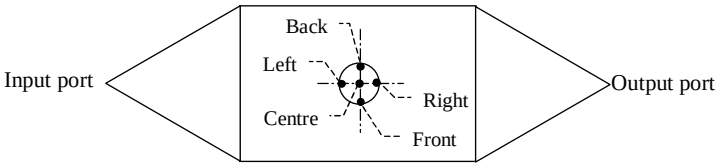


Figure 10. SAR measurement positions

Table 7: Dielectric properties of HEPES and DMEM at 22.2°C and 37°C.

Liquid	Temperature °C	ε′	ε″	σ (Sm^{-1})
HEPES[1]	22.2	76.7	32.2	1.61
	37.0	60.1	21.8	1.10
DMEM[2]	22.4	76.8	34.1	1.71
	37.0	68.7	40.3	2.02

[1] N-2-Hydroxyethylpiperazine-N-2-Ethanesulfonic Acid, [2] Dulbeco's Modified Eagle's Medium.

Conclusions

The MTHR programme has adopted sound metrological principles to ensure the studies funded within the programme produce meaningful, and reproducible results. The National Physical Laboratory has provided consultancy to the researchers within the programme and has characterised and calibrated some of the exposure systems used. Human volunteer studies into handset exposure have used standard exposure handsets that generate the main characteristics of both the RF and magnetic fields produced by real GSM and TETRA handsets. The exposure level of 1.4 Wkg^{-1} 10 g averaged SAR ensures volunteers are not exposed above ICNIRP guideline levels. The base station exposure system produces exposures representative of a GSM macrocell base station at 10 mWm^{-2}. The system also generates representative UMTS signals. Both systems facilitate double blind experimental protocols. For the *in vitro* studies within the programme, the system used to generate exposures have been traceably calibrated to National Standards at NPL. Unwanted heating effects in one system were rectified, and previously reported effects of RF exposure could not then be replicated.

Acknowledgements:

The author would like to acknowledge the help and support of: Phil Chadwick (MCL); Myles Capstick (University of York); Bachir Belloul (Red-M Limited); David de Pomerai, Adam Dawe and Steve Greedy (University of Nottingham); Elaine Fox, Stacy Eltiti and Denise Wallace (University of Essex); Rod O'Connor (Babraham Institute); Andrew Gregory and Michael Hall (NPL) and members of the Dosimetry Working Group, UK Mobile Telecommunications and Health Research Program.

References

[1]"Mobile Phones and Health", Report of the Independent Expert Group on Mobile Phones (the Stewart Report), May 2000, ISBN 0-85951-450-1, (www.iegmp.org.uk/report/text.htm)

[2] Hall, M, "Measurement of electromagnetic flux density from mobile handsets", NPL Report DEM-ES(RES) 004, April 2006.

[3] ETSI Standard TS145 005 V6.11.0 (2005-09), "Digital Cellular Telecommunications System (Phase 2+); Radio Transmission and Reception" (www.etsi.org)

[4] ETSI Standard EN 300 392-2 V2.1.1 (2000-12). "Terrestrial Trunked Radio (TETRA) Voice plus Data (V+D), Part 2: Air Interface (AI)". (www.etsi.org)

[5] IEEE C95-1, "IEEE Standard for Safety Levels with respect to Human Exposure to Radio Frequency Electromagnetic Fields, 3 kHz to 300 GHz", IEEE 1999.

[6] Chadwick, P, "Assessment of Specific Absorption Rates from Second Generation Airwave Equipment: TETRA radios and accessories, MCL report, January 2003, (www.mcluk.org).

[7] Dimbylow P, Khalid M, and Mann S, (2003), “Assessment of specific energy absorption rate (SAR) in the head from a TETRA handset”, Phys Med Biol, 48, 3911-3926.

[8] British Standard BS EN 503361:2001. “Basic standard for the measurement of specific absorption rate related to human exposure to electromagnetic fields from mobile phones (300 MHz – 3 GHz)”.

[9] Belloul, B, “EM Exposure System: Technical Reference Manual”, Version 1.4, Dec 2005, CDS Doc: GCD-RTG 1291/2004. (www.red-m.com)

[10] S M Mann, T G Cooper, S G Allen, R P Blackwell and A J Lowe, “Exposure to Radio Waves near Mobile Phone Base Stations”, NRPB-R321, 2000, ISBN 0 85951 455 2

[11] Cooper TG, Mann, SM, Khalid, M, and Blackwell, RP. “Public exposure to radio waves near GSM microcell and picocell base stations”, J Radiat Prot, 26, 2006, 199-211.

[12] 3GPP TS 25.141 V6.3.0 (2003-09) “Technical Specification Group Radio Access Network; Base Station (BS) conformance testing (FDD) (Release 6)”, (www.3gpp.org/ftp/Specs/html-info/25141.htm)

[13] Crawford, ML, “Generation of standard fields using TEM transmission cells”, IEEE Trans. on EMC, 1974, 16 (4), pp. 189 - 195.

[14] Schuderer J, Kuster N, “Effect of the meniscus at the solid/liquid interface on the SAR distribution in Petri-dishes and flasks”, Bioelectromagnetics 2003, Feb; 24(2), 103-8.

[15] Pokovic, KT, T.Schmid and N.Kuster, “Robust set-up for Precise Calibration of E-field probes in Tissue Simulating Liquids at Mobile Phone Frequencies”, Proceedings ICECOM 1997, pp 120 – 124, Dubrovnik, Croatia Oct 12-17.

[16] Daniells C, Duce I, Thomas D, Sewell P, Tattersall J, de Pomerai D.. “Transgenic nematodes as biomonitors of microwave-induced stress”, Mutat Res, 1998, 399:55–64.

[17] de Pomerai D, Daniells C, David H, Allan J, Duce I, Mutwakil M,Thomas D, Sewell P, Tattersall J, Jones D, Candido P, “Non-thermal heat-shock response to microwaves”. Nature, 2000, 405:417–418.

[18] de Pomerai D, Daniells C, David H, Allan J, Duce I,MutwakilM, Thomas D, Sewell P, Tattersall J, Jones D, Candido P, “Microwave radiation induces a heat-shock response and enhances growth in the nematode Caenorhabditis elegans”, IEEE Transact Micr Theor Tech, 2000, 48:2076–2081.

[19] Dawe A S, Smith B, Thomas D W P, Greedy S, Vasic N, Gregory A, Loader B, and de Pomerai D, “A small temperature rise may contribute towards the apparent induction by microwaves of heat-shock gene expression in the nematode, Caenorhabditis elegans”, Bioelectromagnetics, 2006, 27(2), 88-97.

[20] Collin A., Cueille M., O'Connor R, Leveque P. (2005) Dosimetry and Microdosimetry including Electromagnetic, Thermal and Convection for in vitro Microwave exposure System. XXVIIIth General Assembly of the International Union of Radio Science (URSI), paper KP.4(0140), New Delhi, India.

[21] Cueille M., Collin A., O'Connor R., Leveque P. (2005) Dosimetry based on Electromagnetic, Thermal and Convection simulations for in vitro Microwave Exposure System. Proceedings BioEM 2005, Dublin, pp. 462-463.

TOWARDS A STANDARDIZATION OF SAR NUMERICAL EVALUATION

L. CATARINUCCI, A. COLUCCIA, L. TARRICONE

D.I.I. UNIVERSITY OF LECCE, LECCE – ITALY
mail: luca.catarinucci@unile.it; luciano.tarricone@unile.it

Abstract
The numeric evaluation of the specific absorption rate (SAR) referred to a certain quantity of biological tissue, plays a main role when radioprotection aspects connected to the interaction between humans and electromagnetic (EM) fields are investigated, as highlighted in the related guidelines both in European Community (ICNIRP) and in USA (IEEE C95.1).
Nevertheless, it is important to observe how SAR values are strongly influenced by many factors as, for instance, the shape of the volume containing the reference mass; such a shape is imposed as cubical in IEEE guidelines, whilst this is not clearly stated in ICNIRP ones. Moreover, several other aspects, such as the optimum discretization step or the treatment of internal air (just to mention some of them), cause discrepancies among results obtained by different research groups.
In this work an overview on some SAR algorithms is firstly presented, and a discussion on their potential differences reported. Then, such algorithms and new ones proposed by the authors, are used to evaluate the SAR in some practical human-antenna interaction cases. The remarkable differences highlighted from the comparison, enforce the necessity to individuate an algorithm to be elected as "canonical", as discussed in conclusion of the work.

Introduction
The frequent exposure to the field emitted by electromagnetic (EM) sources is nowadays a matter of fact; consequently, in recent years, there has been an increasing public concern about the possible risks for human health due to the interactions with antennas. For this reason, the major public organizations in the world have established safety guidelines for radiofrequency (RF) exposure, as for instance the recently revised IEEE RF Safety Standard C.95.1-2006 [1], adopted in United States, and the International Commission on Non-Ionizing Radiation Protection (ICNIRP) Safety Standard [2], adopted in European Community. Such guidelines are based on the specific absorption rate (SAR) averaged over a certain reference tissue mass, usually 1 g, 10 g or the whole body mass; safety limits are accurately fixed distinguishing among different categories of workers and different body parts, and they are also frequently updated as a consequence of the results produced by the scientific community. The last confirmation of that is given by the introduction for the first time in a guideline [1] of new safety limits specific for the pinna, after the publication of some works, aiming at demonstrating the necessity of paying due attention to the anatomic details of the ear and to their effects in the exposure to cellular phones [3]-[5]; such diversification had not been considered neither in the previous IEEE standards [6], [7] nor in ICNIRP ones.
Nevertheless, in contraposition to the constant attention dedicated to the refinement of the safety limits, diversifying them in terms of kinds of workers, exposure time and exposed body portions, it is quite evident a lack of indications about how the SAR should be evaluated; indeed, despite the apparent easiness of the formulae for the SAR evaluation, such relations actually open themselves to different interpretations which could cause discrepancies in the estimation of the absorbed energy. As well known, in fact, the SAR is defined as the "time derivation of the incremental energy absorbed by, or dissipated in, an incremental mass contained in a volume element of a given density, normalized to that mass", which can be synthesized as:

$$SAR = \frac{\partial}{\partial t}\left(\frac{\partial W}{\partial m}\right). \tag{1}$$

In the context of RF and/or microwave (MW) exposure, where the energy absorption by tissues is only due to the Joule effect, two more convenient forms are often used, allowing the SAR evaluation from either electric field or temperature measurement through the following formulae:

$$SAR = \frac{\sigma |E^2|}{2\rho} = c\frac{\Delta T}{\Delta t}, \quad (2)$$

Where σ [S/m] is the tissue conductivity, E[V/m] the electric field, ρ [kg/m^3] the tissue density, c the tissue specific heat capacity and ΔT [°C] the temperature change caused by the exposure for a time Δt [s].
Consequently, considering the first of the (2), the SAR averaged over a certain reference mass, can be written as:

$$SAR_{rm} = \frac{\int_{V(rm)} \sigma |E|^2 / 2 \; dv}{\int_{V(rm)} \rho \; dv}, \quad (3)$$

Where rm is the reference mass (usually 1g, 10g or the whole body mass) and $V(rm)$ is the volume containing rm.
It can be noted that, although the shape of the volume containing the reference mass does not affect the divisor in (3), which is anyhow equal to rm, its impact on the dividend could be relevant; the distribution of the electric field, in fact, varies greatly from point to point inside the tissues, so that the use of different volumes could generate strong discrepancies.
It is reasonable wondering, hence, how the shape of the volume containing the reference mass can impact the SAR value itself and if, consequently, such a shape must conveniently be standardized. Can, for instance, the SAR averaged over 10 g of tissue assume a different value if the volume shape is changed? If so, which is the most appropriate shape to be considered?
The just opened problem is almost completely neglected in international guidelines. Despite the common sense would suggest that a spherical volume should be the most logical choice, because it does naturally select the set of points which are as close as possible to the evaluation point, IEEE guideline bases its safety limits on cubical volumes. Even more debatable is the position assumed on ICNIRP standards, where the absolute lake of indications in matter, leave the scientist the faculty of the choice.
Moreover, it is commonly accepted from the scientific community, that the use of numerical dosimetry for the energy absorption estimation is the most appropriate approach; experimental dosimetry, in fact, evidences strong difficulties both in using real subjects and in carrying out adequately accurate phantoms, capable therefore to correctly reproduce the human characteristics. Vice versa, the use of EM full-wave methods, such as the Finite Difference Time Domain (FDTD) algorithm or the Finite Element Method (FEM), jointly with the availability in literature of some accurate numerical phantoms, as for instance the one proposed in [8] or the one proposed in [9], allows the rigorous evaluation of the SAR also in complex realistic human-antenna exposure problems. However, when numerical methods are used, a spatial discretization must be implemented, thus accentuating even more the problems connected to the SAR evaluation. In such a case, in fact, the averaged SAR can be computed through the following formula:

$$SAR_{rm} = \frac{\sum_{i \in \bar{V}(rm)} \sigma_i |E_i|^2 / 2}{\sum_{i \in \bar{V}(rm)} \rho_i}, \quad (4)$$

where the index i indicates the generic elementary cell of the discretized space and $\bar{V}(rm)$ the discretized volume containing the reference mass rm. The use of a volume $\bar{V}(rm)$ consisting of several cells, is itself a degree of freedom and consequently a source of non-uniqueness of the results, the SAR value being dependent on which cells are chosen, among the several possible, to better represent the desired volume shape. Moreover, also the spatial discretization step could play a major role: a space step as large as a significant portion of the reference mass, for instance, besides emphasizing the just mentioned problem, causes strong discrepancies between rm and the actual considered averaging mass.
To the topics now pointed out, some others can be added, each one increasing the uncertainty to the estimated SAR values. The peak SAR values, for instance, are often founded in points close to the human surface, where

the chosen volume shape must be modified in order to consider only tissue and not air. Which is the best algorithm in that sense?
Moreover, as well known, if the FDTD method is used, the obtained electric field components are not centered in the elementary cells [10]. Recently, some algorithms have been proposed to refine SAR calculation [11], and they are herein discussed.
Furthermore, another key-point is the one of how to treat the presence of internal air, which is also here specifically addressed.
More specifically, in the following sections some commonly used SAR algorithms will be described and compared, and some new ones proposed by the authors presented. Such algorithms are then applied to a difficult case of interaction between humans and radio base station antennas (RBA) using both cubical and spherical reference volumes, and results showed and discussed.

Common SAR numerical algorithms

In this section, a brief overview of the most commonly adopted algorithms for the numerical evaluation of the SAR, is presented. Despite the appreciable differences among the algorithm structures, it is important to highlight here that the main goal of this treatment is neither the individuation of an algorithm to be elected as a reference, nor the eventual discredit of some of them; on the contrary, in fact, what is sustained in this work is that, although different numerical strategies give out different SAR values, none of them contravene any of the indications reported in the safety guidelines.
One of the usually adopted approaches, for instance, computes the SAR_{rm} on a certain point by considering the contributes coming from the cells which belong to a cubical volume centered in that point. In [12] and [13] such a volume is prefixed, i.e. is the same for each computation point, and it is dimensioned in order to roughly contain the reference mass. The non modifiability of the volume shape causes the evaluation of the SAR in presence of air together with tissues and consequently an averaged value obtained integrating over a mass different from rm. In order to avoid the evaluation of the SAR in cases where a too large portion of the volume does not contain tissues, a maximum tolerable percentage of air is imposed: if the percentage of air is superior to the fixed limit, SAR remains undetermined.
It is important to observe that such an approach does not allow the evaluation of the absorbed energy in the most external points of the exposed target where, though, high SAR values or even the peak SAR itself, are located.
Furthermore, also where the volume does not contain air, it is often impossible to reach exactly rm using a cube, the number of needed cells being strongly dependent on the discretization step.
In order to avoid some of the listed problems, parallelepipeds instead of cubes are used in [14], but also this solution is not devoid of lacks; such a choice, in fact, forces the use of a volume which is unbalanced respect to the evaluation point and, consequently, causes the use of too far contributes.
A first improvement of the previous techniques can be obtained through the use of a cubic volume which dynamically adjusts itself in order to consider exactly the rm and tolerates up to a certain percentage of air, as proposed in [11]. The algorithm builds a sequence of cubes of dimension progressively increasing till a mass superior to rm is reached. At each step the percentage of air is evaluated and if it is greater than the prefixed limit, the SAR in that point remains undetermined. Vice versa, the last cube of the sequence with mass inferior than rm is used as the core for the SAR evaluation and only an accurately evaluated portion of the adjacent cells is added in order to exactly reach rm. Anyhow, a big limit of this algorithm remains: the incapability to determine the SAR in points closed to the surface of the exposed target; in [15] a further improvement in that sense is proposed. The concept of a volume perfectly cubical is not considered indispensable anymore; the cells are assembled around the reference one by following established criteria and excluding the air. The algorithm, here named Adaptive Cube (AC), stops the insertion of new cells when the total mass is equal to rm for each computed value, but the shape of the volume is given by the set of cells which better approximate a cube intersected with non-tissue points. In such a way, in each point, included those belonging to the most external regions, the SAR can be evaluated.
The comparison among the presented numerical techniques shows that even radically different algorithms for the evaluation of the SAR can comply with the few indications reported in RF safety guidelines, despite it is easily

predictable that they could generate discrepant results. Consequently, an integration of the guidelines with detailed indications on a SAR numerical algorithm to be elected as a reference, appears to be at least expected.

New kinds of SAR algorithms

The conceptual differences among the commonly used algorithms for the SAR numerical evaluation and the consequent observations reported at the end of the previous section, pave the way to a more deep theoretical discussion about how the algorithms should be conceived. Even if at a first glance it could seem a mere implementation problem, it addresses instead to a more general consideration: which is the most suitable volume shape for the SAR evaluation? If it is true that when numerical methods and orthogonal meshes are used, it is quite easy and natural to choose cubical volumes which contain 1g or 10g (the rm) of tissue, it is as much true that the acceptance of such an assumption signifies to be aware of the limits which derive from that, and that the obtained results could be at least debatable.

Anyhow, even if, for instance, the AC algorithm is basically oriented towards cubical shapes, the eventual presence of air could cause a strong deformation of the volume, such as in the case of the SAR evaluated in the fingers, where the cube becomes more likely similar to a thin parallelepiped. This is not surprising, the choice of the cube being justified only by its implementation easiness; nevertheless, it is reasonable wondering which should be the most appropriate volume, regardless to eventual implementation problems.

To the opinion of the authors, there is no doubt that a spherical volume is the best one. Spheres, in fact, select the most close cells to a reference point, thus allowing the most natural evaluation of the SAR; any other volume, in fact, would take into account too far contributes, as for the cube case, where the vertexes are considered instead of more close points.

Nevertheless, to adequately take into account a spherical volume when discretized spaces are considered, some observations are necessary. In a continuous space, in fact, it is possible to determine an ideal sphere (ideal circle in 2D) which contain exactly a quantity of tissue equal to rm, but in a discretized space this is quite complicated. For the 2D case, an hypothetical ideal circle is reported in Figure 1; the yellow cell in the center is the one where the SAR must be evaluated. Some of the cells are entirely contained in the ideal circle, whilst some others (the violet ones in Figure 1) are intersected by that circle; such cells are called here “peripheral cells” and will play a major role in the formulation of new algorithms. The SAR, in fact, should ideally be calculated by adding the contribute of the internal cells to the contribute of the partial volumes of the peripheral cells, so that the approximation of such partial volumes becomes the real difficulty of spherical algorithms.

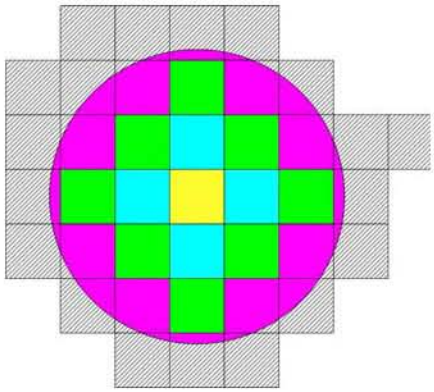


Figure 1. Representation of the ideal circle which includes the rm.

In the following four new algorithms will be presented, all based on spherical volumes, even though the same strategies can be easily applied to cubical volumes.

A: Onion Skin Algorithm

The first algorithm which is here proposed considers a sphere as the reference volume and, when necessary, modifies the shape in order to include only tissues and not air. The strategy that regulates the addition of a new cell to the partial volume, gives the name to the proposed algorithm: “Onion Skin” (OS); if the mass contained in a sphere of radius r (onion) is inferior to rm, in fact, new cells are added selecting them out among those belonging to the layer which radius is $r+1$ (skin). Such an algorithm is similar to the AP one proposed in [15] apart from the shape of the volume.

The main steps of the algorithm for the evaluation of the SAR_{rm} in a cell of coordinates $< x, y, z >$ can be synthesized as follows:

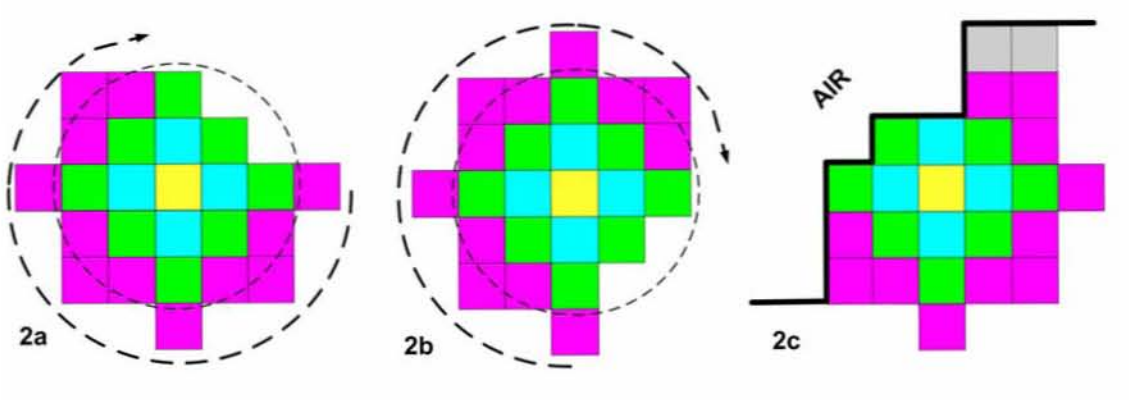


Figure 2. Onion Skin algorithm applications examples.

1. initialize the radius $r = 1$ and set the center in $< x, y, z >$;
2. select the set of possible candidate cells as those belonging to the layer of radius r centered in $< x, y, z >$ and representative of tissues (air is excluded);
3. add one of the individuated cell to the partial volume and compute the new partial mass pm.
4. repeat step 3 until all the cells individuated in 2 have been added or the condition $pm \geq rm$ is verified;
5. if $pm \geq rm$ has not been verified yet, impose $r = r + 1$ and come back to 2. Else (the volume is founded) go to 6;
6. Evaluate the SAR_{rm} by using the individuated volume.

The method guarantees that the desired 1g or 10g of rm are obtained with a tolerance on the order of a fraction of the last added cell mass. It is quite evident that the algorithm is based on the iterated addiction of layers to the central cell until rm is reached; it is highly probable, though, that the last layer will not be completed, thus causing an unbalancing of the volume respect to the cell in $< x, y, z >$. In Figure 2, a bi-dimensional schematization of the volume individuated by the OS algorithm is reported for a simple case of absence of air and supposing that 25 cells guarantee a mass of almost rm. The different colors of the cells individuate different layers. More specifically, in Figure 2a the reference cell (the yellow one) is supposed to be far enough from every air region so that for each successive layer all the cells can be considered potential candidates to be part of the averaging volume; as apparent, three complete layers and a partial one are needed. The cells of the last layer, however, could be chosen in different ways as evidenced in Figure 2b, and consequently the obtained SAR could assume different values. This represents the most substantial lake of the OS algorithm. Finally, Figure 2c shows what happens when the evaluation cell is quite close to air regions, with the consequent modification of the volume shape in order to guarantee anyhow an averaging mass equal to rm as well as the use of only tissue cells.

B: Graded Peripheral Cells Algorithm

As previously observed, the best way for considering spherical volumes in orthogonal meshes, would be that of taking into account the whole contribute coming from all the cells entirely contained in the ideal sphere, and the partial contribute given by the peripheral cells. The problem, actually not trivial, consists on the accurate evaluation of the partial volume to be considered for each of the peripheral cells; this problem is quite difficult to solve analytically because of the high number of possible intersections between spheres and cubes: approximations are, hence, strongly necessary.

The herein proposed approach, called Graded Peripheral Cells (GPC), considers an equal fraction of all the peripheral cells, regardless to the effective volume individuated by the ideal sphere (or ideal circle in 2D). The algorithm analyzes all the non-air cells around the evaluation point, and marks them as internal, external or peripheral, respect to the ideal sphere; in order to perform such an operation, the number of vertexes internal to the sphere is computed.

Once such a preprocessing analysis has been performed, the mass of the internal cells is known, as well as the remaining quantity necessary for reaching rm. Such a quantity is considered as equally distributed among all the peripheral cells which proportionally contribute to the final SAR value.
In Figure 3 the individuated resultant volume is reported for the same case of Figure 2a. The small internal squares sketched inside the peripheral cells, represent the considered portion of mass. By comparing such a volume with the one obtained with the OS algorithm, it can be noticed how the problem of the unbalancing respect to the central cell is substantially bypassed. Nevertheless, the assumption that all the peripheral cells contribute with the same mass, seems to be too approximate, because some of the cells are only slightly intersected from the ideal sphere whilst some others are almost completely internal. The next proposed algorithms can be considered as a refinement of the GPC one, aimed at better approximate the ideal situation described in Figure 1.

C: Graded Peripheral Vertex Algorithm

The Graded Peripheral Vertex (GPV) algorithm represents a more refined version of the GPC algorithm. As previously shown, in fact, in GPC the same portion of mass is considered for each one of the peripheral cells; if a method is found for discriminate how much of a cell is internal to the ideal sphere, a non-uniform weighting can be effectively applied. Actually, the same strategy used for discriminating if a cell is or not peripheral, can be extended in that direction; a cell is peripheral, in fact, if at least one vertex is internal to the ideal sphere and contemporaneously at least one vertex is external. The number of internal vertexes, hence, could be a good parameter to be used. Despite it is still an approximation, it is evident that a cell with only one internal vertex contributes with a portion of its volume larger than that of a cell with more internal vertexes.
The GPV algorithm, hence, calculates the portion of a peripheral cell to be considered, proportionally to the number of internal vertexes; more specifically, if $1 \le n \le 8$ ($1 \le n \le 4$ in 2D cases) is the number of internal vertexes of one of the examined cells, then n 8 of its mass is considered. Figure 4 shows, reporting also the number of internal vertexes for each peripheral cell, how the application of the GPV algorithm allows a better distribution of the mass respect to the GPC and the OS ones, increasing the accuracy of the approximation respect to the ideal case of Figure 1 and thus improving the quality of the result.

D: Graded Peripheral Vertex-3 Algorithm

The Graded Peripheral Vertex-3 (GPV3) algorithm is a modification of the GPV algorithm, where the contribute of each peripheral cell is not proportional to the number of internal vertexes n, but to its cube (its square in 2D), i.e. to n^3. This criterion is based on the observation that the dependence of the internal volume on the number of internal vertexes is, in most cases but not always, almost cubical. In such an algorithm, hence, the mass of a cell is divided into 64 parts (16 in 2D) and n^3 64 is the fraction of mass (and volume) considered for a peripheral cell with n internal vertexes.
Even if none among GPV and GPV3 is definitively better than the other, above all in 3D cases the GPV3 seems to guarantee better approximations.

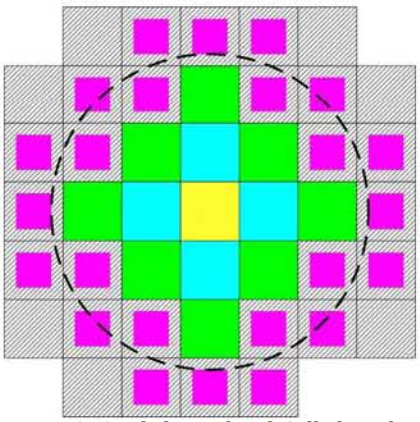


Figure 3. Graded Peripheral Cell algorithm application

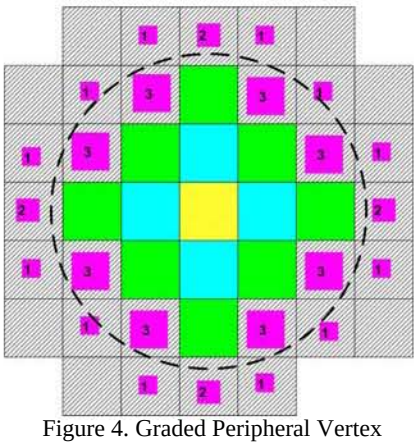


Figure 4. Graded Peripheral Vertex algorithm application

Results

In this section some of the presented algorithms are tested on a practical case and results compared and discussed. More specifically the difficult problem of the interaction of a human with the field emitted by a radiobase station

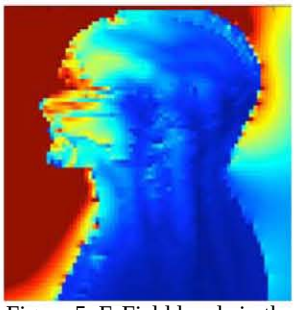


Figure 5. E-Field levels in the studied case

Peak SAR comparison		
SAR Algorithm	**Peak SAR (1g)**	**Peak SAR (10g)**
Adaptive Cube (AC)	**27.93**	**14.39**
Onion Skin (OS)	**27.00**	**14.32**
Graded Peripheral Cell (GPC)	**27.65**	**14.73**
Graded Peripheral Vertex (GPV)	**27.89**	**14.78**
Graded Peripheral Vertex-3 (GPV3)	**28.03**	**14.85**

Table I. Peak SAR values using different algorithms.

antenna has been solved by using the FDTD method [16], and the SAR averaged over 1g and over 10g of tissue has been evaluated in each point of the exposed subject (which is the numerical phantom proposed in [8]). In Figure 5 the electric field distribution in a section of the head is reported. Five different algorithms have been used: the AC one, representative of the cubical shape algorithms, the Onion Skin one, which applies the same strategies of the AC but to spherical volumes, and the three successive refinements, respectively GPC, GPV and GPV3. The other presented algorithms, instead, have not been tested, because their inability to evaluate the SAR in superficial points makes the comparison with most sophisticated strategies impossible.

In Table I the peak SAR values are reported both for $rm = 1g$ and for $rm = 10g$. It can be observed that all the tested algorithms give comparable results. This is not surprisingly: even if the algorithms are quite different, in fact, the peak SAR is found in the proximity of the phantom surface where the electric field assumes the highest values all around a region as large as many rm. In such points, the volumes are also strongly deformed by the phantom shape, so that the refinement strategies becomes unappreciable. Anyhow, it is important to recall again that, among the possible, only algorithms which can evaluate the SAR everywhere in the phantom have been tested; the others algorithms, such as the one proposed in [12] and [13] or the one proposed in [14], would have been unable to determine the SAR in such points. This observation is itself enough to justify the requirement of a standardization of the SAR numerical evaluation techniques.

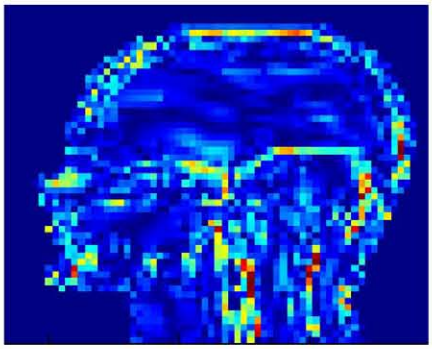


Figure 6. AC versus OS: percentage difference in each phantom point.

In order to appreciate, though, the differences among the various algorithms, all the SAR values, and not only the peak one, should be compared.

In Figure 6, for instance, the percentage difference among AC and OS is graphically reported. The chromatic scale, from blue to red, represents increasing differences from 0 up to 45%. It is quite apparent the strong diversity in some investigated phantom points, even though only the shape, and not the strategy, differentiates the algorithms.

In Table II, instead, the GPV3 algorithm is used as the reference one, and the percentage difference with the others is reported. More specifically two parameters are computed: the average percentage difference and the maximum percentage difference.

	Percentage Difference			
SAR Algorithm	**SAR (1g)**		**SAR (10g)**	
	Average %	**Maximum %**	**Average %**	**Maximum %**
AC versus GPV3	**8.43**	**99.08**	**5.12**	**69.95**
OS versus GPV3	**6.90**	**95.39**	**3.31**	**53.71**
GPC versus GPV3	**4.93**	**90.14**	**0.14**	**3.04**
Graded Peripheral Vertex (GPV)	**2.66**	**42.89**	**0.08**	**2.33**
Graded Peripheral Vertex-3 (GPV3)	**---**	**---**	**---**	**---**

Table II. Average and Maximum percentage difference respect to GPV3 algorithm.

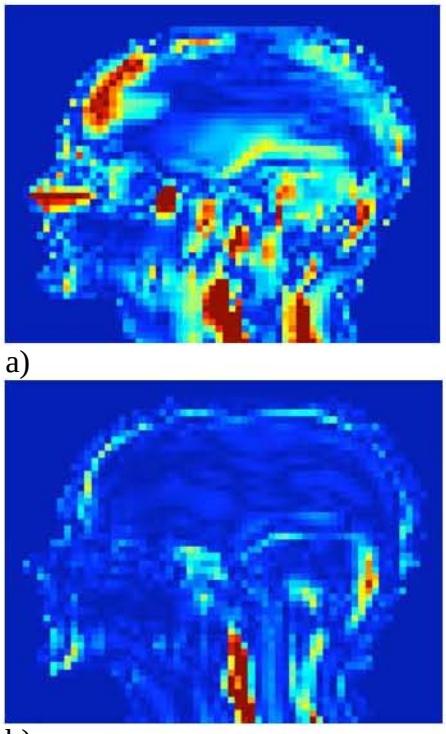
Through the analysis of the data reported in the table, some conclusions can be drawn. First of all, by improving the accuracy of the algorithms, all the percentages decrease. As expected, hence, by using more refined spherical algorithms a better discrimination of the absorbed power in the various points can be performed, so that the SAR values can be better estimated. Also, it can be observed that differences referred to the SAR_{10g} are always inferior to those referred to the SAR_{1g} and this for two different reasons: first of all, by increasing the rm, the consequent smoothing effect due to the integration over a bigger volume causes the attenuation of the differences among the methods. Secondly, the number of peripheral cells increases with the volume and the contribute of each of them becomes less relevant.

Even more interesting are the deductions coming from the analysis of the maximum percentage error; two sophisticated algorithms, such as OS and GPV3, give in some points difference up to 90% for the SAR_{1g} and up to 50% for the SAR_{10g}. Even two quite similar algorithms, GPV and GPV3, show strong differences in the 1g case. In order to better appreciate the impressive differences among the algorithms in every points of the phantom head, finally, the percentage difference of GPV3 respect to OS and respect to GPC for the SAR_{1g} are reported in Figure 7.

Conclusions

In this work some commonly adopted algorithms for the numerical evaluation of the Specific Absorption Rate (SAR) averaged over a certain mass have been reported and some new ones have been presented and compared. Among the most important conclusions which can be drawn, the main aspect seems to be that of the necessity of a standardization of the techniques for the SAR calculation. The discrepancies among results obtained through different algorithms are impressive, even though all of the tested techniques do not contravene any of the indications, probably inadequate, reported in the most important radiofrequency safety standards. This enforces, also, a more detailed discussion about the consideration of local SAR values.

The work itself gives some indications in that sense, discussing the role plaid by the shape of the integration volume along with other important issues. The use of a spherical volume rather than a cubical one, represents for the authors the main necessary modification, and the four proposed algorithms could be used as the starting point which paves the way to a more deep discussion.



a)

b)

Figure 7. GPV3 versus OS (a) and GPV3 versus GPC (b) percentage difference in each phantom point.

References

[1] IEEE C95.1 – 2006, “Standard for Safety Levels with Respect to Human Exposure to Radiofrequency Electromagnetic Fields, 3 kHz to 300 GHz”, IEEE Standards C95.1, Coordinating Committee 28.4, 2006.

[2] ICNIRP, “Guidelines for limiting exposure to time-varying electric, magnetic and electromagnetic fields (up to 300 GHz),” Health Phys.: International Commission on Non-Ionizing Radiation Protection (ICNIRP), vol. 74, pp. 494-522, 1998.

[3] O.P. Gandhi, Gang Kang, “Inaccuracies of a plastic "pinna" SAM for SAR testing of cellular telephones against IEEE and ICNIRP safety guidelines”, MTT IEEE Trans. on MTT, Volume 52, Issue 8, Part 2, Aug. 2004 Page(s):2004 – 2012

[4] Beard et al, “Comparisons of computed mobile phone induced SAR in the SAM phantom to that in anatomically correct models of the human head”, IEEE Transaction on EMC, Volume 48, Issue 2, May 2006 Page(s):397 – 407

[5] M. Burkhardt, N. Kuster, “Appropriate modeling of the ear for compliance testing of handheld MTE with SAR safety limits at 900/1800 MHz”, IEEE Trans. on MTT, Volume 48, Issue 11, Part 1, Nov. 2000 Page(s):1927 – 1934

[6] ANSI C95.1-1982, “American National Standard Safety Levels With Respect to Human Exposure to Radiofrequency Electromagnetic Fields, 300 kHz to 100 GHz”, The Institute of Electrical and Electronics Engineers, Inc., New York, NY.

[7] IEEE C95.1 – 1999, “IEEE Standard for Safety Levels With Respect to Human Exposure to Radiofrequency Electromagnetic Fields,

3 kHz to 300 GHz" IEEE Standard C95.1, 1999.
[8] I. C. Zubal, C. R. Harrell, E. O. Smith, Z. Rattner, G. Gindi, P. B. Hoffer, "Computerized 3D Segmented Human Anatomy", Medical Physics, 21, 2, pp. 299-304, 1994.
[9] P. A. Mason, J. M. Ziriax, W. D. Hurt, T. J. Walters, K. L. Ryan, D. A. Nelson, K. I. Smith, and J. A. D'Andrea, "Recent advancements in dosimetry measurements and modeling," in Radio Frequency Radiation Dosimetry, B. J. Klauenberg and D. Miklavcic, Eds. Norwell, MA: Kluwer, 2000, pp. 141–155.
[10] A. Taflove, 'Computational Electrodynamics: The Finite-Difference Time-Domain Method', Norwood, MA, Artech House, 1995
[11] K. Caputa, M. Okoniewski, M. A. Stuchly, "An algorithm for computations of the power deposition in human tissue, IEEE Antennas Propagat. Mag., vol. 41, pp. 102-107, Aug. 1999.
[12] K. S. Nikita et al, "A Study of Uncertainties in Modeling Antenna Performance and Power Absorption in the Head of a Cellular Phone User", IEEE Transactions on MTT, vol. 48, n.12, Dec. 2000.
[13] Jianqing Wang, Osamu Fujiwara, Soichi Watanabe, Yukio Yamanaka, "Computation With a Parallel FDTD System of Human-Body Effect on Electromagnetic Absorption for Portable Telephones", IEEE Transactions on MTT, vol. 52, n. 1, January 2004.
[14] O.P. Gandhi, G. Lazzi, C.M. Furse, "Electromagnetic Absorption in the Human Head and Neck for Mobile Telephones at 835 and 1900 MHz", IEEE Transactions on MTT, vol. 44, n.10, October 1996.
[15] A. Lee, J. Pack, "Study of the Tissue Volume for Spatial-Peak Mass-Averaged SAR Evaluation", IEEE Transactions on EMC, vol. 44, n. 2, May 2002.
[16] L. Catarinucci, P. Palazzari, L. Tarricone, "Human Exposure to the Near-Field of Radiobase Antennas: a Full-wave Solution using Parallel FDTD", IEEE Trans. on MTT, March 2003.

ON THE USE OF A GRID REFINEMENT ALGORITHM IN FDTD FOR EVALUATING THE SAR IN VARIOUS EXPOSURE CONDITIONS

R. PONTALTI, A. VACCARI, C. MALACARNE, L. CRISTOFORETTI

ITC-IRST - CENTRO PER LA RICERCA SCIENTIFICA E TECNOLOGICA

VIA SOMMARIVE, 18 - 38050 POVO, TRENTO – ITALY

Abstract

Whole-body averaged and local SAR depends on many factors including stature, gender and posture of the exposed subject. In RF dosimetry, various numerical phantoms of women and men are gradually becoming available as well as numerical techniques able to virtually rotate the main joints in order to change their posture. Other variables which deserve investigation are field polarization and impinging direction of the incident wave. To assess the SAR distributions in these structures a high spatial resolution of the human numerical models is mandatory. At the same time, it is usually requested to model a large embedding domain which may accommodate a near field source. This imposes the use of subgridding techniques. Practical examples of the FDTD implementation with a domain refinement algorithm, in the range 100 MHz – 4 GHz, are reported

Introduction

Numerical phantoms involving sophisticated complex permittivity representations of the human body are a useful tool for investigating the connection between external fields and induced internal SAR. These phantoms are obtained either by image segmentation and assignment of the proper permittivity values to each tissue or by semi-automatic methods which take into account the complex permittivity variations into every tissue. Both methods use sets of anatomical images obtained by CT (Computerized Tomography) or by Magnetic Resonance Imaging (MRI).

The human exposure was first studied by using models of a man in standing position frontally impinged by a plane wave with vertical polarization, having these states been recognized as generally maximizing the absorption. Nevertheless, these conditions (male model, standing position and plane wave) are too generic to accurately evaluate the exposure in a realistic environment. Different postures, body shape and composition can determine SAR differences. A number of postures have already been studied [1][2] and, in the last years some works focussed on the gender differences [3].

After having developed their own male [4] and female phantoms [5], the authors used them in some works dedicated to the understanding of the differences found in the whole body averaged SAR between male and female [3][6].

Recently they developed a technique for numerically rotating the main joints of the body preserving, at the same time, a reasonably realistic anatomic aspect. Since a posture in which a subject spends a considerable part of its living time is sitting, arms and legs of the male phantom were rotated in a way to simulate that condition.

A paper published very recently [2] demonstrates that different parts of the body (trunk, limbs or forelimbs) may show their own resonance when stimulated with the proper frequency and polarization. It causes a large variety of conditions determined by the posture and by the parameters of illumination, depending on the relative orientation of the field with specific portions of the body which – in case of a more complex posture than standing with aligned arms – cannot be anymore considered as a simple linear antenna.

The attention is focused on the range of the RF spectrum located above the body resonance (here meant standing, i.e. about 40 or 80 MHz depending on grounded or isolated condition), in which the largest part of artificial sources for broadcasting and mobile communication is allocated: 0.1–4 GHz.

For calculating SAR distribution the Finite-difference time-domain (FDTD) solution method of Maxwell's equations, a widely used numerical technique in computational electromagnetics, has been used. It is commonly retained that only analyses at frequencies corresponding to wavelengths no shorter than 10 times the space sampling size are fairly accurate. But when, at a given frequency, the structures' electrical density augments, such as in biological tissues, wavelengths are unavoidably shortened. Many efforts have then been made to develop local mesh refinement algorithms for the FDTD method. A reported problem of the various attempts is their tendency to become unstable.
In this work, a robust and economic subgridding algorithm has been used [7] to achieve higher spatial resolution in the region of interest. This method, called filtering-based (FB) subgridding, is applied to allow a refined calculation of SAR, while maintaining a rather large cushion of free space all around the bodies.
It is as economic as possible, both in terms of memory request and in the number of floating point operations. To this end we devised a coupling scheme between two FDTD meshes, one of them having an higher resolution by a factor of 3, 5 or 7 than the other. The subgridding algorithm at the fine-coarse interface is based on a spatial-differentiation low-pass filter which is analytically justified. It requires only a certain number of extra floating point operations, but no extra memory allocation.
Firstly this work considers the DAM phantom developed in our laboratories and the numerical algorithm used to rotate the principal joints (arms, legs and hips). A brief description of the used subgridding technique will follow. Finally, some examples about the use of the subgridding technique applied to a real dosimetric problem are shown. In particular it will be studied the comparison of whole body averaged SAR in seated and standing male models undergone to various exposure conditions in terms of H or V polarization and frontal or lateral incidence.

Numerical human body model

A semi-automatic procedure to develop numerical human Dielectric Anatomical Models (DAM) was developed in the last years at the ITC-irst laboratory. The procedure is based on MRI image acquisition and by relating grey levels of each voxel to the proper complex permittivity value. The rationale is briefly described as follow. Detailed description of the technique is reported in [4], [5].
Whole body MRI scanning of a male (height: 1.73 m, weight: 63.8 kg) and female (height: 1.62 m, weight: 48.7 kg) volunteers (to obtain mDAM and fDAM respectively) were carried out. The acquisition of the images was performed by a 1 Tesla whole-body imager (1T, 42.5 MHz); body and head coils were used. Data sets were processed to improve the erected posture of the body. Ankle angle was also modified to ameliorate the contact of the feet with the ground. Afterwards, the images were interpolated, obtaining models of 5,999,472 voxels (fDAM) and of 7,795,509 voxels (mDAM), 2×2×2 mm^3 each. After the processing needed to correct the MR image non-uniformities, an automatic technique has been applied to obtain the dielectric models (Figure 1).

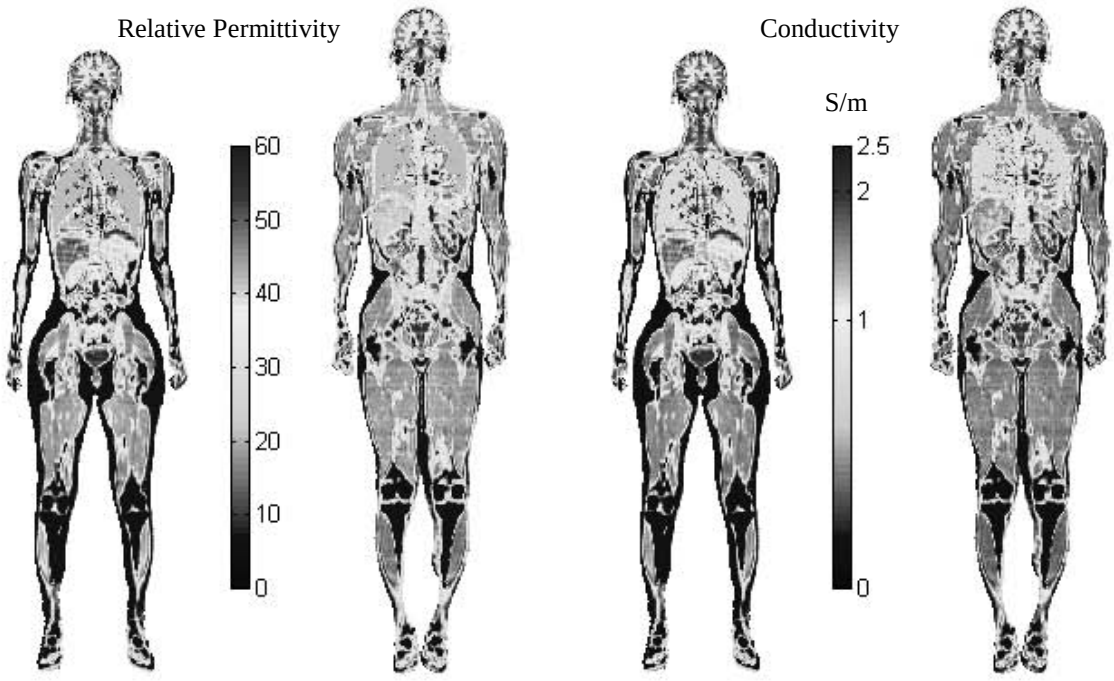


Figure 1. Relative permittivity and conductivity at 2 GHz for the female (left) and the male (right) models

To correlate the image grey levels to the complex permittivity values, transfer functions based on mixture theory were implemented for both high water content and low water content tissues. Since the equations of mixture theory were obtained from data over the frequency range 0.1 ÷ 18 GHz, the validity of the transfer functions lies in this same range.

Rotation of joints

In recent dosimetric studies, the attention has been increasingly devoted to the realistic representation of the human body; this means that, while initially only an average male man in standing position was considered, nowadays many phantoms of different heights, weights, genders, ages and positioned in different postures have been represented [1][2]. Among these aspects, the present work focuses its attention to the development of a modified phantom repostured in order to represent a seated man, being this latter a very frequent condition, both for workers and general public. However, aim of this study was not only to reach such kind of result, but more generally to develop a numerical algorithm able to manipulate the original numerical phantom, in order to model as many postures as possible.

The problem of the realistic geometric modelling of humans has been faced in many fields, from dosimetry to mechanobiology or computer graphics [8][9]. In these latter fields a very high level of anatomical modelling have been reached, with accurate representations of the organs both from a geometrical, anatomical and even dynamic point of view. The starting point in these cases is the detailed knowledge of the internal structures, which are segmented [10]. In this way each single structure is not only geometrically well-confined, but also dynamically characterised, and therefore able to discriminate that, for example, only the muscle is able to undergo active contraction or that the rigidity of the bone actually prevent its deformation.

Conversely, the original phantom used in this study is not segmented. While this condition enables on the one side the highest accuracy in the dielectric properties dispersion modelling, on the other side it partially hinders the accuracy in performing joint movements.

Nevertheless, some general criteria are anyway applicable, such as: to deform as little as possible the rigid structures like the bones, to preserve the total length of each deformed part (alongside its central axis), and finally to properly modify some regions (muscle) in order to maintain the total mass amount constant guaranteeing at the same time a good anatomical resemblance. It is evident that, in this case, the criteria are no longer applicable to well-defined districts, but rather to regions principally containing one tissue or the other.

The procedure followed to obtain the seated phantom is summarisable as follows:

- first of all the sub-volumes to rotate were identified and isolated, one at a time, from the remaining part of the body. In this specific case four sub-volumes were obtained: one for the legs, one for the pelvis and the two latter for the arms;
- for each sub-volume some ‘fiducial point’ couples (one point in the subvolume, the other one in the remaining part) were located. These were chosen in correspondence of the interface–the region that will be deformed the least– in order to facilitate the successive re-assembling of the two parts;
- the rotation plane and axis were defined with respect to the sub-volume and this latter was considered as a succession of slices parallel to the rotation plane and one voxel thick;
- each slice was further subdivided longitudinally in order to obtain several geometrical structures (called *fibres* hereafter in the text), parallel one to the other and roughly following the direction of the part to bend. The aim of this operation is to guarantee the necessary continuity alongside the structure (for example the wrapping around the elbows, knees, etc.);
- in correspondence of each slice there was one only *fibre* which passed through the rotation axis. This *fibre* underwent the only rotation operation, whilst, as the *fibres* were away from the central one, they underwent also a deformation. It is worth noting that, considering the slices where the bone was present, the central *fibre* coincided just with the bone and was therefore suitable to represent its rigid behaviour.
- Besides the rotation, other two types of deformations were applied: i) in correspondence of the rotation axis surroundings, in order to guarantee the necessary continuity of the tissue in this region, and ii) the height augmentation of the most external *fibres* containing tissues, applied in correspondence of the middle part of the segment(s) upper (and lower) with respect to the rotation axis. All these operations were applied at *fibre* level.

  The first operation consisted in the assignment of a new value–obtained by interpolation of the nearest voxel values– to both the new empty voxels and those superimposed as a consequence of the rotation. The second deformation had instead the aim to reproduce the muscle augmentation as a consequence of its contraction (active in the case of the upper-limb, and passive for the lower-limb). This latter kind of deformation was customizable, by initially setting two parameters which had effect, the first, on the amplitude of the deformation, and the second on the extent of the region to deform. These operations were performed in an automated way through an algorithm implemented by the authors.

The figure 2 shows, as an example, the different effects obtained by applying some kinds of deformations to the DAM's original left arm (a), and thus obtaining a simply rotated arm (b) or a rotated arm with augmented muscle in correspondence of the upper-limb (active contraction, (c)), or both the upper- and lower-limb (active and passive contraction, (d)).
A direct consequence of these kinds of deformations was a little mass variation. In particular, even the rotation without muscle augmentation led to a mass increasing as long as the structure to bend was rather thin (arm, legs), but the mass was found to be reduced while bending larger structures such as the pelvis. Therefore, particular attention had to be paid in assigning the suitable deformation parameters, in order to guarantee the total mass conservation.
A picture of the final result, that is the seated DAM phantom, is shown in Figure 3, laterally on the right.

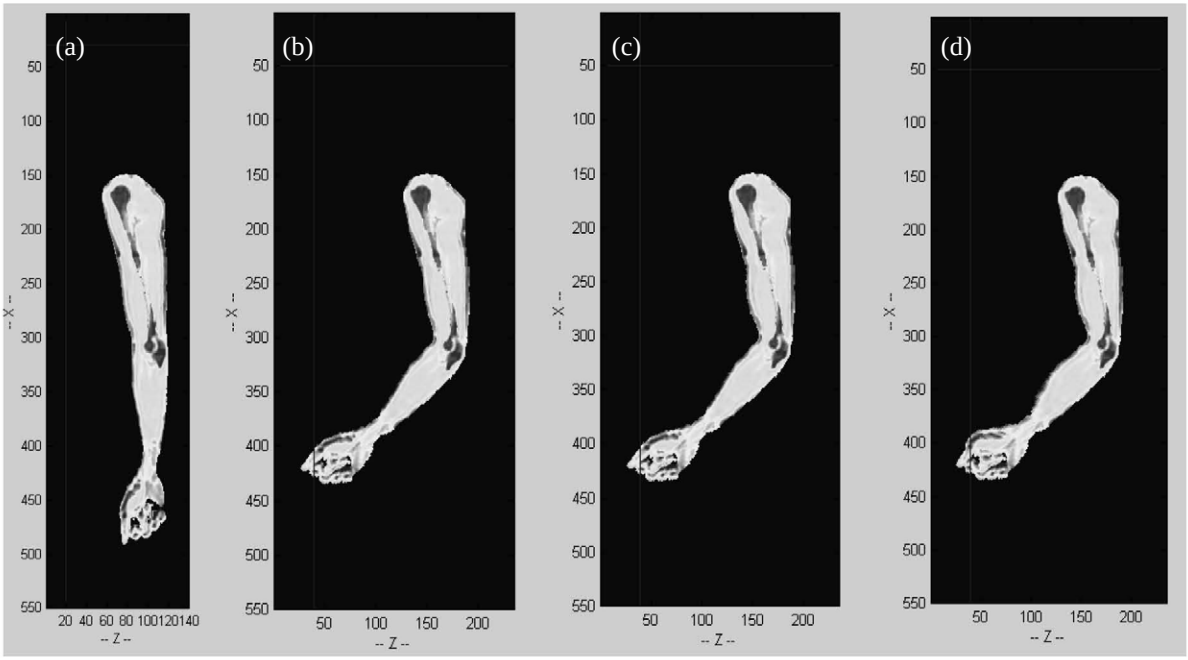


Figure 2: The pictures show four slices corresponding to the same depth of the DAM arm: in the original position (a), bended with a rotation of 45 degrees (b), as well as deformed to reproduce the muscle contraction, only in correspondence of the upper-arm (c), or both in the upper- and fore-arm. The white curves roughly indicate the regions where the deformations were applied.

FDTD calculation

Following a well known procedure, in classic FDTD [11] one writes centred finite difference analogues of the six partial differential scalar equations corresponding to the two Maxwell's curl time domain ones. Due to the particular choice of the lattice fields' sampling points, such finite equations are second-order accurate, both in space and time. As an initial value problem (IVP) fully explicitly formulated, the classic FDTD method is subjected to a stability condition, the so-called Courant–Friedrichs–Lewy (CFL) condition.
Moreover, the FDTD method needs to be supplemented by a suitable boundary condition (BC) on the outer surface of the computational domain to truncate the lattice and thus overcoming finite memory allocation capabilities. To this end many authors developed special BCs which are known, in the FDTD community, as absorbing boundary conditions (ABCs) or radiation boundary conditions (RBCs). They permit a mesh truncation with a minimum amount of back-reflection into the computational domain.
In our work we implement the anisotropic PML condition [12], which makes use of a uniaxial anisotropic lossy Maxwellian (i.e., unsplit) material. Our absorbing layer depth is standardized to 20 extra cells. Special care has to be given to the 8 corner, the 12 edges and the 6 faces of such an additional outer absorbing lattice. The coefficients for the various sub-regions and other relevant parameters are pre-calculated before the FDTD iterations start. Cubic smooth onsets of the conductivities are also used. A very low residual reflectivity is accomplished.
We also adopt the so-called "pulsed" FDTD method, which makes use of compact excitation pulses and an in-line discrete Fourier transform (DFT) of the system response. The DFT is updated every space sampling point at each time iteration. A plane wave excitation is launched on the six faces of a so-called Huygens' box, by means

of the addiction of electric and magnetic surface equivalent currents, which permit the total field, here meant incident+scattered, is present within the box but only the scattered one travels outside his volume. This allows an optimal functioning of the RBCs since they work on fields having lower amplitude than that of the total field and with incidence near to the normal to the boundary. The conditions on this box are parameterized in order to launch the desired excitation (i.e., progressive or regressive plane waves with different polarizations) without changing and/or recompiling the code. The model of the body target is contained in a sub-domain separately dealt with by the subgridding FDTD routine, which works coupled with the exterior one.
In [7] it is demonstrated that refining techniques are prone to instabilities because the interface between fine and coarse grids can trigger the onset and/or the amplification of high frequency components. This is due to the different numerical dispersion properties of the two grids. In particular, components which may freely propagate in one grid may have frequency greater than the Nyquist limit of the other one. Usually these frequencies are over the maximum frequency of interest and then may be treated as spurious components. The countermeasure proposed in [7], and here implemented, is to filter out such frequencies directly at the fine-coarse interface. That is why we call the technique FB-algorithm (Filtering Based).
It is not straightforward to deal with filters in time domain calculations such the FDTD method. In principle, simple low pass filters are applicable by using recursive techniques. The problem is that they would introduce phase delays which generate unphysical propagation and ultimately lead to instabilities. On the other hand, implementing a zero-delay filter would imply having at hand the whole time history of the quantity to be filtered, a thing which is impossible because of the evolutive nature of the FDTD method itself.
The problem has been solved [7] by transforming the temporal double derivative and his higher orders (used to implement the filter) into a set of spatial ones by means of the wave equation. Without entering in details here, the filtering action is obtained by a sort of spatial averaging with given weight coefficients. Acting at the space level permits the in-line updating during the time iterations. This allows a drastic mitigation of the instabilities, giving us the chance of using straight refinement factors of up to 7 or more, without resorting to the recursive nesting of grids (as instead it was usually done in case of use of such high refinements) which is severely computationally onerous.

Results and conclusions

In order to complement the findings of [2] who found that posture may give rise to secondary resonance peaks, a number of frequencies in the range 0.1–4 GHz have been evaluated. For each of them, the male phantom was accommodated in two postures (sitting and standing) and exposed in H or V polarization with the wave impinging the body frontally and laterally. The results are summarized in Figures 3 and 4. Since our method for obtaining the phantom does not allow going down below 100 MHz, we could not evaluate the resonant region of the spectrum. Nevertheless, results in the analyzed range are very important for radioprotection studies since the large part of broadcasting and mobile communication sources are located within it.
By using the data published in [13] it has been observed that, for Visible Human phantom, an empirical relationship holds for a 0.9 GHz plane wave exposure. It states that the whole body averaged SAR may be approximately calculated as 0.6 times the flux of the Poynting vector, times the minimal rectangular area circumscribing the largest coronal section of the body (it was illuminated frontally) and divided by the weight of the body.
By analyzing our phantoms, we found that the factor 0.6 is equivalent to the ratio between the area of the largest coronal section of the body and the minimal rectangular area circumscribing it. Then the above mentioned empirical relationship may be rewritten as:

$$SAR_{wb} \approx S\frac{A}{M} \qquad \{1\}$$

where S is the power density in W/m^2, A is the body area meant as the maximum cross section perpendicular to the wave number vector, and M is the mass of the body. This is not surprising, because it establishes that the power absorbed by the body is the Poynting flux by the section area; then this power distributes in the body and the averaged SAR is calculated dividing it by the body weight.
It is expected that this holds just at high frequencies where the absorption is eminently superficial. For this reason we report this approximated value only above 3 GHz in the graphs.
Since the computational burden involved in the calculation is rather high we could not provide results on a dense set of frequencies; thus, in case a fine structure were present in the spectrum, it would not be discriminated. However, it is probably unrealistic that a highly irregular behaviour in the SAR_{wb} would occur between a data point and the other one, even though they are rather sparse.
In [2] sub-resonances were seen slightly above 100 MHz for the sitting posture. Although we cannot confirm those results until a very dense set of frequency points will be available, we may draw some conclusions from the data here reported.

In the grounded state (as are the phantoms in the present study) main body resonance for the standing posture, occurs around 40 MHz. At 100 MHz, first point of our set, the tail of the resonance peak is still evident when the polarization is vertical in both orientations. It is more pronounced in the standing posture despite the sitting one has a shorter equivalent height and, consequently, a resonant frequency nearer to 100 MHz. Probably, since the shape of the body does not resemble anymore a linear antenna, the absorption is smeared on a larger, but less intense, resonance peak. It is also evident from the graphs that the peak is polarization-dependent: the SAR_{wb} is minimal at 100 MHz with horizontal polarization, which seems instead to show its maxima around 500 MHz or above.

Probably the most remarkable conclusion which can be drawn by the graphs is how good the very simple formula {1}, is able to provide an order-of-magnitude SAR_{wb} estimation above 500 MHz for both body orientations (frontal and lateral). The larger difference between the two body orientations is found for the standing posture, where the cross sectional area exposed to the wave almost doubles in passing from lateral to frontal orientation. Minor differences are instead visible for the seated case where the frontal cross section is diminished by the femurs' region with respect to the standing one.

These preliminary results suggest that, despite the roughness of formula {1}–which takes into account neither the dielectric properties of the body, nor its shape along the propagation direction–it gives reasonably good approximation of the SAR averaged over the whole body, at least above 500 MHz.

A conclusive statement about fulfilling of ICNIRP [14] limit can also be formulated: thresholds for whole body averaged SAR is 0.4 and 0.08 W/kg for occupational and general public, respectively. From that, the reference levels, under conservative assumptions, were calculated as: 10 and 2 W/m^2, till 400MHz, a linear connection follows up to 50 and 10 W/m^2 at 2 GHz and above this frequency values remain unchanged till 300 GHz. Scaling the SAR_{wb} to these limits allows the threshold of Figures 3 and 4 to be calculated. As it is shown in the graphs, the standing posture with frontal exposure and vertical polarization remain the conditions for which the absorption goes nearer to threshold although never reaching them.

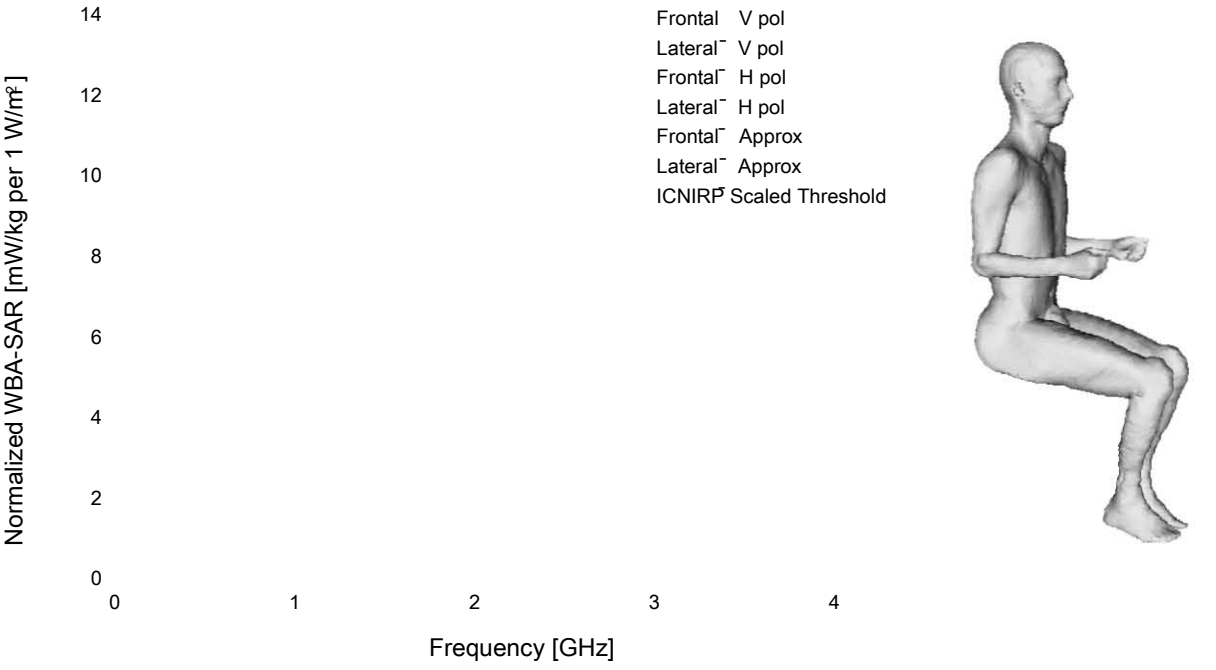


Figure 3: Whole body averaged SAR (Poynting flux of 1 W/m^2) for the sitting male phantom. In black and gray the frontal and lateral exposition, respectively. The polarization is vertical (solid lines) or horizontal (dashed lines). Approximated values are obtained by formula {1}. Dotted line is the scaled ICNIRP threshold which is applicable for both occupational and general public.

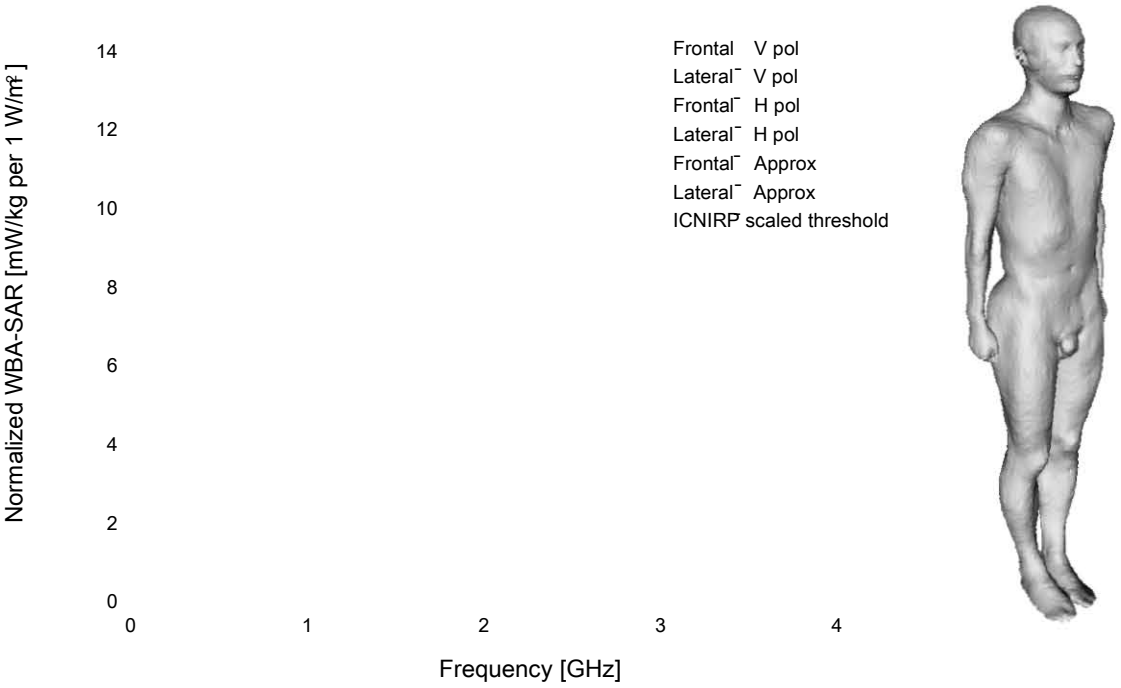


Figure 4: Whole body averaged SAR (Poynting flux of 1 W/m^2) for the standing male phantom. In black and gray the frontal and lateral exposition, respectively. The polarization is vertical (solid lines) or horizontal (dashed lines). Approximated values are obtained by formula {1}. Dotted line is the scaled ICNIRP threshold which is applicable for both occupational and general public.

References

[1] R. P. Findlay and P. J. Dimbylow, Effects of posture on FDTD calculations of specific absorption rate in a voxel model of the human body, *Physics in Medicine and Biology*, 50, 3825–3835, 2005

[2] R. P. Findlay and P. J. Dimbylow, FDTD calculations of specific energy absorption rate in a seated voxel model of the human body from 10 MHz to 3 GHz, *Physics in Medicine and Biology*, 51, 2339–2352, 2006

[3] L. Sandrini, A. Vaccari, C. Malacarne, L. Cristoforetti and R. Pontalti, RF dosimetry: a comparison between power absorption of female and male numerical models from 0.1 to 4 GHz, *Physics in Medicine and Biology*, 49, 2, 5185-5201, 2004

[4] M. Mazzurana, L. Sandrini, A. Vaccari, C. Malacarne, L. Cristoforetti and R. Pontalti, A semi-automatic method for developing an anthropomorphic numerical model of dielectric anatomy by MRI, *Physics in Medicine and Biology*, Vol. 48, No. 19, 3157-3170, 2003

[5] M. Mazzurana, L. Sandrini, A. Vaccari, C. Malacarne, L. Cristoforetti and R. Pontalti, Development of numerical phantoms by MRI for RF electromagnetic dosimetry: a female model, *Radiation Protection Dosimetry*, 111, 4, 445-451 2004

[6] R. Pontalti, L. Sandrini, A. Vaccari, C. Malacarne and L. Cristoforetti, Body-District Averaged-SAR in Female and Male Subjects Exposed to RF Plane Wave. *Proceedings of the 3rd International Workshop on Biological Effects of Electromagnetic Fields* - Volume I, Kos, Greece, 4-8 October 2004, P. Kostarakis Ed., pp. 447-456

[7] A. Vaccari, R. Pontalti, C. Malacarne, L. Cristoforetti, A Robust and Efficient Subgridding Algorithm for the Finite-Difference Time-Domain Simulation of Maxwell's Equations, *Journal of Computational Physics*, 194, 117-139, 2004

[8] J. W. Fernandez, P. Mithraratne, S. F. Thrupp, M. H. Tawhai, P. J. Hunter, "Anatomically based geometric modelling of the musculo-skeletal system and other organs",Biomechan Model Mechanobiol Vol. 2, pp 139–155, 2004

[9] J. Teran, E. Sifakis, S. S. Blemker, V. Ng-Thow-Hing, C. Lau, and R. Fedkiw, "Creating and Simulating Skeletal Muscle from the Visible Human Data Set", IEEE Transactions On Visualization And Computer Graphics, Vol. 11, No. 3, pp 317–328, May/June 2005

[10] F. Dong, G. J. Clapworthy, M. A. Krokos, and J. Yao, "An Anatomically-Based Approach to Human Muscle Modeling and Deformation", Ieee Transactions On Visualization And Computer Graphics, Vol. 8, No. 2, pp 154–170, April/June 2002

[11] K.S. Yee, Numerical solution of initial boundary value problems involving Maxwell's equations in isotropic media, *IEEE Trans. Antenna Propagat*. 14, 302–307, 1966

[12] S. D. Gedney, "An anisotropic perfectly matched layer-absorbing medium for the truncation of FDTD lattices," *IEEE Trans. Antennas Propagat.*, vol. 44, pp. 1630–1639, Dec. 1996

[13] P. Bernardi, M. Cavagnaro, S. Pisa, and E. Piuzzi, "Specific absorption rate and temperature elevation in a subject exposed in the far-field of radio-frequency sources operating in the 10-900-MHz range", *IEEE Trans. on Biomed. Eng.*, vol. 50, no. 3, pp. 295 -304, Mar 2003

[14] ICNIRP, "Guidelines for limiting exposure to time-varying electric, magnetic, and electromagnetic fields (up to 300 GHz)", *Health Physics*, vol. 74, pp. 494–522, 1998

INFLUENCE OF MICROWAVE RADIATION ON CELL MEMBRANE STIFFENING

GEORGE SAJIN[(*)], TUDOR SAVOPOL[(**)], MARIA SAJIN[(**)] EUGENIA KOVACS[(**)], IRINA MIRON[(**)]

[(*)]NATIONAL RESEARCH INSTITUTE FOR MICROTECHNOLOGIES, STR. EROU IANCU NICOLAE 32B, 077190, BUCHAREST, ROMANIA
[(**)]"CAROL DAVILA" MEDICAL UNIVERSITY, BIOPHYSICAL RESEARCH DEPARTMENT, STR. DIONISIE LUPU 37, BUCHAREST, ROMANIA

Abstract
The purpose of our experiments was to measure the effects of 1800 MHz microwave radiation on membrane anisotropy of a human blood monocitar and trombocitar cell population. Power level of the applied CW microwave radiation was low enough to consider it to be athermal. Experience demonstrates that the natural tendency to decrease of cell membrane anisotropy is favourised by microwave irradiation. This tendency maintains after the ceasing of microwave irradiation.

Introduction
Due to the extensive use of electromagnetic fields in everyday life, more information is required to detect the mechanisms of interaction and the possible side effects of microwave radiation on the structure and function of the organism. The target of these experiments was to find the effects of 1800 MHz microwave radiation on human cells. This frequency was chosen because it is used for the extension of mobile telephony systems. The biologic parameter followed in experiments was the membrane anisotropy of human blood monocytes and trombocytes.

Experimental method

Principle of the method
The membrane fluidity of irradiated and nonirradiated human blood cells was monitored by fluorescence anisotropy measurements of TMA – DPH labeled cells. Fluorescence anisotropy was measured before, during and after microwave irradiation of human blood monocytes and trombocytes.

The principle of the method consists in labeling the cellular membrane with a specific fluorescent dye. TMA – DPH with the formula shown in Fig.1 binds on the hydrophilic external surface of the cell membrane.

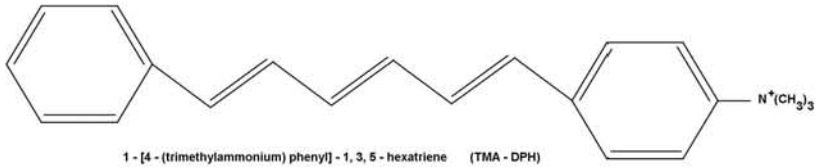


Fig.1. Formula of 1 – [4 – (trimethilammonium) phenyl] – 1, 3, 5 – hexatriene (TMA – DPH)

The biological sample is then illuminated with vertically polarized light.

Upon excitation of a molecule with vertically polarized light, the molecule will emit a fluorescent radiation more or less polarized, depending on the degrees of freedom of the molecule during the lifetime of the excited state. Depolarization degree of fluorescent light is a measure of the fluorophore freedom and therefore it is a measure of fluidity of the surrounding medium. Both the absorption and the emission of polarized light by a molecule are due to electronic transitions. A molecule can absorb a photon only if the molecular transition moment lies in the polarization plane of the exciting incident light. Reciprocal, when it comes back in the initial

status, the excited molecule emits light polarized in the plane of molecular transition moment. It follows that from a populations of molecules randomly oriented, illuminated with polarized light, only a sub-population will be excited (those with the molecular transition moment properly oriented).

An excited molecule will remain in this status only a small (some nanoseconds) time – naturally lifetime of excited status. After this time it will relax emitting polarized light in the manner described above. If during naturally lifetime of excited status the molecule changes its position (due to the thermal agitation) the emitted light will be in other direction that the absorbed exciting light. It follows that, naturally, the emitted light from this molecular population will have a polarizing index smaller than the incident light. The depolarizing degree is a measure of the freedom of movement of the molecules in the fluid, therefore a measure of the fluidity.

Usually, the incident light is vertically polarized and the measurement of the polarization of the emitted light are made in vertical (I_{VV}) and in the horizontal plane (I_{VH}) where the indexes v and h refers to the vertical, respectively horizontal polarizing plane.

The monitored parameter is the fluorescence anisotropy index **r** of the emitted light defined as:

$$r = \frac{I_{VV} - GI_{VH}}{I_{VV} + 2GI_{VH}} \quad (1)$$

where:

I_{VV} = recorded intensity of vertically polarized fluorescence light when excitation light is vertically polarized;

I_{VH} = recorded intensity of horizontally polarized fluorescence light when excitation light is vertically polarized;

G = correction factor depending on the fluorimeter used in measurements; it is due to the imperfection of the detection system and of monochromators.

$$G = \frac{I_{HV}}{I_{HH}} \cong 1 \quad (2)$$

where:

I_{HV} = recorded intensity of vertically polarized fluorescence light when excitation light is horizontally polarized;

I_{HH} = recorded intensity of horizontally polarized fluorescence light when excitation light is horizontally polarized;

The wavelength of excitation and emission light were $\lambda_{excitation}$ = 356 nm and $\lambda_{emission}$ = 429 nm, respectively.
By measuring the depolarizing of the light emitted by this fluorescent material it is possible to evaluate the membrane fluidity. A high value of anisotropy means the stiffening of the membrane and inverse, a low value corresponds to a more fluid membrane.

The purpose of our experiments was, using the above exposed method, to measure the membrane anisotropy of a monocitar human blood cell population irradiated with 1800 MHz microwave radiation and to compare it with the membrane anisotropy of non-irradiated cells.
Biological material (blood platelets) used in experiments was taken over from two healthy human donors and separated by centrifugation. Labeling of the blood cell (monocytes and trombocytes) membranes was done in 5 μl of TMA – DPH stock solution (0.5 mM TMA – DPH in dimetylformamide – DMF) and 1 ml of cell suspension were added to 1 ml Ringier solution in a fluorimeter cuvette with dimensions 1×1×5 cm^3.

Microwave experimental setup

The experimental arrangement allows simultaneous application of the polarized light and of the microwave radiation. The microwave experimental setup, it is presented in Fig.2. It consists in a microwave generator followed by a variable attenuator and an isolator with the role to prevent the reflected waves to reach the emitting device. The microwave chain contains two 20 dB directional couplers mounted as in Fig.2 in order to measure the direct and reflected power traveling in setup. Via two identical detectors, two voltages proportional

with the direct and reflected microwave powers are displayed on the voltmeters (1) and (2). Prior the beginning of the experiments a calibration step is performed.

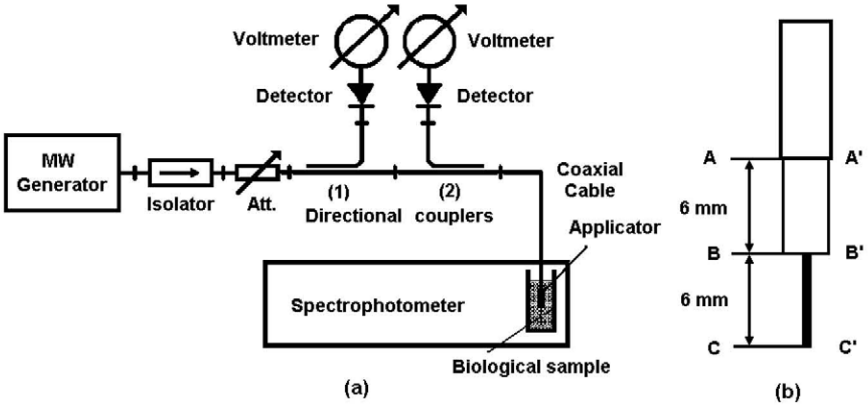


Fig.2. The microwave setup (a) and the applicator (b)

The radiating element is a λ/2 antenna (applicator) made using a semi-rigid cable. The external metallic shield of the cable was removed on a length of 12 mm (section AA') and the cable dielectric was removed on a length of 6 mm (section (BB') exposing 6 mm of central conductor. The antenna is introduced in the container in such a manner that the exposed dielectric and the central conductor are totally submersed in the biological fluid (up to the section AA').
The microwave power level effectively injected in the biological sample is the difference between direct power level and reflected power level and minus the losses in cables and transitions.

Experiments and results

Experiments on human monocytes membrane anisotropy
From the power balance previously presented results a microwave power of approx. 70 mW CW effectively injected in the biological sample. Because the content of the mini-container is approx. 4 g of biological sample it results a SAR = 18 mW/g.

Anisotropy of monocyte membrane was measured for 90 min at time intervals of 5 min. In the first 30 min the microwave radiation was not applied so that the anisotropy variation in this time interval vas considered as a measure for natural anisotropy decrease. In the next 30 min the biological samples were irradiated in the conditions presented above. Finally, for the last 30 min the microwave radiation was interrupted but the measurements continued at the same time interval of 5 min each in order to see the evolution of anisotropy following the irradiation.

The obtaining results are displayed in Tab.1 prior to, during and after the microwave irradiation. The normalization was made to the values of anisotropy at the beginning of the experiments. One can see that the natural tendency of anisotropy is to decrease (in the first 30 min) and this tendency is maintained during the irradiating session and also after the interruption of microwave application.

In order to have a better understanding of the microwave effects, a number of samples pairs were chosen following the criterion of closest values of the rate of the anisotropy decrease in the first 30 min (without microwave irradiation). One of the components of each pair was then irradiated with microwaves and the other was kept as reference. The rate of anisotropy decrease was measured during the microwave application and in the post-irradiation time.

The results for four pairs of biological probes are presented in Table 2. There is shown the difference between rates of the anisotropy decrease in the two biological samples in each pair. One may see an increasing rate of this parameter during the irradiation time, tendency maintained also in post-irradiation time.

TABLE 1
DECREASING OF THE ANISOTROPY (NORMALIZED VALUES)

Pre-irradiation		Irradiation		Post-irradiation	
Time (min)	Value	Time (min)	Value	Time (min)	Value
5	0,974	35	0,884	65	0,846
10	0,953	40	0,886	70	0,848
15	0,921	45	0,878	75	0,808
20	0,910	50	0,867	80	0,841
25	0,904	55	0,835	85	0,850
30	0,900	60	0,847	90	0,811

TABLE 2
DIFFERENCE BETWEEN ANISOTROPY DECREASE RATES OF THE MONOCYTIC CELLS IN EACH SAMPLE PAIR.

Time (min)	Differences in rates of anisotropy decrease (absolute values)			
	1st pair	2nd pair	3rd pair	4th pair
0	0.000	0.000	0.000	0.000
5	0.010	0.010	0.018	0.000
10	0.009	0.016	0.005	0.004
15	0.011	0.014	0.014	0.006
20	0.010	0.026	0.006	0.003
25	0.012	0.006	0.004	0.005
30	0.011	0.018	0.018	0.005
35	0.013	0.023	0.060	0.006
40	0.014	0.010	0.026	0.008
45	0.026	0.013	0.036	0.019
50	0.027	0.022	0.024	0.017
55	0.025	0.017	0.044	0.015
60	0.035	0.063	0.048	0.014
65	0.040	0.066	0.033	0.022
70	0.034	0.050	0.028	0.021
75	0.032	0.064	0.029	0.027
80	0.041	0.046	0.042	0.028
85	0.032	0.055	0.041	0.033
90	0.039	0.083	0.004	0.034

The results showing the anisotropy increasing rate were drawn for the first and the second biological sample pairs in Fig.3 … 6.

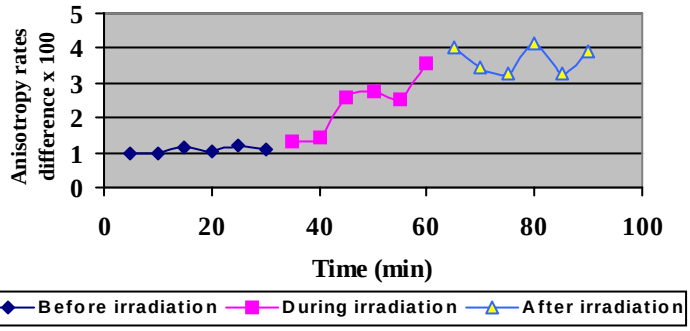


Fig.3. Anisotropy decreasing rate for the first biological monocytic sample pair (see Table II)

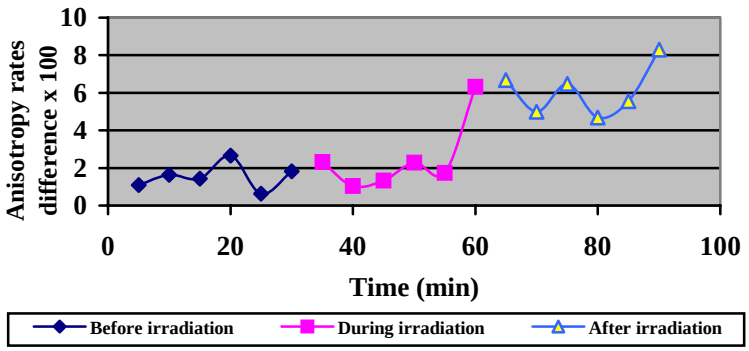


Fig.4. Anisotropy decreasing rate for the second biological monocytic sample pair (see Table II)

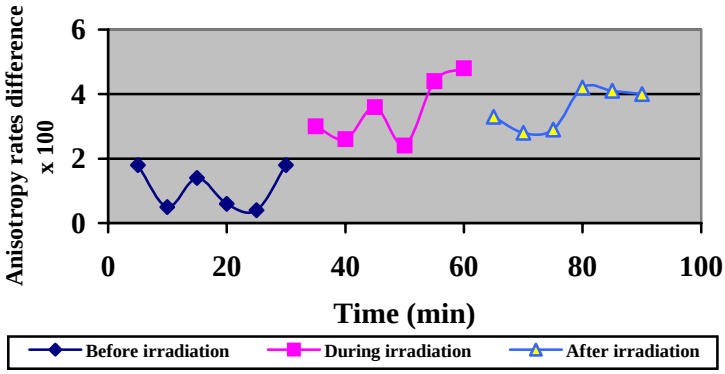


Fig.5. Anisotropy decreasing rate for the third biological monocytic sample pair (see Table II)

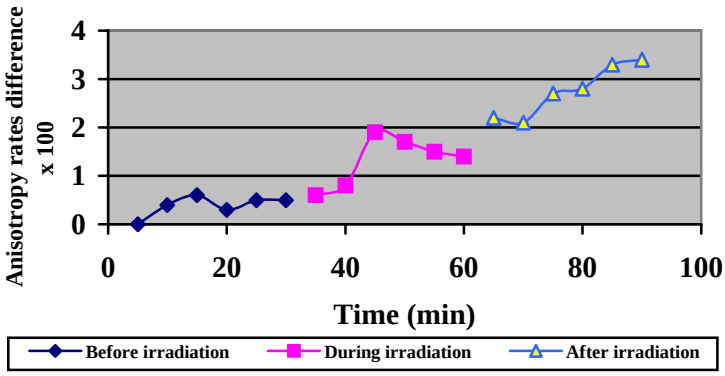


Fig.6. Anisotropy decreasing rate for the fourth biological monocytic sample pair (see Table II)

Experiments on human trombocytes membrane anisotropy

Experiments made using a trombocitar population obtained from human blood are similar with those concerning monocitar population. The same microwave irradiation setup was used. There are, nevertheless, some differences.

a) The experiments were made using two microwave power levels: 7 mW and 60 mW, meaning SAR values of 1.75 mW/g and respectively 15 mW/g.

b) The total experimental time was 3 h, each measurement being made at 5 min time interval. The microwave irradiation was applied in the second hour of the experiment (between minutes 60 and 120).

c) In each day was made an experiment using the same trombocitar concentrate. There were four experiments in four days but, for the sake of space saving, only the results of first two experiments are presented. The other results are very similar.

The power levels are done at the point (a).

The values of anisotropy obtained in these experiments are presented in Table 3 and the graphs representing these values are presented in Figs. 7 – 10.

TABLE 3

NORMALIZED VALUES OF TROMBICYTIC MEMBRANE ANISOTROPIES OBTAINED BY MICROWAVE IRRADIATION

Time (min)	First day experiments		Second day experiments	
	7 mW	60 mW	7 mW	60 mW
0	1.000	1.000	1.000	1.000
10	0.972	0.993	1.030	0.980
20	0.974	1.003	0,980	1.024
30	1.001	0.995	0.962	1.000
40	0.961	0.970	0.97	0.975
50	1.000	0.952	0.93	0.950
60	0.960	0.982	0.95	0.951
70	0.968	0.980	0.922	0.962
80	0.961	0.969	0.913	0.957
90	0.921	0.971	0.918	0.971
100	0.950	0.961	0.892	0.950
110	0.926	0.954	0.887	0.938
120	0.940	0.960	0.861	0.930
130	0.962	0.950	0.862	0.900
140	0.93	0.948	0.864	0.870
150	0.932	0.945	0.888	0.870
160	0.92	0.915	0.880	0.800
170	0.908	0.900	0.847	0.770
180	0.912	0.874	0.830	0.720

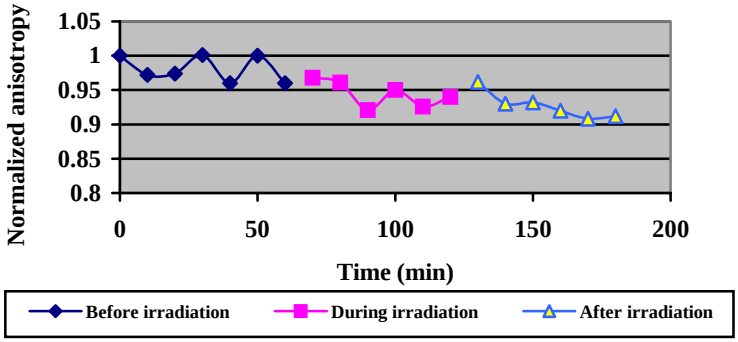


Fig.7. Evolution of the trombocytes membrane anisotropy in the first day of experiments. Applied microwave power: 7 mW

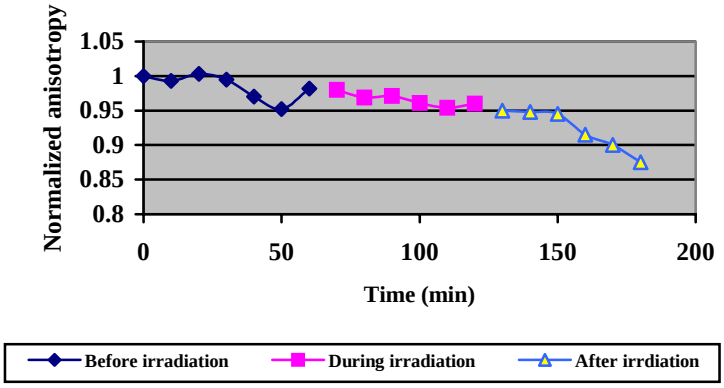


Fig.8. Evolution of the trombocytes membrane anisotropy in the first day of experiments. Applied microwave power: 60 mW

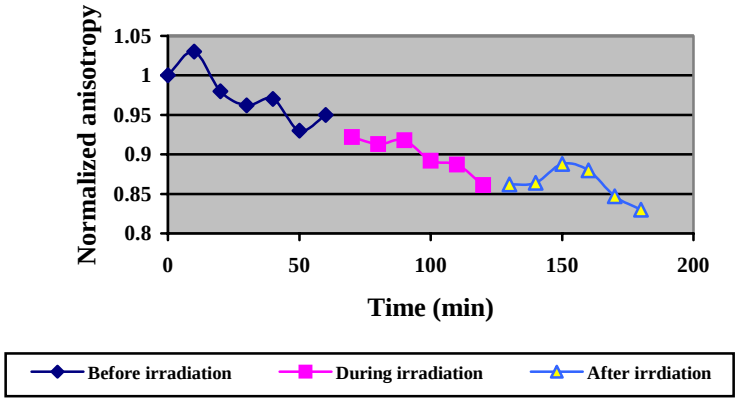


Fig.9. Evolution of the trombocytes membrane anisotropy in the second day of experiments. Applied microwave power: 7 mW

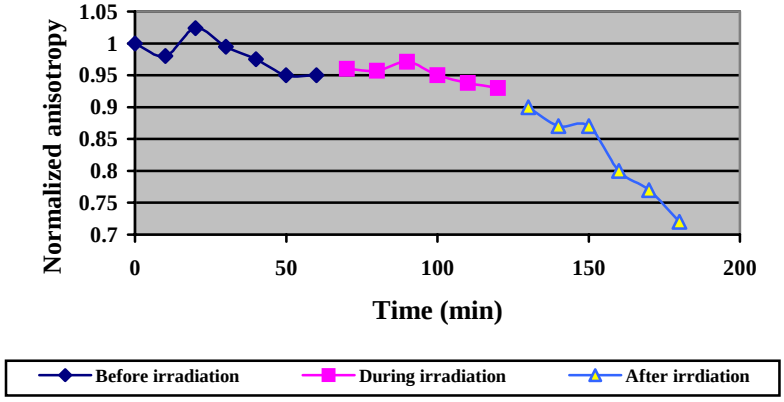


Fig.10. Evolution of the trombocytes membrane anisotropy in the second day of experiments. Applied microwave power: 60 mW

Conclusions

In the above presented experiments power level of the applied microwave radiation was low enough to consider it to be athermal. From the numerical data and the drawings presented in this paper one may conclude the following:

a) During the experience (with or without microwave irradiation) the tendency of anisotropy of human blood monocytes membrane anisotropy is to decrease;

b) This decrease is greater when 1800 MHz microwave radiation is applied. This tendency is maintained after the ceasing of microwave irradiation.

c) For a better emphasizing of this result, for monocytes cellular population, samples pairs of blood samples were chosen following the criterion of closest values of the speed of the anisotropy decrease in the first 30 min. The speed of the anisotropy decrease was evaluated in the time and after the microwave irradiation. The result is presented in Table 2 and in Figs 1 and 2, showing the same effect on the speed of anisotropy decrease.

d) For a population of trombocytic cells, the anisotropy of the cellular membrane, also, decrease both during and after ceasing of the microwave radiation..

e) The slope of the decreasing curve is greater after irradiation with 60 mW microwave radiation. It seems like RF radiation favours the decrease rate of membrane anisotropy.

Acknowledgements

This paper is the result of studies made in National Research Institute for Microtechnologies, Bucharest, Romania, on the basis of the Project 31CEEX 103/2005.

CARDIOVASCULAR RISK IN PHYSIOTHERAPISTS UNDER ELECTROMAGNETIC RADIATION

KATIA VANGELOVA, MICHEL ISRAEL, CHRISTO DEYANOV, MICHAELA IVANOVA

NATIONAL CENTER OF PUBLIC HEALTH PROTECTION,
15 ACAD. IVAN GESHOV BLVD, 1431 SOFIA, BULGARIA

Abstract

The aim of the study was to assess the long-term effects of electromagnetic radiation (EMR) on cardiovascular system of medical staff in physiotherapies. 52 exposed subjects (4 male and 48 female; aged 47.3 ± 8.7 yrs.) and a control group of 52 subjects, matched by sex and age, with similar job characteristics except for EMR were studied. The EMR exposure from appliances emitting at 50 Hz, 150 kHz, 27.12 MHz, 2.45 GHz was assessed. The workload and psychosocial factors were followed, too. The cardiovascular risk factors arterial pressure, lipid profile, body mass index, waist/hip ratio, smoking, alcohol consumption, nutrition, family history of cardiovascular disease were studied. The incidence of hypertension was moderate with the studied physiotherapists (26.9 % v.s. 23.8 % with the control group). The total cholesterol (TC) and low-density lipoprotein cholesterol (LDL-C) were significantly higher in the exposed group. The odds ratios indicate higher chance of becoming dyslipidemic with the exposed to EMR subjects [for TC OR (95 % CI) = 1.570 (1.048 – 2.351) and for LDL-C OR (95 % CI) = 1.840 (1.158 – 2.924)]. In conclusion, our data show that the EMR exposure of the medical staff in physiotherapies is associated with the adverse effects on cardiovascular system.

Key words: Arterial hypertension, dyslipidemia, EMR exposure, long-term effects, health risk

Introduction

Physiotherapetists are exposed to many risks in their work environment, some common for the health care workers, and some specific for the profession, such as the exposure to electromagnetic radiation (EMR), emitted from pulsed magnets, d'Arsonvale devices, equipment for microwave and high frequency diathermy, optical sources (UV, IR and visible), lasers. Some of the devices emit electromagnetic radiation above the exposure limits, rising health concerns.

The general health status of physiotherapiscs is largely unknown (Cromie et al. 2002), but some studies suggest possible adverse health effects of the EMR exposure, including increased risk of cardiovascular diseases. Hamburger et al. (1983) found positive relation between the EMR exposure and heart disease in physiotherapists, but in the study the exposure was categorized as either high or low on the base of mean number of employed years and mean number of treatments delivered by week. More attention has been paid to the health risks of radiofrequency EMR exposures in communications, but there still exist controversies concerning the effects of long-term exposures to low-level EMR (recent reviews Repacholi, 1998, Krewski et al. 2001, Vangelova and Deyanov 2003. Jauchem (1997) reviewed the epidemiological studies with a general conclusion that they had not yielded any obvious cardiovascular related hazards on long-term low-level exposures, in spite of the presence of various physiological effects. Our earlier data showed high rate of hypertension in broadcasting and TV station operators (Israel and Tomov, 2000). A second study was carried by our group in 49 broadcasting and 61 TV station operators (Vangelova et al. 2006) in order to confirm the previous findings, enlarged with serum lipids, and showed significantly higher chance of becoming hypertensive and dyslipidemic in broadcasting and TV station operators exposed to radiofrequency EMR. Slight, subclinical ECG abnormalities, accompanied by symptoms of sympathicotony in heart variability, shifts in the diurnal rhythms of blood pressure and heart rate in 77 AM broadcasting station operators (0.7-1.5MHz) were reported (Bortkiewicz, 1995; Szmigielski, 1998). Szmigielski (2000) confirmed the above data in a study on 38 workers in radio transmitting centers, exposed to 10-30 MHz EMF.

The aim of the study was to assess the long-term effects of EMR on the cardiovascular system of medical staff in physiotherapies.

Material and methods

The cardiovascular risk was assessed in 52 physiotherapists (4 males and 48 females) working with EMR emitting devices of age 47.3 ± 8.7 years and length of service 23.0 ± 9.5 years. A control group of 52 subjects from the same hospitals were examined, matched by sex, age and shift work schedules, with similar job characteristics except for the EMR. Their age was 47.8 ± 8.5 and length of service of 21.6 ± 4.6 years. The investigated subjects signed an informed consent.

EMR exposure assessment

There are a variety of sources of EMR in physiotherapies, emitting in the frequency range from constant fields (F = 0 Hz) to optic radiation. This puts substantial difficulties to the elaboration of a precise workplace exposure assessment, complicated by variety of situations in different cabinets, number of patients, etc. The scope of the devices in the studied units is the following:

- Devices for local thermotherapy ("Chinese vacuum cleaner" – Qi Gong);
- Equipment for galvanotherapy, ion - galvanotherapy and electrostimulation, "bipulsator" (for therapy with electric pulses), diadynamic;
- Devices for local franklinization – "ion shower";
- Equipment for low frequency diathermy, diathermal ion galvanization and diathermal electrostimulation;
- D'Arsonvale devices;
- Equipment for treatment with magnetic/electric field within the radiofrequency (RF) range (27.12 MHz), and with microwaves (2,45 GHz) for inductive-thermal therapy;
- Microwave electropyrexia;
- Devices for photo-therapy:
  - Solariums;
  - UV lamps for individual UV therapy;
  - UV sources application of the PUVA method of therapy;
  - Lamps of types "SOLUX" and "INFRAROUGE";
  - Laser diodes, gas lasers and other sources of coherent light.

We used the approach of individual assessment of EMR in physiotherapies, described earlier (Israel and Tschobanoff, 2006). In order to establish unified conditions for exposure assessment for different frequencies (over the overall frequency range) we applied a general unified indicator associated with the energetic irradiation dose, according to the ICNIRP Guidelines (1), ACGIH TLVs (2), and the Bulgarian National Standards (3, 4).

The energy load of the human organism is defined for three cases as a derived quantity of energy falling at external irradiation: $\boldsymbol{W_E}$, $\boldsymbol{W_H}$ and $\boldsymbol{W_S}$, based on dispersed energy per time unit on human body during the official working shift. Measurable quantities are used – intensities and power density according to the distance from the generator to the measuring device and the respective frequency range of the single photon.

SAR is the specific value of power absorbed by the recipient; ***SA*** is the specific value of the respective absorbed energy according to the calculated ***SAR***.

As ***SAR*** is introduced by the dimension of base metabolism of an adult man (175 cm/70 kg) the dimension of ***SA*** is the dimension of ***SAR*** by the time, that is

$$SA = SAR.t \quad [J/kg]$$

The two types of quantities - $\boldsymbol{W_E}$, $\boldsymbol{W_H}$ and $\boldsymbol{W_S}$ on the one side, and ***SAR, SA*** on the other do not differ substantially in conditions of air equivalent environment and a human body situated in it.

SAR is introduced through Human Equivalent Antenna. If the respective effective area is $\boldsymbol{A_e}$, then through relationships between the dimensions of the quantities ***W*** and ***SA*** following by the definition for power and from the way of determining human body exposure, the quantity ***W*** corresponds to whole body value of ***SA*** at constant body weight and unchanging mean conductivity of the tissue, standardized to the effective exposure area $\boldsymbol{A_e}$. The magnitude of the latter on its part depends on the mutual orientation of a standing person and the intensity of the falling electric field ***E***.

The measurable quantity in all cases is the same – ***E [V/m].*** Consequently $\boldsymbol{W_E}$ will incorporate the definition of ***SA*** and vice versa.

The exposure duration: real exposure time at work with a device $\boldsymbol{T_{app}}$ ***[h]***, followed by chronometer measurements, and a total duration of the working shift ***T [h***.were registered. The duration time is introduced by the number of devices and the number of patients serviced by the individual.

The method was unified for the equipment, the distances to the particular device and the mandatory restrictions to the behavior of the physicist/engineer, performing the measurement. The major characteristics of the method are the 6 mandatory distances to the different types of generators determined depending on the frequency range of the radiation. They conform to the requirements for measurement in the far and near field zones and the requirements for determination of ***SAR*** in different cases of electromagnetic energy falling on a standing human.

The dose as a function of the squared mean measured intensity was presented by the ***SAR*** quantity. Our calculation formulation were based on the vision of the averaged dose: the dose (calculated with the actual measured values of the field and exposure time) multiplied by the mean geometric value of the partial doses on the distance from the physician/nurse to the patient r_1 and the dose of the same to another characteristic distance (one of the cited – r_i, i ≠ 1). Thus a characterizing quantity was obtained which is a non-dimensional growing sum $\overline{D}$:

$$\overline{D} \approx \sum \frac{1}{q} \sqrt{D(r_1)} \sqrt{D(r_{i\neq 1})}$$

Here ***1/q*** was a non-dimensional quantity – ratio.

The squared field strength (E^2) used for the dose assessment was equal to the product of the measured intensity of the field at distance r_1 and the sum of weighed intensities of the other 5 distances. The method allows, at unified measurements, the elaboration of individual exposure assessment for each person in physiotherapy through calculations depending on the number of devices, number of patients and the actual configuration of the ward.

Physiotherapy devices and calculated values of the exposure for every device/for one person of the personnel were as follows:

1. Device “Megatherm”:
SAR ≤ 3.71 W/kg
f = 27.12 MHz; basic restrictions (br) for whole body SAR: SAR_{br} = 0.4 W/kg

2. UHF acoustic generator for ultrasound therapy: f ≤ 2.5 MHz:
(measurements in the frequency range f ≤ 2 kHz)

$$j \approx 3.8\ mA/m^2$$

f ≤ 2 kHz; basic restrictions for the induced current: $j_{br} \leq 2\ mA/m^2$

3. UHF 66 (Russia):
SAR ≤ 9.8 W/kg
f ≤ 2 kHz; basic restrictions for the induced current: $j_{br} \leq 2\ mA/m^2$

4. Magnet N 80 (Bulgaria):

$$j \approx 0.31\ A/m^2$$

5. Magnet NM (Bulgaria):

$$j \approx 0.28\ A/m^2$$

Light sources (polychromatic):
restrictions according to ACGIH (2004):
IR: $S \leq 1.8.t^{-3/4}\ W/cm^2$ (for cornea and lens)
IR: $S \leq 0.6/\alpha\ W/cm^2.sr$ (for retina protection)
IR (with blue light filter – B1): 1 $\mu W/cm^2$, and : $t_{max} \leq 10\ mJ/cm^2/S$
UV and visible light: $t_{max} \leq 0.003\ J/cm^2/S$

6. Quartz (UVB-1, UVB, UVA, Visible:

$$S \approx 17.6\ mW/cm^2$$

7. Solux Infrarouge, without filters:

$$S \approx 286.1\ mW/cm^2$$

8. Solux Infrarouge, with filter B1:

$$S \approx 4.9\ mW/cm^2$$

9. Interferenz - Endovak:

$$j \approx 0.69\ A/m^2$$

$f \leq 100$ kHz; basic restrictions for the induced current: $j_{br} \leq 1\ A/m^2$

10. Diadynamik (Bulgaria):

$$j \approx 0.15\ mA/m^2$$

11. Galvanostat (Bulgaria):

$$j \approx 0.15\ mA/m^2$$

$f = 150 \div 300$ kHz; basic restrictions (br) for whole body SAR: $SAR_{br} = 0.4$ W/kg

12. D'Arsonval:
SAR ≤ 0.4 W/kg
$f = 27.12$ MHz; basic restrictions (br) for whole body SAR: $SAR_{br} = 0.4$ W/kg

13. UHF 66 (Russia):
SAR ≤ 9.8 W/kg
$f = 2450$ MHz; basic restrictions (br) for whole body SAR: $SAR_{br} = 0.4$ W/kg;
for limbs $SAR_{loc} = 20$ W/kg
for head $SAR_{loc} = 10$ W/kg

14. Radarmed (2 devices):
with symmetric applicators
SAR ≤ 0.31 W/kg
with conical applicator
SAR ≤ 5.3 W/kg
Light sources (polychromatic):
restrictions according to ACGIH (2004):
IR: $S \leq 1.8.t^{-3/4}$ W/cm^2 (for cornea and lens)
IR: $S \leq 0.6/\alpha$ W/cm^2.sr (for retina protection)
IR (with blue light filter – B1): 1 μW/cm^2, and : $t_{max} \leq 10$ mJ/cm^2/S
UV and visible light: $t_{max} \leq 0.003$ J/cm^2/S

The relative values for the whole frequency range in each physiotherapy were calculated and the obtained quota was much larger than 1.

Confounding factors as noise, microclimate and psychosocial factors were followed and showed no differences between the groups.

The cardiovascular risk was assessed on the base of arterial pressure, lipid profile, body mass index (BMI), waist circumference, smoking habits, family history for cardiovascular disease, etc. The arterial pressure was measured with Hg sphygmomanometers two times in a period of three months. The hypertension was defined using the JNC VI (1997), as well as preliminary physicians diagnosis. Weight, height and circumferences at the narrowest part of the waist were recorded, and the BMI was calculated.

Blood for analysis was obtained after an overnight fast. The lipid profile included the following indices: total cholesterol (TC), high density lipoprotein cholesterol (HDL-C), low density lipoprotein cholesterol (LDL-C), triglycerides and TC/HDL-C ratio. The assessment of the lipid indices was performed with enzymatic tests. The HDL was separated by precipitation of LDL and VLDL and the cholesterol was assayed in the HDL fraction. The LDL-C was calculated using the formula of Friedewald for triglycerides < 4.3 mmol/l. The ratio TC/HDL-C was calculated, too.

The data were analyzed using SPSS software. Analysis of variance (one-way ANOVA), correlation analysis, $\chi 2$ and odds ratio were applied.

Results

The incidence of hypertension was moderate in the medical staff and did not differ significantly between the studied groups (26.9 % with the staff exposed to radiofrequency EMR v.s. 23.8 % with the control group). No significant differences both in systolic and diastolic blood pressure (SBP and DBP) were found between the exposed group in comparison to the control one (Table 1). The BMI did not significantly differ between the studied groups, but the waist was slightly higher with the exposed group. The TC, HDL-C and LDL-C were significantly higher in the radiofrequency EMR exposed group with comparison with the control group.

Table 1.
The blood pressure, anthropometric and metabolic variables of medical staff from physioterapies, exposed to EMR and control group

Indices/Groups	Medical staff from physioterapies	Control group
SBP (mmHg)	124.8 ± 19.7	122.4 ± 16.2
DBP (mmHg)	80.2 ± 12.6	78.2 ± 8.5
BMI (kg/m^2)	24.5 ± 3.8	23.3 ± 3.6
Waist (cm)	83 ± 11.9	81.5 ± 11.1
TC (mmol/l)	5.44 ±1.06**	4.97 ± 0.69
HDL-C (mmol/l)	1.53 ± 0.28*	1.39 ± 0.34
LDL-C (mmol/l)	3.42 ± 0.91**	3.07 ± 0.70
Triglycerides (mmol/l)	1.23 ± 0.71	1.19 ± 0.57
TC/HDL-C ratio	3.64 ± 1.02	3.57 ± 0.87

* $p < 0.05$; ** $p < 0.01$

The rate of distribution of some of the main cardiovascular risk factors is presented in Table 2. Significantly higher rate TC > 5.2 mmol/l and LDL-C > 3.4 mmol/l was found with the exposed to EMR medical staff, with higher significance for LDL-C. The odds ratios indicate higher chance of becoming dyslipidemic with the exposed to EMR subjects [for TC OR (95 % CI) = 1.570 (1.048 – 2.351) and for LDL-C OR (95 % CI) = 1.840 (1.158 – 2.924].

Table 2.
The frequency of distribution of the main cardiovascular risk factors in medical staff from physioterapies, exposed to EMR and a control group.

Indices	Medical staff from physioterapies	Control group	χ^2	Corrected χ^2	P
TC > 5.2 mmol/l	59.6 %	36.5 %	5.254	5.200	.018
HDL-C < 1 mmol/l	14.9 %	28.8 %	2.781	2.752	NS
LDL-C > 3.4 mmol/l	55.3 %	26.9 %	8.267	8.183	.004

The rate of smoking was high in both studied groups, slightly higher in the control one (44.2 % v.s. 40.4 % in the medical staff from physioterapies). There were no considerable differences in the self reported degree of smoking (33.3 % of the medical staff from physioterapies smoked 5-10 cigarettes/day, 57.1 % smoked 10-20 cigarettes/day and 9.5 % more than 20 cigarettes/day while in the control group 39.1 % smoked 5-10 cigarettes/day, 47.8 % smoked 10-20 cigarettes/day and 13 % more than 20 cigarettes/day). 47.6 % of the medical staff from physioterapies smoked for more than 20 years v.s. 43.5 % of the control group. There was no difference in the proportion of self reported drinkers between the investigated groups, nor in the number of beverages per week among the alcohol users. The self reported nutrition habits and physical activity during the free time did not differ between the groups, too.

Discussion

Our data show higher rate of dyslipidemia with the exposed to EMR physiotherapists, thus supporting the findings of Hamburger et al. (1983) for positive relation between the EMR exposure and heart disease in physiotherapists and confirming the data for higher rate of dyslipidemia under EMR exposure in other occupational groups as broadcasting and TV transmitting operators (Vangelova et al. 2006). The greater chance of becoming dyslipidemic of the physioterapetists exposed to EMR was confirmed by the calculated odds ratio. We suppose that the variations of TC and LDL-C were mediated to some extent by the stress system. Our data show significant EMR exposure-effect on the excretion rates of stress hormones in physiotherapists (Israel et al. 2006) and in other occupational groups (Vangelova et al., 2005). The elevation of stress hormones under

occupational stressors has been shown to interact with cardiovascular risk factors (Rosmond 1998, Fraser et al. 1999, Vrijkotte et al. 1999, Chrousos, 2000).

The higher rate of dyslipidemia in the medical staff from physioterapies can be associated mainly with the EMR exposure as the confounding factors as noise, microclimate, work organization, work control, work content, etc. were controlled (unpublished data), and the studied subjects had the same social class, found to be an important confounder (Boggild et al., 1999b). Although our study was controlled we do not exclude some synergistic effects of EMR with other occupational stressors, as emotional load of dealing with patients, work tasks requiring intense concentration, a feeling for risk of infections, strain, etc.

The rate of hypertension was similar in the exposed to EMR and control group medical staff for difference of earlier findings for higher rate of hypertension in broadcasting and TV transmitting operators working under radiofrequency EMR (Bortkiewicz 1997, Israel and Tomov, 2000, Vangelova et al. 2006). There are several differences between the cited previous studies and the present one. First, the EMR exposure was different. The physioterapetists were exposed for very short periods of time to high intensities, while the studied broadcasting and TV transmitting operators were exposed during all the working time, but with lower intensities. Second, the job task was quite different. The broadcasting and TV transmitting operators work was monotonous, while the job task of physiotherapetists was mobile, associated with emotional load of dealing with patients. Third at the last, but not at the least of importance, the broadcasting and TV transmitting operators groups consisted mainly of males, while the medical staff from physioterapies were mainly females. So the gender differences might contribute to inconsistency of the results concerning hypertention. There are data that the impact of stress is greater on arterial pressure in men and on indices associated with insulin resistance, as lipid profile indices, in females (Chrousos, 2000).

The body mass index did not differ between the groups, but the medical staff from physioterapies had more centrally disposed adipose tissue, well known risk factor for cardiovascular disease (CVD). The rate of smoking was high in the two studied groups, slightly higher in the control one. The differences in the self reported degree of smoking and the duration of smoking between the studied groups were negligible. No differences of self-reported alcohol consumption, nutrition habits, physical activity were found.

Summing up, our data suggest that the medical staff exposed to EMR was at greater risk of becoming dyslipidemic. Further studies are needed to investigate the effect of EMR on cardiovascular risk factors in the medical staff in physiotherapies, using an approach of studying the personal long-term EMR exposure in order to reach better understanding of the possible adverse effects of EMR on cardiovascular system.

References

1. Bulgarian National Standard 14425 –90. Labour protection. Electromagnetic fields – radiofrequency range. Admissible values and requirements for control (in Bulgarian).
2. Bulgarian National Standard 17137-90. Labour protection. Electromagnetic fields – microwave range. Admissible values and requirements for control (in Bulgarian).
3. Boggild, H., Suadicani, P., Hein, H.O., Gyntelberg F. Shiftwork, social class, and ischaemic heart disease in middle aged and elderly men; a 22 year follow up in the Copenhagen male study. Occup. Environ. Med. 1999 (b): 56(9): 640-645.
4. Bortkiewicz, A., Zmyslony, M., Gadzicka, E. Ambulatory ECG monitoring in workers exposed to electromagnetic fields. J. Med. Eng. Technol. 1997; 21(2): 41-46.
5. Chrousos, G.P. The role of stress and the hypothalamic-pituitary-adrenal axis in the pathogenesis of metabolic syndrome: neuroendocrine and target tissue-related causes. Intern. J. Obesity 2000; 24 (Suppl. 2): S50-5.
6. Cromie J.E., Robertson V.J., Best M.O. Occupational health in physiotherapy: General health and reproductive outcomes. Austr. J. Physiotherapy 2002; 48: 287-294.
7. Fraser, R., Ingram, M.C., Anderson, N., Morrison, C., Davies, E., Connell, J.M.C. Cortisol effects on body mass, blood pressure, and cholesterol in general population. Hypertension 1999; 3: 1374-8.
8. Hamburger S., Logue L.G., Silvermen P.M. Occupational exposure to non-ionizing radiation and an association with heart disease: An exploratory study. J.Chronic Diseases 1983; 36:791-802.
9. ICNIRP. Guidelines for limiting exposure to time-varying electric, magnetic and electromagnetic fields (up to 300 GHz). Health Physics 1998; 74(4): 494–522.
10. Israel, M., Tomov, P. Epidemiological study of the effect radiofrequency radiation on operators in radio, TV and relay stations. Proceedings of Eastern European Regional EMF Meeting and Workshop (M. Israel, M. Repacholi, eds.), 2000; VM-OFSET Sofia: pp. 145-154.
11. Israel, M., Tschobanoff, P. Exposure to non-ionizing radiation of personnel in physiotherapies. In: Bioelectromagnetics. S. N. Ayropetyan and M. S. Markov (eds.), Springer Press, 2006:
12. Israel, M., Vangelova K., Velkova D., Ivanova M. Stress hormone reactivity in medical staff exposed to electromagnetic radiation. Proceedings of the 4th International Workshop on Biological Effects of

Electromagnetics, 2006, Crete, Greece (in print).
13. Jauchem, J. Exposure to extremely–low–frequency and radiofrequency radiation: cardiovascular effect in humans. Int. Arch. Occup. Environ. Health 70, 9-21 (1997).
14. JNC VI. Classification of blood pressure of adults of age 18 years and older. Arch. Intern. Med. 1997; 157: 2413-2446.
15. Krewski, D., McBride, M., Salem, T. Potential health risks of radiofrequency fields from wireless telecommunication devices. J. Toxicol. Environm. Health 2001; 4 (B): 1-143.
16. Repacholi, M.H. Health effects of exposure to non-thermal levels of radiofrequency fields. Bioelectromagn. 1998; 19: 155-168.
17. Rosmond, R., Dallman, M.F., Bjorntorp, P. Stress related cortisol secretion in men: Relationships with abdominal obesity and endocrine, metabolic and hemodinamic abnormalities. J. Clin Endocrinol. Metab. 1998; 83: 1853-1859.
18. Szmigielski, S., Bortkiewicz, A., Gadzicka, E. Alterations of diurnal rhythms of blood pressure and heart rate of workers exposed to radiofrequency electromagnetic fields. Blood Press. Monit. 1998; 3(3): 323-330.
19. Szmigielski, S., Sobiczewska, A., Kubacki, R. Dysregulation of autonomic control of cardiac function and shift of diurnal rhythms of blood pressure in workers exposed to RF electromagnetic fields. In: Mobile Telephones and Health – and Update of the Latest Research (Bolton S. and Gemmel C., eds), 1999; Rad City and Financial Document Department Print Consultancy, Surrey, UK: pp. 117-136.
20. Threshold Limit Values for Chemical Substances and Physical Agents & Biol. Exp. Indices, ACGIH, Signature Publications, 2004.
21. Vangelova K., Israel M., Mihailov S. The effects of low level radiofrequency electomagnetic radiation on the excretion rates of stress hormones in operators during 24 hour shifts. Centr. Eur. J. Public Health 2002; 10, 23-27.
22. Vangelova K., Deyanov C. The effect of electromagnetic fields on the synthesis and secretion of melatonin, stress hormones and cardiovascular system. Review. Problems in Hygiene 2003; XIV (2): 41-47 (in Bulgarian).
23. Vangelova K., Israel M. Variations of melatonin and stress hormones under extended shifts and radiofrequency electromagnetic radiation. Rev. Environ. Health 2005, 20 (2): 151-161.
24. Vangelova K., Deyanov C., Israel M. Cardiovascular risk under radiofrequency electromagnetic radiation. Int. J. Hyg. Environ. Health 2006; 209: 133-138.
25. Vrijkotte, T.G.M, van Doornen, L.J.P, de Gues, E.J.C. Work stress and metabolic and hemostatic risk factors. Psychosom Med 1999; 61: 796-805.

RF-ABSORPTION AND TEMPERATURE ELEVATIONS IN THE INNER EAR AND THE EYE DUE TO EXPOSURE FROM HANDHELD DEVICES IN THE 400 MHZ TO 1850 MHZ RANGE

G. SCHMID[1], R. ÜBERBACHER[1], T. SAMARAS[2]

[1]ARC SEIBERSDORF RESEARCH GMBH, A-2444 SEIBERSDORF, AUSTRIA
[2]RADIOCOMMUNICATIONS LABORATORY, DEPARTMENT OF PHYSICS, ARISTOTLE UNIVERSITY OF THESSALONIKI; GR-54124 THESSALONIKI, GREECE

ABSTRACT

In order to allow detailed numerical RF dosimetry and computation of RF-induced temperature elevations in small anatomical structures, numerical models of the human eye and the inner ear organs (cochlea, labyrinth, auditory nerve, hearing bones) were developed based on frozen section techniques at a spatial resolution of 0.1 mm. After inserting these high resolution models into a commercially available head model, FDTD computations of SAR distribution and temperature elevations due to RF absorption were carried out using the SEMCAD X simulation platform. Generic models of handsets at 400 MHz, 900 MHz and 1850 MHz, operated in close proximity to the head, were considered as radiation sources.

Due to the heterogeneity in the area of the cochlea and the labyrinth (actually comprising highly conductive liquids surrounded by compact bone), the results showed a highly heterogeneous SAR distribution and SAR-peaks inside the cochlea and the labyrinth. However, temperature computations showed, that temperature elevations inside these organs are well below 0.1°C, when considering typical output power values of handheld devices (maximum for 400 MHz exposure).

In case of frontal exposure maximum temperature elevations in the eye of approximately 0.6°C were found for typical device output powers.

I. INTRODUCTION

The analysis of RF-power absorption and RF-induced temperature elevations in the human head, caused by handheld mobile communication devices, has been investigated in numerous scientific publications in recent years (e.g. [1]-[18]). In most cases computational techniques based on the Finite Difference Time Domain (FDTD) method were used for solving both the electromagnetic and the thermodynamic problem; the latter was mostly described by the Pennes' *Bioheat Transfer Equation* (BHTE) [19]. However, a detailed quantitative comparison of the results reported by these studies is difficult because of the variety of considered exposure situations and RF-source power levels, as well as the different head models used, which significantly affect the correlation between mass averaged Specific Absorption Rate (SAR) in the head and the temperature increase in specific tissues, as reported by [10]. When relating the temperature increase to the maximum10g averaged SAR in the head, the reported maximum temperature elevations in brain tissue are ranging between approximately 0.05°C/(W/kg) and 0.16°C/(W/kg). Concerning eye exposure, plane wave irradiation was considered in most cases in the past, mainly at frequencies beyond 1 GHz. Relating the maximum temperature increases in the eye found by these studies to the incident power density, the reported values are ranging between 0.003 °C/(W/m^2) and 0.006°C/(W/m^2).

The original spatial resolution of the numerical head models used in the above mentioned studies was usually not better than approximately 0.5 mm in horizontal direction and 1-2 mm in vertical direction (except [18], which were using 0.25 mm resolution for the eye). Due to this fact, anatomically small structures like the inner ear organs are, if at all, not accurately represented in these head models. Consequently, no detailed analysis of RF absorption in these organs and structures was possible so far.

In order to enable detailed RF dosimetry in the inner ear organs and in a detailed model of the eye, numerical models of the inner ear and the eye at a spatial resolution of 0.1mm x 0.1mm x 0.1mm were developed in this study and first results regarding RF-absorption and temperature elevations caused by generic phone models in the frequency range 400 MHz – 1850 MHz are presented.

II. MATERIAL AND METHODS

II.1. High resolution anatomical models of the inner ear and the eye

For developing the numerical model of the inner ear, vertical slices at a separation distance of 0.1 mm of a section of the left hemisphere of a real male human head (provided by the Center for Anatomy and Cell Biology, Medical University of Vienna) were obtained by frozen section technique (figure 1).
Each slice was scanned at a resolution of 1200 dpi using a commercially available document scanner (HP ScanJet 3970). Based on these digital images the segmentation (0.1 mm x 0.1 mm) of the *cochlea*, the *vestibulum*, the *canales semicirculares*, the *auditory ossicles* and the *tympanic membrane* as well as the conversion into a SAT-File format was carried out by IT'IS Foundation, Zurich, Switzerland. Exactly the same procedure was used for the development of the eye model, where *cornea*, *sclera*, *lens* and the optic nerve were distinguished during segmentation.

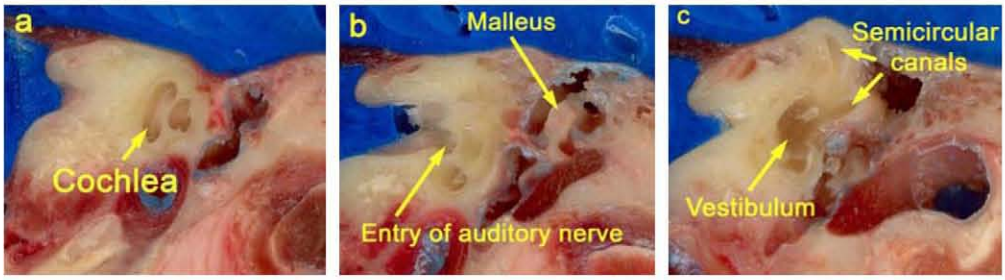


Figure 1: Examples of vertical cross sections through the human inner ear

Using the FDTD-based simulation platform SEMCAD X, the developed high resolution models of the inner ear organs and the eye were then inserted into a commercially available male head model based on the visual human data set (0.5 mm x 0.5 mm horizontal, 2 mm vertical resolution, 47 different tissue regions). In case of the inner ear model, the tympanic cavity, the external auditory canal as well as the auditory nerve were added by manual modeling and adjusted correspondingly in order to have an anatomically correct representation (figure 2). The yellow colored structure in the close-up view in figure 2 corresponds to the inner space of the labyrinth (cochlea, vestibulum, semicircular canals), which is filled with approximately 200 µl of perilymph- and endolymph-liquid. This structure is embedded in the highly compact petrous bone. In case of the eye model the lens' nucleus was added manually (figure 3).

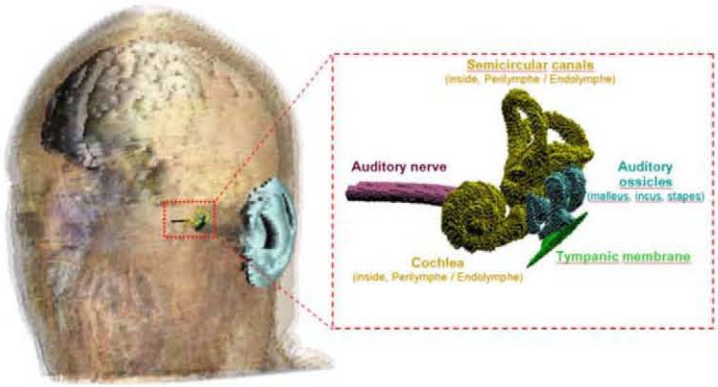


Figure 2: Anatomically correctly positioned high resolution inner ear organs inside a commercially available numerical head model

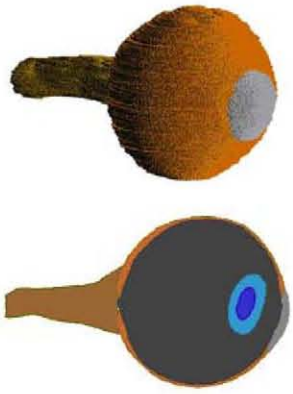


Figure 3: High resolution eye model in 3D view (top) and in a horizontal cross section (bottom)

II.2. Considered exposure conditions

Three different generic models of handsets, one per frequency, were considered as radiation sources. At 400 MHz a resonant helix antenna (axial length 61 mm, helix diameter 8.6 mm, wire diameter 1 mm, 14 turns) on top of metallic box (130 mm x 50 mm x 30 mm) was considered as a representative model for a hand held radio set such as used for example in a TETRA system. For 900 MHz and 1850 MHz quarter wave

monopoles (diameter 2 mm) on top of a metallic box (100 mm x 40 mm x 20 mm) were chosen as representatives for mobile phones of the GSM900 and the DCS1800 and UMTS systems, respectively. For each radiation source lateral exposure in "Tilt" position as well as frontal exposure with a distance between the antenna's feedpoint and the left eye of approximately 2.5 cm were considered. Figure 4 shows the 6 different exposure conditions.

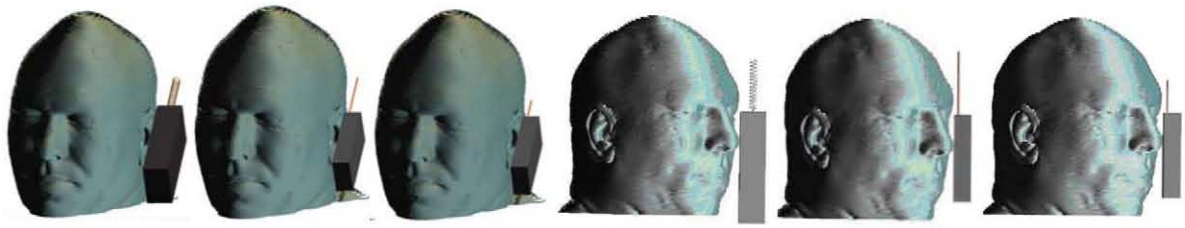


Figure 4: Considered exposure conditions. left: lateral exposure in "tilt" position at 400 MHz, 900 MHz and 1850 MHz, right: frontal exposure at 400 MHz, 900 MHz and 1850 MHz

II.3. Computational techniques used

The FDTD based SEMCAD X simulation platform was used for both the electromagnetic as well as the thermodynamic computations. The used thermodynamic solver was based on Pennes' BHTE and both the electromagnetic as well as the thermodynamic computations were carried out on the same FDTD grid, using a graded mesh with mesh size between 0.25 and 5 mm. However, in the irradiated hemisphere the maximum grid step was kept below 1.5 mm and constant at 0.25 mm in the region of the high resolution models of the inner ear region and the eye. This resulted in a total of approximately 20-25 million FDTD cells, depending on the considered source model.

II.4. Tissue parameters and boundary conditions

For the dielectric properties of the tissues values according to [20] were taken. With respect to the thermal properties 19 different materials were allocated to the more than 50 different tissue regions in the head model (including the high resolution inner ear and eye). Table 1 lists the used thermal properties, which were derived from several sources in the literature (e.g. [1],[13],[21]).

Table 1: Thermal tissue properties used

material	density [kg/m³]	specific heat [J/kg.K]	thermal conductivity [W/m.K]	perfusion [ml/min.kg]	metabolic heat [W/kg]
blood	1060	3780	0.51	10000	0
bone	1850	1300	0.39	11.5	0.15
brain average	1040	3650	0.55	608.5	9.70
cartilage	1100	3521	0.46	50	0.18
cerebellum	1040	3670	0.55	510	9.70
cerebrospin. fluid	1005	4116	0.59	0	0
cornea	1076	3793	0.52	38	0.32
fat (not infiltrated)	920	2493	0.24	25.3	0.15
gland tissue	1040	3600	0.53	3059	9.79
grey matter	1040	3684	0.57	608.5	9.70
lens	1080	3133	0.43	0	0
marrow	1020	3120	0.32	219	5.50
muscle	1045	3580	0.5	26.6	0.67
nerve tissue	1040	3582	0.46	37.7	9.61
skin dry	1140	3600	0.37	86.6	0.18
skin wet	1140	3600	0.37	86.6	0.18
tongue	1045	3580	0.5	26.6	0.67
vitreous humor	1003	3997	0.59	0	0.34
white matter	1040	3611	0.5	262.5	9.70

At the thermal boundary between the head model and the ambient a heat transfer of 8 W/(m^2K) at a nominal ambient temperature of 25°C was assumed. Thermal boundaries between air filled cavities inside the head model and their bounding tissues were assumed to be 4 W/(m^2K) at 37°C, except for the nasal cavity and the ear channel, where 30 W/(m^2K) at 35°C and 6.3 W/(m^2K) at 35°C were chosen, respectively.

III. RESULTS

Lateral exposure

Figure 5 depicts the distribution of SAR (not averaged, normalized to 1W radiated power) in a cross section of the head through the cochlea for all three frequencies considered. With respect to the inner ear, relatively high local SAR values appear inside the peri-/endolymph-filled labyrinth compared to the surrounding bone, especially at 400 MHz. This is due to the relatively high conductivity of peri-/endolymph, which is very similar to cerebrospinal fluid. In the last row of figure 5 the SAR distribution on the surface of middle- and inner ear organs (labyrinth, auditory nerve, tympanic membrane, auditory ossicles, compare figure 2) is shown.

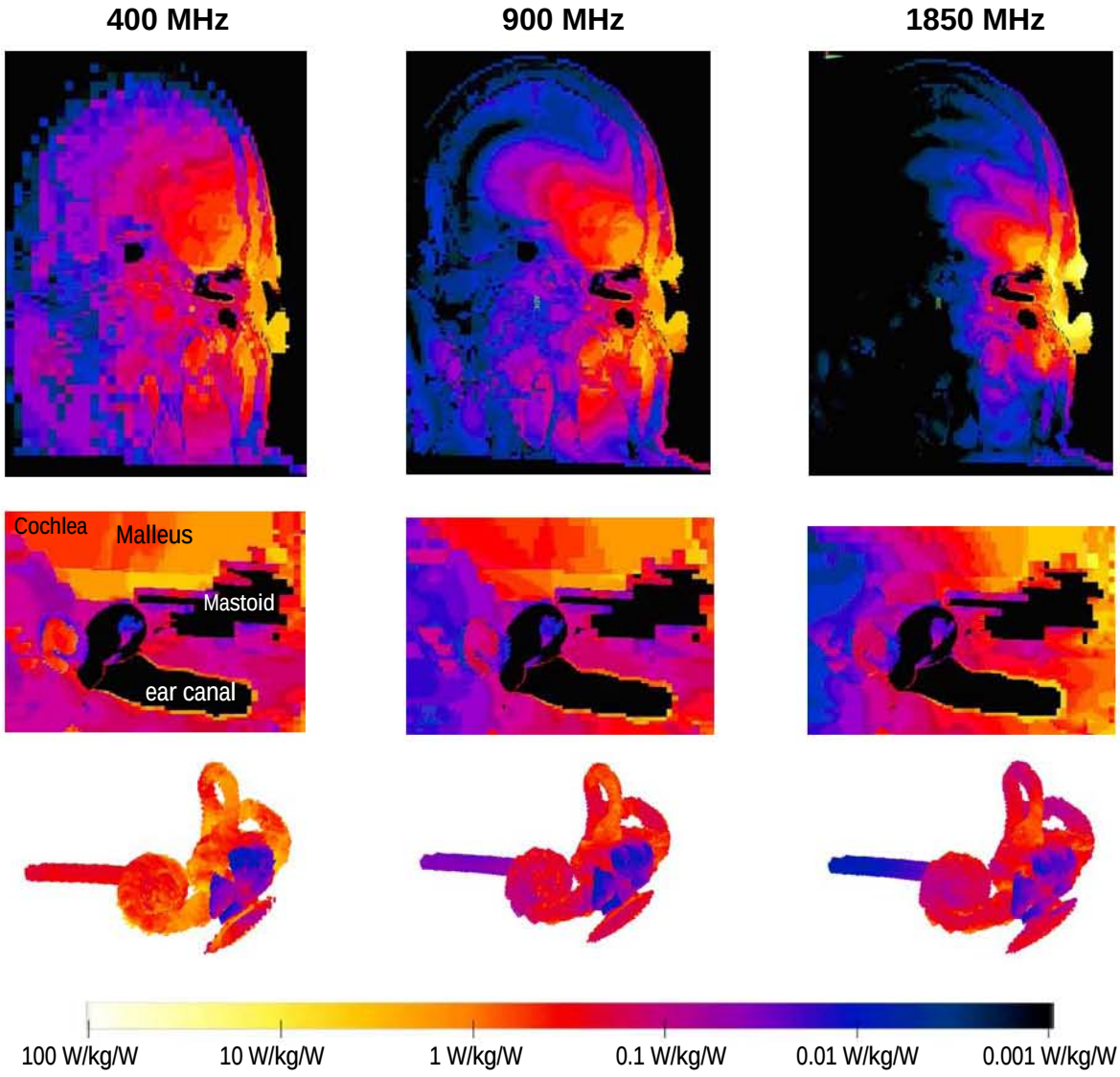


Figure 5: SAR distributions (not averaged, normalized to 1W source power) in a cross section of the head through the cochlea for 400 MHz (left column), 900 MHz (center column) and 1850 MHz (right column). At the bottom the SAR distribution on the surface of the middle- and inner ear organs is shown.

Despite of the inhomogeneous distribution of SAR inside the head, the thermodynamic computations show only very low temperature increases in it. Figure 6 illustrates the maximum temperature elevation in specific tissues, within the time period from switching on the radiation until thermal equilibrium is reached (after approx. 20 minutes). Note that the values in figure 6 are normalized to the case of a 10g averaged SAR of 2 W/kg in the head, i.e., the limit for localized exposure according to [22] and [23].

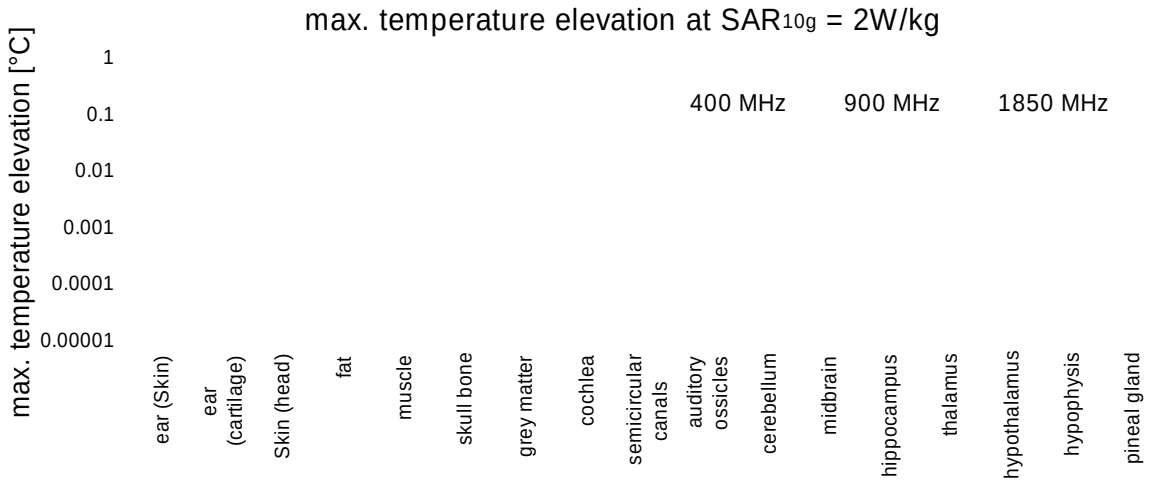


Figure 6: Maximum temperature elevation in specific tissues and organs due to a lateral exposure according to the current limit for localized exposure according to [22] and [23].

As it can be seen from the figure maximum temperature elevations are highest for 400 MHz due to the high penetration depth and the more homogeneous heating of the head, which causes lower temperature gradients and therefore less effective heat conduction inside the head. However, the absolute values of the obtained temperature elevations are rather small. They are below 0.05°C for grey matter, below 0.025°C in the inner ear organs and below 0.01°C in deep brain tissues. More superficial tissues as bone, muscles, fat and the skin on the head showed an increase in temperature between 0.1°C and 0.25°C. The absolute maximum temperature increase was obtained in the skin of the pinna and was approximately 0.9°C.

Front exposure

The distribution of SAR in case of having the radiation source in front of the left eye is shown in figure 7. Non averaged SAR values, normalized to 1 W radiated power are shown in a horizontal cross section of the head through the eye.

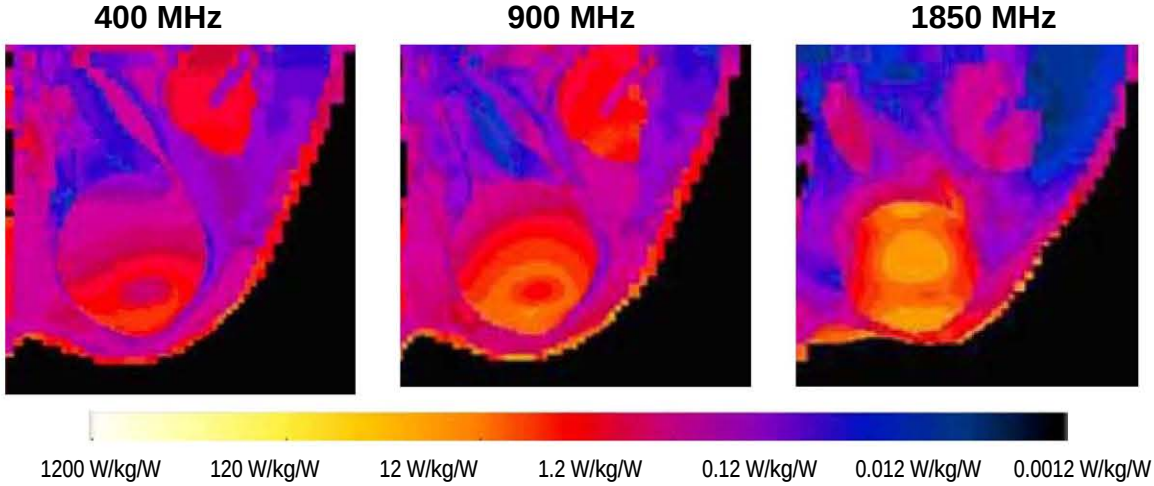


Figure 7: SAR distributions (not averaged, normalized to 1W source power) in a cross section of the head through the eye for 400 MHz (left column), 900 MHz (center column) and 1850 MHz (right column).

RF absorption in the eye increases with frequency and at 1850 MHz a “standing wave pattern” with a SAR maximum approximately in the center of the eye can be observed. This is due to the fact that at 1850 MHz the eye diameter is approximately one wavelength (in tissue) of the radiation frequency.
The maximum temperature elevations in specific tissues, within the time period from switching on the radiation until thermal equilibrium is reached (after approx. 20 minutes) are depicted in figure 8. Again the given values are normalized to the case of a 10g averaged SAR of 2 W/kg in the head.

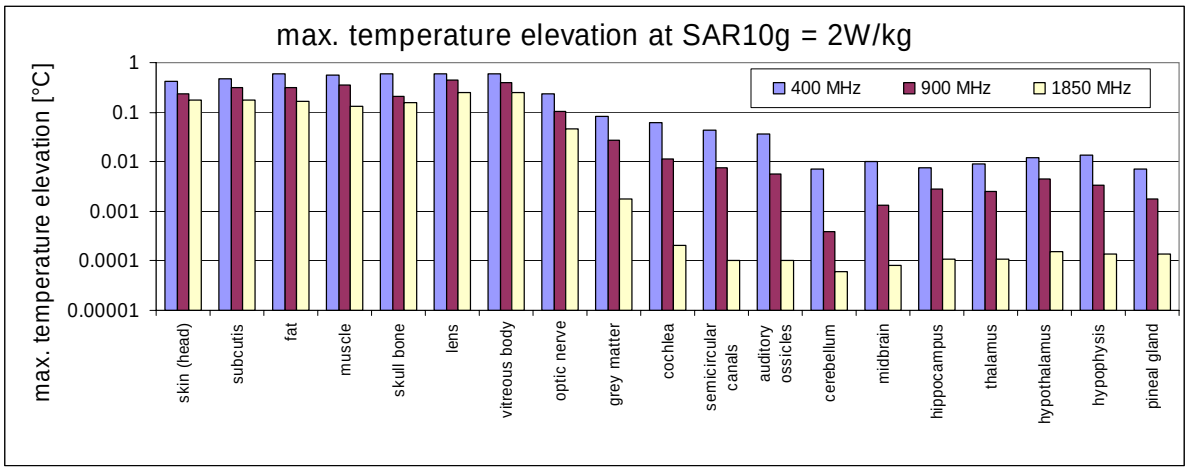


Figure 8: Maximum temperature elevation in specific tissues and organs due to a frontal exposure according to the current limit for localized exposure according to [22] and [23].

Although the highest peak SAR values in the eye were obtained for the high (1850 MHz) frequency, the maximum temperature elevations appear again for a 400 MHz irradiation. The absolute maximum temperature elevation was observed in the lens and was approximately 0.6°C. Maximum temperature elevations in other (superficial) tissues are approximately in the same order of magnitude, ranging from 0.2°C to 0.6°C. In the optic nerve and in grey matter tissue temperature elevations up to approximately 0.25°C and 0.09°C were found, respectively. Interestingly, the temperature elevations in the middle and inner ear regions appear somewhat higher during frontal exposure compared to the case of lateral exposure. This effect, however needs to be investigated further, because it might be affected by the different spatial discretizations of the computation domain used for frontal and lateral exposure.

Influence of perfusion and ambient temperature
In order to estimate the impact of variations in the ambient temperature and in blood perfusion, computations (at 400 MHz) were carried out with tissue perfusion (all tissues) reduced to 50% of the nominal values listed in table 1, and an ambient temperature of 35°C (instead of a nominal value of 25°C). All other parameters remained unchanged. The results clearly show that for tissue regions deep inside the head a change in ambient temperature does not play an important role, whereas a reduction of perfusion by 50% increases the observed maximum temperature elevations by up to a factor of 2.5 in these tissues. For more superficially located tissues (skin, cartilage, fat, subcutis, bone) both perfusion as well as ambient temperature play a role with respect to the maximum temperature elevation.

Pulsed radiation
Current safety standards, e.g. [22], define the basic restriction for localized exposure in terms of a 6 minute average SAR. This means that for shorter times higher temporal peak SAR values are allowed. Therefore we investigated (at 400 MHz) the effect of pulsed radiation by applying short exposure peaks (in terms of 10g averaged SAR) of 4 W/kg, 12 W/kg and 72 W/kg for 180 s, 60 s and 10 s within a continuously repeated 6 minute interval, respectively. All of these cases lead to a 6 minute average SAR of 2 W/kg. The comparison of the pulsed exposure with a continuous wave exposure at 2 W/kg showed increased maximum temperature elevations for the mentioned kind of pulsed exposure. Tissues deep inside the head were significantly more affected by this effect than superficial tissues. The worst of the considered cases was the repeated 10 s / 72 W/kg lateral exposure, which, for example, leads to a relative increase of the maximum temperature elevation in the skin by a factor of 2 compared to a factor of 11 in the hypothalamus.

IV. CONCLUSION

In general, the obtained results showed that for exposure situations typical for usage of modern digital mobile phones the RF-induced temperature elevations inside the head are rather small. Although a very heterogeneous pattern of RF power dissipation could be observed due to the significantly different dielectric properties of the different tissues, no temperature "hot spots" are to be expected due the efficient heat transfer mechanisms taking place in the tissues (heat conduction and heat transfer by perfusion). As far as comparable, when relating the maximum temperature elevations to the 10g averaged SAR in the head, our results are in line with results reported by other authors ([1]-[18]), even though our results appear to be at the lower end of the range of RF-induced temperature elevation stated in [1]-[18]. This might be caused by the specific properties of the used head model (based on the visual human data set) with respect to its tissue composition [10].
The observation that, with respect to the maximum RF-induced temperature elevations, inner tissues are significantly more affected by pulsed radiation at constant 6 minute averaged SAR than superficial tissues might be of biological interest, because heat perception mainly takes place inside the superficially located skin. However, it has to be noted that the time course of the exposure and the required peak RF power leading to such effects (a single high peak in repeated 6 minute intervals) are not typical for mobile communication devices.

ACKNOWLEDGEMENTS

This work was sponsored by the Federal Office for Radiation Protection, Germany, in the frame of the German Mobile Telecommunication Research Program. Furthermore the authors gratefully acknowledge the support by Prof. Manfred Tschabitscher, Center for Anatomy and Cell Biology, Medical University of Vienna, and Anja Klingenböck, IT'IS, Zurich, Switzerland.

REFERENCES

[1] G. M. J. van Leeuwen, J. J. W. Lagendijk, B. J. A. M. van Leersum, A. P. M. Zwamborn, S. N. Hornsleth and A. N. T. J. Kotte, "Calculation of change in brain temperatures due to exposure to a mobile phone", Phys Med Biol, vol. 44, pp. 2367-2379, 1999.

[2] O. P. Gandhi, Q.-X. Li and G. Kang, "Temperature rise for the human head for cellular telephones and for peak SARs prescribed in safety guidelines", IEEE Trans Microwave Theory Techn, vol. 49, pp. 1607-1613, 2001.

[3] J. Wang and O. Fujiwara, "FDTD computation of temperature rise in the human head for portable telephones", *IEEE Trans Microwave Theory Techn*, vol. 47, pp. 1528-1534, 1999.

[4] International Commission on Non-Ionizing Radiation Protection, "Guidelines for limiting exposure to time-varying electric, magnetic, and electromagnetic fields (up to 300 GHz)", *Health Physics*, vol. 74, pp. 494-522, 1998.

[5] P. Bernardi, M. Cavagnaro, S. Pisa and E. Piuzzi, "Specific absorption rate and temperature increases in the head of a cellular-phone user", *IEEE Trans Microwave Theory Techn*, vol. 48, pp. 1118-1126, 2000.

[6] P. Bernardi, M. Cavagnaro, S. Pisa and E. Piuzzi, "Power absorption and temperature elevations induced in the human head by a dual-band monopole-helix antenna phone", *IEEE Trans Microwave Theory Techn*, vol. 49, pp. 1118-1126, 2001.

[7] P. Wainwright, "Thermal effects of radiation from cellular telephones", *Phys Med Biol*, vol. 45, pp. 2363-2372, 2000.

[8] T. V. Yioultsis, T. I. Kosmanis, E. P. Kosmidou, T. T. Zygiridis, N. V. Kantartzis, T. D. Xenos and T. D. Tsiboukis, "A comparative study of the biological effects of various mobile phone and wireless LAN antennas", *IEEE Trans Magn*, vol. 38, pp. 777-780, 2002.

[9] A. Hirata, M. Morita and T. Shiozawa, "Temperature increase in the human head due to a dipole antenna at microwave frequencies", *IEEE Trans Electromagn Compat*, vol. 45, pp. 109-116, 2003.

[10] A. Hirata and T. Shiozawa, "Correlation of maximum temperature increase and peak SAR in the human head due to handset antennas", *IEEE Trans Microwave Theory Techn*, vol. 51, pp. 1834-1841, 2003.

[11] J. A. Scott, "A finite element model of heat transport in the human eye", *Phys Med Biol*, vol. 33, pp. 227-242, 1988.

[12] A. Taflove and M. E. Brodwin, "Computation of the electromagnetic fields and induced temperatures within a model of the microwave-irradiated human eye", *IEEE Trans Microwave Theory Techn*, vol. 23, pp. 888-896, 1975.

[13] P. Bernardi, M. Cavagnaro, S. Pisa and E. Piuzzi, “SAR distribution and temperature increase in an anatomical model of the human eye exposed to the field radiated by a user antenna in a wireless LAN”, *IEEE Trans Microwave Theory Techn*, vol. 46, pp. 2074-2082, 1998.
[14] A. Hirata, G. Ushio and T. Shiozawa, “Calculation of temperature rises in the human eye exposed to EM waves in the ISM frequency bands”, *IEICE Trans Comm*, vol. E83-B, pp. 541-548, 2000.
[15] A. Hirata, S. Matsuyama and T. Shiozawa, “Temperature rises in the human eye exposed to EM waves in the frequency range 0.6-6GHz”, *IEEE Trans Electromagn Compat*, vol. 42, pp. 386-393, 2000.
[16] A. Hirata, H. Watanabe and T. Shiozawa, “SAR and temperature increase in the human eye induced by obliquely incident plane waves”, *IEEE Trans Electromagn Compat*, vol. 44, pp. 592-594, 2000.
[17] A. Hirata, “Temperature increase in human eyes due to near field and far field exposures at 900 MHz, 1.5 GHz and 1.9 GHz”, IEEE Trans Electromagn Compat, vol. 47, (1), pp.68-76, 2005
[18] V.V.M. Flyckt, B.W. Raaymakers, H.Kroeze, J.J.W. Lagendijk,"Temperature rise in the human eye and orbit due to RF exposure calculated with a realistic vascularized model: temperature distributions and the enormous impact of cooling by perfusion", 17th International Zurich Symposium on Electromagnetic Compatibility, Singapore, 2006
[19] H. H. Pennes, “Analysis of tissue and arterial blood temperatures in the resting human forearm”, J Appl Physiol, vol. 1, pp. 93-122, 1948.
[20] Gabriel S, Lau RW, Gabriel C (1996c). ”The dielectric properties of biological tissues: III. Parametric models for the dielectric spectrum of tissues”, Phys. Med. Biol. 41:2271-2293.
[21] F.A. Duck, ”Physical Properties of Tissue, A comprehensive reference book”, Academic Press Ltd., London, 1990, ISBN 0-12-222800-6
[22] ICNIRP International Commission on Non-Ionizing Radiation Protection, “Guidelines for limiting exposure in time-varying electric, magnetic and electromagnetic fields (up to 300 GHz)”, Health Physics 74, 494-522, 1998.
[23] IEEE Std C95.1-2005, “Standard for Safety Levels with Respect to Human Exposure to Radio Frequency Electromagnetic Fields, 3 kHz to 300 GHz”, IEEE, New York, USA, 19.04.2006

MODEL FOR NECK WHEN ESTIMATING EXPOSURE TO ELECTRIC FIELDS AT 400 KV SUBSTATIONS

TONI LÅNGSJÖ[1], JARI LATVA-TEIKARI[1], JARMO ELOVAARA[2], LEENA KORPINEN[1,3]

[1] LAB.OF ELECTRICAL ENGINEERING AND HEALTH, TAMPERE UNIV, OF TECH., P.O. BOX 692, 33101 TAMPERE, FINLAND
[2] FINGRID OYJ, P.O. BOX 530, 00101 HELSINKI, FINLAND
[3] FACULTY OF TECH., THE DEPARTMENT OF ELECTRICAL ENGINEERING AND AUTOMATION, UNIV. OF VAASA, P.O. BOX 700, 65101 VAASA, FINLAND

Abstract

Directive 2004/40/EC sets action and exposure limit values for people working in electric and magnetic fields. Electric field action values for 50 Hz frequency might be exceeded in existing 400 kV air-insulated substations. Therefore measurements in Finnish 400 kV substations were conducted to find out whether the limit value of induced current density (10 mA/m^2) is exceeded in the human central nervous system. One of the most critical areas is the neck. Measurements were made with a specific system connected to the test person, who simulated practical work in actual and practical working conditions. The developed system measures the current induced in the head as well as the total current induced in the body of the test person.

The maximum average current density in the cross-sectional area of 40 cm collar-size neck was 6.81 mA/m^2, even if the action value for the electric field strength was clearly exceeded. The margin to the limit value 10 mA/m^2 is obvious, but further analysis was necessary due to individual variations etc. Consequently, a model for analyzing current densities in the cross-sectional area of the neck, especially in central nervous system, was developed.

The model described 9 different tissues in the neck area. Currents and current densities in the tissues were calculated when the average current density had a given value. The result was that only 0.13 % of the total current in the neck area flows through the spinal cord causing in it a current density 0.72 mA/m^2 when the average current density in the neck area is 6.81 mA/m^2 (collar size 40 cm assumed). Thus, it seems that the substation workers are not exposed to current densities in practical work situations within the body, which would exceed the directive's limit value.

Keywords: *occupational exposure, induced current density, central nervous system*

1. Introduction

Power frequency electric and magnetic fields occur in electricity generation, transmission, distribution and consumption. Occupational exposure to electric fields is common especially in electricity transmission and distribution. Accordingly, exposure in certain places is larger than in other places. In 400 kV air-insulated outdoor substations the exposure of the workers to the electric fields is one of the largest areas. We will concentrate on electric fields instead of magnetic fields, because in 400 kV outdoor substations electric fields in practice cause more remarkable current density in the human body than magnetic fields.

The European Union (EU) sets action and limit values for occupational exposure to electric fields in directive 2004/40/EC. The action value for 50 Hz electric field is set as electric field strength and it is 10 kV/m. In case action value is exceeded the employer has to make sure the limit value will not be exceeded. Limit value is set as induced current density in the central nervous system in the head or trunk and it must not exceed 10 mA/m^2. Limit value is set to protect tissues in the central nervous system for acute effects of exposure. [1]